SYNTHESIS, EPR SPECTROSCOPY, AND MATRIX-ISOLATION DECAY KINETICS OF TRIPLET CYCLOBUTANEDIYLS

Thesis by

MICHAEL B. SPONSLER

In Partial Fulfillment of the Requirements

for the Degree of

Doctor of Philosophy

California Institute of Technology

Pasadena, California

1987

(Submitted February 6, 1987)

To Diana

Acknowledgements

Of the many people who deserve mention, Dennis Dougherty merits special comment. As my advisor, Dennis has contributed tremendously to my growth at Caltech, personal as well as scientific. I very much admire the balanced approach he adopts with any undertaking, always sensitive to the various considerations of scientific importance, pedagogical value, and probability of success. I am most grateful for the leadership model Dennis has provided.

A large amount of credit is also due to the other members of the Dougherty group, both past and present. Work and leisure in the group have been truly pleasurable experiences. I also thank others in the division, including professors, students, staff members, and shop personnel for their willingness to help in any matter.

Several people deserve special acknowledgement for their help in preparing this thesis. Gwen Anastasi did a tremendous job of typing such a large volume in such a short time. Dave Stauffer was invaluable as a proofreader, and Brenda and Carlos Quintero provided much-needed help when the deadline grew near.

Abstract

Chapter 1

Bicyclo[1.1.1]pentanone (**11**) has been prepared in two steps, the key reaction being the ozonolysis of 2-phenylbicyclo[1.1.1]pentan-2-ol (**24**). The microwave spectra of five isotopic species of **11** have been obtained, allowing a complete r_s structure determination for the heavy atoms. Analysis of Stark-effect measurements has shown the dipole moment to be along the a principle inertial axis with a magnitude of 3.164(5) D. These results are compared with those obtained using molecular mechanics (MM2), MNDO, and Hartree-Fock ab initio theory with STO-3G and 3-21G basis sets. On heating, **11** undergoes cycloreversion to allylketene (**31**). The activation parameters and solvent effects for this process suggest that the reaction is concerted and that the transition state is relatively nonpolar. The predominant photochemical pathway for **11** is decarbonylation to bicyclobutane (**34**). Cycloreversion to **31** is a minor reaction mode. Both the thermal and photochemical results are rationalized by considering the high strain energy and novel geometrical features of **11** and, in the latter case, the unusually high energy of its $^1(n\pi^*)$ state.

Chapter 2

Ab initio theoretical methods have been applied to cyclobutanediyl. The geometry of the triplet biradical was optimized under the constraints of D_{2h} symmetry. At the

optimum geometry, the singlet-triplet energy gap was found to be 1.74 kcal/mol, with the ground state being the triplet. The closure reaction to bicyclo[1.1.0]butane (**34**) was investigated using a linear synchronous transit reaction coordinate. A barrier of 6.6 kcal/mol was obtained for the singlet surface, representing an upper limit to the actual barrier. Calculations on 1,3-dimethylcyclobutanediyl (**12**) show that the methyl groups do not strongly affect the singlet-triplet gap, reducing it to 1.47 kcal/mol.

Chapter 3

The synthesis and EPR spectroscopy of 1,3-divinyl- and 3-ethyl-1-vinylcyclobutanediyl (**46-Vin** and **-EV**) are described and compared with results for other cyclobutanediyls. The triplet biradicals were generated by photolysis of the appropriate 2,3-diazabicyclo[2.1.1]-hex-2-enes (**47**) in frozen-solvent matrices at cryogenic temperatures. A general synthetic scheme allowing the preparation of many diazenes has been developed. The key step is the photochemical addition of methyltriazolinedione to 1,3-dicarbomethoxybicyclo[1.1.0]butane (**49**), giving the dicarbomethoxyurazole **15**. The triplet EPR spectra offer valuable insights into the electronic structure of the cyclobutanediyls and the role played by the substituents. Both zero-field splitting and hyperfine coupling emerge as sensitive gauges for determining the distribution of spin density in the biradicals.

Chapter 4

The nonexponential decay kinetics of 1,3-divinyl- and 3-ethyl-1-vinylcyclobutanediyl (**46-Vin** and **-EV**) has been quantitatively analyzed in the 20-54 K temperature range using two methods based upon a distribution of first-order rate constants. A numerical procedure for fitting of decay traces based upon an assumption of distribution shape has been modified to allow fitting of the signal growth during photolysis as well as the decay. This method successfully reproduced our data using a variety of distribution shapes. A new method for analysis of dispersive kinetics, called distribution slicing, has been developed. This method allows detailed determination of distribution shapes and is complementary to decay-trace fitting in several other ways. The two methods have been combined to eliminate several problems encountered in the separate methods, allowing the determination of approximate activation parameters. An approximate log A value of 7.5 was determined for the decay of **46-Vin** along with most-probable activation energies in the range 1.2 to 1.7 kcal/mol, depending on the matrix material. Using the same log A value, **46-EV** gives most-probable activation energies of 1.4 and 0.9 kcal/mol in MTHF and heptane, respectively. The stability of these biradicals relative to the dialkyl cyclobutanediyls was rationalized in terms of hypothetical potential energy surfaces.

TABLE OF CONTENTS

LIST OF TABLES

LIST OF FIGURES

INTRODUCTION

Elucidation of an organic reaction mechanism very often involves determining whether the process is stepwise or concerted. The nature of the intermediate in the stepwise path, typically a biradical, is central to the question of pathway. Therefore, direct information regarding the structures of such reactive intermediates is crucial for the detailed study of mechanism.

Most of the current knowledge about biradicals has been obtained indirectly through product and kinetic studies.[1] Compared to free radicals, relatively few biradicals have been directly characterized, despite their broad acceptance as intermediates in both thermal and photochemical reactions. The radical reactions of combination and disproportionation are much faster for biradicals, being intramolecular. For this reason, investigators have often turned to theoretical calculations for the structural information required in mechanistic determinations. However, biradicals, with their complex electronic interactions, have also proven to be great challenges to theorists.[2] As a result, direct experimental observations are necessary to calibrate and corroborate the calculations.

Biradicals are commonly defined as single molecules that contain two free radicals. A more general description based on molecular orbital theory is sometimes preferable: a molecule that has a pair of singly occupied degenerate, or

nearly degenerate, nonbonding molecular orbitals (NBMOs).[2] There are two low-lying states in a biradical, that in which the two lone electrons are paired (singlet) and that in which they are unpaired (triplet). Singlet (S) and triplet (T) may differ markedly in their properties,[3] and the energy separation between the two states, commonly called the S-T gap, is of fundamental importance in the characterization of a biradical. A large part of the challenge for theorists lies in the accurate calculation of the S-T gap.[2,4] Unfortunately, experimental determination of this quantity is even more difficult, and there is no generally applicable method available.

Biradicals may be classified as either localized or delocalized, the latter class representing the vast majority of directly observed biradicals. A delocalized biradical is one in which the two unpaired electrons are conjugated in the same planar π system. Belonging also to the class of non-Kekule molecules,[5] these biradicals have no closed-shell form, barring the formation of σ bonds. A large number of the known delocalized biradicals are derivatives of trimethylenemethane (1),[6] tetramethyleneethane (2),[7] and m-quinodimethane (3).[8]

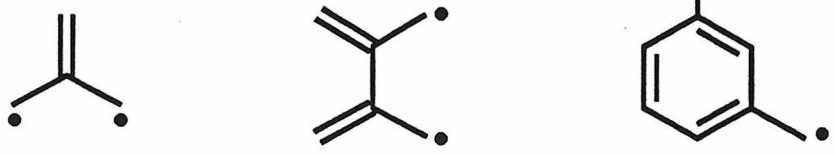

In contrast, localized biradicals have their unpaired electrons in separate, nonconjugated radical substructures. One or both of the radicals may in fact be delocalized, residing in, for example, allylic or benzylic substructures. The first direct observation of a hydrocarbon localized biradical was made by Buchwalter and Closs in 1975 when they recorded the triplet EPR spectrum of cyclopentane-1,3-diyl (**4**).[9] The biradical was generated by photolysis of 2,3-diazabicyclo[2.2.1]hept-2-ene (**5**) in frozen cyclohexane at cryogenic temperatures. The triplet signal decayed non-exponentially in the temperature range from 1.3 to 40 K and displayed temperature-independent initial rates below 20 K. The decay process was assigned to the closure reaction giving bicyclo[2.1.0]pentane (**6**) and was proposed to proceed via heavy-atom tunneling. Analysis of the kinetics based on the Bell tunneling model gave an activation energy of 2.3 kcal/mol using an approximate pre-exponential factor of 10^8.

4

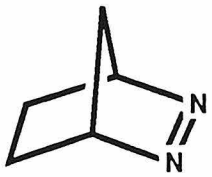

5

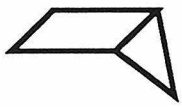

6

Although Closs' success offered hope for characterization of other localized biradicals, extension to other systems has been almost uniformly unsuccessful. Other azoalkane ring systems gave no triplet spectra,[10] and even simple methyl substitutions on the diazabicycloheptene system

resulted in loss or weakening of the signals.[9] Ab initio calculations by Goldberg and Dougherty[11] suggested that the reason for these failures lies in a fine balance of electronic interactions affecting the S-T gap. In particular, they found that the S-T gap in (0,0)-trimethylene (7) is strongly dependent on the C-C-C angle, the triplet being favored for angles between 96° and 120°.[12] Their results helped to illuminate the important structural features that allow detection of **4**.

7

8

Goldberg and Dougherty also proposed cyclobutane-1,3-diyl (**8**) as a good candidate for EPR detection, having a calculated S-T gap of 1.7 kcal/mol, nearly twice that found for **4** (0.9 kcal/mol).[11] (Extensions of this theoretical work are described in Chapter 2.) The azoalkane precursor, 2,3-diazabicyclo[2.1.1]hex-2-ene (**9**), was therefore prepared by Chang and Dougherty.[13] Upon photolysis at cryogenic temperatures, however, no triplet signal was observed.[14] The photochemistry of **9** (eq. 1) was shown to depart from that of most azoalkanes, and this was suggested as a possible reason for the failure of the EPR experiment. Instead of the desired C-N cleavage, the excited triplet of **9** undergoes mainly β C-C cleavage to give the nitrogen-retained product **10**, as shown by sensitization studies.

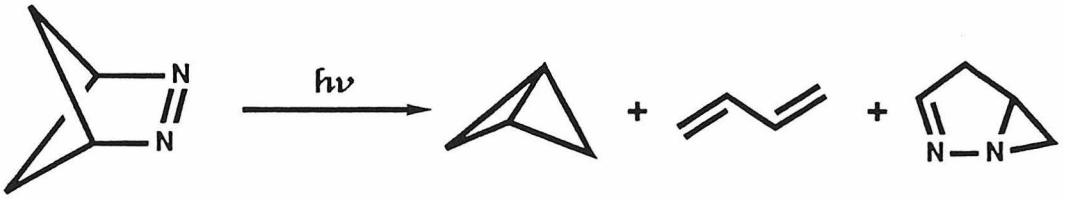

(1)

9 **10**

In order to avoid this problem of photochemistry, an alternative precursor to **1** was sought. For this purpose, bicyclo[1.1.1]pentanone (**11**) was prepared; its synthesis, chemistry, and structure (microwave and theoretical) are described in Chapter 1. The EPR experiment using **11** also failed to produce a triplet spectrum. The failure of both precursors suggests that despite its large predicted S-T gap, **8** is too reactive to be observed.

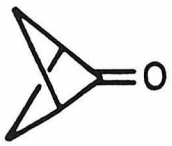

11

The second direct observation of a localized biradical came nearly a decade after the first, in 1984, when Jain, Snyder and Dougherty obtained the triplet EPR spectrum of 1,3-dimethylcyclobutane-1,3-diyl (**12**).[15] As for **4**, the triplet signal was generated by photolysis of the azoalkane precursor, 1,4-dimethyl-2,3-diazabicyclo[2.1.1]hex-2-ene (**13**). The photochemistry of **13**[16] was completely analogous to that of **9**, eliminating this as a possible cause for failure in the generation of **8**. Temperature-insensitive, nonexponential decay was observed for **12** in the temperature

range from 4 to 25K, suggesting a tunneling process. The Bell model was used with most-probable rates (obtained by a distribution-modeling method described in Chapter 3) for decay of **12** in 2-methyltetrahydrofuran (MTHF) to obtain an activation energy of 0.75 kcal/mol (assuming the same pre-exponential factor as that of Closs: 10^8). The decay process was shown to be closure, giving 1,3-dimethylbicyclo [1.1.0]-butane (**14**). Extension of the kinetic analysis to **8**, assuming identical parameters except for mass, showed that the analogous tunneling process should be fast enough to make **8** unobservable.

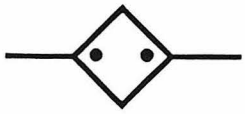

12

13

14

Encouraged by the successful observation of **12**, we then sought to characterize other cyclobutanediyls. Our goal was to investigate the effects of various radical substituents on triplet biradical spectroscopy and stability. Concerning stability, we reasoned that four separate effects might be observed. First, the triplets might be stabilized by substituents that are known to stabilize free radicals. Second, addition of mass to the molecule might reduce the tunneling decay rate. Third, increasing the size of the substituents might slow the closure reaction due to steric interactions with the solvent matrix. A combination of these

three effects is presumably responsible for the observation of 12 but not 8.[16] Finally, substituents may influence the S-T gap, perhaps greatly affecting triplet stability.

A general scheme for the synthesis of bridgehead-substituted 2,3-diazabicyclo[2.1.1]hex-2-enes was needed. This was accomplished through the preparation of the dicarbomethoxy urazole 15 and subsequent functional-group modification of the ester groups. Conversion of the resulting urazoles to azoalkanes was achieved via standard procedures. This synthetic scheme, which is described in detail in Chapter 3, allowed the preparation of many azoalkanes, including the diethyl (16), ethyl vinyl (17), and divinyl species (18).[17]

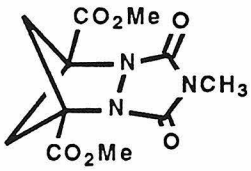

15

16

17

18

When photolyzed at cryogenic temperatures, 16, 17, and 18 produce triplet EPR spectra, which have been assigned to 19, 20, and 21, respectively. The observed zero-field and hyperfine splittings are fully supportive of the assignments and offer valuable information about the distribution of spin density in the biradicals. As expected, the delocalizing vinyl substituents lower the spin density on the ring carbons. The splittings in 19 are identical to those in the dimethyl biradical 12, indicating that the two species are electronically equivalent.[16]

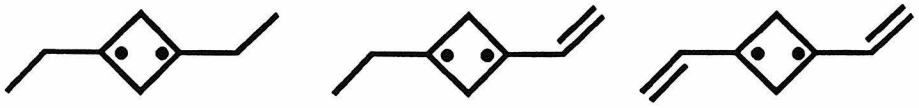

19 **20** **21**

Comparison of the kinetic stabilities to closure for the four cyclobutanediyls, **12** and **19-21**, significantly unravels the various substituent effects upon stability. Qualitatively, the triplet biradicals are increasingly stable in the series **12**, **19**, **20**, and **21**, with a relatively small difference between the last two. The stability difference between **12** and **19** can be attributed only to substituent mass or size effects, since the two biradicals are electronically equivalent, as noted above. The size effect is believed to be small, since tunneling analysis, based only on mass differences, quantitatively accounts for the observed kinetics. Mass and size effects can be eliminated in the comparison of **19-21**, due to the similarity between the ethyl and vinyl groups. Stability differences in this series can be attributed solely to radical delocalization. Though the S-T gaps are also expected to be different, the effect on stability should be in the opposite direction. Delocalization of the radicals away from each other should reduce exchange interactions, which favor the triplet. Thus, one might expect a smaller S-T gap and hence faster intersystem crossing to the singlet in **20** and **21**.

Quantitative analysis of the decay kinetics, which was nonexponential in all cases, was not straightforward, and substantial effort was applied to this task.[18] Non-exponential kinetics are quite common for matrix-isolated, first-order processes and are usually interpreted as a consequence of the matrix-site effect.[9,19] The microenvironments of different molecules in a solid matrix are not necessarily identical, so they may display different properties, such as different reaction rates. Thus, instead of a single rate constant, a reaction may be characterized by a distribution of rate constants. The observed decay is then a superposition of two or more exponential decays.

Several methods exist in the literature for analysis of kinetics based on a distribution model,[20] but we found most of them to give poor results, presumably due to assumptions that are invalid for the present case. One procedure, which requires the assumption of a distribution shape (e.g., Gaussian) over the logarithm of rate constant,[19b,20a,21] accurately reproduced our decay traces. This method was modified to include the growth during photolysis as well as the decay, and from it most probable rate constants were obtained.

Arrhenius plots using the most probable rate constants were highly curved for **12** and **19**, consistent with a tunneling decay process as discussed earlier. However, **20** and **21** gave linear Arrhenius plots, indicating an absence of tunneling. Such Arrhenius behavior has very rarely been

observed at cryogenic temperatures,[19d,22] owing partly to the difficulty in the experiments, but also probably to a relative minority of low temperature, non-tunneling reactions.

In order to further probe the distribution of rate constants, a different type of kinetic experiment, called "distribution slicing," was designed. This procedure not only strongly supported the distribution model used in the kinetic analysis, but also validated the assumption that the distribution has a Gaussian shape. In addition, the method served to double-check and refine the decay-fitting results. Briefly, the procedure involves generating the intermediate at a temperature below the decay range (or otherwise as low as possible) and observing the relative amounts of decay upon warming the matrix to successively higher temperatures for given time intervals. The intensity measurements are always made at the lowest temperature. Warming the matrix in effect takes a "slice" off the distribution, since the sites with higher rate constants will decay preferentially. By taking several slices and measuring their relative sizes, one can obtain an approximate distribution. Combination of the distribution slicing and decay-fitting procedures led to a convenient, self-consistent method for determining the distribution and approximate activation parameters of an Arrhenius process. This method and its application to cyclobutanediyls are described in detail in Chapter 3.

The activation parameters obtained for **20** and **21** are shown in Table I. The pre-exponential factor is similar to values reported for other triplet biradical processes.[22] Comparison with the results for **19**[16] prompts a remarkable conclusion. Since the S-T gaps of **20** and **21** are suspected to be smaller than that of **19**, the activation energies should also be smaller if the barrier represents an intersystem crossing process (see Figure I). The larger values suggest that for **20** and **21**, at least part of the activation energy represents a barrier on the singlet surface. In other words, the singlet biradicals may be true intermediates and thus may be observable under appropriate conditions.

Table I. Activation Parameters for **21** and **20**

		
	MTHF	
log A	7.5 ± 2[a]	7.5[b]
E_0,kcal/mol	1.665	1.347
σ^c,kcal/mol	0.488	0.493
	Heptane	
log A	7.5[b]	7.5[b]
E_0	1.430	0.903
σ	0.430	0.503
	$CDCl_3$	
log A	7.5[b]	
E_0	1.203	
σ	0.408	

[a]Approximate value. [b]Assumed value. [c]Standard deviation of an assumed Gaussian-E_a distribution.

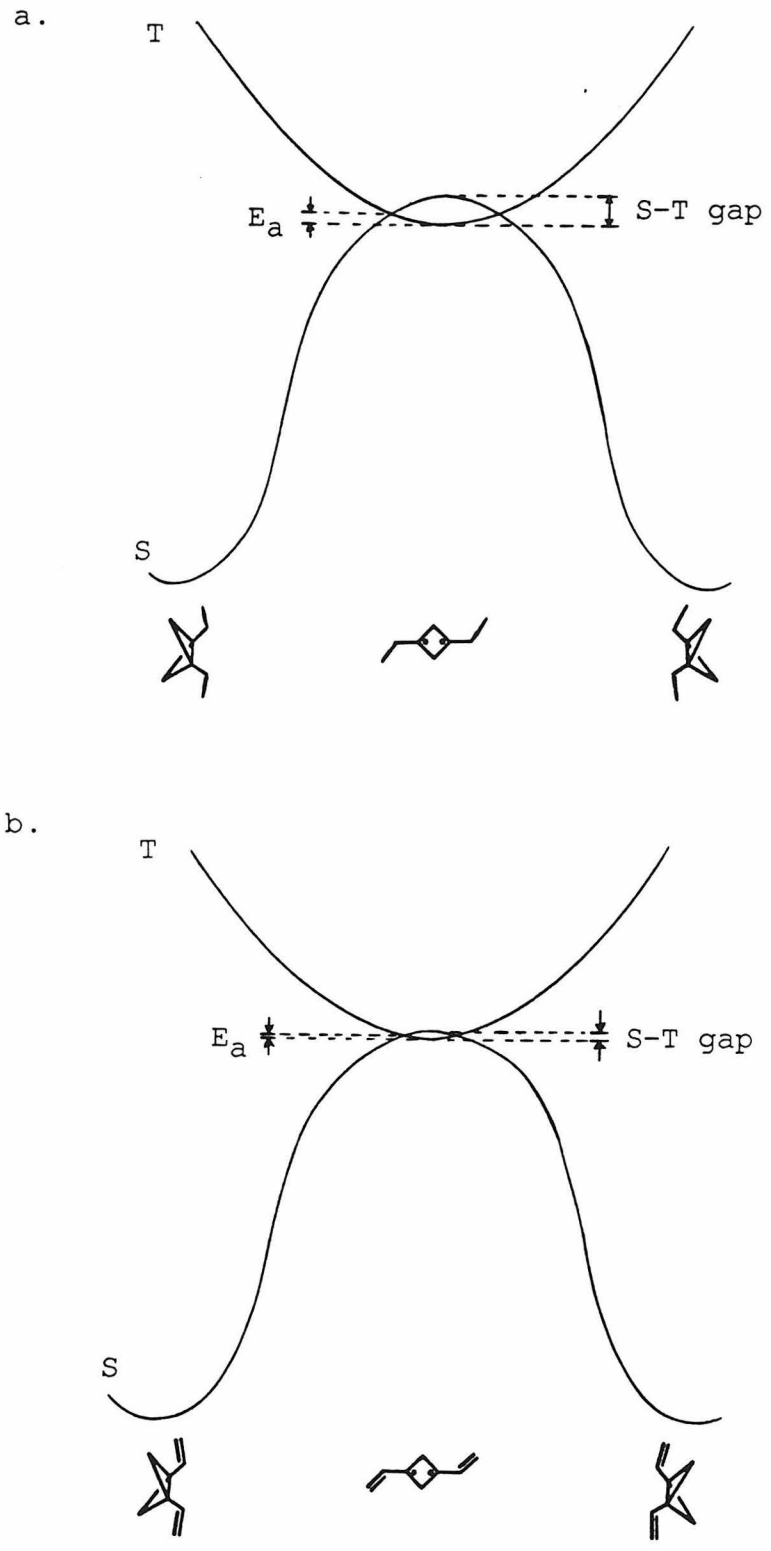

Figure I. Hypothetical potential surfaces for a) **19** and b) **21**, considering only differences in the S-T gap.

References

1. (a) Borden, W. T., Ed. "Diradicals"; Wiley: New York, 1982. (b) Berson, J. A. In "Rearrangements in Ground and Excited States"; de Mayo, P., Ed.; Academic Press: New York, 1980; Vol. 1, Chapter 5. (c) Wagner, P. J., Ibid.; Vol. 3, Chapter 20.
2. Salem, L.; Rowland, C. Angew. Chem., Int. Ed. Engl. 1972, 11, 92-111.
3. Turro, N. J.; Kraeutler, B. In "Diradicals"; Borden, W. T., Ed.; Wiley: New York, 1982; Chapter 6.
4. Davidson, E. R., Ibid.; Chapter 2.
5. Borden, W. T., Ibid.; pp. 23-39.
6. Dowd, P. Acc. Chem. Res. 1972, 5, 242-248.
7. Dowd, P.; Chang, W.; Paik, Y. H. J. Am. Chem. Soc. 1986, 108, 7416-7417. Note that if 2 adopts a bisected, D_{2d} geometry, the radicals are then delocalized separately and the biradical should be classified as localized.
8. Platz, M. S. In "Diradicals"; Borden, W. T., Ed.; Wiley: New York, 1982; Chapter 5.
9. Buchwalter, S. L.; Closs, G. L. J. Am. Chem. Soc. 1979, 101, 4688-4694.
10. Goldberg, A. H.; Dougherty, D. A., unpublished results.

11. Goldberg, A. H.; Dougherty, D. A. J. Am. Chem. Soc. 1983, 105, 284-290.

12. A similar result was obtained independently by others: Doubleday, C., Jr.; McIver, J. W., Jr.; Page, M. J. Am. Chem. Soc. 1982, 104, 6533-6542.

13. Chang, M. H.; Dougherty, D. A. J. Org. Chem. 1981, 46, 4092-4093.

14. Chang, M. H.; Dougherty, D. A. J. Am. Chem. Soc. 1982, 104, 2333-2334.

15. Jain, R.; Snyder, G. J.; Dougherty, D. A. J. Am. Chem. Soc. 1984, 106, 7294-7295.

16. Jain, R. Ph.D. Dissertation, California Institute of Technology, 1987.

17. The synthesis and spectroscopy of these and other cyclobutanediyls are described in a forthcoming publication: Jain, R.; Sponsler, M. B.; Coms, F. D.; Dougherty, D. A., manuscript in preparation.

18. Sponsler, M. B.; Jain, R.; Coms, F. D.; Dougherty, D. A., manuscript in preparation.

19. (a) Siebrand, W.; Wildman, T. A. Int. Rev. Phys. Chem. 1986, 5, 251-257. (b) Jankowiak, R.; Richert, R.; Bassler, H. J. Phys. Chem. 1985, 89, 4569-4574. (c) Hudson, R. L.; Shiotani, M.; Williams, F. Chem. Phys. Lett. 1977, 48, 193-196. (d) Pagni, R. M.; Watson, C. R., Jr.; Bloor, J. E.; Dodd, J. R. J. Am. Chem. Soc. 1974, 96, 4064-4066.

20. (a) Albery, W. J.; Bartlett, P. N.; Wilde, C. P.; Darwent, J. R. J. Am. Chem. Soc. 1985, 107, 1854-1858. (b) Doba, T.; Ingold, K. U.; Siebrand, W. Chem. Phys. Lett. 1984, 103, 339-342. (c) Austin, R. H.; Beeson, K.; Eisenstein, L.; Frauenfelder, H.; Gunsalus, I. C.; Marshall, V. P. Phys. Rev. Lett. 1974, 32, 403-405.

21. Siebrand, W.; Wildman, T. A. Acc. Chem. Res. 1986, 19, 238-243.

22. Fisher, J. J.; Michl, J. J. Am. Chem. Soc. 1987, 109, 583-584.

CHAPTER 1

BICYCLO[1.1.1]PENTANONE

Cyclobutanone derivatives have attracted much attention due to their rich thermal chemistry and photochemistry and the insight which their spectral properties offer concerning the nature of the carbonyl functional group.[1] Surprisingly, one of the simplest and perhaps most fundamental of the bicyclic cyclobutanones, bicyclo[1.1.1]pentanone (**11**), had not been reported prior to the present investigation.[2] This highly strained, symmetrical ketone might be expected to display novel spectroscopic, thermal, and photochemical properties due to its severe ring constraints.

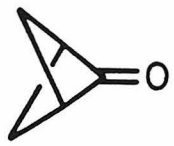

11

Our own interest in **11** arose from its potential as a precursor to the localized triplet biradical cyclobutane-1,3-diyl (**8**). In an earlier study in our group, Chang and Dougherty prepared[3] 2,3-diazabicyclo[2.1.1]hex-2-ene (**9**) but found that photolysis of **9** at 8.5 K in the cavity of an EPR spectrometer did not produce a signal corresponding to **8**.[4] We had also performed <u>ab initio</u> calculations[5] that predict a triplet ground state for **8** -- a necessary criterion for success in such EPR experiments. Many substituted cyclobutanediyls have since been observed by EPR,[6] supporting this prediction for **8**. Therefore, an alternative photochemical precursor to **8** was sought. We chose **11** by

analogy to Dowd and Sachdev's successful use of 3-methylene-cyclobutanone (22) as a precursor to the trimethylenemethane biradical.[7]

8

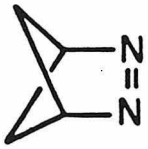

9

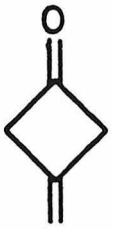

22

We describe herein a simple synthesis of 11 and characterization of its spectral, thermal, and photochemical properties. Through microwave measurements on several isotopic species of 11, a substitution structure has been obtained, and several theoretical structures are reported for comparison. Although 11 has not proven to be a viable EPR precursor to 8, its chemical and spectroscopic behavior sheds new light on several aspects of cyclobutanone chemistry.

Synthesis and Spectroscopic Characterization

Ketone 11 was prepared by using a simple, two-step sequence (eq. 1.1). Photolysis of commercially available cyclobutyl phenyl ketone (23) using the method of Padwa et al. produced 2-phenylbicyclo[1.1.1]pentan-2-ol (24). Ozonolysis[9] of 24 in CH_2Cl_2 afforded 11 as a colorless oil after purification by azeotropic distillation and preparative gas chromatography. GC analysis of the reaction mixture revealed that the yield of 11 was ca. 8%. Losses during purification were unavoidable, due to the high volatility of 11, and the isolated yield was 4%. We anticipate that this procedure

will be more useful for the preparation of substituted bicyclopentanones, for which isolation should be less problematical. Despite the low yield, the brevity of the overall synthesis makes useful quantities of **11** easily available.

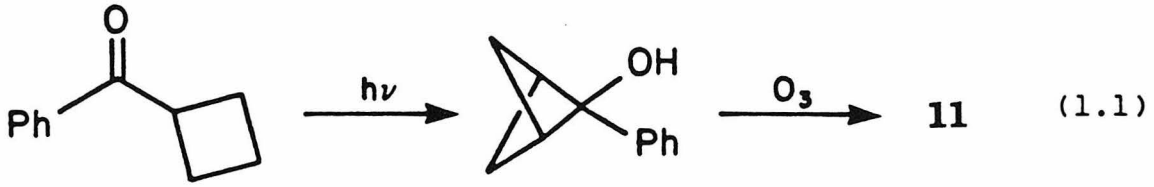

(1.1)

23 **24**

For comparison, ozonolysis of 1-phenylcyclohexanol (25) under the same conditions resulted in a 67% GC yield of cyclohexanone, suggesting that ring strain in **24** or **11** also contributes to the low yield of **11**. Alcohol **25** can also be oxidized to cyclohexanone by using ruthenium tetraoxide.[10] We therefore attempted oxidation of **24** with ruthenium tetraoxide using Sharpless' procedure.[11] However, a much lower yield of **11** was observed, and 3-oxocyclobutyl phenyl ketone (**26**) and benzoic acid were observed among the products. The formation of these products is consistent with the above suggestion that the low yield of **11** is probably due in part to attack of the oxidizing agent on the strained ring system.

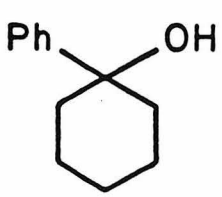

25

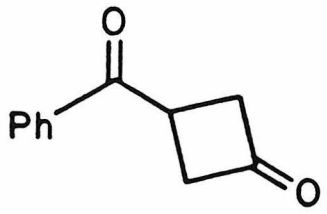

26

Structure proof for **11** rests on the range of spectroscopic data discussed below, exact mass determination and chemical behavior. In particular, reduction of **11** with $NaBH_4$ (eq. 1.2) in methanol gives a product whose ^1H NMR spectrum is identical with that reported by Wiberg and Williams[12] for bicyclo[1.1.1]pentan-2-ol (**27**).

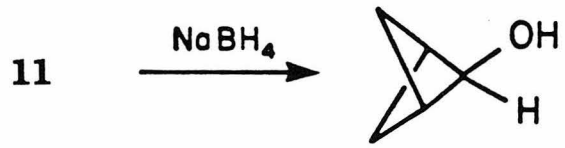

(1.2)

27

Ketone 1 is quite strained, as demonstrated by the infrared carbonyl stretch at 1810 cm^{-1}. This value is intermediate between that of cyclobutanone (1788 cm^{-1})[13] and cyclopropanone (1813 cm^{-1}).[14] In the closely related molecule, tricyclo[2.1.0.$0^{2,5}$]pentanone (**28**), the carbonyl stretch appears at 1775 cm^{-1}.[15] This suggests that the ketone moiety in **11** is actually more strained than that in **28**, presumably because the carbonyl C-C-C angle is larger in **28** due to the presence of the constrained bicyclobutane skeleton.

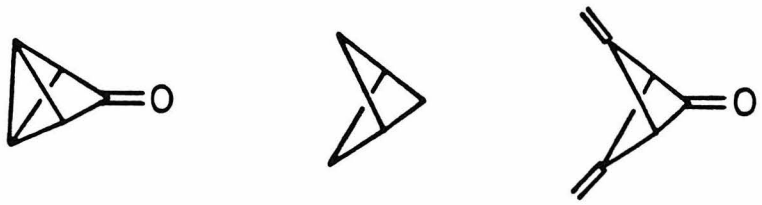

28 **29** **30**

The ^{1}H NMR spectrum of **11** in $CDCl_3$ exhibits a sharp singlet at 3.01 ppm ($H_{bridgehead}$) and slightly broadened singlets at 1.80 ppm (H_{exo}) and 1.49 ppm (H_{endo}). The assignment of the exo and endo protons was based on comparison with the methylene protons in bicyclo[1.1.1]-pentane (**29**, 1.84 ppm)[16] and the observation that the endo protons are in the anisotropic shielding region of the carbonyl.[17]

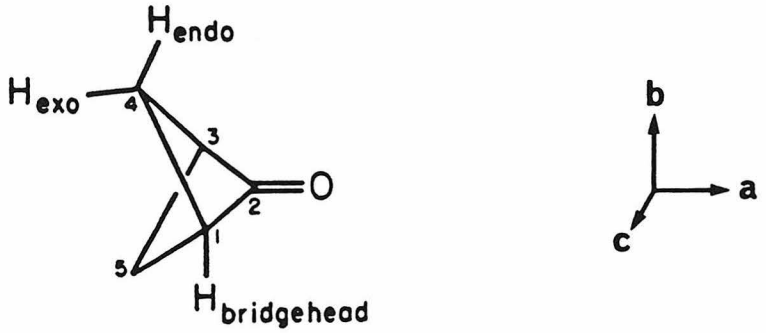

The ^{13}C NMR spectrum has resonances at 189 ppm (C_2), 55 ppm (C_1), and 36 ppm (C_4). The carbonyl ^{13}C singlet appears at higher field than normal for ketones, but the same observation has been reported for other polycyclic ketones,[18] including 4,5-bis(methylene)bicyclo[1.1.1]pentanone (**30**), for which the carbonyl peak appears at 172.1 ppm.[19]

The ultraviolet spectrum of **11** shows an unusually high energy $n\pi^*$ transition for an alicyclic ketone. The band shows no vibrational structure and has λ_{max} 247 nm (ε_{max} 14) in n-pentane. This is, to our knowledge, the shortest wavelength $n\pi^*$ absorption reported for a saturated aliphatic ketone. Such a blue shift is not characteristic of strained

ketones, as shown by the λ_{max} of 279 nm for cyclobutanone[13] and 310 nm for cyclopropanone.[14]

In an effort to understand the origin of this blue shift, we recorded the photoelectron spectrum of **11**, shown in Figure 1.1.[20] The first ionization is well separated from other bands and displays a vertical ionization potential of 9.51 eV. The observed IP for **11** is slightly lower than the IP for acetone (9.70 eV),[21] and thus the high-energy $n\pi^*$ transition does not result from an unusually low-lying n orbital. At present we feel that this effect is most likely due to adverse electron repulsions in the $n\pi^*$ state between the electron that is formally in a π^* orbital and the endo C-H bonds, as these bonds protrude directly into the region of the π^* orbital.

We attempted to observe emission from **11** in 2-methyltetrahydrofuran (degassed) at both room temperature and at 77 K. Using an excitation wavelength of 247 nm, we observed no emission from 247 to 360 nm. This negative result is consistent with Lee's observation that the excitation spectrum of cyclobutanone drops to zero for excitation wavelengths less than 290 nm.[22]

Microwave Spectra and Structure

The microwave spectra of five isotopic species of **11** have been studied: the parent molecule and four others in which a single heavy atom was isotopically substituted. The three ^{13}C species were studied in natural abundance, but the

^{18}O species was isotopically enriched by exchange with $H_2{}^{18}O$. From the spectra of these compounds, the complete structure of the heavy-atom frame has been determined.

The measurements in Table 1.1 consist of a selected group of a-type R and Q branch transitions for the parent species and a more limited group of R-branch transitions for the less abundant species. In general, the measurement of a feature is reproducible to within several kHz. Measurements are routinely made to the kHz place, used in the fitting procedures exactly as measured, and reported in their entirety. For the purpose of fitting, each feature is assigned an uncertainty, which is an estimate of how well that measurement may be expected to represent the true center of the assigned line. Typically this is of the order of tens of kHz and is set even higher for poorly shaped or partially blended features.

In order to account for the effect of centrifugal distortion on the rotational constants, transitions were selected for the normal species from which all of the quartic distortion constants could be determined. Since it was not convenient to determine all the high-order parameters for the other species, parameters that were not determined were fixed to the corresponding value of the parent species. The ^{18}O species' D_J was estimated from the parent's by assuming that D_J varies as the square of (B + C). This assumption is valid even for the much more extreme isotopic changes between NH_2D and NH_2H.[23] Since the distortion constants are so much

^{18}O species was isotopically enriched by exchange with $H_2{}^{18}O$. From the spectra of these compounds, the complete structure of the heavy-atom frame has been determined.

The measurements in Table 1.1 consist of a selected group of a-type R and Q branch transitions for the parent species and a more limited group of R-branch transitions for the less abundant species. In general, the measurement of a feature is reproducible to within several kHz. Measurements are routinely made to the kHz place, used in the fitting procedures exactly as measured, and reported in their entirety. For the purpose of fitting, each feature is assigned an uncertainty, which is an estimate of how well that measurement may be expected to represent the true center of the assigned line. Typically this is of the order of tens of kHz and is set even higher for poorly shaped or partially blended features.

In order to account for the effect of centrifugal distortion on the rotational constants, transitions were selected for the normal species from which all of the quartic distortion constants could be determined. Since it was not convenient to determine all the high-order parameters for the other species, parameters that were not determined were fixed to the corresponding value of the parent species. The ^{18}O species' D_J was estimated from the parent's by assuming that D_J varies as the square of (B + C). This assumption is valid even for the much more extreme isotopic changes between NH_2D and NH_2H.[23] Since the distortion constants are so much

Table 1.1 Measured Rotational Transitions of Bicyclo-[1.1.1]pentanone in MHz.

Measured Transitions of the Normal Isotopic Species

Transition	*Frequency(unc.)*	*Obs. – Calc.*	*Transition*	*Frequency(unc.)*	*Obs. – Calc.*
R – branches			*Q – branches*		
$1_{0,1} - 0_{0,0}$	7072.480(60)[a]	−0.063			
$5_{0,5} - 4_{0,4}$	35242.512(20)	0.020	$9_{1,8} - 9_{1,9}$	7689.545(20)	−0.022
$5_{1,5} - 4_{1,4}$	34903.135(20)	−0.003	$10_{1,9} - 10_{1,10}$	9323.471(20)	−0.007
$5_{1,4} - 4_{1,3}$	35768.254(20)	−0.006	$11_{1,10} - 11_{1,11}$	11070.987(20)	−0.004
$5_{2,4} - 4_{2,3}$	35348.760(50)	0.056	$24_{2,23} - 24_{0,24}$	35410.330(100)	−0.064
$5_{2,3} - 4_{2,2}$	35468.688(50)	−0.039	$25_{2,24} - 25_{0,25}$	37016.086(50)	0.020
$5_{3,3} - 4_{3,2}$	35381.687(150)	0.094	$14_{2,12} - 14_{2,13}$	7605.157(20)	−0.036
$5_{3,2} - 4_{3,1}$	35384.281(150)	−0.132	$15_{2,13} - 15_{2,14}$	9277.898(20)	−0.005
$5_{4,2} - 4_{4,1}$	35375.066(30)[b]	−0.016	$16_{2,14} - 16_{2,15}$	11095.435(20)	0.026
$5_{4,1} - 4_{4,0}$	35375.066(30)[b]	−0.036	$27_{3,25} - 27_{1,26}$	35862.859(20)	0.010
$10_{0,10} - 9_{0,9}$	69924.558(20)	0.004	$20_{3,17} - 20_{3,18}$	8162.696(20)	0.020
$10_{1,10} - 9_{1,9}$	69659.836(20)	0.037	$21_{3,18} - 21_{3,19}$	9952.020(20)	0.035
$10_{1,9} - 9_{1,8}$	71293.672(20)	−0.037	$22_{3,19} - 22_{3,20}$	11909.528(20)	−0.035
$10_{2,8} - 9_{2,7}$	71365.906(20)	0.018	$26_{4,23} - 26_{2,24}$	33611.461(20)	−0.001
$10_{3,7} - 9_{3,6}$	70913.756(20)	−0.006	$29_{4,26} - 29_{2,27}$	35929.331(20)	0.002
$10_{6,5} - 9_{6,4}$	70758.566(50)[b]	−0.085	$30_{4,27} - 30_{2,28}$	36998.721(20)	−0.003
$10_{6,4} - 9_{6,3}$	70758.566(50)[b]	−0.086	$57_{6,52} - 57_{4,53}$	68874.909(100)	−0.034
$10_{7,4} - 9_{7,3}$	70749.024(20)[b]	−0.020	$60_{6,54} - 60_{6,55}$	66255.569(100)	−0.017
$10_{7,3} - 9_{7,2}$	70749.024(20)[b]	−0.020	$59_{7,53} - 59_{5,54}$	66302.425(50)	0.006
$10_{8,3} - 9_{8,2}$	70742.025(20)[b]	0.012	$48_{8,41} - 48_{6,42}$	68888.693(50)	0.025
$10_{8,2} - 9_{8,1}$	70742.025(20)[b]	0.012	$49_{8,42} - 49_{6,43}$	66969.811(50)	−0.028
$10_{9,2} - 9_{9,1}$	70736.377(50)[b]	0.036	$70_{8,62} - 70_{8,63}$	66290.276(100)	0.002
$10_{9,1} - 9_{9,0}$	70736.377(50)[b]	0.036	$60_{9,52} - 60_{7,53}$	68834.063(50)	0.002

a. Numbers in parentheses are estimated uncertainties in units of the least significant digit.
b. Fitted as a blend whose *Obs.-Calc.* is the average of those listed.

Table 1.1 Measured Rotational Transitions of Bicyclo-[1.1.1]pentanone in MHz. (continued)

Measured Transitions of Isotopically Substituted Species

Transition	*Frequency(unc.)*	*Obs. – Calc.*	*Transition*	*Frequency(unc.)*	*Obs. – Calc.*
	$^{13}C_4$			$^{13}C_2$	
$5_{0,5} - 4_{0,4}$	34821.015(50)[a]	0.030	$5_{1,5} - 4_{1,4}$	34764.231(150)	0.025
$5_{1,5} - 4_{1,4}$	34452.462(50)	−0.031	$5_{1,4} - 4_{1,3}$	35622.607(50)	−0.046
$5_{2,4} - 4_{2,3}$	34959.406(50)	0.008	$5_{2,4} - 4_{2,3}$	35206.233(50)	0.057
$5_{2,3} - 4_{2,2}$	35115.800(50)	−0.034	$5_{2,3} - 4_{2,2}$	35323.969(50)	0.070
$5_{3,3} - 4_{3,2}$	35004.480(50)[c]	2.123	$5_{3,3} - 4_{3,2}$	35239.918(100)[b]	1.489
$5_{3,2} - 4_{3,1}$	35004.480(50)[c]	−2.154	$5_{3,2} - 4_{3,1}$	35239.918(100)[b]	−1.244
$5_{4,2} - 4_{4,1}$	34994.302(50)	0.060	$5_{4,2} - 4_{4,1}$	35232.100(100)[b]	0.079
$5_{4,1} - 4_{4,0}$	34994.302(50)	0.026	$5_{4,1} - 4_{4,0}$	35232.100(100)[b]	0.060
$10_{0,10} - 9_{0,9}$	68964.539(50)	0.004	$10_{0,10} - 9_{0,9}$	69651.238(50)	0.021
$10_{1,10} - 9_{1,9}$	68721.269(50)	0.011	$10_{1,10} - 9_{1,9}$	69384.269(50)	−0.050
$10_{2,9} - 9_{2,8}$	69753.653(50)	−0.024	$10_{1,9} - 9_{1,8}$	71007.475(250)	−0.297
$10_{3,8} - 9_{3,7}$	70061.062(50)	0.006	$10_{2,9} - 9_{2,8}$	70288.041(50)	0.001
$10_{3,7} - 9_{3,6}$	70212.951(50)	0.029	$10_{2,8} - 9_{2,7}$	71070.941(150)	−0.238
$10_{4,7} - 9_{4,6}$	70051.441(250)	0.175			
$10_{4,6} - 9_{4,5}$	70058.246(250)	−0.299		^{18}O	
$10_{5,6} - 9_{5,5}$	70019.815(50)[b]	0.044			
$10_{5,5} - 9_{5,4}$	70019.815(50)[b]	−0.120	$10_{0,10} - 9_{0,9}$	66518.964(50)	0.015
$10_{6,5} - 9_{6,4}$	70000.846(50)[b]	0.011	$10_{1,10} - 9_{1,9}$	66231.413(50)	0.001
$10_{6,4} - 9_{6,3}$	70000.846(50)[b]	0.009	$10_{1,9} - 9_{1,8}$	67728.637(50)	0.003
$10_{7,4} - 9_{7,3}$	69988.788(50)[b]	0.009	$10_{2,9} - 9_{2,8}$	67052.152(50)	−0.039
$10_{7,3} - 9_{7,2}$	69988.788(50)[b]	0.009	$10_{2,8} - 9_{2,7}$	67702.494(50)	0.009
$10_{8,3} - 9_{8,2}$	69980.192(50)[b]	0.003	$10_{3,8} - 9_{3,7}$	67244.534(50)	−0.030
$10_{8,2} - 9_{8,1}$	69980.192(50)[b]	0.003	$10_{3,7} - 9_{3,6}$	67313.457(50)	−0.004
$10_{9,2} - 9_{9,1}$	69973.445(100)[b]	−0.019	$10_{4,7} - 9_{4,6}$	67230.851(250)[b]	1.440
$10_{9,1} - 9_{9,0}$	69973.445(100)[b]	−0.019	$10_{4,6} - 9_{4,5}$	67230.851(250)[b]	−0.965
			$10_{5,6} - 9_{5,5}$	67209.639(100)[b]	0.132
	$^{13}C_1$		$10_{5,5} - 9_{5,4}$	67209.639(100)[b]	0.092
			$10_{6,5} - 9_{6,4}$	67197.842(100)[b]	0.106
$5_{0,5} - 4_{0,4}$	35109.720(50)	0.037	$10_{6,4} - 9_{6,3}$	67197.842(100)[b]	0.105
$5_{1,5} - 4_{1,4}$	34808.919(50)	0.025	$10_{7,4} - 9_{7,3}$	67189.992(100)[b]	0.039
$5_{1,4} - 4_{1,3}$	35551.328(100)	−0.026	$10_{7,3} - 9_{7,2}$	67189.992(100)[b]	0.039
$5_{2,4} - 4_{2,3}$	35189.862(50)	0.014	$10_{8,3} - 9_{8,2}$	67184.014(100)[b]	−0.105
$5_{2,3} - 4_{2,2}$	35280.407(50)	−0.053	$10_{8,2} - 9_{8,1}$	67184.014(100)[b]	−0.105
$5_{3,3} - 4_{3,2}$	35215.328(150)[b]	0.713	$10_{9,2} - 9_{9,1}$	67179.281(100)[b]	−0.009
$5_{3,2} - 4_{3,1}$	35215.328(150)[b]	−1.147	$10_{9,1} - 9_{9,0}$	67179.281(100)[b]	−0.009
$5_{4,2} - 4_{4,1}$	35209.559(150)[b]	0.078			
$5_{4,1} - 4_{4,0}$	35209.559(150)[b]	0.067			
$10_{0,10} - 9_{0,9}$	69771.353(50)	−0.025			
$10_{1,10} - 9_{1,9}$	69503.721(50)	−0.009			
$10_{2,9} - 9_{2,8}$	70283.989(50)	0.034			
$10_{2,8} - 9_{2,7}$	70909.719(100)	−0.000			

a. Numbers in parentheses are estimated uncertainties in units of the least significant digit.
b. Fitted as a blend whose *Obs.-Calc.* is the average of those listed.
c. Resolved, but fitted as a blend because of very strong Stark effect.

smaller than the rotational constants, any errors introduced by fixing some quartic terms negligibly affect the molecular structure determination.

Fitting the data in Table 1.1 using a standard S reduction Hamiltonian in a I^R prolate representation[24] leads to the rotational and distortion constants of Table 1.2 and gives the observed-calculated frequencies in Table 1.1. In the fit the data are weighted inversely as the square of the assigned uncertainties.

All the heavy atoms of the molecule have been isotopically substituted, so it is possible to obtain the substitution coordinates, r_s, of these atoms with the aid of Kraitchman's equations.[25] The difference between the r_s and the equilibrium structure, r_{eq}, for heavy atoms is usually small, on the order of thousandths of Angstroms. This method is reviewed and discussed extensively by Gordy and Cook.[24]

The r_s heavy atom a, b, and c coordinates are given in Table 1.3. The A rotational constants were not used in any final structural determinations, because the uncertainties for the substituted species were large compared to those of the B and C rotational constants. Because of the high symmetry of the molecule, the standard relationships for substitution in a plane or on an axis of symmetry could be used.[24] The degree to which the derived constants obey these relationships is shown by the changes in the planar moments also given in Table 1.3. This serves to verify the assumed C_{2v} structure. The uncertainties listed in Table 1.3 reflect

Table 1.2 Rotational Parameters of Bicyclo[1.1.1]-pentanone

Parameter	Parent	$^{13}C_4$	$^{13}C_1$	$^{13}C_2$	^{18}O
A /MHz	7231.1980(44)[a]	7117.53(55)	7134.88(72)	7232.24(65)	7231.41(46)
B /MHz	3623.0689(14)	3596.1488(63)	3594.4824(78)	3608.1130(52)	3436.9680(87)
C /MHz	3449.4758(14)	3399.3790(55)	3445.6141(58)	3435.8727(45)	3280.3342(87)
D_J /kHz	0.3533(74)	0.342(15)	0.328(20)	...[b]	0.319(40)[c]
D_{JK} /kHz	6.566(12)	6.504(40)	6.58(78)	...	6.345(48)
D_K /kHz	−4.74(22)	...	...	...	...
d_1 /kHz	−0.022353(28)	...	...	...	...
d_2 /kHz	−0.012621(40)	...	...	...	...
H_{JK} /Hz	0.0143(12)	...	...	...	...
h_2 /Hz	0.0000530(79)	...	...	...	...
RMS /MHz[d]	0.039	0.084	0.074	0.127	0.086
χ[e]	0.918	0.541	0.684	1.009	0.659

a. Numbers in parentheses are standard deviations(1σ) in units of the least significant digit.
b. Untabulated parameters are fixed to the parent's values.
c. Fixed as described in text.
d. Rms is the root mean square standard deviation of the fit.
e. χ is the standard deviation of the weighted errors $(Obs. - Calc.)/(estimated\ uncertainty)$.

Table 1.3 Substitution Coordinates, Changes in the Planar Moments, and Determinable Hydrogen Parameters

	C_4, C_5	C_1, C_3	C_2	O
a / Å	−1.0181(2)[a]	−0.4045(4)	0.7643(8)	1.9649(1)
b / Å	±1.0685(3)	0.	0.	0.
c / Å	0.	±0.9775(3)	0.	0.
ΔP_a / amu Å^2	1.044(3)	0.165(4)	0.585(3)	7.555(2)
ΔP_b / amu Å^2	1.116(3)	−0.001(4)	−0.004(3)	−0.000(2)
ΔP_c / amu Å^2	0.001(3)	0.944(4)	−0.006(3)	−0.002(2)

	Experimental[a]	*MM2*	*MNDO*	*STO* − 3*G*	3 − 21*G*
$c_H - c_{C_1}$ / Å	1.076	1.113	1.082	1.086	1.070
$\frac{1}{2}\sum(b_H)^2$ / Å^2	5.48	5.52	5.71	5.52	5.43
$\frac{1}{2}\sum(a_H)^2$ / Å^2	5.20	4.94	4.97	4.42	4.88
$\frac{1}{2}\sum a_H$ / Å	3.20	3.00	3.11	3.10	3.08

a. The numbers in parentheses are experimental uncertainties in units of the least significant digit. The hydrogen parameters are not substitution coordinates and may contain significant vibrational contributions which are not estimated here. See text for discussion.

primarily the experimental uncertainties of the rotational constants and contain no estimates of the vibrational contributions. For substitutions on the A axis the stated error spans the two values obtained using either ΔI_b or ΔI_c.

The hydrogens were not substituted. From the parent, only one first moment and three second-moment relationships are available to determine the six coordinates necessary for the unique determination of the hydrogen positions. Only the $\underline{c}$ coordinate of the hydrogen bonded to C_1 is determinable directly from a second-moment relationship. The determinable hydrogen parameters are listed in Table 1.3 and compared with those calculated from theoretically derived hydrogen positions relative to the experimental heavy atom frame. Because these parameters are derived in a way that does not compensate for vibrational effects, they cannot be compared in detail with theoretically derived parameters. They are included primarily for completeness and are consistent with the theoretical results.

The experimental structure of **11** (see Table 1.4) can be compared with the electron diffraction structure of the parent hydrocarbon, bicyclo[1.1.1]pentane (**29**).[26] The relevant structural parameters in **29** are the C-C bond length of 1.545 Å, the C_1-C_2-C_3 angle of 73.3°, and the interbridgehead C..C distance of 1.845 Å.[26] The C-CH_2-C angles of **11**, and of course the C-C(O)-C angle, are larger than the analogous angles in **29** due to the presence of the carbonyl. As a result, the interbridgehead distance is

Table 1.4 Structure of Bicyclo[1.1.1]pentanone

	Experimental[a]	*MM2*	*MNDO*	*STO* – 3*G*	3 – 21*G*
Bond Lengths/Å					
C=O	1.201	1.201	1.205	1.204	1.193
$C_1 - C_2$	1.524	1.528	1.552	1.547	1.549
$C_1 - C_4$	1.573	1.573	1.576	1.558	1.580
$C_1 \ldots C_3$	1.955	1.899	1.931	1.933	1.962
$C_1 - H$	...	1.114	1.082	1.086	1.070
$C_4 - H_{exo}$	...	1.116	1.100	1.086	1.079
$C_4 - H_{endo}$	...	1.117	1.101	1.087	1.079
Bond angles/deg.					
$C_1C_2C_3$	79.8	76.8	76.9	77.3	78.6
$C_1C_4C_3$	76.9	74.2	75.6	76.7	76.8
C_2MC_4[b]	119.9	120.1	119.0	119.5	119.5
C_2C_1H	...	126.1	129.0	129.9	130.0
HCH	...	113.9	107.9	111.1	112.6
CH_2 tilt[c]	...	−0.5	1.4	1.5	1.9
μ/Debye	3.16	3.07	2.48	2.10	3.36

a. The r_o experimental structural parameters have been rounded to the place in which differences from equilibrium parameters may appear.
b. M is the $C_1 \ldots C_3$ midpoint.
c. Angle between bisectors of the HC_4H and $C_1C_4C_3$ angles. A positive value denotes a tilt away from the carbonyl.

greater by 0.11 Å. The C_1-C_2 length is smaller than the C-C length in 29, as expected for an sp^2-sp^3 bond. The C_1-C_4 bond length is larger by 0.028 Å. This lengthening could be a consequence of the expected orbital mixing between π^* (C-O) and σ (C_1-C_4). However, 1,3-nonbonded repulsive interactions, which were used to rationalize the long bonds in cyclobutane,[27] can also explain the lengthening in this case. Simple geometrical considerations show that the larger interbridgehead C..C distance in 11 relative to 29 brings the two CH_2 groups closer together, amplifying 1,3 repulsions. These repulsions can be alleviated by stretching the C_1-C_4 bonds.

It has been noted[28] that ketones with smaller C-C(O)-C angles should have shorter C=O bonds due to rehybridization. Although the effect is generally quite small, our results for 11 do support this analysis.

Theoretical Structures

The structure and dipole moment of 11 were calculated using four currently popular theoretical methods: molecular mechanics (MM2),[29] MNDO,[30] and Hartree-Fock (HF) ab initio MO theory[31] with STO-3G[32] and 3-21G[33] basis sets. The experimental structure and dipole moment of 11 are compared in Table 1.4 with the various theoretical results. In making such comparisons, one should keep in mind that the different methods give different types of structural parameters.[34] The microwave structure reported here is a substitution

structure, while the ab initio and MNDO calculations give equilibrium structures. MM2 has been parameterized to fit diffraction structures.[29] Therefore, only large differences between the experimental and theoretical structures (0.1 Å or 1^{o}) should be taken as significant.

All four computational methods give reasonably satisfactory results. The MM2 geometry is surprisingly good, considering the special problems encountered in treating small rings with this method[35] and the substantial overestimation by MM2 of the C-C bond length in **29** (calculated to be 1.566 Å).

Ab initio calculations using the 3-21G basis set come closest to reproducing the experimental structure. In accord with Wiberg and Wendoloski's results,[36] even the STO-3G minimal basis set produces a structure in reasonable agreement with experiment. MNDO also produces a reasonable structure.

Dipole Moment

The Stark effects of the 5_{05}-4_{04} and the 5_{15}-4_{14} transitions of the common isotopic species in its vibrational ground state have been precisely measured. The dipole moment was determined by measuring the Stark frequency shifts of all the observable M components at a given electric field and solving for μ in the power series expression

$$\Delta\nu(M) = \mu^2E^2[A + BM^2 + CM^4E\mu^2 + \ldots].$$

The coefficients A and B were calculated from the direction cosine matrix elements and energy levels of the distortable rotor. The coefficient C is important only for the 5_{15}-4_{14} transition and is due almost entirely to the Stark repulsion between the members of the K_a = 1 asymmetry doublets. This was calculated from the dipole moment matrix elements and energy level spacings between the members of the asymmetry doublets by expanding the solution of the two level problem. The data and the results of the dipole moment calculation are given in Table 1.5. The dipole moment lies along the a axis and has a value of 3.164(5) D, derived from a weighted average of the values determined from the individual M components.

The dipole moment of 11, 3.16 D, is similar to those of related ketones, some of which are shown in Table 1.6. Of the theoretical methods used, MM2 best reproduced the dipole moment with a value of 3.07 D. However, this close agreement is fortuitous. Using MM2, we calculated dipole moments of 2.92 - 3.07 D for a selection of ten ketones whose experimental moments span a much larger range of 2.87 D - 3.35 D (see Table 1.6). In addition, the small variations for different structures calculated by MM2 do not correlate with the experimental trends in any way.

MNDO tends to underestimate the dipole moments of carbonyls (the error for acetone is 0.39 D).[37] The results presented here follow this trend, but the error is quite large (0.69 D). The dipole moment calculated by using HF and

Table 1.5 Stark Effect Measurements[a]

M	$5_{05} - 4_{04}$ Observed Shift	Observed-Calculated	$5_{15} - 4_{14}$ Observed Shift	Observed-Calculated
0	−15.009	−0.028	−0.963	−0.015
1	−11.253	0.039	1.348	−0.004
2	...[b]	...	8.196	0.001
3	18.264	0.035	19.410	0.012
4	44.033	−0.027	34.755	−0.007
Stark Coefficients				
A	-1.5907×10^{-7}		-1.2024×10^{-7}	
B	3.9181×10^{-8}		2.9232×10^{-7}	
C			-7.224×10^{-17}	
E^2	9.408×10^{6}		0.7872×10^{6}	
μ	3.164(5)[c]		3.164(5)[c]	

a. Units are Shifts/MHz, A $B/(\mathrm{MHz}/\mathrm{E}^2\mu^2)$, $C/(\mathrm{MHz}/\mathrm{E}^4\mu^4)$, E/(V/cm), and μ/D.
b. Unmodulated, calculated shift = −0.222 MHz.
c. Uncertainty is determined assuming possible errors of ±50 kHz in shift and ±0.2% in field.

Table 1.6 Comparison of MM2 Ketone Dipole Moments with Experimental Values

Ketone	Dipole Moment (D)	
	Experimental	MM2[a]
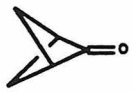	3.16[a]	3.07
	2.93[b]	2.92
	2.89[c]	3.01
	3.25[d]	2.95
	2.87[e]	2.92
	3.35[f]	2.98
	3.18[g]	3.04
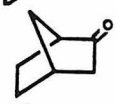	3.23[h]	2.96
	2.99[i]	3.00
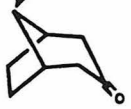	3.11[j]	2.92

[a]This work. [b]Swalen, J. D.; Costain, C. C. J. Chem. Phys. 1959, 31, 1562-1574. [c]Scharpen, L. H.; Laurie, V. W. J. Chem. Phys. 1968, 49, 221-228. [d]Kim, H.; Gwinn, W. D. J. Chem. Phys. 1969, 51, 1815-1819. [e]Ohnishi, Y.; Kozima, K. Bull. Chem. Soc. Jap. 1968, 41, 1323-1325. [f]Coffey, D., Jr.; Ho, C. Y. J. Mol. Spectrosc. 1971, 40, 158-163. [g]Coffey, D. Jr.; Ho, C. Y. J. Mol. Spectrosc. 1972, 42, 47-52. [h]Kriegen, H. Soumen Kemist. 1958, 31B, 348-353. [i]Durig, J. R.; Lopata, A. D.; Li, Y. S. J. Mol. Struct. 1975, 26, 85-94. [j]Waegell, B.; Jefford, C. W. Bull. Soc. Chim. Fr. 1964, 844-854.

the 3-21G basis set is high by only 0.20 D. The difference between the 3-21G dipole moment and the STO-3G moment (low by 1.07D) reflects differences in the basis sets rather than in the optimized structures, since the 3-21G moment at the STO-3G structure is 3.426 D.

Thermal Chemistry

Cyclobutanones characteristically undergo thermal [2+2] cycloreversions to give ketene and olefin products.[38] In **11**, there are four degenerate modes for cycloreversion, all of which lead to allylketene (**31**) (eq. 1.3). Cycloreversion is indeed observed and proceeds much more readily than that for any other cyclobutanone of which we are aware.

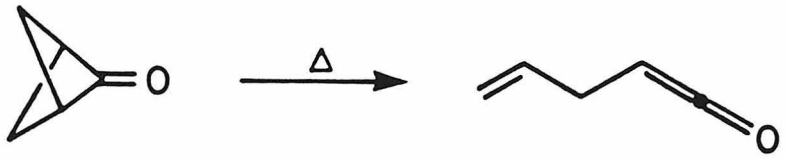

(1.3)

11 **31**

Thermolysis of **11** in degassed benzene-d_6 solution at 80 to 122 ^{o}C yielded four major products of long (relative to **11**) GC retention times and a series of minor products with progressively longer retention times. GC-MS analysis clearly indicates that all of these products are of high molecular weight relative to **11**. Molecular weights corresponding to trimer and tetramer were observed. The ^{1}H NMR spectrum of the mixture is dominated by a strong, characteristic allyl pattern with signals at 2.1, 4.9, and 5.5 ppm, and the ^{13}C

NMR spectrum supports the presence of allyl groups with peaks at 28, 116, and 136 ppm. These data are consistent with the formation of 31 followed by oligomerization.

Strong support for the formation of 31 was obtained from the thermolysis of 11 at 100 °C in methanol-d_4.[39] Methyl-d_3 4-pentenoate-2-d (32) was obtained in nearly quantitative yield, presumably by the trapping of 31 with solvent. In addition, we prepared and studied the decomposition of 1-diazo-4-penten-2-one (33), which should decompose thermally or photochemically via the Wolff rearrangement[40] to yield 31. Indeed, photolysis of 33 in benzene-d_6 yielded several products including, as 60% of the mixture, two components that coeluted on two different capillary GC columns with two of the major products obtained from 11. Although decomposition of 11 does not provide the identical mixture obtained from 33, the different temperature and mode of generation of 31 can explain this difference. Thus, the dominant, if not exclusive, thermal reaction mode of 11 is cycloreversion to 31.

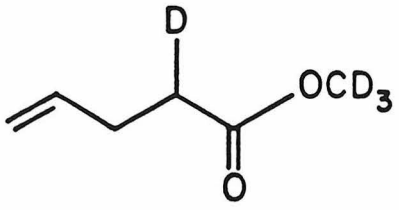

32

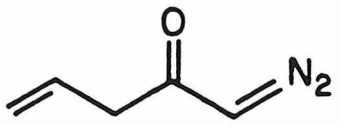

33

The kinetics of the thermal decomposition of 11 in C_6D_6 followed strictly first-order behavior through at least two half-lives, as monitored by multiple ^1H NMR integration. The

activation parameters, obtained over a 40° temperature range, are given in Table 1.7 along with others selected for comparison. Most cyclobutanones require temperatures in excess of 180 °C for measurable decomposition, and nearly all of the studies reported in the literature have been done in the gas phase.[38] In contrast, 11 decomposes readily around 100 °C, allowing convenient study in the solution phase. In order to make our solution-phase results[41] more amenable to comparison with the earlier studies, however, we carried out the gas-phase decomposition of 11 at 100 °C and approximately 0.2 torr. The reaction rate was comparable to solution-phase decomposition at the same temperature, and the same products were obtained, though in different relative yields. This variation in product composition between solution- and gas-phase experiments is not surprising, given that oligomerization is involved.

Thermal decomposition of cyclobutanones has been postulated to proceed by a polar, concerted mechanism,[1c] in contrast to the decomposition of cyclobutanes, which is thought to involve biradical intermediates.[42] In order to address the question of polarity in the transition state, the decomposition of 11 was carried out in acetonitrile-d_3 and methanol-d_4 at 100 °C. The decomposition proceeded 1.8 times faster in acetonitrile and 7.7 times faster in methanol than it did in benzene at that temperature.[43] In view of these relatively modest rate enhancements,[44] we believe that the transition state is only weakly polar.

Table 1.7 Activation Parameters for Cyclobutanones and Cyclobutanes

Compound	Products	E_a kcal/mol	log A	Ref.
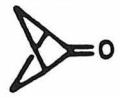		28.6	12.9	a
		49.0	15.3	b
		51.9	14.6	c
		62.5	15.6	d
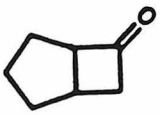		48.6	14.2	e
		60.7	14.8	f

[a]This work. [b]Srinivasan, R. J. Am. Chem. Soc. 1968, 90, 2752-2754. [c]See ref. 38c. [d]Carr, R. W., Jr.; Walters, W. D. J. Phys. Chem. 1963, 67, 1370-1372. [e]Cocks, A. T.; Egger, K. W. J. Chem. Soc., Perkin Trans. 2 1972, 2014-2018. [f]See ref. 42e.

This conclusion seemingly contradicts the findings of Egger[1c] and of Frey and Smith[45] that charge-stabilizing substituents on C_3 of cyclobutanone markedly enhance the rate of gas-phase thermal decomposition, indicating a polar transition state. These results need not be contradictory, however, if we accept that substitution of charge-stabilizing groups on C_3 of cyclobutanone can induce polar character in the transition state, and in doing so stabilize it. In the absence of such substituents, the reaction proceeds through a relatively nonpolar transition state.

In distinguishing between biradical and concerted pathways, activation parameters can be very useful.[46] Log A is generally slightly lower for cyclobutanones than for the corresponding cyclobutanes (Table 1.7), indicating more order in the transition state for cyclobutanones relative to cyclobutanes. This trend is especially pronounced in the case of 11. The concerted transition state should have a highly ordered, twisted structure to provide good overlap in the allowed $\sigma^2_s + \sigma^2_a$ process.[42a] This is consistent with a low log A value. In contrast, a biradical path would appear inconsistent with such a small log A value. Note that the contribution to log A due to solvent reordering in the transition state is expected to be small, given the weakly polar nature of the reaction.

The activation energy is also inconsistent with a two-step process for 11. If we assume a biradical mechanism for the cycloreversions of both 11 and 29, then we must

account for the fact that the activation energy for **11** is 20 kcal/mol less than that for **29**. The difference in intrinsic bond dissociation energies can account for at most 5 kcal/mol of this difference.[47] It seems unlikely that the remaining difference of 15 kcal/mol could be explained by differences in strain energies between **11** and **29** or between their respective transition states. In fact, we have carried out MNDO calculations on both molecules and found the strain energies[48] to be nearly identical.[50] We thus conclude that the much lower E_a for decomposition of **11** vs. **29** is due to stabilization of the transition state for **11** by virtue of the fact that it is a concerted process.

Photochemistry

The photochemistry of cyclic ketones has been widely studied.[1a,b,52] As a consequence of their greater strain energy, cyclobutanones exhibit photochemistry[1a,b,d] that differs markedly from their higher homologues. Structure **11** is a highly strained cyclobutanone, and its photochemistry is similar in most respects to that of other cyclobutanones. The observed differences may be explained in terms of the higher strain energy, the higher energy of the $n\pi^*$ state and geometric considerations.

Several processes are generally observed in cyclobutanone photochemistry, all of which are thought to be initiated by α-cleavage to an acyl alkyl biradical. Decarbonylation, fragmentation to ketene plus olefin, and

ring expansion to oxacarbene are generally observed from cyclobutanones, whereas intramolecular disproportionation (ketene and enal) products are usually observed only in larger ring ketones.[1a,b]

Photolysis of 11 in cyclohexane-d_{12} with Vycor-filtered light at room temperature (eq. 1.4) affords bicyclo[1.1.0]-butane (34) in ca. 70% yield, along with a small amount (1-2%) of cyclobutene (35). A characteristic allyl pattern was observed in the ^1H NMR spectrum of the mixture and a white solid was formed; these products have not been identified, but they are likely to have been derived from the ketene 31 (see below).

(1.4)

34 35

Examination of the photolysis results shows that decarbonylation is by far the most important process for 11. The yield of decarbonylation product (34) is much higher than is normally observed for saturated cyclobutanones,[1a] and the yields of cycloreversion and ring expansion products are correspondingly lower.

These observed relative yields can be rationalized in terms of energetic and geometric considerations. First, decarbonylation is generally more important for ketones that are highly strained,[53] and 11 is one of the most strained

cyclobutanones that has been studied. Second, the $n\pi^*$ absorption of **11** is about 14 kcal/mol higher in energy than for most ketones. This extra energy is comparable to the estimated barrier to loss of CO from the first-formed acyl alkyl biradical,[54] in this case **36**, and could thus greatly accelerate this process.

36

In addition, a pathway expected to compete with decarbonylation, β-cleavage to give cycloreversion product **31**, may be disfavored by geometric considerations. In the optimum geometry for cleavage of 1,4-biradicals, the radical p orbitals are parallel to the breaking σ bond,[55] allowing for high overlap in the transition state. However, the alkyl radical p orbital in **36** is constrained by the four-membered ring to remain nearly perpendicular to the breaking σ bond, unless the ring becomes severely twisted. This effect should serve to lower the relative yield of cycloreversion products.

That cycloreversion is occurring in **11** was suggested by the allyl resonances in the product mixture. To confirm this result, we carried out a photolysis of **11** in methanol-d_4 in the presence of sodium bicarbonate (eq. 1.5). This leads to

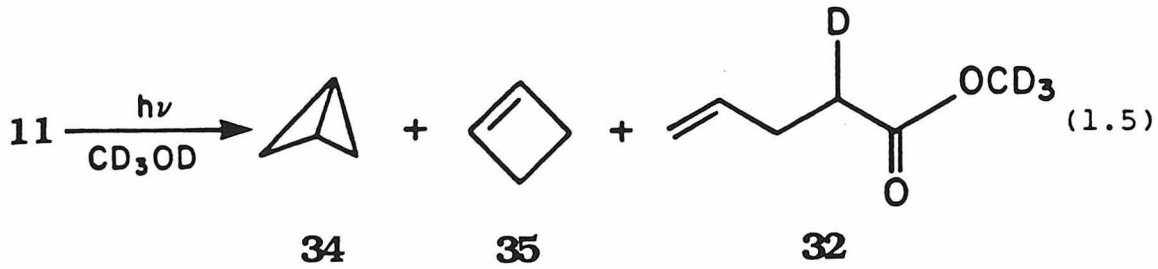

(1.5)

34 35 32

a mixture of **34** and **35** in yields comparable to the cyclohexane experiment, and also to **32** (15%). The presence of **32** provides strong evidence for the formation of **31**. Sodium bicarbonate is necessary to consume acidic products that are formed during the photolysis. In the absence of base, a substantial amount of the dimethyl ketal **37** is formed, and the bicyclobutane product (**34**) undergoes acid-catalyzed addition of methanol.[56] In the presence of bicarbonate, the formation of **37** is completely inhibited,[57] but small amounts of bicyclobutane methanolysis products are still observed.

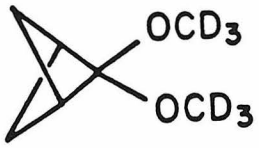

37

A striking feature of the methanolic photolysis experiment is the absence of 3-(methoxy-d_3)-2-oxa-bicyclo[2.1.1]hexane-3-d (**38**), which would be formed by trapping of the oxacarbene **39** by the solvent (eq. 1.6). The ring expansion of cyclic ketones to cyclic acetals is relatively rare for five-membered and larger ring ketones but is general for cyclobutanones.[58] Moreover, the yield of ring-expanded ketal is generally higher for ketones with more

strain.[58b] The absence of ring expansion in the case of 11 may be rationalized by noting that the oxacarbene 39 should be more strained than a typical cyclobutanone-derived oxacarbene and that ring expansion must compete with an especially favorable decarbonylation (see above).

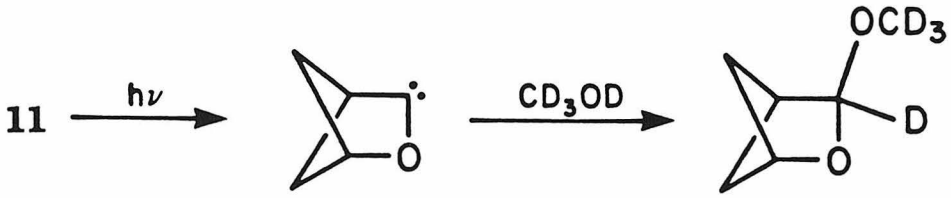

39 38 (1.6)

Gas-phase photolysis of 11 at room temperature gives mixtures of 34 and 1,3-butadiene (40) in a ratio that depends on pressure (eq. 1.7). No allyl signal was observed in the ^{1}H NMR spectrum, but a transparent film on the inside of the tube was observed. This film probably arises from polymerization of 31.

34 40 (1.7)

The formation of 40 in the gas-phase photolysis, but not in solution phase, suggests that this product derives from vibrationally activated bicyclobutane. The formation of 40 has been observed from direct heating of 34[59] and also from chemically activated 34 produced in the gas-phase thermolysis of azoalkane 9.[60] Thus, it is not surprising that

40 is formed in photolysis of 11, and only in the gas phase, where collisional deactivation is slow. A control photolysis of 34 under the same conditions showed that 40 is not formed from secondary photolysis. We cannot rule out an alternative route to 40 involving secondary photochemical CO extrusion from ketene 31 to give a carbene that can rearrange to 40, although one would not anticipate significant pressure dependence in this route.

Finally, we must consider the formation of cyclobutene (35) as a very minor product in the photolysis of 11. One possibility is the formation of cyclobutane-1,3-diyl (8), which undergoes mainly closure to 34, with a small fraction undergoing a 1,2-hydrogen shift to give 35. Cyclobutene was not observed in the direct photolysis of azoalkane 9,[4] which also yields 34. Additionally, thermolysis of 9 in solution produces biradical 8, but only ring closure to 34 ensues; no cyclobutene is formed.[3,60] This lack of a hydrogen shift in 8 has been rationalized as resulting from a stereoelectronic effect.[61] However, the high strain energy of 11 and the large amount of energy absorbed (247 nm = 116 kcal/mol) lead to a very large amount of excess vibrational energy in the fragmentation products. The formation of 35 from 8 could be the result of such chemical activation, although such processes are quite rare in solution.

Alternatively, the acyl alkyl biradical 36 could undergo intramolecular hydrogen abstraction to give 2-cyclobutenecarboxaldehyde (41), which then decarbonylates

photochemically to give 35. Analogous enal products are common from larger ring ketones,[52a,b] but are very rare from cyclobutanones,[1a] presumably because the hydrogen abstraction involves a strained four-membered ring transition state. Once again, however, the extra vibrational energy in 36 could allow for a small yield of this product. Decarbonylation of 41 might be expected to proceed readily, in that cyclobutane is a major product in the photolysis of cyclobutanecarboxaldehyde.[62] In 41, decarbonylation could be further favored by the formation of a stabilized radical, 2-cyclobuten-1-yl, and by the fact that decarbonylation of aldehydes generally proceeds with higher efficiency under shorter wavelength photolysis.[63]

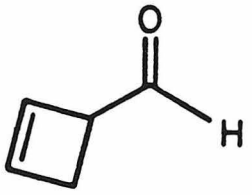

41

A third possibility is the formation of butadiene (40), which undergoes secondary photolysis to 35. This possibility, however, was ruled out by a control photolysis of 40 in cyclohexane-d_{12}. The conversion of 40 to 35 was found much too inefficient to explain the formation of 35 from photolysis of 11.

Conclusion

Useful quantities of ketone 11 can be conveniently prepared in only two steps from commercially available

material. Because of its high strain energy, 11 is much more thermally labile than typical cyclobutanones. The dominant thermal pathway is a concerted, $_{\sigma}2_{s} + _{\sigma}2_{a}$ cycloreversion to allylketene (31), which then oligomerizes. The transition state for this process contains little polar character. Photolysis of 11 results mainly in decarbonylation to produce bicyclobutane (34). A minor pathway is cycloreversion to 31, but no ring expansion (oxacarbene) products are observed.

Experimental Section

A. General Methods. ^{1}H NMR spectra were recorded on a Varian EM-390 spectrometer. Fourier transform NMR were recorded using either a JEOL FX-90Q spectrometer (^{1}H and ^{13}C) or a Bruker WM-500 spectrometer (^{1}H). IR spectra were recorded on a Beckman Model 4240 IR spectrophotometer. UV spectra were recorded using a Beckman Model 25 spectrophotometer. Mass spectra were obtained by the Midwest Center for Mass Spectrometry at the University of Nebraska, Lincoln, NE, or by the Caltech Analytical Facility. The PE spectrum was recorded using an He I UV spectrometer which was built at Caltech and is described in the literature.[64] Fluorescence spectroscopy was performed using a fluorimeter, which has been previously described.[65] Analytical gas chromatography was performed on a Hewlett-Packard 5840A chromatograph equipped with a flame-ionization detector. Retention times are reported for a 30 m x 0.329 mm DB-17 25-μm film on fused silica column with H_2 carrier gas, linear velocity 42 cm/s, and an oven-temperature program starting at 50 °C for 2 min, increasing at 10°/min until reaching and remaining at 200 °C. Preparative gas chromatography was performed on a Varian Aerograph Model 90-P chromatograph with a thermal conductivity detector.

Microwave spectra were obtained with a modified Hewlett-Packard 8460A MRR spectrometer.[66] Stark effect measurements were made by varying the ground-to-base voltage

of the 33 kHz square wave modulation. OCS was used as the calibrant.[67] Spectra of 11 were obtained by opening a bulb containing a degassed sample to the spectrometer and allowing it to warm from 77 K until pressures of 15-30 mtorr were established in the sample cell. The three ^{13}C isotopic species were studied in natural abundance. Although these spectra were readily observed, some lines were partially blended. These have been assigned larger experimental errors. Because of the high density of weak lines in the spectrum, it was not possible to assign transitions due to ^{18}O in natural abundance. Therefore, the sample was enriched by adding an excess of $H_2{}^{18}O$ and allowing the oxygen to exchange overnight. The resulting ^{18}O spectrum was then of strength comparable to that of the normal isotopic species.

B. Synthesis. 2-Phenylbicyclo[1.1.1]pentan-2-ol (24). The method of Padwa and co-workers[8] was used, except that the crude product was purified by flash chromatography[68] on 70-230-mesh silica gel using a 3:1 mixture of pentane and ethyl acetate, yielding 3.6 g of 24 from 10 g of 23 (Aldrich).

Bicyclo[1.1.1]pentanone (11). A 1000-mL three-necked round-bottomed flask was charged with 3.6 g (22.5 mmol) of 24 and 600 mL of dichloromethane and equipped with a magnetic stirrer and a dry ice/acetone condenser with drying tube. The flask was cooled with an ice bath, and ozone was bubbled through the solution at about 0.8 mmol/minute by using a gas

dispersion tube and paraffin film to close the opening around the dispersion tube. The ice and dry ice were regularly replenished, and the ozone flow was stopped after 6 h. The mixture was allowed to stir overnight at room temperature and was then filtered through a pad of silica gel. All but about 25 mL of the solvent was removed by careful atmospheric distillation using a 12-cm vacuum-jacketed Vigreux column. The solution was transferred to a 50-mL flask, and more solvent was removed to leave about 10 mL of solution. The product was then purified by azeotropic distillation as follows. A 500-mL flask was installed as receiver and 10 mL of pentane was added to the product solution via an addition funnel. Approximately 10 mL of distillate was collected, followed by addition of another 10 mL of pentane, and distillation. This process was repeated 24 times or until none of the product 11 remained in the residue, as determined by capillary GC (t_R 3.4 min). Dichloromethane (90 mL) was added to the combined distillate, and the mixed solvent was removed by distillation using the vacuum-jacketed column, stopping when the distillation temperature rose from 30 ^{o}C to 32 ^{o}C. The solution was transferred to a smaller flask, and 1 volume of dichloromethane was added for every 3 volumes of solution. Distillation was continued in this manner to concentrate the product solution to about 3 mL. If any of the distillates contained any of the product (by GC), then they were concentrated as above. The resulting solutions were further purified by preparative gas chromatography (25%

DEGS on Chromosorb WAW-DMCS, 60/80 mesh, 5 ft x 3/8 in., 80 °C, 60 mL/min He, t_R 14 min), using a glass coil with vacuum stopcocks in dry ice/acetone to collect the product (collection efficiency, 74%). (Once the coil contained some of the product, better efficiency was obtained by using liquid nitrogen.) The product (∿70 mg, 4%) was then vacuum-transferred from the collection coil in dry ice/CCl_4 to a small bulb with a vacuum stopcock in liquid N_2 for storage (in freezer): ^{1}H NMR ($CDCl_3$) δ 1.49 (s, H_{endo}), 1.80 (s, H_{exo}), 3.01 (s, $H_{bridgehead}$); ^{13}C NMR ($CDCl_3$) δ 35.61 (C_4, $^1J_{CH}$) = 152 Hz), 55.10 (C_1, $^1J_{CH}$ = ∿173 Hz), 188.64 (C_2) (for comparison, 29;[16] $^1J_{C(1)-H}$ = 164 Hz, $^1J_{C(2)-H}$ = 144 Hz); IR ($CDCl_3$) 3030, 3002, 2900, 1810, 1791, 1758, 1185 cm^{-1}; UV (n-pentane) λ_{max} 247 nm (ε 14); mass spectrum (EI), m/e (relative intensity) 82 (100), 54.8 (29), 54 (41), 53 (42), 39 (48), 28 (85); exact mass calcd for C_5H_6O 82.04186, found 82.04194.

Ozonolysis of 1-Phenylcyclohexanol (25). 1-Phenylcyclohexanol (100 mg, 0.57 mmol, Alfred Bader Chemicals) was dissolved in 50 mL of dichloromethane in a 100-mL round-bottomed flask. The solution was cooled in an ice bath, and ozone (∿0.8 mmol/min) was bubbled through the solution. After 2.5 h, the ozone flow was stopped and the solution allowed to warm. Cyclohexanone was identified as the major product by ^{1}H NMR, TLC, and GC; yield 67% (by GC).

RuO_4 Oxidation of 24. Oxidation of 130 mg (0.81 mmol) of 24 was performed by using the ternary solvent (CCl_4/CH_3CN/-

H_2O) method of Sharpless et al.[11] Starting material was gone after ∿1 day, although **11** was not detected by TLC. The reaction was worked up after 3 days, yielding ∿2% of **11** (by GC). The product mixture (in CH_2Cl_2) was separated into acidic and neutral fractions by extraction with aqueous NaOH. The acidic fraction was found by ^1H NMR to consist of benzoic acid and a material to which we tentatively assigned the structure of cyclobutanecarboxylic acid, in a ratio of about 1:1. The neutral fraction was analyzed by ^1H NMR and GC and found to contain a 1:1 ratio of **23** (t_R 13.4 min) and 3-oxocyclobutyl phenyl ketone (**26**, t_R 16.5 min). A small amount of **23** was present in the starting material as an impurity, though probably not enough to account for the **23** observed in the product mixture. Further purification of **26** by flash chromatography (pentane/ethyl acetate, 4:1) gave a pale yellow oil: ^1H NMR ($CDCl_3$) δ 3.4 (m, 4H), 4.0 (p, 1H), 7.5 (m, 3H), 8.0 (dd, 2H); IR ($CDCl_3$) 3060, 2910, 1792, 1725, 1682, 1580, 1450, 1348, 1225, 1100 cm^{-1}; mass spectrum (EI), m/e (relative intensity) 174 (2), 146 (25), 113 (12), 111 (25), 105 (100), 77 (48), 51 (32).

Reduction of 11 to Bicyclo[1.1.1]pentan-2-ol (27). A solution of 2.5 mg (0.030 mmol) of **11** in 2 mL of pentane (from azeotropic distillation) was placed in a 25-mL round-bottomed flask with 10 mL of methanol and stirred at 0 °C. A 2.2-mg (0.058 mmol) sample of sodium borohydride (Aldrich) was added. After 20 min, 8 μL of 3N hydrochloric acid was added. All but 1 mL of the solvent was removed by

distillation and 10 mL ether was added to the concentrate. The ether solution was washed with water, saturated sodium chloride, again with water, and then dried over sodium sulfate for 1 h. The solution was filtered and the filtrate concentrated to 2 mL by distillation. The concentrate was purified by preparative gas chromatography under the same conditions as for 11, except that a flow rate of 150 mL/min was used; 27 had a retention time of 20 min. We obtained 0.6 mg (0.007 mmol, 23% yield) of 27, which exhibited an ^{1}H NMR spectrum identical with the literature spectrum.[12]

1-Diazo-4-penten-2-one (33). The method of Smith and co-workers[69] was followed, except that the product was purified by flash chromatography by using pentane/ether (2:1): ^{1}H NMR (C_6D_6) δ 2.6 (d, 2H), 4.1 (s, 1H), 4.8 (m, 2H), 5.7 (m, 1H).

C. Thermal Decomposition Studies. All solution-phase thermolyses were performed with samples in degassed (five freeze-pump-thaw cycles) 5-mm NMR tubes. A well-insulated silicone oil bath with a Bayley Model 253 proportional temperature controller was used. The temperature was monitored accurately by using an iron-constantan thermocouple connected to a digital voltmeter.

Decomposition of 11. (a) Kinetics. A stock solution of 24 mg of 11 in 10 mL of benzene-d_6 was prepared and divided into several tubes. The decomposition kinetics were studied in the temperature range between 80 and 122 $^{\circ}$C and

the reaction progress was monitored by 90-MHz ^{1}H NMR spectroscopy, using several integrations over the signals at 0.8 (H_{endo}) and 1.2 ppm (H_{exo}) and the benzene peak as reference. The signal from the bridgehead hydrogens (2.4 ppm) was not used due to interference from products. The reaction was followed through 2 to 2.5 half-lives at each temperature. The rate data were analyzed by using a linear least-squares method, which incorporates error analysis.[70] All rate plots gave correlation coefficients higher than 0.996, and the Arrhenius and Eyring plots had correlations of 0.9999. Two experiments using samples made from different stock solutions (different concentrations) were included, since no decrease in correlation resulted from this inclusion. Errors represent two standard deviations. Rate constant x 10^5 s^{-1} (T, °C): 1.52±0.06 (79.89±0.12), 3.11±0.09 (86.05±0.05), 4.82±0.27 (89.66±0.10), 6.07±0.2 (92.37±0.03), 11.7±0.8 (98.18±0.03), 21.3±1.0 (104.47±0.04), 40.9±2.2 (110.90±0.08), 122±4 (122.34±0.16). E_a = 28.57±0.28 kcal/mol, log A = 12.87±0.16, $\Delta H^{\ddagger}$ = 27.82±0.28 kcal/mol, $\Delta S^{\ddagger}$ = -2.09±0.76 eu.

In order to rule out the possibility of acid catalysis in the thermolysis experiments, the disappearance rate at 100.47±0.08 °C was measured for a sample of 11 in C_6D_6 with 0.2 equiv. of 2,6-lutidine. The measured rate, (15.6±2.1) x 10^{-5} s^{-1}, is within experimental error of the expected rate of 14.4 x 10^{-5} s^{-1}.

The rate of thermal decomposition was also measured for 3 mg of 11 in acetonitrile-d_3 at 100.50±0.04 °C. The rate

plot gave a correlation coefficient of 0.9995 and a rate constant of (26.0±0.8) x 10^{-5} s^{-1}. The rate constant expected for thermolysis of 11 in benzene-d_6 at this expected for thermolysis of 11 in benzene-d_6 at this temperature is 14.4 x 10^{-5} s^{-1}, giving a solvent rate enhancement of 1.8 times for CD_3CN relative to C_6D_6.

The decomposition rate was also measured for 4 mg of 11 in methanol-d_4 with 10 mg of $NaHCO_3$ at 99.98±0.08 °C. The measured rate was (106±7) x 10^{-5} s^{-1} with a correlation coefficient of 0.9994. The expected rate at this temperature with benzene as solvent is 13.7 x 10^{-5} s^{-1}. The rate enhancement is thus 7.7 times for methanol relative to benzene.

(b) Products. (i) Thermolysis of 11 in C_6D_6: ^1H NMR (integration relative to initial starting material) 2.1 (m, 3.3H), 4.9 (m, 1.8H), 5.5 (m, 0.9H); ^{13}C NMR δ 28, 116, 136; GC t_R, min (relative area, GC-MS M^+ if found) 7.4 (16), 10.2 (13), 11.0 (36), 16.8 (35, 246 amu) 22.1 (trace, 328 amu). Trace amounts of several longer t_R components were also detected. The GC yields are given for the 98 °C experiment; the others varied by up to 5%. (ii) Thermolysis of 11 in CD_3CN: ^1H NMR δ 2.4 (m, 3.1H), 3.6 (s, 0.2H), 5.0 (m, 1.8H), 5.8 (m, 0.9H); GC t_R, min (relative area) 3.4 (3), 3.5 (41), 7.4 (4), 10.2 (28), 11.0 (24). (iii) Thermolysis of 11 in CD_3OD (methyl-d_3 4-pentanoate-2-d (32)). ^1H NMR δ 2.3 (m, 2H), 2.4 (m, 1H), 4.98 (d, 1H), 5.05 (d, 1H), 5.8 (m, 1H); t_R 3.5 min, yield 88.5%. An authentic sample of methyl-d_3

4-pentenoate was made by mildly heating 4-pentenoic acid in CD_3OD with 1 drop DCl in D_2O for several hours. The authentic sample had t_R and NMR spectral characteristics identical with the photolysis product, except for the expected differences in integration and coupling constants due to protium substitution. No evidence for divinyl ketone, a possible side product, could be seen by NMR, and there was no evidence for oligomers of any sort by GC. (iv) Gas-phase thermolysis of 11: 1.3 mg (0.016 mmol) of 11 was thermolyzed at 100 °C in a 2-L bulb (∿0.2 torr) for 4 h. Benzene-d_6 (0.5 mL) was vacuum-transferred into the bulb and the solution pipetted into an NMR tube. By GC, 41% of the starting material was left, giving an approximate rate constant of 6×10^{-5} s^{-1}; ^1H NMR δ 1.9 (m, ∿1H), 2.7 (m, ∿2H), 4.9 (m, 2H), 5.7 (m, ∿1H); GC t_R, min (relative area) 7.4 (16), 10.2 (81), 11.0 (3).

Decomposition of 33. (a) Photolysis. Diazoketone 33 (0.8 mg) in 0.5 mL benzene-d_6 in an NMR tube was photolyzed under N_2 for 2.5 h by using Pyrex-filtered light: ^1H NMR δ 2.2 (m, ∿3H), 4.9 (m, .2H), 5.5 (m, ∿1H); GC t_R, min (relative area) 4.5 (16), 6.6 (14), 10.2 (25), 11.0 (35), 14.2 (10). The components with t_R 10.2 and 11.0 coeluted on both DB-5 and DB-17 capillary columns with the corresponding components in a sample from thermolysis of 11.

(b) Thermolysis. Diazoketone 33 (1.5 mg) in benzene-d_6 was thermolyzed at 119.3 °C for 2 h: ^1H NMR δ 2.0 (m, 0.5H), 2.2 (m, 0.5H), 2.6 (m, 0.9H), 4.6 (s, 0.3H), 4.9 (m, 2.6H),

5.5 (m, 1.3H); GC t_R, min (relative area) 6.6 (2), 6.8 (4), 8.5 (8), 10.9 (86). It seems likely that the major product arises from cycloaddition of **31** and **33**.[71]

D. MNDO Calculations. The geometry of **11** was completely optimized (retaining C_{2v} symmetry) giving the geometry shown in Table 1.4; ΔH_f = 31.93 kcal/mol, IP = 10.31 eV. The geometry of **29** was optimized (retaining D_{3h} symmetry), giving C-C = 1.573 Å, C_1-H = 1.083 Å, C_2-H = 1.101 Å, $\angle C_1\text{-}C_2\text{-}C_3$ = 74.1°, ∠H-C-H = 107.6°; ΔH_f = 58.27 kcal/mol, IP = 11.67 eV.

E. Photolysis. All photolyses were carried out on degassed (5 cycles) samples in quartz ESR tubes, using a Hanovia 450-W medium pressure mercury arc lamp with a Vycor 7910 filter sleeve (Ace Glass).

Photolysis of 11 in Cyclohexane-d_{12}. Photolysis of 9 mg of **11** in 0.5 mL of C_6D_{12} at room temperature for 8 h gave a product mixture (90% conversion), which was analyzed by ^{1}H NMR and GC. Bicyclo[1.1.0]butane (**34**) and cyclobutene (**35**) were observed and were identical with authentic samples in both ^{1}H NMR and t_R (both 1.2 min; 2.42 and 2.34 min, respectively, at 30 °C, linear velocity = 22 cm/s); yield of **34** 70%; **35** 1-2% (by NMR, GC). Remainder: ^{1}H NMR δ 2.3 (min, ∿1H), 5.0 (m, ∿0.4H), 5.7 (m, ∿0.2H); GC t_R, min (relative area) 2.5 (5), 9.1 (1), 12.8 (2). A white precipitate was also observed.

Photolysis of 11 in Methanol-d_4. Photolysis of 12 mg of 11 in 0.5 mL of CD_3OD with ∿5 mg of $NaHCO_3$ at room temperature produced a mixture which was analyzed by ^1H NMR and GC. Bicyclo[1.1.0]butane (34): yield (by NMR) 79% (1 h photolysis), 65% (3 h), 61% (5 h). Cyclobutene (35): yield ∿2% (5 h). Methyl-d_3 4-pentenoate-2-d (32) (see Section C): yield 16% (5 h). Cyclobutyl-d methyl-d_3 ether (42): ^1H NMR δ 1.5 (m, ∿1H), 1.7 (m, ∿0.3H), 1.85 (q, ∿1.8H), 2.2 (m, ∿2H), 3.85 (p, 1H); yield ∿6% (5 h). Cyclopropylcarbinyl-d methyl-d_3 ether (43): ^1H NMR δ 0.2 (m, 1.2H), 0.5 (d, 1.9H), 1.0 (sextet, 1H), 3.2 (d, 2H); yield ∿6% (5 h). Retention times for 42 and 43 are 1.8 and 1.9 min, but the elution order was not determined. In the absence of $NaHCO_3$, no 34 was observed, and instead 42 and 43 were each obtained in 44% yield. In this case, the observed product distribution of 42-43 is identical with that reported by Wiberg and Szeimies[56] for the hydrolysis of bicyclobutane to the corresonding alcohols of 42-43. The observed labeling patterns are also nearly identical.

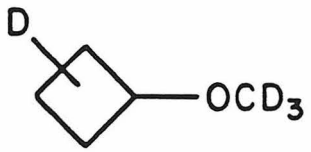

42

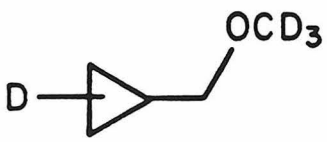

43

1,1-Di(methoxy-d_3)bicyclo[1.1.1]pentane (37) was formed in up to 43% yield from photolysis without $NaHCO_3$ at slightly below room temperature and was the sole observed product from

photolysis at 35-40 °C. ^{1}H NMR δ 1.4 (s, 2H), 2.0 (s, 2H), 2.8 (s, 2H); t_R 3.7 min.

Control Photolysis of 40. 1,3-Butadiene (∿1 mg) in cyclohexane-d_{12} was photolyzed through Vycor for 8.5 h at room temperature. ^{1}H NMR and GC analysis showed that the yield of cyclobutene was less than 20% and that most of the starting material was unchanged.

Gas-Phase Photolysis of 11. Photolysis of 1-3 mg of **11** in an evacuated EPR tube with vacuum stopcock for durations up to 54 h at room temperature, followed by vacuum transfer of benzene-d_6 into the tube, produced bicyclo[1.1.0]butane and 1,3-butadiene as products in a ratio that varied from experiment to experiment, with increasing pressure producing greater quantities of bicyclobutane. A colorless film was also formed on the sides of the tube (detected by filling the empty tube with 5% HF). Photolysis without the Vycor filter increased the rate, and the film on the sides of the tube was yellow instead of colorless.

Control Photolysis of 34. Bicyclo[1.1.0]butane (∿6 mg) was photolyzed in the gas phase for 48 h at room temperature. Benzene-d_6 was vacuum-transferred into the tube and the solution pipetted into an NMR tube. Only **34** was observed.

F. EPR Experiments. All samples were prepared and degassed (5 cycles) in 4- or 5-mm o.d. quartz EPR tubes equipped with high vacuum stopcocks. 2-Methyltetrahydrofuran

(MTHF), cyclohexane, and perfluorokerosene were used as solvents.

A Varian E-line Century Series X-band spectrometer and an Oxford Instruments ESR-900 continuous liquid-helium flow cryostat were used. The samples were photolyzed in the cavity by using an Oriel 1000-W mercury-xenon lamp, operated near 950 W. The light was filtered with water in a quartz vessel and focussed with a quartz lens.

The cavity temperature was measured using a calibrated Lakeshore Cryotonics carbon-glass thermister fitted inside a sample tube. The experiments were run at 4 K. The MTHF and cyclohexane samples exhibited large doublet signals upon photolysis, but no signal that could be attributed to a triplet biradical was observed.

References for Chapter 1

1. (a) Morton, D. R.; Turro, N. J. Adv. Photochem. 1974, 9, 197-309. (b) Stohrer, W. D.; Jacobs, P.; Kaiser, K. H.; Wiech, G.; Quinkert, G. Fortschr. Chem. Forsch. 1974, 46, 181-236. (c) Egger, K. W. J. Am. Chem. Soc. 1973, 95, 1745-1750. (d) Metcalfe, J.; Carless, H. A. J.; Lee, E. K. C. J. Am. Chem. Soc. 1972, 94, 7235-7241.
2. The work described in this chapter has been published: (a) Sponsler, M. B.; Dougherty, D. A. J. Org. Chem. 1984, 49, 4978-4984. (b) McRae, G. A.; Cohen, E. A.; Sponsler, M. B.; Dougherty, D. A. J. Phys. Chem. 1986, 90, 6412-6415.
3. Chang, M. H.; Dougherty, D. A. J. Org. Chem. 1981, 46, 4092-4093.
4. Chang, M. H.; Dougherty, D. A. J. Am. Chem. Soc. 1982, 104, 2333-2334.
5. Goldberg, A. H.; Dougherty, D. A. J. Am. Chem. Soc. 1983, 105, 284-290. See also Chapter 2.
6. Jain, R.; Sponsler, M. B.; Coms, F. D.; Dougherty, D. A., manuscript in preparation. See also Chapter 3.
7. Dowd, P.; Sachdev, K. J. Am. Chem. Soc. 1967, 89, 715-716. Tetramethyleneethane has also been generated from a ketone precursor: Dowd, P. J. Am. Chem. Soc. 1970, 92, 1066-1068.

8. (a) Padwa, A.; Shefter, E.; Alexander, E. J. Am. Chem. Soc. 1968, 90, 3717-3721. (b) Padwa, A.; Alexander, E.; Niemcyzk, M. J. Am. Chem. Soc. 1969, 91, 456-462.

9. Bailey, P. S. "Ozonation in Organic Chemistry", Academic Press: New York, Vol. I, 1978; pp 147-153.

10. Wolfe, S.; Haan, S. K.; Campbell, J. R. J. Chem. Soc., Chem. Commun. 1970, 1420-1421.

11. Carlsen, P. H. J.; Katsuki, T.; Martin, V. S.; Sharpless, K. B. J. Org. Chem. 1981, 46, 3936-3938.

12. Wiberg, K. B.; Williams, V. Z., Jr. J. Org. Chem. 1970, 35, 369-373.

13. Conia, J. M.; Gore, J.; Salaun, J.; Ripoll, L. Bull. Soc. Chim. Fr. 1964, 1976-1980.

14. Turro, N. J.; Hammond, W. B. J. Am. Chem. Soc. 1966. 88, 3672-3673.

15. Maier, G.; Hoppe, M.; Reisenauer, H. P. Angew. Chem., Int. Ed. Engl. 1983, 22, 990-991.

16. Wiberg, K. B.; Connor, D. S. J. Am. Chem. Soc. 1966, 88, 4437-4441.

17. Silverstein, R. M.; Bassler, G. C.; Morrill, T. C. "Spectrometric Identification of Organic Compounds", 4th ed.; Wiley: New York, 1981; pp 187-190.

18. (a) Maier, G.; Pfriem, S.; Schaefer, U.; Malsch, K. D.; Matusch, R. Chem. Ber. 1981, 114, 3965-3987. (b) Hoye, T. R.; Martin, S. J.; Peck, D. R. J. Org. Chem. 1982, 47, 331-337.

31. Gaussian 80 UCSF was used (C_{2v} symmetry retained): Singh, U. C. and Kollmann, P. QCPE 1982, NO. 446.

32. Hehre, W. J.; Stewart, R. F.; Pople, J. A. J. Chem. Phys. 1969, 51, 2657-2664.

33. Binkley, J. S.; Pople, J. A.; Hehre, W. J. J. Am. Chem. Soc. 1980, 102, 939-947.

34. Burkert, U.; Allinger, N. L. "Molecular Mechanics," Amer. Chem. Soc., Washington, D.C., 1982; pp 6-10.

35. Reference 34, pp 116-121.

36. Wiberg, K. B.; Wendoloski, J. J. J. Am. Chem. Soc. 1982, 104, 5679-5686.

37. Dewar, M. J. S.; Thiel, W. J. Am. Chem. Soc. 1977, 99, 4907-4917.

38. (a) Frey, H. M.; Hopf, H. J. Chem. Soc., Perkin Trans. 2 1973, 2016-2019. (b) Carless, H. A. J.; Lee, E. K. C. J. Am. Chem. Soc. 1972, 94, 1-6. (c) McGee, T. H.; Schleifer, A. J. Phys. Chem. 1972, 76, 963-967. (d) Blades, A. T. Can. J. Chem. 1969, 47, 615-617.

39. A small amount of sodium bicarbonate was added to inhibit ketalization.

40. (a) Meier, H.; Zeller, K. P. Angew. Chem., Int. Ed. Engl. 1975, 14, 32-43.

41. For another solution phase study, see: Jones, G., II; Zalk, S. A. Tetrahedron Lett. 1973, 4095-4098.

42. (a) Schaumann, E.; Ketcham, R. Angew. Chem., Int. Ed. Engl. 1982, 21, 225-247. (b) Paquette, L. A.;

Kukla, M. J. Tetrahedron Lett. 1973, 1241-1244. (c) Gerberich, H. R.; Walters, W. D. J. Am. Chem. Soc. 1961, 83, 4884-4888. (d) Benson, S. W.; Nangia, P. S. J. Chem. Phys. 1963, 38, 18-25. (e) Ellis, R. J.; Frey, H. M. J. Chem. Soc. 1964, 4184-4187.

43. Although the product mixtures vary with solvent, the rate comparisons are still valid, since the rate-determining step in all three solvents is presumably the formation of 13.

44. Gassman, P. G. Acc. Chem. Res. 1971, 4, 128-136.

45. Frey, H. M.; Smith, R. A. J. Chem. Soc., Perkin Trans. 2 1977, 2082-2084.

46. Willcott, M. R.; Cargill, R. L.; Sears, A. B. Prog. Phys. Org. Chem. 1972, 9, 25-98.

47. (a) McMillen, D. F.; Golden, D. M. Annu. Rev. Phys. Chem. 1982, 33, 493-532. (b) Benson, S. W. "Thermochemical Kinetics"; 2nd ed.; Wiley: New York, 1976; p 309.

48. Strain energies were calculated as the difference between the heats of formation provided by MNDO and Benson group values.[49]

49. Reference 47b, pp 272-275.

50. Although MNDO calculations on such strained molecules could be fairly inaccurate in an absolute sense,[51] they should be acceptable for discerning such trends among closely related molecules.

51. Dewar, M. J. S.; Thiel, W. J. Am. Chem. Soc. 1977, 99, 4907-4917.

52. (a) Weiss, D. S. Org. Photochem. 1981, 5, 347-420. (b) Chapman, O. L.; Weiss, D. S. Org. Photochem. 1973, 3, 197-288. (c) Yates, P. Pure Appl. Chem. 1968, 16, 93-113. (d) Srinivasan, R. Adv. Photochem. 1963, 1, 83-113.

53. Givens, R. S. Org. Photochem. 1981, 5, 227-346.

54. Kerr, J. A.; Calvert, J. G. J. Phys. Chem. 1965, 69, 1022-1029.

55. Wagner, P. J. In "Rearrangements in Ground and Excited States"; de Mayo, P., Ed.; Academic Press: New York, 1980; Vol. 3, pp 415-417.

56. Wiberg, K. B.; Szeimies, G. J. Am. Chem. Soc. 1970, 92, 571-579.

57. Malatesta, V.; Jennings, M.; Hackett, P. Can. J. Chem. 1983, 61, 366-367.

58. (a) Yates, P. J. Photochem. 1976, 5, 91-106. (b) Morton, D. R.; Turro, N. J. J. Am. Chem. Soc. 1973, 95, 3947-3957.

59. Frey, H. M.; Stevens, I. D. R. Trans. Faraday Soc. 1965, 61, 90-94.

60. Chang, M. H.; Dougherty, D. A. J. Am. Chem. Soc. 1982, 104, 1131-1132.

61. Chang, M. H.; Jain, R.; Dougherty, D. A. J. Am. Chem. Soc. 1984, 106, 4211-4217.

51. Dewar, M. J. S.; Thiel, W. J. Am. Chem. Soc. 1977, 99, 4907-4917.

52. (a) Weiss, D. S. Org. Photochem. 1981, 5, 347-420. (b) Chapman, O. L.; Weiss, D. S. Org. Photochem. 1973, 3, 197-288. (c) Yates, P. Pure Appl. Chem. 1968, 16, 93-113. (d) Srinivasan, R. Adv. Photochem. 1963, 1, 83-113.

53. Givens, R. S. Org. Photochem. 1981, 5, 227-346.

54. Kerr, J. A.; Calvert, J. G. J. Phys. Chem. 1965, 69, 1022-1029.

55. Wagner, P. J. In "Rearrangements in Ground and Excited States"; de Mayo, P., Ed.; Academic Press: New York, 1980; Vol. 3, pp 415-417.

56. Wiberg, K. B.; Szeimies, G. J. Am. Chem. Soc. 1970, 92, 571-579.

57. Malatesta, V.; Jennings, M.; Hackett, P. Can. J. Chem. 1983, 61, 366-367.

58. (a) Yates, P. J. Photochem. 1976, 5, 91-106. (b) Morton, D. R.; Turro, N. J. J. Am. Chem. Soc. 1973, 95, 3947-3957.

59. Frey, H. M.; Stevens, I. D. R. Trans. Faraday Soc. 1965, 61, 90-94.

60. Chang, M. H.; Dougherty, D. A. J. Am. Chem. Soc. 1982, 104, 1131-1132.

61. Chang, M. H.; Jain, R.; Dougherty, D. A. J. Am. Chem. Soc. 1984, 106, 4211-4217.

62. Funke, C. W.; de Boer, J. L. M.; Geenevasen, J. A. J.; Cerfontain, H. J. Chem. Soc., Perkin Trans. 2 1976, 1083-1089.

63. Calvert, J. G.; Pitts, J. N. "Photochemistry", Wiley: New York, 1966; pp 369-370.

64. Houle, F. A.; Beauchamp, J. L. Chem. Phys. Lett. 1977, 48, 457-460.

65. Rice, S. F.; Gray, H. B. J. Am. Chem. Soc. 1983, 105, 4571-4575.

66. Kakar, R. K.; Cohen, E. A.; Geller, M. J. Mol. Spectrosc. 1978, 70, 243-256.

67. Muenter, J. S. J. Chem. Phys. 1968, 48, 4544-4547.

68. Still, W. C.; Kahn, M.; Mitra, A. J. Org. Chem. 1978, 43, 2923-2925.

69. Smith, A. B., III; Toder, B. H.; Branca, S. J.; Dieter, R. K. J. Am. Chem. Soc. 1981, 103, 1996-2008.

70. Irvin, J. A.; Quickenden, T. I. J. Chem. Ed. 1983, 60, 711-712.

71. Ulrich, H. "Cycloaddition Reactions of Hetero-cumulenes"; Academic Press: New York, 1967; pp 96-97.

CHAPTER 2

THEORETICAL CALCULATIONS OF CYCLOBUTANEDIYLS

Theoretical studies have played a tremendously important role throughout the development of the field of biradicals.[1] While it is not the case that calculations have led the way, requiring experiments only for verification, neither is it true that theory has been useful only when the proper experiment is too difficult. Rather, a healthy synergism has existed between theory and experiment. Calculations have guided experimentalists in the choice of interesting systems and in the interpretation of results. At the same time, the theoretical methods have continually improved as data for calibration and comparison have become available. With this view, we undertook an in-depth theoretical study of cyclobutanediyl (**8**) to complement our experimental work.

8

34

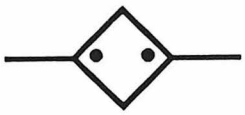

12

Our goals in this work were twofold. First, we wished to investigate the effects of geometry optimization and substituents on the S-T gap of **8**. Second, we planned to theoretically probe the closure reaction to bicyclo[1.1.0]-butane (**34**). The majority of our calculations involved the parent biradical, though a single-point computation of dimethylcyclobutanediyl (**12**) was also done. Unfortunately, molecular size and special problems that arise in the calculation of conjugated radicals[2] made high-quality

calculations of vinyl-substituted cyclobutanediyls impractical.

Computational Methods

Several basis sets have been employed. Unless otherwise stated, the double-zeta Dunning (3s,2p) contraction[3] of Huzinaga's (9s,5p) basis set[4] was used for carbon, along with a similar contraction of Huzinaga's (4s/2s) hydrogen basis set with a scaling factor of 1.2. Other basis sets that were used include 4-31G[5] and STO-3G.[6]

In general, restricted Hartree-Fock (RHF) wave functions were used for triplet biradicals, while singlets were calculated by using the Multiconfiguration Self-Consistent Field (MCSCF) procedure. The MCSCF method yields a two-configuration wave function that serves to correlate the singlet radical electrons to a degree consistent with the RHF triplet.[1a] The RHF-MCSCF combination has been shown to give S-T gaps that are essentially the same as those obtained from much higher levels of theory.[7] The MCSCF method is equivalent to a Generalized Valence Bond (GVB) calculation.[8] This method, using one GVB-orbital pair with two electrons, is denoted GVB(1/2).

Ab initio calculations were normally done with the MQM:GVB2P5 program.[9] Gaussian-80 UCSF[10] was used in some cases to verify results. MQM:UHF[11] was used for unrestricted Hartree-Fock (UHF). Gradient optimization was accomplished using programs from the MQM library.

Cyclobutane-1,3-diyl (8)

Preliminary calculations for cyclobutane-1,3-diyl (8) had been done by Goldberg and Dougherty.[7] Using RHF for the triplet and MCSCF for the singlet, they obtained an S-T gap of 1.7 kcal/mol. (A positive S-T gap indicates a triplet ground state.) This result was taken as strong support that the ground state is indeed the triplet, since the known triplet cyclopentane-1,3-diyl (4) had a smaller calculated gap of 0.9 kcal/mol.[7,12]

Our goals for extending this work were first to obtain an optimized geometry for 8, making sure that the question of ground spin state did not change. We then wished to explore the potential surface near the biradical. In particular, we wished to probe the closure pathway to bicyclo[1.1.0]butane (34). We hoped to determine the existence of a barrier to closure on the singlet surface and also the location of the singlet-triplet crossing points.

Geometry optimization of triplet 8 was achieved by using a gradient method starting with the same model geometry used by Goldberg and Dougherty.[7] The starting guess structure was almost entirely defined by the geometry of 1,3-dimethylene-cyclobutane (44), which had been partially optimized using the STO-3G basis set by Hemmersbach, et al.[13] The only remaining parameter was the C_1-H bond length, which was obtained from a 4-31G-optimized geometry of an appropriate conformation of 2-propyl (45).[14] Repetition of the earlier

calculation was successful, giving an S-T gap of 1.67 kcal/mol.

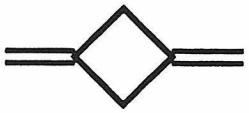

44

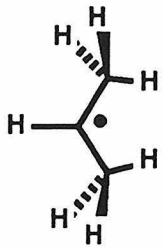

45

The geometry optimization results for triplet **8** are shown in Table 2.1. All geometric parameters were optimized, and D_{2h} symmetry was imposed as a constraint. Only three iterations were performed, and the geometry after the second iteration was taken as optimized, since the energy increased on the last iteration. Despite the low number of iterations, the geometry is considered to be reasonably well optimized, since the structural changes in the second iteration were small. The initial geometry itself was quite good, as demonstrated by the small geometric changes in the optimization and the small energy lowering of 0.3 kcal/mol. The S-T gap increased slightly to 1.74 kcal/mol.

Although our results were unambiguous in assigning the triplet as the ground state of **8**, Tanaka reported calculations in 1984[15] that gave the opposite result. Unfortunately, the exact methods used in his calculations are unclear, but he optimized both singlet and triplet biradicals at the STO-3G level and calculated energies using 4-31G. The UHF method was apparently used both in optimization and energy evaluation. Tanaka reported an S-T gap of -0.4

Table 2.1 Geometry Optimization of Triplet 8: Geometries and Energies[a]

Geometry	1	2	3
χ(C1)	1.060	1.048	1.049
R_{C1-C2}	1.538	1.528	1.531
∠C2-C1-C4	92.90	93.41	93.49
R_{C1-H1}	1.080	1.078	1.065
R_{C2-H3}	1.092	1.086	1.085
θ1	180.00	180.00	180.00
θ2(θ3)	125.60	126.20	126.20
Energy ($^3B_{3u}$)	-154.7822789	-154.7827713	-154.7828277
Energy (^1A_g)	-154.7796083		-154.7800491
S-T	1.67 kcal/mol		1.74 kcal/mol

[a]Distances are in Å; angles are in degrees; energies are in hartrees.

kcal/mol and attributed the different result to the fact that both spin states were optimized in his calculation.

In an attempt to resolve this conflict, we performed several calculations using Tanaka's optimized geometries[15] and basis set (4-31G). We also repeated some of the calculations using Gaussian-80 UCSF in order to verify that there was no error in our program. Our results are summarized in Table 2.2. As we expected, our original S-T gap of 1.7 kcal/mol is insensitive to changes in basis set, program, and the small geometrical changes required by Tanaka's geometries.

We also performed several UHF calculations for comparison to Tanaka's results. UHF has two major disadvantages in calculations of this sort. First, UHF wave functions do not correspond to pure spin states.[16] Second, the wave functions consist of single-electron orbitals with fixed spin, so the converged wave function and its energy depend on the initial assignment of spins.[17] This makes reproduction of published results difficult. We used three initial configurations, and all three yielded a triplet ground state with the singlet 2.49 kcal/mol higher in energy.[18]

Subsequent to these results, Tanaka claimed that he still obtained a singlet ground state, by 1.3 kcal/mol, when he used the RHF-MCSCF method.[19] Comparison of total energies revealed that we agreed precisely on the singlet, but our

Table 2.2 Cyclobutane-1,3-diyl Energies

	Model Geometry	Optimized Triplet	Tanaka's Triplet	Tanaka's Singlet
Dunning-Huzinaga				
Triplet	-154.78228[a]	-154.78283[a]	-154.78253[a]	
Singlet	-154.77961	-154.78005	-154.77964	
S-T Gap	1.67	1.74	1.81	
4-31G				
Triplet			-154.59950[c]	-154.59947[b]
Singlet			-154.59667	-154.59673
S-T Gap			1.77	1.72
			(T) (S)	
S-T Gap			1.74	

[a] MQM: GVB2P5 [b] Gaussian-80 [c] Both Programs

calculations gave a triplet energy 3.0 kcal/mol lower. The fact that our result was reproduced on two separate programs and that it constitutes the lower energy wave function indicates that the error must lie in Tanaka's calculation.

Having established the ground state of the planar biradical, we next wished to investigate the potential surface on the closure coordinate to **34**. We chose the method of linear synchronous transit (LST)[20] to obtain geometric parameters for the intermediate structures. In the LST method, the structures of the reaction coordinate endpoints are first defined by a common set of geometric parameters. Intermediate structures are then obtained by linear interpolation of all parameters. This procedure requires the assumption that the chosen parameters all vary smoothly and simultaneously, which may not be true. However, in the absence of reaction-coordinate data, the LST method is one of the simplest ways to obtain the intermediate structures.

An experimental structure for bicyclobutane (**34**), obtained from microwave data and shown in Table 2.3, was used. RHF calculations for the same geometry and basis set had been reported by Eisenstein and Hirschfeld.[21] Subtracting the correlation energy gained through the MCSCF procedure in our calculation gives a total energy which differs by only 1.1 mhartrees (0.7 kcal/mol) from that reported by Eisenstein.

The geometry specifications for **8** and **34** are shown in Figure 2.1. Application of the LST method gives geometries for five intermediate structures, which are tabulated with

Table 2.3 LST Closure Pathway Geometries[a]

Symm.	D_{2h}	C_{2v}	C_{2v}	C_{2v}	C_{2v}	C_{2v}	C_{2v}
k[b]	0.0000	0.1250	0.2500	0.3750	0.5000	0.7500	1.0000
χ(Cl)	1.049	1.012	0.9741	0.9365	0.8989	0.8237	0.7485
R_{C1-C2}	1.531	1.527	1.523	1.519	1.515	1.506	1.498
ϕ	180.0	172.7	165.4	158.1	150.8	136.2	121.6
R_{C3-H1}	1.065	1.065	1.066	1.067	1.068	1.069	1.071
R_{C2-H3}	1.085	1.086	1.087	1.088	1.089	1.091	1.093
θ1	180.0	173.6	167.1	160.7	154.2	141.3	128.4
θ2	126.2	125.8	125.4	125.0	124.5	123.7	122.9
θ3	126.2	125.6	125.0	124.5	123.9	122.7	121.6

[a] All distances are in Å, angles in degrees.

[b] k = reaction coordinate

a.

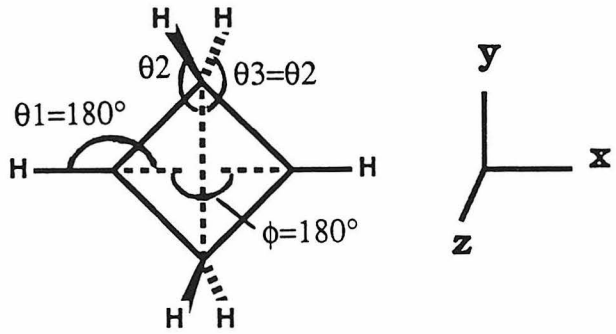

b.

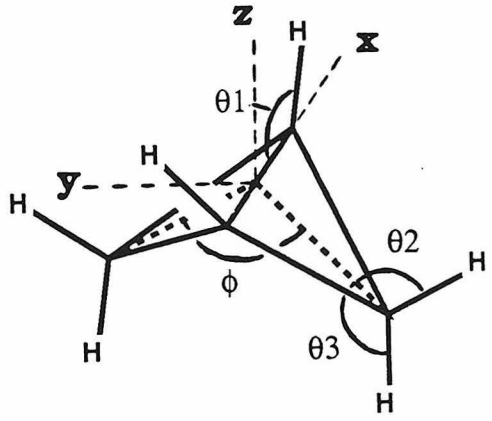

Figure 2.1. Geometric parameters and coordinate systems for a) **8** and b) **34**.

the endpoints in Table 2.3. The reaction coordinate is symbolized by the parameter k, which represents the fraction of the path traveled from **8** to **34**. The intermediate structures are spaced more closely in the region of interest near **8**.

Both singlets (MCSCF) and triplets (RHF) were calculated for each point, and smooth fits to the resulting energies are shown in Figure 2.2. A barrier of 6.9 kcal/mol was found on the singlet surface, located at an approximate k of 0.375. The triplet surface rises evenly toward the bicyclobutane geometry, crossing the singlet surface before the closure barrier.

The singlet surface was further refined by adding electron correlation in the form of restricted configuration interaction (RCI), in which all single and double excitations were allowed from the radical orbitals. The resulting energies are listed in Table 2.4 and compared graphically with the uncorrelated singlet surface in Figure 2.3. The energetic stabilization provided by the RCI is negligible in **8** but increases smoothly along the reaction coordinate, amounting to 2 kcal/mol for **34**. This trend is expected, since correlation is needed more in structures that have larger overlap. The addition of electron correlation reduced the singlet closure barrier to 6.6 kcal/mol.

We must point out that our result of 6.6 kcal/mol represents an upper limit to the closure barrier, since the geometry for **8** was optimized (albeit for the triplet), while the intermediate geometries were obtained through the LST

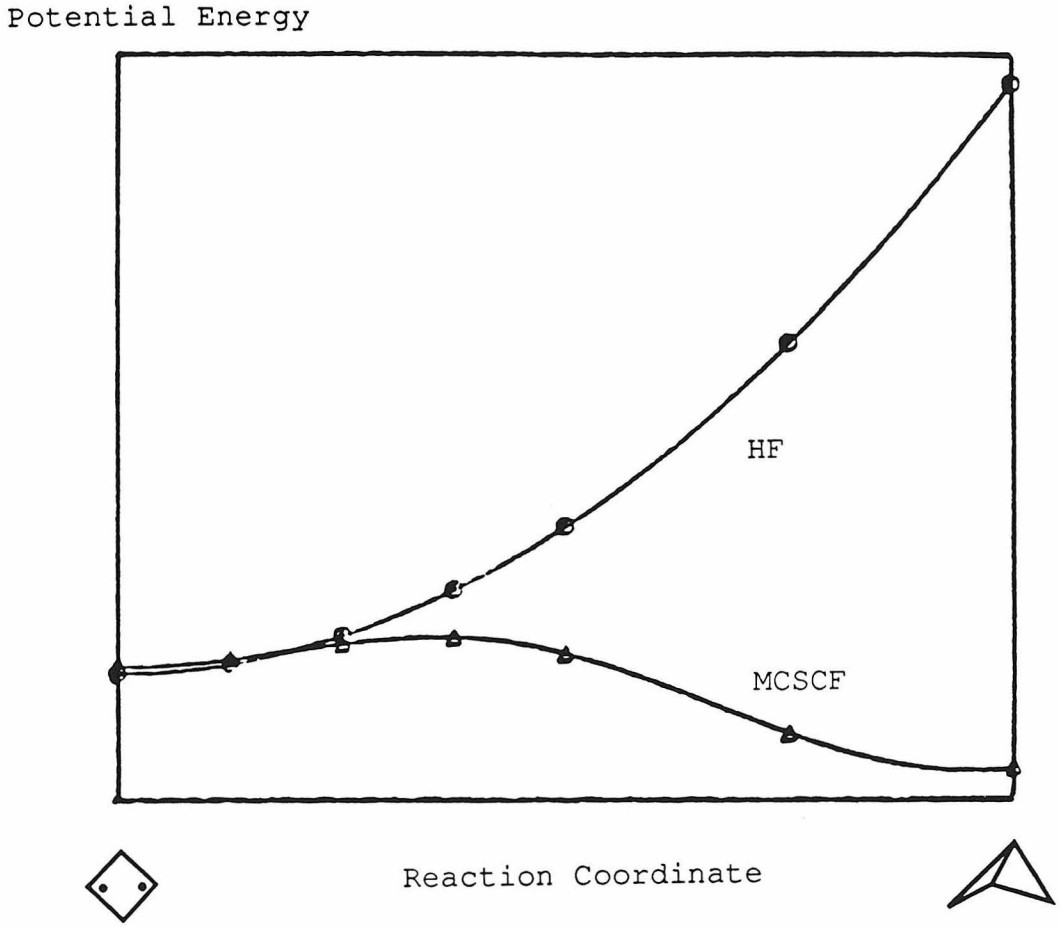

Figure 2.2. Triplet (HF) and singlet (MCSCF) surfaces for the LST closure of **8** to **34**.

Table 2.4 Closure Pathway Energies

k	Singlet, $^1A_1$ CI	Singlet, $^1A_1$ GVB(1/2)	Triplet, $^3B_1$ HF
0.0	-154.7802565	-154.7800491	-154.7828277
0.125	-154.7775123	-154.7772536	-154.7791509
0.25	-154.7718585	-154.7714389	-154.7683575
0.375	-154.7697836	-154.7690252	-154.7511019
0.5	-154.7766022	-154.7753691	-154.7274702
0.75	-154.8070212	-154.8052783	-154.6584312
1.0	-154.8201385	-154.8182952	-154.5609707

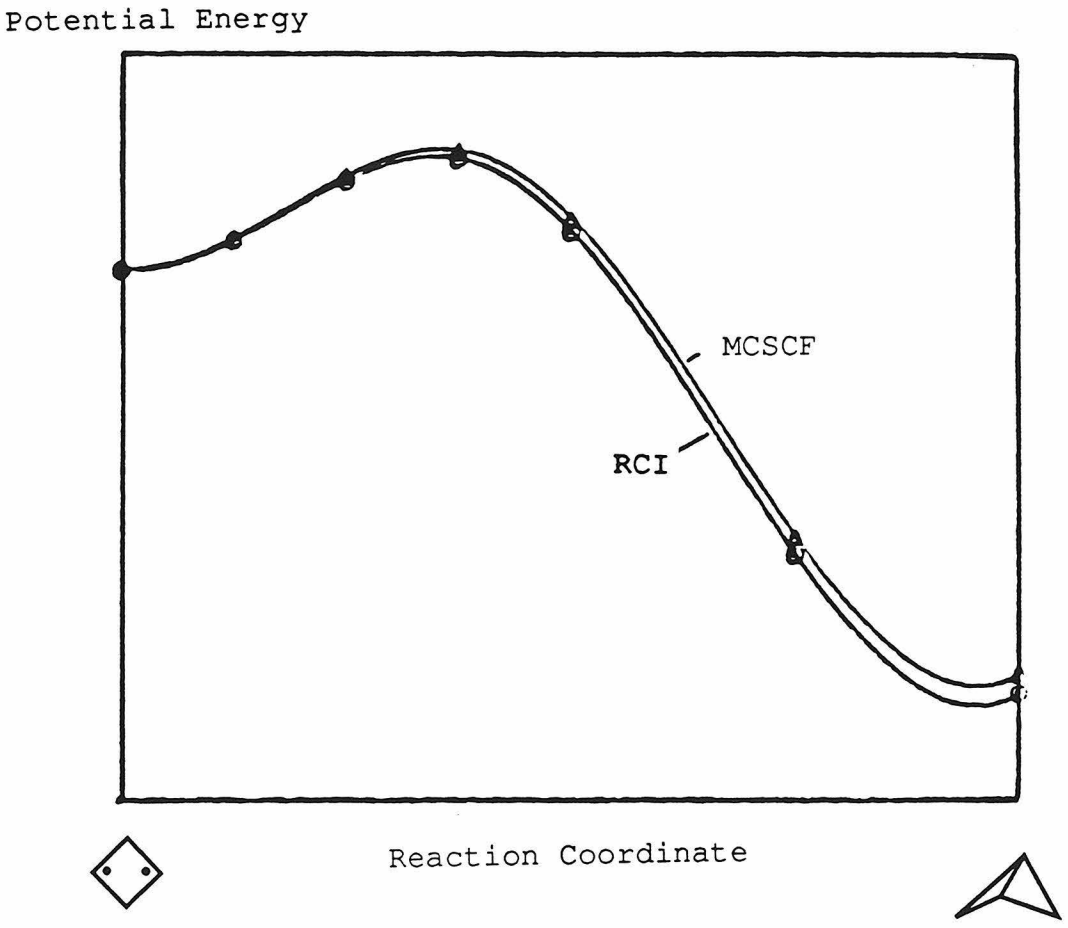

Figure 2.3. Comparison of the singlet MCSCF and RCI closure surfaces.

approximation. Calculation of the "true" barrier at this level of theory would require optimization of the intermediate geometries, holding one parameter, such as the C_1-C_3 distance, fixed.

The upper bound of 6.6 kcal/mol is reasonable in comparison with previous calculations for trimethylene (7). Several theoretical investigations have found that 7 has essentially no barrier in its closure to cyclopropane. For either 7 or 8, the existence of a barrier on the singlet surface may be thought to depend on a competition between build-up of strain energy and bonding character in the early stages of closure. As shown in Figure 2.4, the increase in strain energy is about 9 kcal/mol higher in the closure of 8, so it might be expected to have a higher barrier.

Shortly after our calculations were completed, a very similar, though more extensive, study was reported by Gassman and coworkers.[23] Crystallographic data for several bicyclobutane derivatives led Gassman to investigate theoretically the inversion pathway for the parent, 34. Using GVB(1/2) calculations under the PRDDO approximation with a minimum basis set, he calculated an LST pathway with optimized structures for 8 (D_{2h}) and 34 as endpoints. These results are very similar to ours, showing a barrier of 7.5 kcal/mol located at k = 0.41.

Gassman extended these calculations[23] by optimizing the intermediate geometries, holding the interflap angle (ϕ) constant. The result was a pathway that deviated markedly

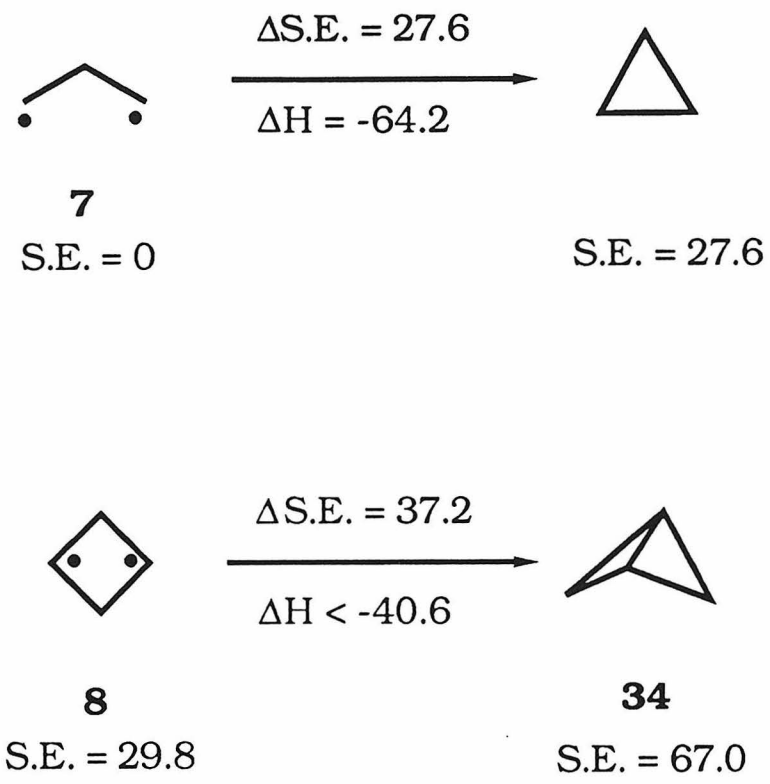

Figure 2.4. Comparison of strain energy increases upon closure of **7** and **8**. See Lowry, T. H.; Richardson, K. S. "Mechanism and Theory in Organic Chemistry"; Harper & Row: New York, 1981; p 150-151. (The strain energy of **8** was assumed equivalent to that of cyclobutene.) See also Reference 26.

from the LST path, most notably in the motions of the hydrogens on C_1 and C_3. In fact, the optimum position of these hydrogens in **8** was found to be 32.8° out of the plane of the ring, reducing the D_{2h} symmetry to C_{2v}. The optimized singlet surface thus obtained has a barrier of 0.8 kcal/mol located at k = 0.10. Another very important result was that the C_{2v} structure for **8** was found to be 4.0 kcal/mol lower in energy than the D_{2h} form. Depending on the behavior of the triplet surface, this finding implies that S-T crossing points may lie very close to the D_{2h} structure.

In order to verify these results and extend them to the triplet surface, we performed calculations for **8** using two further geometries, both with the hydrogens on C_1 and C_3 out of the ring plane by 32.8°, the optimum angle determined by Gassman et al.[23] The first had C_{2v} symmetry, corresponding to a <u>syn</u> deformation, and the second had C_{2h} symmetry, corresponding to an <u>anti</u> deformation. Both structures were otherwise identical to our optimized planar triplet.

Our results agreed with Gassman's[23] in that the C_{2v} singlet is more stable than the D_{2h} form, but we found the stabilization worth only 0.52 kcal/mol, a factor of eight smaller. The triplet energy at the C_{2v} geometry was found to be 0.68 kcal/mol higher than the D_{2h} form, giving an S-T gap of 0.54 kcal/mol for the C_{2v} structure. The C_{2h} deformation has a similar effect, reducing the S-T gap to 0.88 kcal/mol. These results are summarized in Table 2.5 and displayed graphically in Figure 2.5.

Table 2.5 Calculated Total Energies for **8**.

	D_{2h}	C_{2v}	C_{2h}
Triplet (HF)	-154.782828	-154.781749	-154.782155
Singlet (MCSCF)	-154.780049	-154.780880	-154.780749

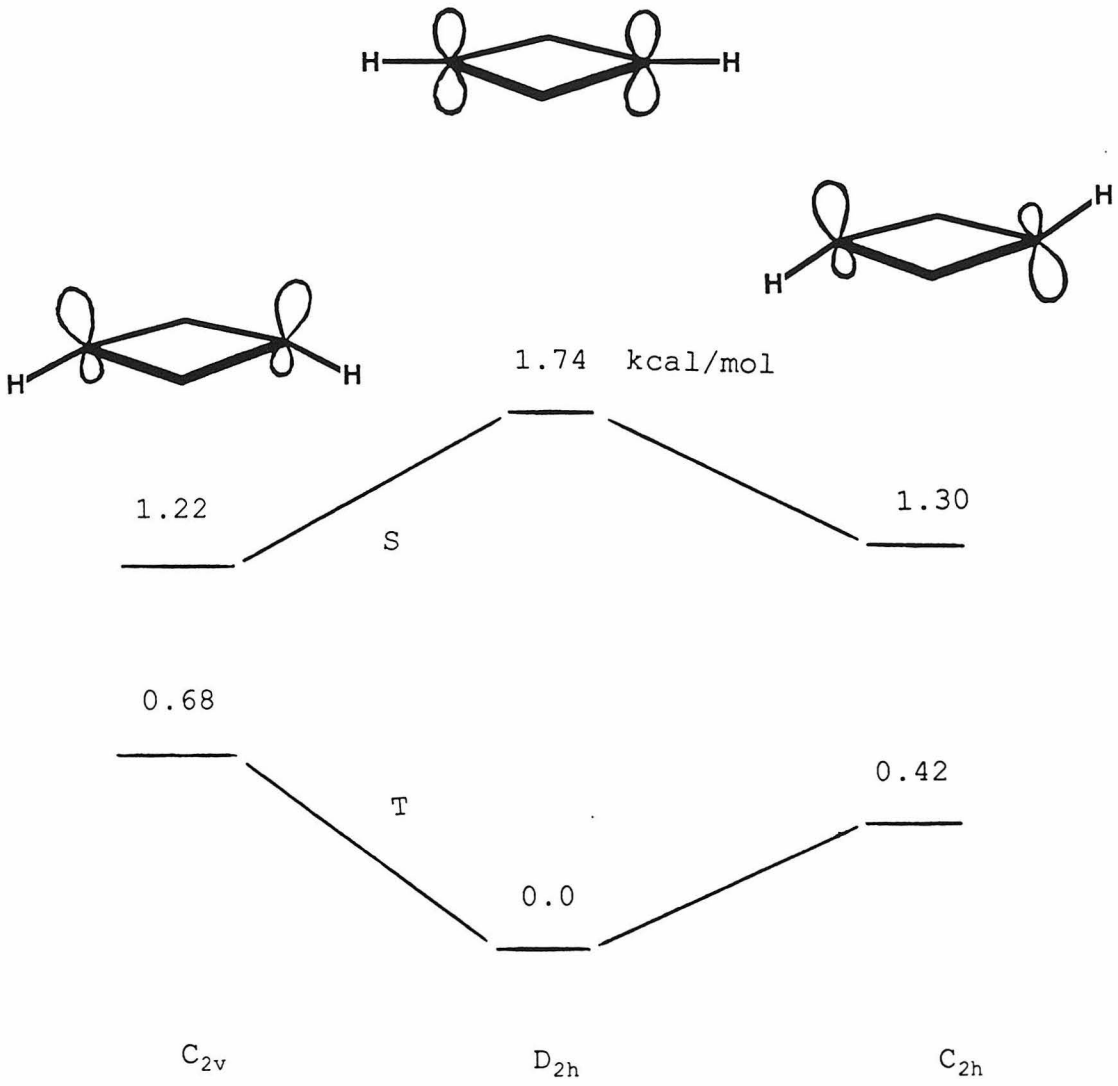

Figure 2.5. Singlet and triplet energy comparison of three geometries of **8**, differing only in the position of the α-hydrogens.

The singlet and triplet closure surfaces of **8** have also been studied by Pranata and Dougherty using MNDO.[24] An S-T gap of 1.4 kcal/mol was found for the D_{2h} biradical. All intermediate geometries were optimized, and a singlet barrier of 8 kcal/mol was found at k = 0.69. MNDO is known to stabilize radical-type intermediates,[25] so this result is not surprising. In general, MNDO is relatively inaccurate for small-ring compounds, and this is vividly demonstrated by its result that the closure of **8** to **34** is endothermic by 4.5 kcal/mol. Experimental evidence suggests that the reaction is exothermic by at least 40.6 kcal/mol.[26]

Gassman's PRDDO calculations[23] and our ab initio calculations also underestimate the exothermicity of the closure reaction, giving 23.2 and 25.0 kcal/mol, respectively. This discrepancy may be attributed to a need for polarization functions for proper calculation of **34**, as suggested by Eisenstein and Hirschfeld.[21]

In way of summary, the various singlet surfaces (our LST-RCI, Gassman's LST,[23] Gassman's optimized,[23] and Pranata and Dougherty's MNDO surfaces[24]) are compared in Figure 2.6.

1,3-Dimethylcyclobutane-1,3-diyl (12)

Having observed a tremendous experimental difference in stability between the parent and dimethyl cyclobutanediyls (the latter has been observed by EPR; the former has not been observed to date), we wished to determine whether any difference would be predicted theoretically. Since only a

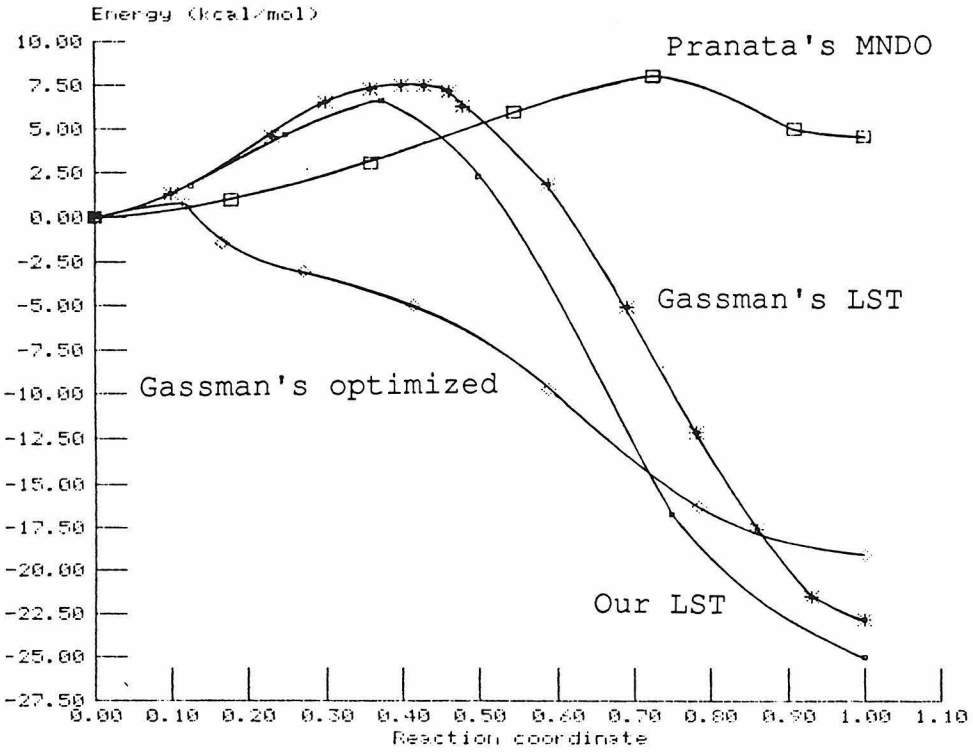

Figure 2.6. Comparison of various singlet closure surfaces for **8**. The energies were normalized to **8**.

small difference was expected as a result of methyl substitution, calculation of **12** could be considered as a control.

A C_{2v} geometry for **12** was used, that in which one C-H bond of each methyl group resides in the plane of the carbons (see Figure 2.7). The geometrical parameters for the ring were taken from the optimized triplet geometry of **8**, and the methyl geometry was taken from an STO-3G optimization of t-butyl radical.[29] Using our standard method, we obtained an S-T gap of 1.47 kcal/mol. (Total energies are given in Figure 2.7.) This result corresponds to a 16% reduction in the S-T gap compared to **8**, confirming the expected similarity.

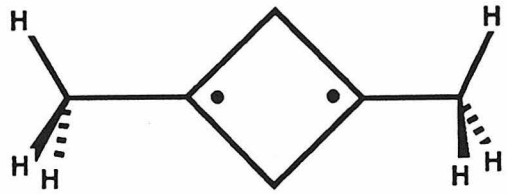

12

C_{2v}

Triplet: -232.837248

Singlet: -232.834909

S-T gap: 1.47 kcal/mol

Figure 2.7. Geometry and results of a calculation on **12**.

References for Chapter 2

1. See for example: (a) Salem, L.; Rowland, C. Angew. Chem., Int. Ed. Engl. 1972, 11, 92-111. (b) Davidson, E. R. In "Diradicals"; Borden, W. T., Ed.; Wiley: New York, 1982; Chapter 2.
2. Borden, W. T.; Davidson, E. R.; Feller, D. Tetrahedron 1982, 38, 737-739.
3. Dunning, T. H., Jr. J. Chem. Phys. 1970, 53, 2823-2833.
4. Huzinaga, S. J. Chem. Phys. 1965, 42, 1293-1302.
5. Ditchfield, R.; Hehre, W. J.; Pople, J. A. J. Chem. Phys. 1971, 54, 724-728.
6. Hehre, W. J.; Stewart, R. F.; Pople, J. A. J. Chem. Phys. 1969, 51, 2657-2664.
7. Goldberg, A. H.; Dougherty, D. A. J. Am. Chem. Soc. 1983, 105, 284-290.
8. Goddard, W. A., III; Dunning, T. H., Jr.; Hunt, W. J.; Hay, P. J. Acc. Chem. Res. 1973, 6, 368-376.
9. Bair, R. A.; Goddard, W. A., III, unpublished work. Bair, R. A., Ph.D. Thesis, California Institute of Technology, 1982.
10. Singh, U. C.; Kollmann, P. QCPE 1982, No. 446.
11. Upton, T. H.; Bair, R. A.; Goddard, W. A., III, unpublished work.
12. Conrad, M. P.; Pitzer, R. M.; Schaefer, H. F., III. J. Am. Chem. Soc. 1979, 101, 2245-2246.

13. Hemmersbach, P.; Klessinger, M.; Bruckmann, P. J. Am. Chem. Soc. 1978, 100, 6344-6347.

14. Pacansky, J.; Dupuis, M. J. Chem. Phys. 1980, 73, 1867-1872.

15. Tanaka, H. Chem. Phys. 1984, 91, 399-410.

16. Amos, T.; Snyder, L. C. J. Chem. Phys. 1964, 41, 1773-1783.

17. McAdon, M. H.; Brusich, M. J.; Goddard, W. A., III, personal discussions.

18. Total energies: triplet, -154.60544; singlet, -154.60941.

19. Tanaka, H., personal communication.

20. Halgren, T. A.; Lipscomb, W. N. Chem. Phys. Lett. 1977, 49, 225-232.

21. Eisenstein, M.; Hirschfeld, F. L. Chem. Phys. 1981, 54, 159-172.

22. (a) Hay, P. J.; Hunt, W. J.; Goddard, W. A., III. J. Am. Chem. Soc. 1972, 94, 638-640. (b) Horsley, J. A.; Jean, Y.; Moser, C.; Salem, L.; Stevens, R. M.; Wright, J. S. J. Am. Chem. Soc. 1972, 94, 279-282.

23. Gassman, P. G.; Greenlee, M. L.; Dixon, D. A.; Richtsmeier, S.; Gougoutas, J. Z. J. Am. Chem. Soc. 1983, 105, 5865-5874.

24. Pranata, J.; Dougherty, D. A., unpublished results.

25. Dewar, M. J. S.; Thiel, W. J. Am. Chem. Soc. 1977, 99, 4907-4917.

26. Bicyclo[1.1.0]butane rearranges to 1,3-butadiene with E_a = 40.6 kcal/mol;[27] however, no ring inversion occurs in the decomposition of bicyclo[1.1.0]butane-2-*exo*-d_1.[28] Therefore, the ring inversion E_a, and hence $-\Delta H$ for closure of **8**, must be higher.

27. Frey, H. M.; Stevens, I. D. R. Trans. Faraday Soc. 1965, 61, 90-94.

28. Wiberg, K. B.; Lavanish, J. M. J. Am. Chem. Soc. 1966, 88, 5272-5275.

29. Lengsfield, B. H., III; Siegbahn, P. E. M.; Liu, B. J. Chem. Phys. 1984, 81, 710-716.

CHAPTER 3

SYNTHESIS AND EPR SPECTROSCOPY OF CYCLOBUTANEDIYLS

In the 20 years since Dowd's report on the EPR spectrum of triplet trimethylenemethane (1),[1] a wide variety of biradicals and related structures have been directly observed by matrix-isolation EPR spectroscopy.[2] The overwhelming majority of such studies have involved non-Kekulé molecules (delocalized biradicals).[3] These are fully conjugated π systems for which one cannot write a classical Kekulé structure with all the electrons paired into bonds. Examples include (1),[1,4] tetramethyleneethane (2),[5] m-quinodimethane (3),[3b] and derivatives of all three. The non-Kekulé nature and the spin preferences of such structures are set by the topologies of the π systems.[6]

In contrast, direct spectroscopic studies of <u>localized</u> hydrocarbon biradicals are rare.[7] Localized biradicals contain two well-defined radical substructures that are not in conjugation with one another in a classical π sense. Note that the radical units themselves can be classically delocalized, such as allyl or benzyl. Localized biradicals are fundamentally different from non-Kekulé or delocalized biradicals, in that there are no simple topological rules for predicting spin state, etc. Rather, features such as ring strain, steric effects and second-order electronic effects (e.g., through-bond coupling) are dominant.[8]

In 1984, Jain, Snyder and Dougherty reported the EPR spectrum of the localized hydrocarbon triplet biradical 1,3-dimethylcyclobutane-1,3-diyl (12).[7b] Almost ten years earlier, Buchwalter and Closs had reported the EPR detection

12

4

of triplet cyclopentane-1,3-diyl(**4**).[7a] This classic study was the first, and until the detection of **12**, the only effort of its kind. At the time, the observation of **4** appeared to signal a turning point in the study of localized biradicals. For the first time, one would be able to directly probe their spectroscopy and reactivity. The many questions concerning the effects of substituents on singlet-triplet preferences and reactivity could be addressed directly. However, the cyclopentanediyl framework proved to be quite sensitive. Minor perturbations led to weak EPR signals or no signals at all.[7a] Thus, a systematic study of the role of substituents on localized biradical spectroscopy and reactivity was not possible.

We now report that the cyclobutanediyl framework is much more robust.[9] A variety of biradicals **46** have been prepared, all of which give intense, interpretable EPR

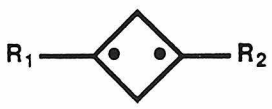

46

	R_1	R_2	Previous label
46-Me	CH_3	CH_3	**12**
-CD_3	CD_3	CD_3	
-Et	C_2H_5	C_2H_5	**19**
-Pr	n-C_3H_7	n-C_3H_7	
-EV	C_2H_5	$CH=CH_2$	**20**
-Vin	$CH=CH_2$	$CH=CH_2$	**21**
-Vin-d_6	$CD=CD_2$	$CD=CD_2$	
-Ph	C_6H_5	C_6H_5	

spectra. Trends in the EPR zero-field splitting (zfs) parameter D have provided insights into the spin distribution of the various cyclobutanediyls. In addition, we have observed interpretable hyperfine couplings (hfc) to the hydrogens of the ring CH_2 groups, which provide further information on the electronic structures of these biradicals. The thermal decay reactions and kinetics of the cyclobutanediyls are described in Chapter 4. The work described herein mainly concerns the synthesis and properties of the divinyl (**46-Vin**) and ethyl vinyl cyclobutanediyls (**46-EV**), but other cyclobutanediyls will be included in much of the discussion for comparison purposes.

Synthesis

The immediate precursors to biradicals **1** are the substituted 2,3-diazabicyclo[2.1.1]hex-2-enes (**47**) which, in turn, are prepared from the appropriate urazoles **48** (see eq. 3.1). Earlier work in our laboratories showed that thermal

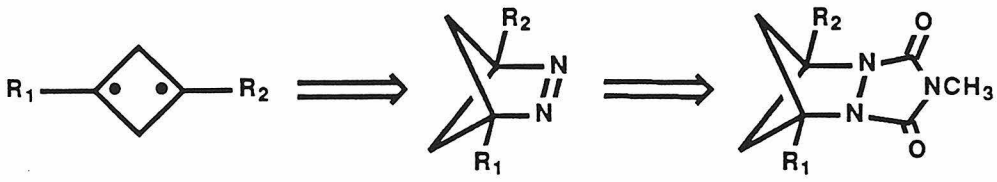

46 **47** **48** (3.1)

addition of N-methyltriazolinedione (MTAD) to bicyclobutanes is a convenient method for the synthesis of such urazoles.[10] However, the reaction was quite sensitive to substituents at

the bridgehead positions of the bicyclobutane, giving very low yields with simple alkyl substituents.[10,11] We now report that the photochemical addition of MTAD to the readily available 1,3-dicarbomethoxybicyclobutane (**49**) produces the bridgehead disubstituted urazole (**15**) in good yield (eq. 3.2).[12] The ester functionality can be efficiently

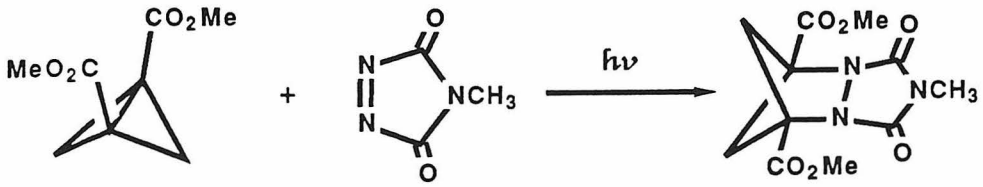

(3.2)

49 **MTAD** **15**

transformed into a variety of substituents using standard synthesis methodologies, while keeping the urazole intact (Scheme 3.1).

Dialdehyde **50** was selected as a key target in an approach to the synthesis of hydrocarbon-substituted urazoles via Wittig reactions. However, its synthesis proved to be surprisingly difficult. We first attempted the direct reduction of **15** to **50**, using both diisobutyl aluminum hydride[13] and sodium bis(2-methoxyethoxy)aluminum hydride,[14] but neither method was successful. Therefore, we decided to adopt a two-step procedure in which the ester functionalities are first reduced to hydroxymethyl groups. This can be achieved easily using either lithium borohydride in THF[15] or sodium borohydride in methanol.[16] Oxidation of the diol **51** was quite difficult, and many procedures, including chromium-based reagents, Swern,[18] lead tetraacetate,[19] and

Scheme 3.1

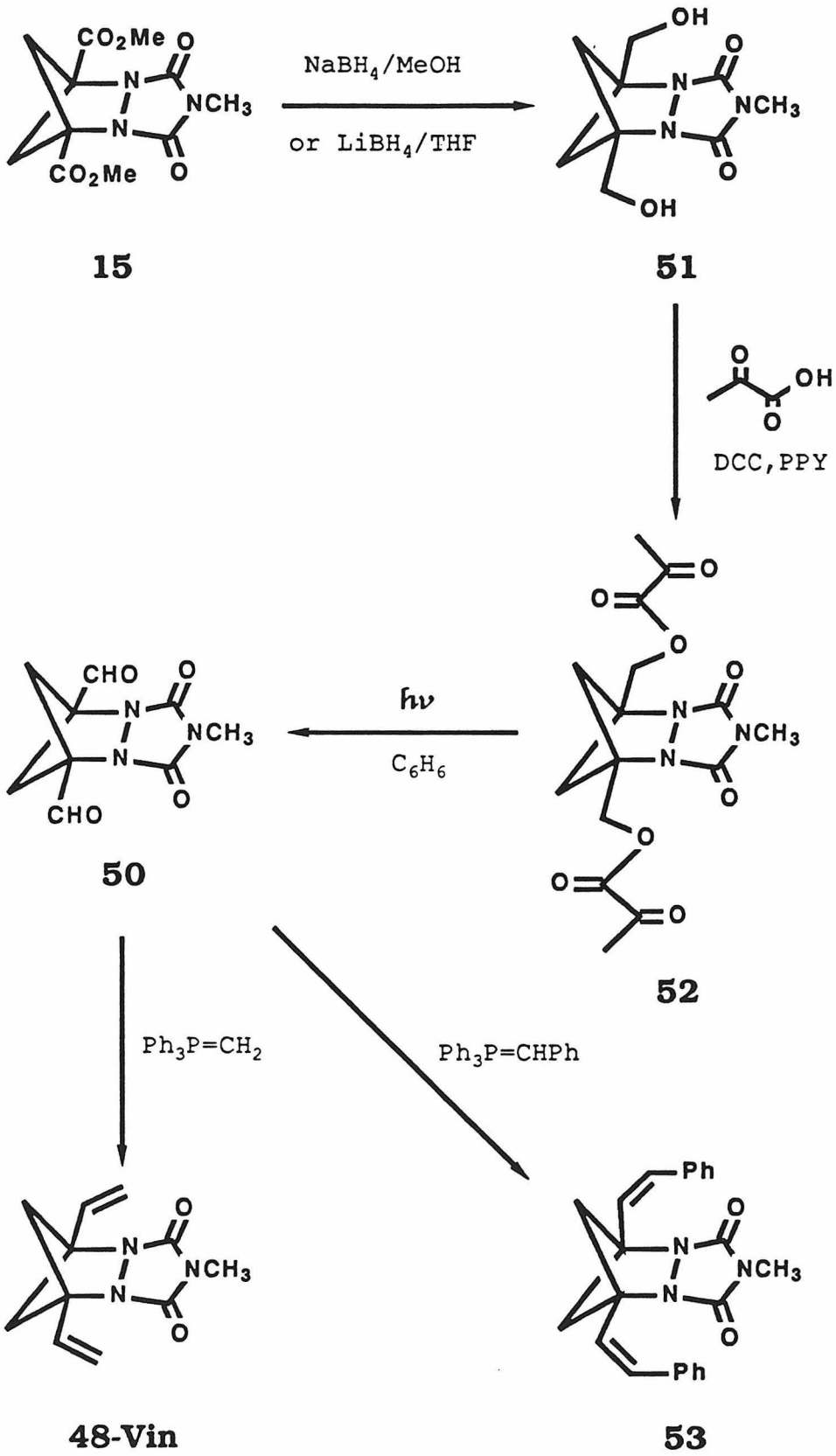
CO2Me
NCH3
CO2Me
NaBH4/MeOH
or LiBH4/THF
OH
OH
15
51
DCC,PPY
CHO
CHO
hν
C6H6
50
52
Ph3P=CH2
Ph3P=CHPh
Ph
Ph
48-Vin
53

N-phenyltriazolinedione oxidations failed. Though some of these methods left the starting material unchanged, others appeared to fail only in the isolation of the product. Believing that hydration of the dialdehyde might be the problem, we sought a completely water-free method. The pyruvate-photolysis procedure employed by Binkley[21] appeared attractive, since the aldehyde product is obtained in solution without work-up. Dicyclohexylcarbodiimide esterification[22] of the diol with pyruvic acid afforded the dipyruvate **52** in essentially quantitative yield (Scheme 3.1). Pyrex-filtered photolysis of **52** in dilute benzene solution gave the dialdehyde **50**, which indeed hydrates readily. Therefore, the product was used without isolation in Wittig reactions to give diene urazoles **48-Vin** and **53**. The stereochemistry of **53** was shown to be predominantly cis,cis, even under Wittig reaction conditions which normally favor trans products.

Inversion of distyryl urazole **53** to produce the presumably more stable trans,trans isomer (**54**) was attempted by using several methods,[23] though with no success. Neither direct photolysis, benzophenone-sensitized photolysis, nor contact with palladium on carbon showed any signs of olefin inversion. Photolysis in the presence of iodine[24] effected the desired inversion, but the reaction was very inefficient and the mixture was degraded after approximately 50% conversion to the cis,trans isomer (**55**).

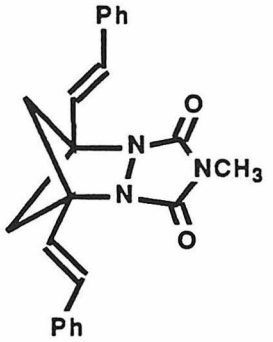

54

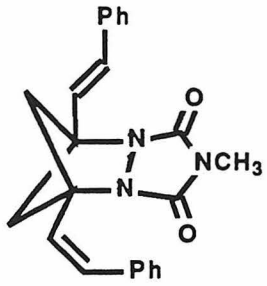

55

Deuterated divinyl urazole **48-Vin-**d_6 was prepared by following the above procedure with sodium borodeuteride in the reduction step and deuterated phosphonium salt in the Wittig reaction (eq. 3.3).

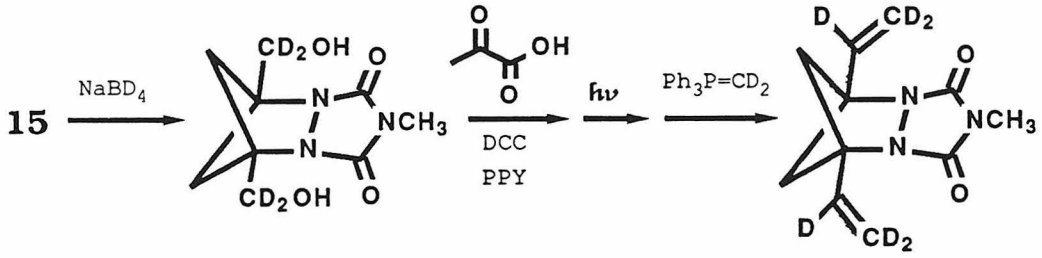

51- $\underline{d}_4$ **48-Vin-**$\underline{d}_6$ (3.3)

The less symmetrical ethyl vinyl urazole **48-EV** was prepared by using two different methods (Scheme 3.2). Catalytic hydrogenation of the divinyl urazole **48-Vin** with one equivalent of hydrogen resulted in a 1:2:1 mixture of **48-Vin, -EV,** and **-Et,** which could be separated by preparative TLC and HPLC. The separation was quite difficult, however, so an alternate route was sought. The second method employed an epoxide moiety as a protecting group. Partial epoxidation of **48-Vin** with m-chloroperbenzoic acid produced **56,** which was

Scheme 3.2

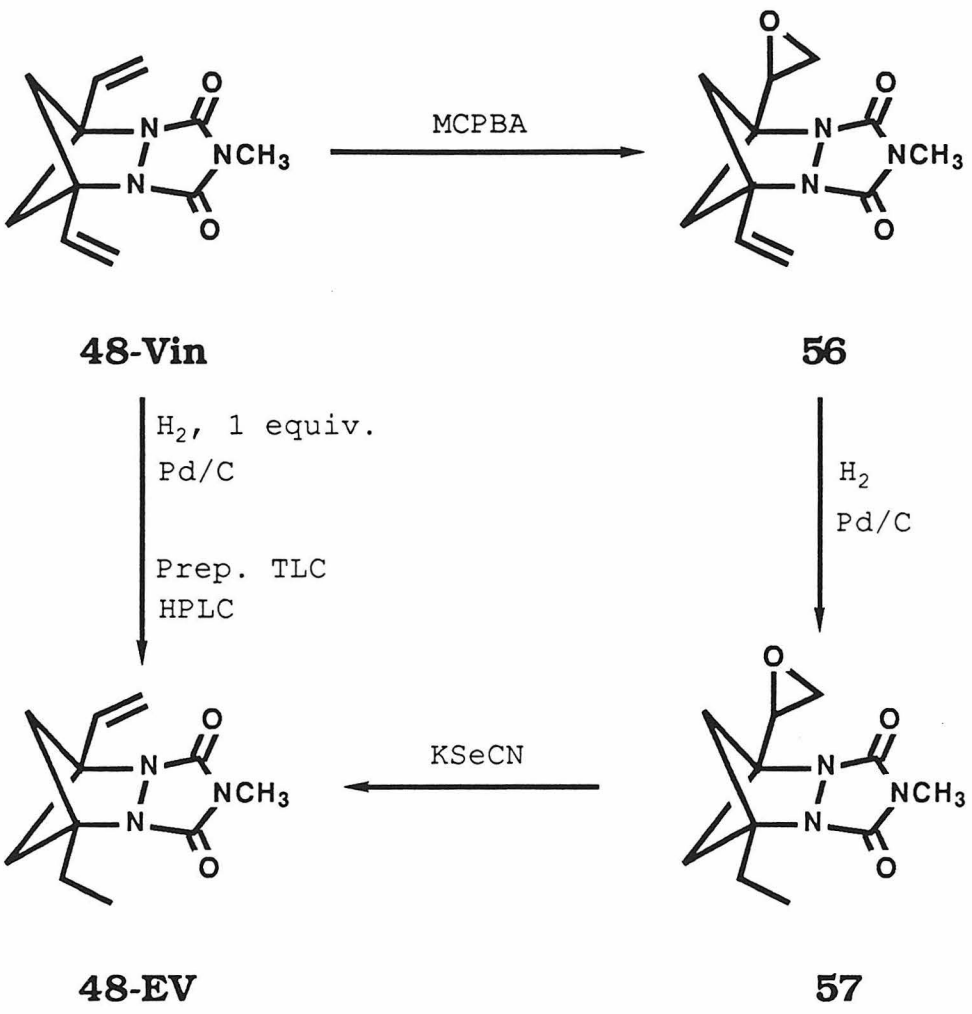
MCPBA
48-Vin
56
H2, 1 equiv.
Pd/C
Prep. TLC
HPLC
H2
Pd/C
KSeCN
48-EV
57

easily separated from remaining starting material by flash chromatography.[25] Hydrogenation afforded **57**, which was deoxygenated with potassium selenocyanate[26] to give **48**.

These studies, and others we have described,[27] illustrate the insensitivity of the urazole moiety to a wide variety of synthetic procedures. Thus, we anticipate that an even wider array of substituted diazabicyclohexenes will be accessible.

Two methods were employed for the conversion of the urazoles to diazenes. The standard route involving a base hydrolysis (refluxing KOH/2-propanol) followed by oxidation via the copper complexes[10] proved successful for **47-Vin** and **-EV** (eq. 3.4). Liberation of the diazenes from their copper complexes was done at -50 °C to prevent decomposition of the thermally unstable (see below) diazenes. No copper complex was obtained upon hydrolysis/oxidation of distyryl urazole **53**.

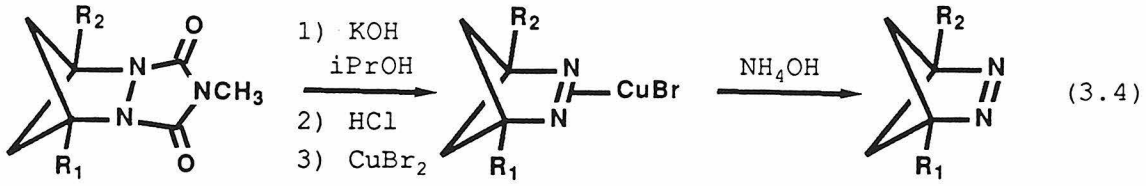

(3.4)

48 **47**

An alternative procedure developed in our laboratories[27] was found more convenient in the preparation of **47-Vin** and **-EV** (eq. 3.5). This procedure involved partial hydrolysis of the urazoles and isolation of the product semicarbazides (**58**). Oxidation of the semicarbazides at

-50 °C with nickel peroxide then afforded the desired diazenes. The two isomers of **58-EV** were obtained in approximately equal amounts (by TLC), and both were converted smoothly to **47-EV**.

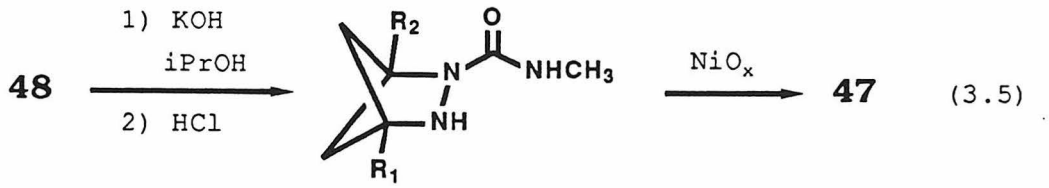

(3.5)

58

An obstacle to the success of the nickel peroxide method was the propensity of the semicarbazides to rearrange. These rearrangements were not studied extensively, but they appeared to involve cleavage of a ring C-C bond and incorporation of oxygen to give five-membered ring heterocycles. For instance, **58-Vin** reacted to give two more polar compounds, which have been tentatively assigned the structures **59** and **60**. These side reactions were minimized by using precautions such as room-temperature hydrolysis, exclusion of oxygen, and immediate oxidation of the semicarbazide. Rearrangement was not a problem for **58-EV** under these conditions, but it was unavoidable for distyryl semicarbazide **61**, thus precluding isolation of the diazene **62**.

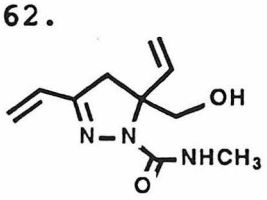

59

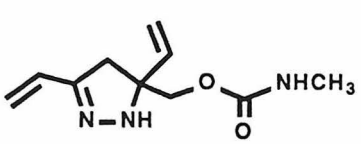

60

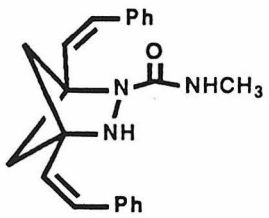

61

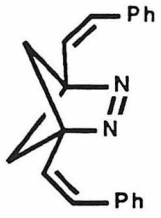

62

Diazene Reactivity. As for the parent diazabicyclohexene,[10] the thermal decompositions of all the diazenes described here cleanly produce the analogous bicyclobutane as the sole product. As observed for other ring systems,[28] the stability of the diazenes **47** is highly dependent upon the radical-delocalizing ability of the bridgehead substituents. The parent and alkyl-substituted diazenes are stable up to about 100 °C,[10] while the ethyl vinyl diazene **47-EV** decomposes with a half-life of ca. 6 hours at room temperature. The **47-Vin** and **-Ph** both decompose at temperatures above -30 °C.

The photochemistry of the various diazenes differs dramatically. The simplest cases are **47-Vin** and **-EV**, both of which give only the corresponding bicyclobutanes **63** upon either direct or sensitized photolysis, independent of temperature (eq. 3.6). The photochemistry of the parent

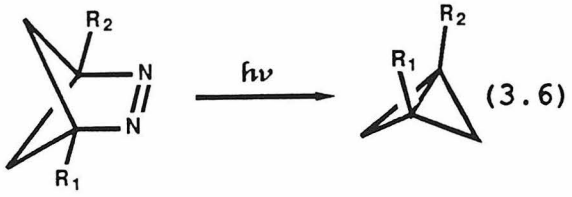

(3.6)

	Direct or Sensitized	T	Solvent
47-Vin	direct	-50 °C	$CDCl_3$
	sens.(thioxan.)	-50 °C	$CDCl_3$
	direct	77 K	$CDCl_3$
	direct	-80 °C	CD_3OD
	direct	4 K	$CDCl_3$
	sens.(Ph_2CO)	4 K	$CDCl_3$
47-EV	direct	-50 °C	$CDCl_3$
	sens.(thioxan.)	-50 °C	$CDCl_3$
	direct	77 K	$CDCl_3$

diazene (**9**) has been reported previously,[29] and the dimethyl diazene shows completely analogous behavior.[11] For these diazenes, direct photolysis gives mainly the corresponding bicyclobutane, but triplet sensitized photolysis affords

predominantly nitrogen-retained products, 1,2-diazabicyclo [3.1.0]hex-2-enes (**64**). Product ratios are also strongly temperature-dependent.

9

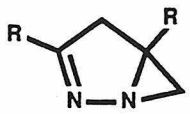

R = H, Me

64

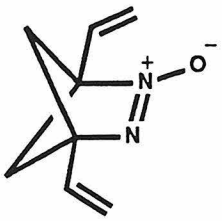

65

We also prepared the divinyl azoxy compound, **65**, in order to investigate its viability as a precursor to **46-Vin**. An azoxy precursor has been used successfully in the matrix isolation of a reactive isoindene.[30] We followed the general synthetic procedure of Olsen and Snyder[31]: potassium hydroxide hydrolysis of urazole **48-Vin** in the presence of hydrogen peroxide. As expected from the behavior of the other azoxy compounds,[31] **65** is significantly more stable than the diazene **47-Vin**, being indefinitely stable at room temperature. Thus, ease of synthesis and handling make **65** attractive as a possible alternate precursor. The photochemistry of **65**, however, proved to be far too inefficient to allow accumulation of **46-Vin** in the cryogenic matrix.

EPR Spectroscopy

Photolysis of frozen solutions of the diazenes **47** in 2-methyltetrahydrofuran (MTHF) and a variety of other solvents at 4 K produces EPR spectra for the corresponding triplet cyclobutanediyls (Figure 3.1). Spectra were obtained

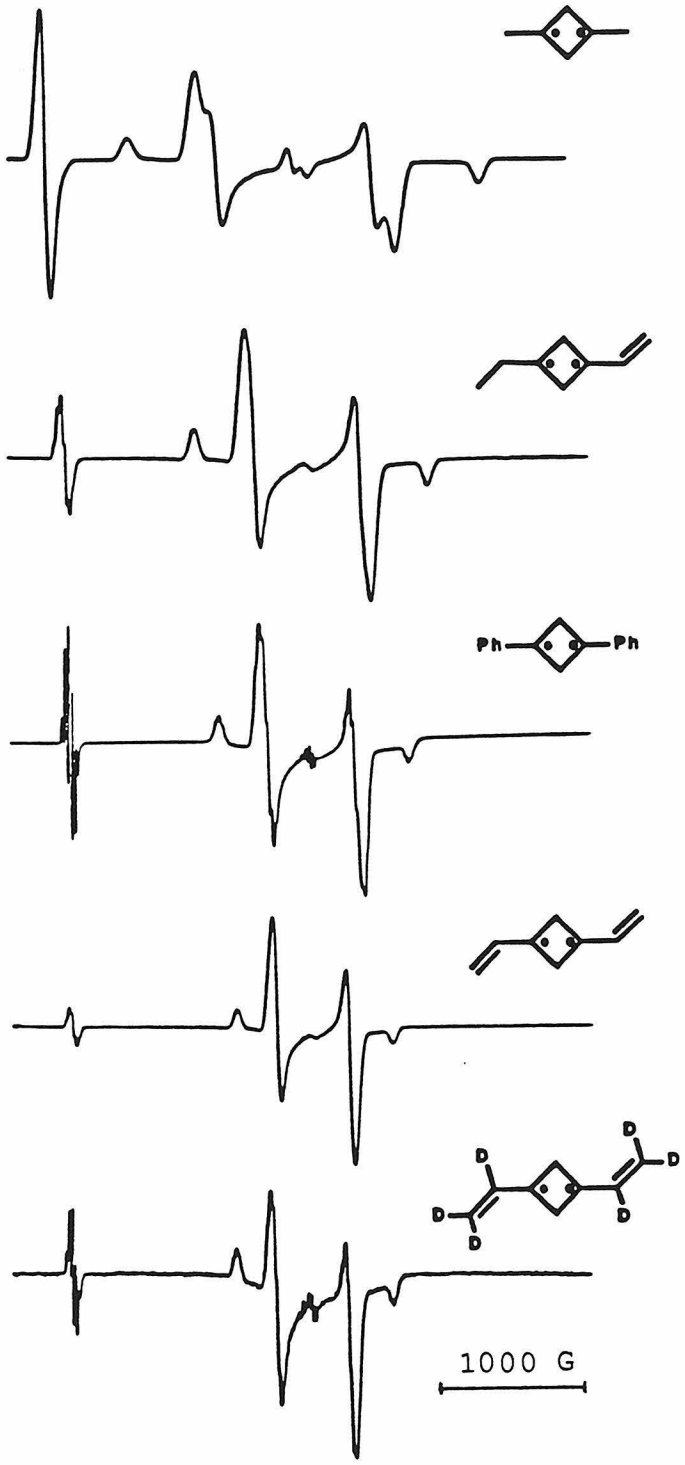

Figure 3.1. EPR Spectra for various cyclobutanediyls in MTHF at 4 K.

for **46-Vin** in each of ten different solvents employed: MTHF, heptane, pentane, pentane-d_{12}, chloroform-d_1, dichloromethane, iodomethane-$\underline{d}_3$, adamantane, methanol/ethanol (1:1), and methylcyclohexane/isopentane (4:1). The only sample that failed to produce an EPR signal was a sample of **47-Vin** adsorbed on silica gel. Spectra of **46-EV** were obtained in the two solvents tried, MTHF and heptane.

Surprisingly, benzophenone-sensitized photolysis of **47-Vin** at 4K was less efficient for generating triplet **46-Vin**, even though the diazene was depleted <u>more</u> efficiently. This observation is difficult to explain in terms of diazene photochemistry, since one would normally expect that a more efficient entry onto the triplet diazene surface would yield a larger signal. The reduced efficiency might be due to destruction of the biradical through a benzophenone triplet-cyclobutanediyl triplet annihilation.

The EPR spectra in Figure 3.1 are completely consistent with the proposed structures, both within the cyclobutanediyl series and with respect to the literature of organic triplets. Valuable information about the electronic structure of the cyclobutanediyls is obtainable from both the zero-field splittings (zfs) and the hyperfine couplings (hfc). Before discussing these features in detail, we will provide a brief overview of triplet EPR spectroscopy.[32]

Triplet EPR - Basic Principles. The EPR spectroscopy of organic triplets is highly informative but somewhat

different from the more common EPR of doublets (free radicals).

The first important difference concerns the energy-level pattern. In a doublet, the two spin states ($m_s = \pm 1/2$) are degenerate. Application of an external magnetic field splits these levels, and an allowed ($\Delta m_s = 1$) transition between them can be observed. The spectrum consists of one line, which may be extensively split by hyperfine coupling. In contrast, the three spin states of a triplet are nondegenerate, even in the absence of an external magnetic field. This zero field splitting (zfs) results from a dipolar coupling between the unpaired spins. In effect, the unpaired spins create an internal magnetic field that splits the magnetic sublevels. The sublevels are further split by application of an external magnetic field, and the usual resonance conditions are produced. Most importantly, the dipolar coupling, and hence the zfs, depend strongly on the average distance, r, between the unpaired spins. In particular, the interaction varies as $1/r^3$. The relative energies of the three triplet levels are typically described by two zfs parameters, D and E. It is D that varies as $1/r^3$, while E is a probe of the symmetry of the biradical.

The second difference between doublet and triplet EPR is that, typically, the former is obtained in fluid media, while the latter must be obtained normally in frozen glasses or solids. Thus, doublet spectra are nicely isotropic, but triplet spectra are highly anisotropic. Because there are

three levels, one would expect two allowed ($\Delta m_s = 1$) transitions in a triplet. However, in a sample of randomly oriented, but nonreorienting triplets, each orientation produces its own pair of resonances. Fortunately, one can, in effect, selectively observe those molecules that have one of their three principal magnetic axes nearly aligned with the external magnetic field (the canonical orientations). There are thus 3x2=6 transitions observed. In addition, a technically "forbidden" $\Delta m_s = 2$ transition is frequently seen at half-field. As discussed below, this transition is intrinsically less anisotropic than the $\Delta m_s = 1$ transitions, and so only a single, broad line is observed. It is a simple matter to extract the zfs parameters D and E from such spectra, and thereby obtain an estimate of the average separation of the spins. Thus, triplet EPR provides an extremely informative probe of biradical structure.

Zero-Field Splitting. The cyclobutanediyl zfs parameters, obtained from the spectra in Figure 3.1, are listed in Table 3.1. As expected, the biradicals with fully saturated substituents show identical zfs, with $|D/hc| = 0.112\ cm^{-1}$. As delocalizing substituents are introduced, the average distance between the unpaired electrons increases and the D-value therefore decreases. Thus, $|D/hc|$ is substantially lowered in **46-EV** to $0.074\ cm^{-1}$, and a further reduction to $0.050\ cm^{-1}$ is observed for **46-Vin**. The value of $|D/hc| = 0.084$ for **4**[7a] is consistent with a larger radical separation in the five-membered ring as compared to the

Table 3.1 Zero-Field Splitting Parameters for Various Biradicals

Biradical	Experimental |D/hc| cm^{-1}	Experimental |E/hc| cm^{-1}	Calculated |D/hc| cm^{-1}	Calculated |E/hc| cm^{-1}
	0.112	0.005	0.1125	0.0055
	0.112	0.005		
	0.112	0.005		
	0.112	0.005		
	0.074	0.003	0.0744	0.0031
	0.050	0.001	0.0498	0.0017
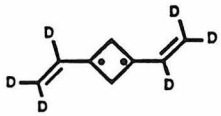	0.050	0.001		
	0.060	0.002	0.0608	0.0024
	0.084	0.002	0.0825	0.0035

[a]Scaled from the actual calculations using a factor of 0.6069.
[b]Scaled from the actual calculations using a factor of 0.4450.

dialkylcyclobutanediyls (2.37 Å[33] vs. 2.10 Å,[34] by ab initio optimization).

These observed trends have been correlated quantitatively with zfs calculated by using a semiempirical method, which has been described in the literature.[35] In these calculations, alkyl-substituted radical centers were assumed to have completely localized spins, while the delocalized radical fragments were assigned "experimental" spin densities determined for allyl or benzyl radical from hyperfine measurements.[36] A plot of experimental versus calculated D-values (Figure 3.2) shows very good correlation, giving a least-squares line that passes through the origin. The calculated D-values, which have been scaled using the slope from Figure 3.2, are shown in Table 3.1 for comparison with the experimental values.

When D-values were calculated using Huckel spin densities, such a good correlation was not obtained; the calculated values for **46-Vin** and **-Ph** were too low. Huckel theory fails to account for spin polarization,[37] an electron-correlation effect, which is important in conjugated radicals. In allyl radical, for example, spin polarization causes increased spin density on the terminal carbons and negative spin density on the central carbon. The good correlation in Figure 3.2 indicates that the extent of spin polarization in **46-Vin** and **46-Ph** is similar to that of the constituent radicals.

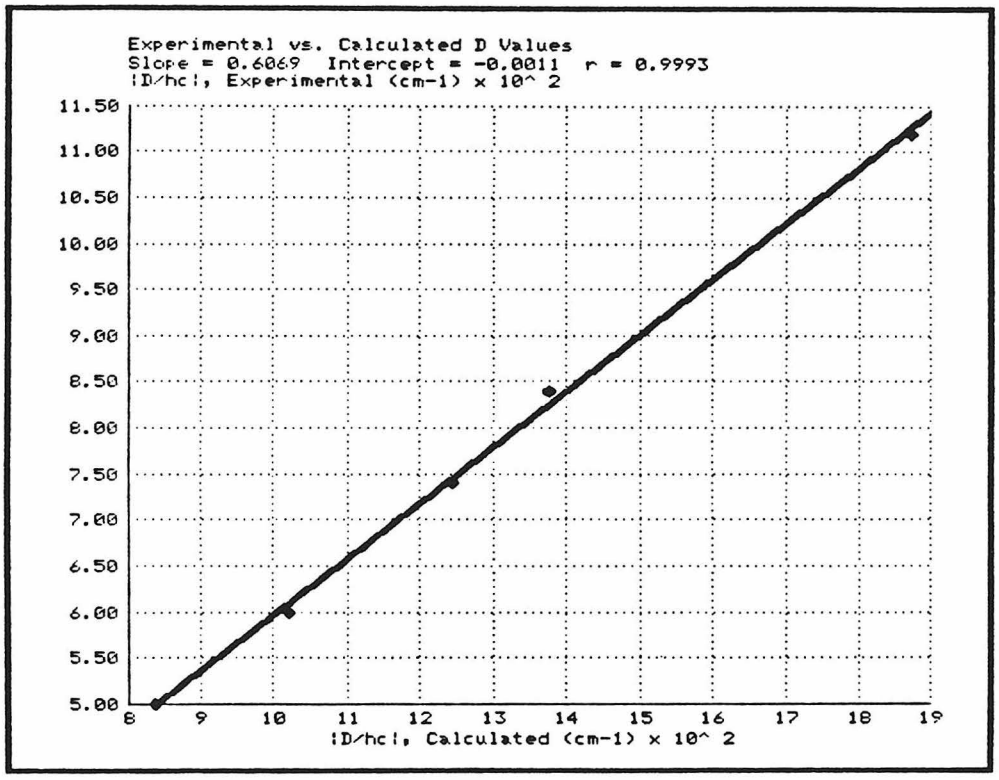

Figure 3.2. Correlation between experimental and calculated D-values.

A similar correlation has been obtained for the experimental and calculated E-values (Figure 3.3), though the agreement is not as good. The accurate calculation of E-values is more difficult, since they represent much smaller energy separations. The correlation is thus considered quite good. The scaled, calculated E-values are displayed in Table 3.1.

Hyperfine Coupling. Five of the cyclobutanediyls display hfc in their half-field ($\Delta m_s = 2$) transitions (Figure 3.4a). Observation of hfc in triplet EPR of randomly oriented samples[27,38] is unusual due to the inherent anisotropy. When hfc is observed, it is often uninterpretable due to the orientational anisotropy.[7a] Further complications can arise if the hfc is itself anisotropic, which is often the case for coupling to α protons.[39] Fortunately, few α couplings are possible in the cyclobutanediyls, since the radical centers on the ring are tertiary. Therefore, the majority of the hfc is attributable to β coupling, which is normally isotropic in organic radicals.[39]

Of the cyclobutanediyls that show hfc, only **46-Vin-**$\underline{d}_6$ and **-Ph** display splittings that may be interpreted without simulation. For these cases, well-defined five-line patterns are observed, which may be attributed to coupling with the four β-protons on the ring. Both molecules also exhibit hfc in the $\Delta m_s = 1$ transition, though the splittings are only slightly resolved (Figure 3.5). For **46-Ph**, the $\Delta m_s = 2$ lines

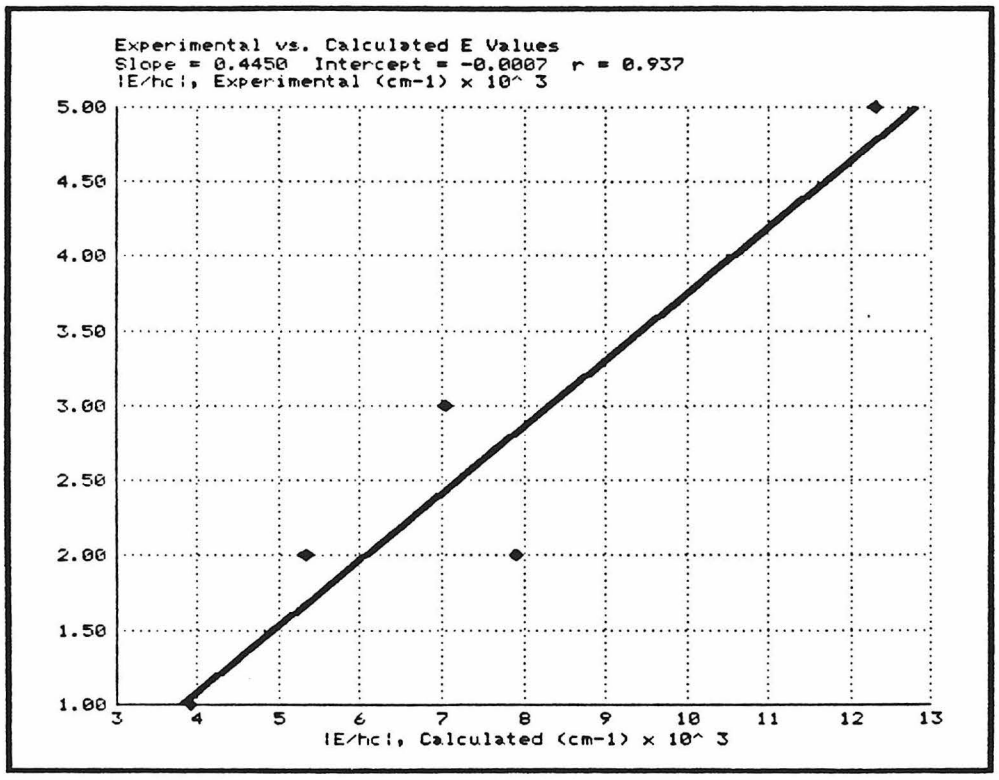

Figure 3.3. Correlation between experimental and calculated E-values.

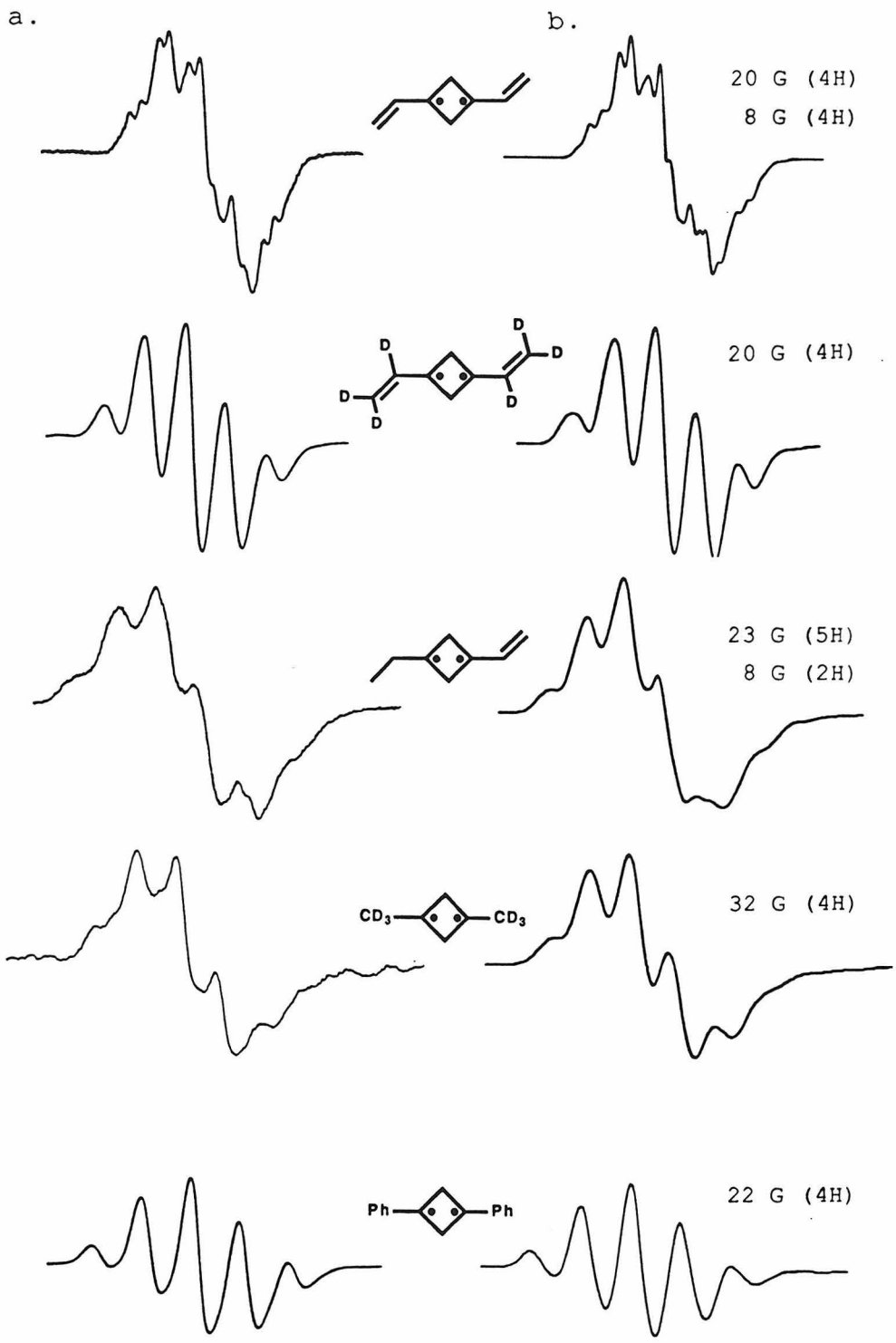

Figure 3.4. Hyperfine in the half-field transitions of various cyclobutanediyls: a) experimental, b) simulation.

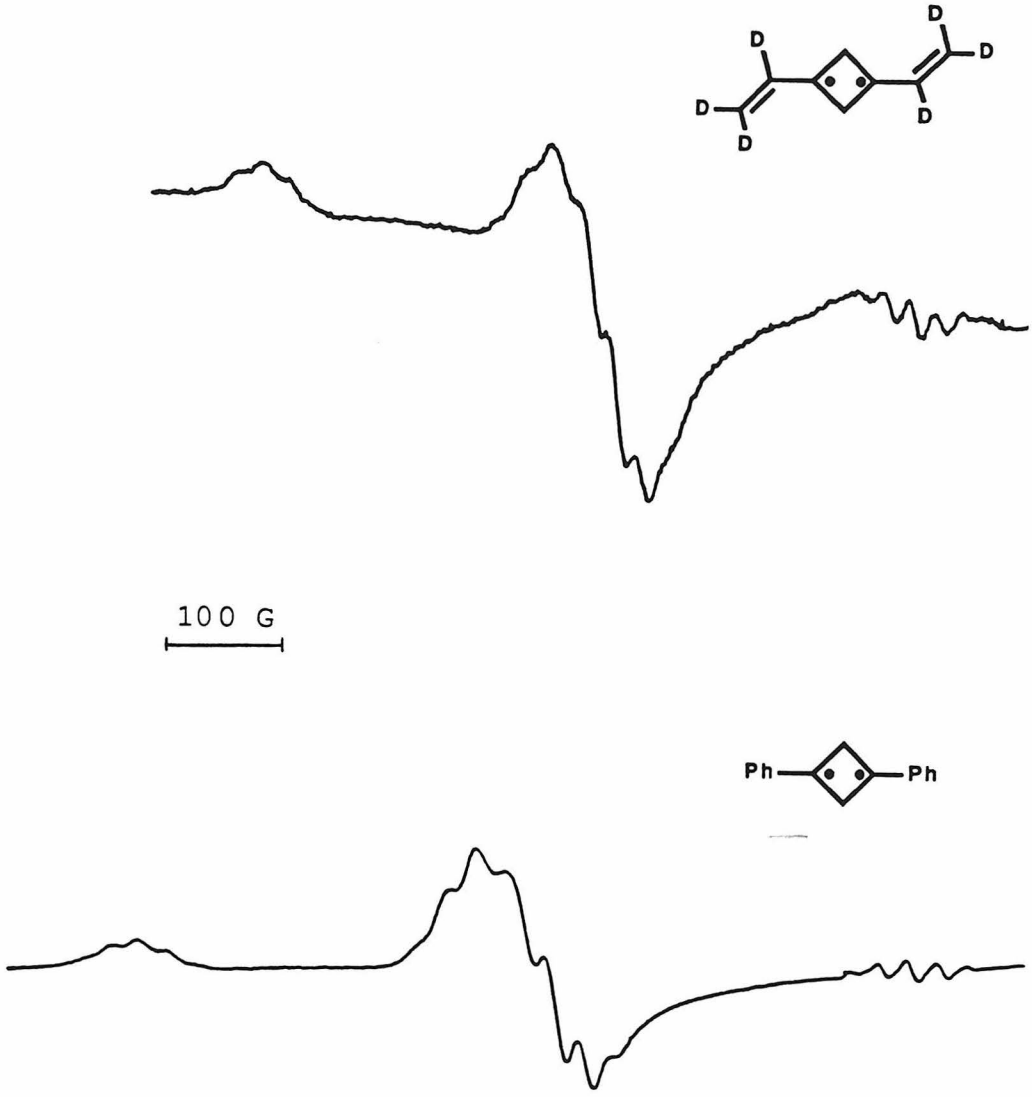

Figure 3.5. Hyperfine in the $\Delta m_s=1$ transitions of **46-Vin-**$\underline{d}_6$ and **-Ph**. The transitions at the right are double-quantum transitions, which also show hyperfine coupling.

are extremely well resolved, indicating that the α-couplings due to the ortho and para phenyl protons must be very small. For **46-Vin-$\underline{d}_6$** the deuteria and residual vinylic protons (the vinylic CH_2 groups are only 68% deuterated) serve to broaden the lines. The coupling magnitudes are consistent with the assignments, as explained below.

Interpretation of the hfc for the remaining biradicals required spectral simulation. Our program,[11] based on the algorithm of Kottis and Lefebvre,[40] produced simulations in very good agreement with the actual spectra, despite the approximations of isotropic hfc and equal transition probabilities. The simulations for the five cyclobutanediyls are shown in part b of Figure 3.4 for comparison to the actual spectra in part a. The coupling constants used to produce the simulations are shown in the same figure. The β-ring proton coupling constants were determined in each case and are tabulated in Table 3.2.

The simulations illuminate three sources of complexity in the hfc. For **46-CD_3**, the asymmetry in the five-line pattern cannot arise from either interfering couplings or anisotropic hfc, since the simulator reproduced the pattern based on isotropic hfc. Therefore, the complexity must arise from orientational anisotropy. All of the observed hfc patterns display this effect to some degree, but it should be strongest in the case that has the highest D-value, **46-CD_3**.

Another source of complexity is coupling from other protons in the molecule. The large number of lines observed

Table 3.2 Hyperfine Coupling Constants for Cyclobutanediyls

Biradical	a_H, ring (G) Experimental	Calculated
	32	31.3
	23	24.8
	22	21.0
	20	18.4
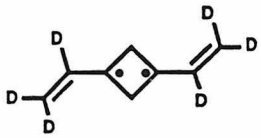	20	

for **46-Vin** is due to <u>two</u> sets of four protons, each set with different coupling constants. The vinylic CH_2 protons produce an 8 G coupling, which is significantly smaller than the coupling in allyl radical (14 G).[36] However, being an α-coupling, it may be anisotropic. The hfc was broadened by this coupling in **46-Vin-**$\underline{d}_6$, mainly due to incomplete deuteration. The simulation for this biradical is actually a statistically weighted average over the $\underline{d}_2$ through $\underline{d}_6$ compounds and was obtained <u>prior</u> to the experimental spectrum.

A third source of hfc complexity, displayed by **46-EV**, is conformational flexibility. Even though **46-EV** has six β-protons, only six lines are observed in the major coupling. The hfc was successfully simulated by using five protons with equal coupling constants. However, due to this ambiguity in the assignment of **46-EV**, its coupling constants are the least certain of the constants obtained. Presumably, the ethyl CH_2 protons cannot effectively couple simultaneously. This effect is undoubtedly the reason hfc is not resolved in the protiated dialkylcyclobutanediyls.

The magnitude of the β-ring proton coupling serves as another gauge of spin density on the ring carbons. As is apparent from Table 3.2, the coupling constants decrease with increased delocalization, just as the zfs does. Hfc constants for β-protons (a_H^β) in organic radicals have been shown to follow the relation,[41]

$$a_H^\beta = \rho C \cos^2 \theta, \qquad (3.7)$$

where ρ is the spin density on the α carbon, C is a constant that has been empirically assigned the value of 42.5 G, and θ is the angle between the axis of the α carbon radical p orbital and the β C-H bond. Assuming the ring geometry (i.e., θ) to be the same for the four cyclobutanediyls in Table 3.2, a plot of a_H^β vs. ρ should be linear, passing through the origin with a slope of $C\cos^2\theta$. Such a plot is shown in Figure 3.6, using the same spin densities which were used in the zfs correlation. The origin was included in the least-squares analysis due to the small number of points.

The correlation of the plot in Figure 3.6 is relatively good; the coupling constants implied by the linear correlation are shown in Table 3.2. The largest discrepancy arises from **46-EV**, whose coupling constants were already described as the least certain. The slope from Figure 3.6 can be set equal to $C\cos^2\theta$, which gives $\theta = 31^\circ$. This angle is in good agreement with the optimized structure for **8** (Chapter 2), which gives $\theta = 27^\circ$.

Our work on cyclobutanediyls has shown that triplet EPR spectroscopy can provide detailed information about the electronic structures of biradicals and in particular the distribution of spin density. Toward this end, both zfs and hfc measurements serve as sensitive gauges capable of

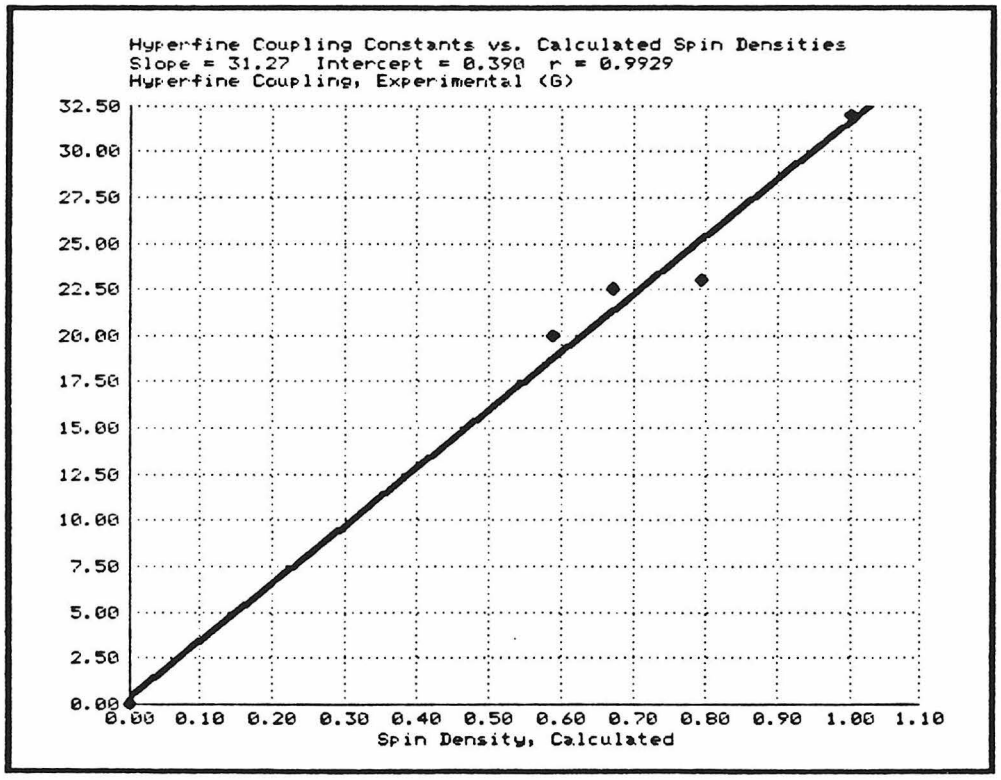

Figure 3.6. Correlation between experimental hfc constants for the β-ring protons in **46** and spin densities determined from the corresponding radicals.

discerning small differences in a series of related molecules.

Biradical Photochemistry

All of the cyclobutanediyls studied undergo photochemistry, as demonstrated by decay of the triplet EPR signal upon photolysis with light of appropriate wavelengths. This phenomenon, also observed for cyclopentanediyl, **4**,[7a] can be conveniently studied by recording photochemical action spectra using the EPR spectrometer as a detector.[42] If the photochemistry is wavelength-independent, then the action spectrum of a biradical should be the same as its absorption spectrum.

The action spectra of **46-Vin** and **-EV** are identical within experimental error and closely resemble the literature absorption spectrum of allyl radical.[43] In both cases, photochemical decay of the triplet signal is accompanied with the growth of a doublet signal, suggesting a hydrogen-abstraction mechanism.

EXPERIMENTAL SECTION

General. ^{1}H NMR spectra were recorded on a Varian EM-390 spectrometer. Fourier transform NMR spectra (^{1}H and ^{13}C) were recorded on a JEOL FX-90Q, GX-400 or Bruker WM-500 spectrometer. Ultraviolet spectra were recorded on a Hewlett-Packard 8451A diode array spectrophotometer. Infrared spectra were recorded using a Shimadzu IR-435 or a Mattson Instruments Sirius 100 FT-IR spectrometer fitted with a Starlab minicomputer. Mass spectra were obtained by the Caltech Analytical Facility and the U.C. Riverside Analytical Facility. Analytical gas chromatography was performed on a Hewlett-Packard 5840A chromatograph equipped with a flame-ionization detector. High pressure liquid chromatography was performed using a Perkin-Elmer Series 2 liquid chromatograph.

1,7-Dicarbomethoxy-4-methyl-2,4,6-triazatricyclo-[5.1.1.$0^{2,6}$]nonane-3,5-dione (15). A methylene chloride solution of 1,3-dicarbomethoxybicyclobutane[44] (3.29 g, 19.4 mmol) and MTAD (2.74 g, 24.3 mmol) was photolyzed with a Hanovia 450-W medium-pressure, mercury arc lamp and a Pyrex filter. Filtration and recrystallization from ethyl acetate afforded 3.28 g (11.6 mmol, 60%) of **15** as a white solid; mp 176.5-177.5 °C; ^{1}H NMR ($CDCl_3$) δ 2.26 (m, 2H), 2.69 (m, 2H), 3.03 (s, 3H), 3.85 (s, 6H); ^{13}C NMR ($CDCl_3$) δ 26.0 (NCH_3), 45.0 (CH_2), 53.2 (OCH_3), 68.9 (bridgehead), 159.7 (NCO),

164.4 (OCO); IR ($CHCl_3$) 3037, 2956, 1793, 1750 (sh), 1719, 1442, 1397, 1322, 1237, 1163, 1066 cm^{-1}; UV (CH_2Cl_2) λ_{max} 246 nm (ε 270); mass spectrum (EI) m/e 283, 251, 224, 194, 168, 167 (100), 166, 152, 139, 135.

Anal. Calcd. for $C_{11}H_{13}N_3O_6$: C, 46.65; H, 4.63; N, 14.84. Found: C, 46.60; H, 4.63; N, 14.87.

1,7-Bis(hydroxymethyl)-4-methyl-2,4,6-triazatricyclo-[5.1.1.$0^{2,6}$]nonane-3,5-dione (51). Sodium borohydride (2.85 g, 75.3 mmol) was added carefully to a stirred suspension of **15** (2.13 g, 7.53 mmol) in 50 mL methanol. The resulting solution was refluxed under nitrogen for 2 h. After cooling to room temperature, 3N hydrochloric acid (ca. 20 mL) was added to neutralize the solution. The methanol was removed by rotary evaporation and the resulting aqueous solution freeze-dried. Extraction with ethanol and flash chromatography[25] (9:1 methylene chloride, ethanol; R_f = 0.35) gave 1.31 g (5.77 mmol, 77%) of **51** as a colorless oil; ^1H NMR ($CDCl_3$) δ 1.92 (m, 4H), 2.98 (s, 3H), 3.72 (t, 2H), 4.03 (d, 4H); ^{13}C NMR ($CDCl_3$) δ 26.1 (NCH_3), 42.8 (CH_2), 60.2 (CH_2O), 73.6 (bridgehead), 160.8 (CO); IR ($CDCl_3$) 3440, 2930, 1760, 1692, 1550, 1265 cm^{-1}; mass spectrum (EI) m/e 227, 196, 139, 113, 112 (100), 109, 95, 83, 59; exact mass calcd 227.0906, found 227.0907.

1,7-Bis(pyruvyloxymethyl)-4-methyl-2,4,6-triazatri-cyclo[5.1.1.$0^{2,6}$]nonane-3,5-dione (52). To a solution of diol **51** (1.54 g, 6.8 mmol) in 10 mL methylene chloride was

added pyruvic acid (1.74 g, 19.8 mmol) and 4-pyrrolidinopyridine (PPY, 200 mg, 1.3 mmol). 1,3-Dicyclohexylcarbodiimide (DCC, 4.08 g, 19.8 mmol) was then added carefully to this solution. The reaction was stopped after 20 min. Filtration, removal of solvent and flash chromatography over carefully dried (overnight in oven) silica (1:1 ethyl acetate, methylene chloride; R_f = 0.36) gave 2.44 g (6.6 mmol, 98%) of **52** in the form of a yellow oil; ^{1}H NMR ($CDCl_3$) δ 1.85 (m, 2H), 2.3 (m, 2H), 2.4 (s, 4H), 2.98 (s, 3H), 4.85 (s, 6H); ^{13}C NMR ($CDCl_3$) δ26.5 (NCH_3) 33.3 (CH_3), 42.7 (CH_2) 61.2 (OCH_3), 70.3 (bridgehead), 159.6 and 159.8 (CO_2 and CON), 190.7 (CO).

1,7-Diethenyl-4-methyl-2,4,6-triazatricyclo-[5.1.1.0^{2,6}]nonane-3,5-dione (48-Vin). A solution of dipyruvate **52** (100 mg, 0.27 mmol) in 250 mL benzene (freshly distilled from calcium hydride under nitrogen) was photolyzed for 3 h with a Hanovia 450-W medium-pressure, mercury arc lamp and a Pyrex filter.[21] The solution was poured into a 500 mL flask and the solvent was removed until only about 40 mL remained. This dialdehyde solution was degassed and used immediately in the next step.

To a degassed suspension of methyl triphenylphosphonium bromide (486 mg, 1.36 mmol) in 40 mL benzene (freshly distilled from calcium hydride under nitrogen) was added a 1.47 M solution of n-butyllithium (0.83 mL, 1.23 mmol), and the yellow reaction mixture was allowed to stir for 1 h. The

previously prepared dialdehyde solution was then added to the stirred ylide solution via cannula. The reaction mixture turned an orange-rust color. After 20 min, 25 mL of 5% aqueous hydrochloric acid was added and the color disappeared. The layers were separated and the aqueous layer was extracted with diethyl ether (2 x 50 mL). The combined organic layer was washed with 20 mL each of 5% hydrochloric acid, a saturated solution of sodium bicarbonate, and water. This solution was then dried over magnesium sulfate, filtered, rotovapped and flash chromatographed to obtain 31.2 mg (0.14 mmol, 52%) of the diene as a colorless oil; ^{1}H NMR ($CDCl_3$) δ 2.05 (m, 2H), 2.19 (m 2H), 3.02 (s, 3H), 5.40 (m, 4H), 6.45 (dd, 2H); ^{13}C NMR ($CDCl_3$) δ 25.6 (NCH_3), 46.4 (CH_2), 72.6 (bridgehead), 119.8 (CH_2), 130.4 (CH), 159.9 (CO); IR ($CDCl_3$) 2940, 1776, 1710, 1446, 1392, 1008 cm^{-1}; mass spectrum (EI) m/e 219, 218, 178, 161, 134, 133, 105 (100%), 91; exact mass calcd 219.1008, found 219.1007.

1,7-Bis(<u>cis</u>-2-phenylethenyl)-4-methyl-2,4,5-triaza-tricyclo[5.1.1.$0^{2,6}$]nonane-3,5-dione (53).

To a degassed solution of benzyl triphenyl phosphonium chloride (380 mg, 0.98 mmol) in 20 mL THF was added slowly <u>n</u>-butyllithium (0.64 mL, 1.47 M, 0.94 mmol.) The ylide solution was allowed to stir at room temperature for 1 h. Dialdehyde **50** (prepared from 156 mg, 0.43 mmol **52** as described in the procedure for **48-Vin**), was added via cannula. The mixture was stirred for 20 min, then 15 mL of

5% hydrochloric acid was added. The layers were separated and the organic layer was washed with saturated sodium bicarbonate and water. The solution was dried over magnesium sulfate and purified using flash chromatography (pentane/ethyl acetate, 2:1) to give 61 mg (38%) of a colorless oil. ^{1}H NMR indicated a 12:1 mixture of **53** and **55**. Higher **53**:**55** ratios were obtained by running the reaction in toluene at -78 °C. ^{1}H NMR (**53**, $CDCl_3$) δ 1.34 (dd, 2H), 1.63 (dd, 2H), 3.00 (s, 3H), 5.91 (d, 2H, $^1J_{CH}$ = 12.0 Hz), 6.87 (d, 2H, $^1J_{CH}$ = 12.0 Hz), 7.02 (m, 4H), 7.13 (m, 6H); ^{13}C NMR ($CDCl_3$) δ 25.9, 48.4, 70.1, 122.8, 127.2, 127.4, 128.1,135,3, 135.7 159.6l; IR ($CDCl_3$) 2920, 1770, 1610, 1445, 1390, 1180, 1010, cm^{-1}; mass spectrum (EI) m/e 371, 370, 297, 294, 280, 258, 257, (100), 256, 254, 230, 129; exact mass calcd 371.1634, found 371.1638.

Photolysis of 53 in the presence of iodine. cis,cis-Distyryl urazole **53** (27 mg) was dissolved in 0.5 mL carbon tetrachloride in an NMR tube with a few iodine crystals. The dark purple solution was photolyzed using a Hanovia 450 W mercury-arc lamp with Pyrex filter. After 3 h photolysis, ^{1}H NMR indicated a 1:1 mixture of **53** and **55**. ^{1}H NMR (**55**, CCl_4) δ 1.82 (dd, 2H), 1.93 (dd, 2H), 2.99 (s, 3H), 6.06 (d, 1H, 12.0 Hz), 6.35 (d, 1H, 16.1 Hz), 6.56 (d, 1H, 16.1 Hz), 6.86 (d, 1H, 12.0 Hz). After 6 h photolysis, a black, intractable precipitate had formed.

1,7-Bis(hydroxydideuteriomethyl)-4-methyl-2,4,6-

triazatricyclo[5.1.1.$0^{2,6}$]nonane-3,5-dione (51-$\underline{d}_4$). Sodium borodeuteride was used in the procedure for the synthesis of **51** to obtain **51-$\underline{d}_4$**. ^{1}H NMR ($CDCl_3$): δ 1.92 (m, 4H), 2.98 (2, 3H), 3.55 (br s, 2H), 4.03 (br s, 0.19H: 91% D).

1,7-Bis(trideuterioethenyl)-4-methyl-2,4,6-triazatricyclo[5.1.1.$0^{2,6}$]nonane-3,5-dione (48-Vin-$\underline{d}_6$). The procedure for **52** was followed using **51-$\underline{d}_4$** in order to prepare **52-$\underline{d}_4$**. The procedure for **48-Vin** was then followed, substituting **52-$\underline{d}_4$** and trideuteriomethyl triphenylphosphonium iodide. $\underline{t}$-Butyllithium was used in place of n-butyllithium, and the ylide solution was stirred for 6.5 h. ^{1}H NMR ($CDCl_3$) δ 2.05 (m, 2H), 2.19 (m, 2H), 3.02 (s, 3H), 5.40 (m, 1.28H: 68% D), 6.45 (br s, 0.18H: 91% D).

1,4-Diethenyl-2,3-diazabicyclo[2.1.1.]hex-2-ene (47-Vin). Method A. A mixture of potassium hydroxide (258 mg, 86%, 3.96 mmol), in 0.5 mL 2-propanol was thoroughly degassed by nitrogen bubbling then heated to reflux. A degassed solution of urazole **48-Vin** (107 mg, 0.49 mmol) in 2 mL 2-propanol was added and the resulting mixture refluxed under nitrogen for 2 h. The solvent was then removed in a stream of nitrogen. The resulting paste was cooled in ice, acidified with degassed 3 N hydrochloric acid, and warmed to 40 °C for 10 min. The mixture was cooled in ice and neutralized with 1 mL degassed 1 N ammonium hydroxide. A degassed solution of cupric bromide (273 mg, 1.22 mmol) in

0.5 ml water was added with stirring, followed by 1 mL degassed 1 N ammonium hydroxide (added slowly, making sure the solution did not become alkaline). The reddish-brown precipitate was filtered, washed with water, ethanol, and ether, and then air-dried. A second crop of precipitate was collected after adding more ammonium hydroxide to the filtrate. A total yield of 110 mg copper complex was obtained and stored in the freezer until needed.

The copper complex (35 mg) was placed in a 2 mL Mixxor® extractor (Rainin) with 1 mL dichloromethane and cooled to -50 °C in a dry ice/acetonitrile bath. Cold, concentrated ammonium hydroxide (1 mL) was added and the layers were mixed, producing a yellow organic layer and a dark blue aqueous phase. The aqueous phase was removed and the organic layer extracted seven more times, or until the aqueous extracts became colorless. A bath-jacketed fritted funnel was loaded with layers (8 mm) of magnesium sulfate and grade V alumina and a pad of glass wool, then flushed with nitrogen. The funnel and receiving flask were cooled to -78 °C (dry ice/acetone), the absorbents wetted with dichloromethane, and the product solution was transferred onto the adsorbents via Teflon cannula. Vacuum was applied to the receiving flask while excess nitrogen was supplied above the filter, and the adsorbents were washed with 5 mL cold dichloromethane. The solvent was removed from the filtrate at -50 °C on a vacuum line, leaving **40-Vin** (8 mg,

38%, measured by NMR integration vs. t-butyl methyl ether as an internal standard) as a pale yellow oil.

Method B. A degassed solution of urazole **48-Vin** (31 mg, 0.14 mmol) in 2.5 mL 2-propanol was added to potassium hydroxide (84 mg, 87%, 1.30 mmol) under nitrogen at room temperature. The mixture was heated to 45 °C with stirring for 40 min. The heating bath was removed and the solvent was evaporated in a stream of nitrogen. The resulting paste was cooled in ice, acidified with degassed 3N hydrochloric acid, heated to 40 °C for 10 min, cooled again in ice, and made slightly basic (pH 8) with degassed 1 N ammonium hydroxide. The aqueous solution was extracted with 8 x 0.5 mL portions of degassed dichloromethane, passing all extracts through magnesium sulfate under nitrogen. The solvent was removed in a stream of nitrogen, giving yellow crystals of **58-Vin**. ^{1}H NMR ($CDCl_3$) δ 1.83 (m, 2H), 1.98 (m, 2H), 2.79 (d, 3H), 5.22 (m, 4H), 6.04 (dd, 1H), 6.59 (br s, 1H), 6.65 (dd, 1H). The crystals were redissolved in 2 mL degassed dichloromethane and cooled to -50 °C. Nickel peroxide (351 mg, 1.40 mmol active oxidant) was added from a solid-addition ampoule and the mixture was stirred at -50 °C for 1.5 h. The mixture was then filtered through Celite at -78 °C and the solvent removed on a vacuum line at -50 °C. Yield ~15 mg (~80%). ^{1}H NMR($CDCl_3$, -60 °C) δ 2.09 (m, 2H), 2.53 (m, 2H), 5.4 (m, 4H), 6.59 (dd, 2H); ^{13}C NMR ($CDCl_3$) δ 63.7 ($^1J_{CH}$ = 147.8 Hz), 88.1, 119.6 ($^1J_{CH}$ = 157.0 Hz), 132.0 ($^1J_{CH}$ = 157.0 Hz); UV

($CDCl_3$) λ_{max} 345 nm.

Decomposition of 58-Vin. The semicarbazide **58-Vin** was found to decompose under several conditions to give two lower Rf compounds which have been tentatively assigned the structures of **59** and **60** based on the spectral data below. Decomposition was faster in acetone than in chloroform or dichloromethane and the rate was apparently independent of the amount of oxygen present, even though incorporation of an oxygen atom was indicated by the mass spectrum of **59**. **59**: ^1H NMR ($CDCl_3$, 500 MHz) δ 2.80 (d, 1H, J=18 Hz), 2.88 (d, 3H, J=5), 2.95 (d, 1H, J=18), 3.83 (d, 1H, J=13), 3.88 (m, 1H), 5.03 (d, 1H, J=19), 5.21 (d, 1H, J=12), 5.43 (d, 1H, J=19), 5.55 (d, 1H, J=12), 5.67 (br d, 1H, J=10), 6.03 (dd, 1H, J=12,19), 6.07 (br s, 1H), 6.52 (dd, 1H, J=12,19); ^1H NMR ($CDCl_3$, D_2O exchange): peaks at δ 5,67, 6.07 disappeared, δ 2.88 became singlet, δ 3.88 became doublet (J=13 Hz, AB pattern with δ 3.83), otherwise identical to above; IR ($CDCl_3$) 3420, 3260, 2900, 1710(sh), 1655, 1535, 1430, 1415, 1310 cm^{-1}; mass spectrum (EI) m/e 209, 178, 121(100), 86, 84. **60**: ^1H NMR ($CDCl_3$, 500 MHz) δ 2.84 (d, 3H, J=5 Hz), 3.00 (d, 1H, J=18), 3.12 (d, 1H, J=18), 4.16 (d, 1H, J=13), 4.57 (d, 1H, J=13), 5.15 (d, 1H, J=19), 5.22 (d, 1H, J=12), 5.43 (d, 1H, J=19), 5.54 (d, 1H, J=12), 6.05 (br s, 2H), 6.30 (dd, 1H, J=12,19), 6.52 (dd, 1H, J=12,19); ^{13}C NMR ($CDCl_3$) δ 26.6, 43.3, 69.1, 79.8, 114.9, 121.9, 129.3, 138.0, 151.2, 156.0; IR ($CDCl_3$) 3420, 3180, 2910, 1720, 1660, 1530, 1430, 1415,

1300 cm^{-1}.

7-Ethenyl-4-methyl-1-oxiranyl-2,4,6-triazatricyclo-[5.1.1.$0^{2,6}$]nonane-3,5-dione (56). Divinyl urazole **48-Vin** (65 mg, 0.30 mmol) was dissolved in 4 mL chloroform with m-chloroperbenzoic acid (62 mg, 0.36 mmol) and heated to reflux under nitrogen for 2 h. After washing with saturated sodium bicarbonate the resulting mixture of **56** and **48-Vin** was separated by using flash chromatography with pentane/ethyl acetate (5:4) as solvent. The recovered **48-Vin** was resubmitted to the epoxidation conditions and separated, resulting in a combined yield of 22 mg of **56** (0.094 mmol, 52% based on 26 mg recovered **48-Vin**) as a colorless oil. ^{1}H NMR ($CDCl_3$) δ 1.9 (m, 4H), 2.63 (m, 1H), 2.97 (m, 1H), 3.03 (s, 3H), 3.68 (m, 1H), 5.37 (m, 2H), 6.42 (dd, 1H); ^{13}C NMR ($CDCl_3$) δ 25.7, 42.0, 44.8, 45.5, 71.6, 72.9, 120.1, 130.0, 159.1, 160.2.

7-Ethyl-4-methyl-1-oxiranyl-2,4,6-triazatricyclo-[5.1.1.$0^{2,6}$]nonane-3,5-dione (57). To a stirred solution of **56** (22 mg, 0.094 mmol) in 4 mL ethyl acetate was added a small amount of activated palladium on carbon, giving a grey suspension. The flask was evacuated and filled with hydrogen at atmospheric pressure for 1 h. The mixture was again degassed, then filtered through Celite. Rotary evaportaion gave **51** (21 mg, 0.089 mmol, 95%) as a colorless oil. ^{1}H NMR ($CDCl_3$) δ 1.04 (t, 3H), 1.9 (m, 6H), 2.61 (m, 1H), 2.92 (m, 1H), 3.02 (s, 3H), 3.65 (m, 1H); ^{13}C NMR

($CDCl_3$) δ 9.2, 22.1, 25.6, 40.7, 43.3, 45.5, 47.7, 72.0, 74.5, 159.8.

1-Ethenyl-4-methyl-7-ethyl-2,4,6-triazatricyclo-[5.1.1.$0^{2,6}$]nonane-3,5-dione (48-EV). Potassium selenocyanate (15 mg, 0.10 mmol) was added to a stirred solution of **57** (21 mg, 0.089 mg) in 3.5 mL methanol/water (10:1). The solution was refluxed under nitrogen for 12 h, then filtered through glass wool, diluted with 10 mL water, and extracted with ether. The ether solution was dried over magnesium sulfate and purified by flash chromatography using pentane/ethyl acetate (7:4). 13 mg **48-EV** (66%) was obtained as a colorless oil. ^1H NMR ($CDCl_3$) δ 1.07 (t, 3H), 1.87 (m, 2H), 2.02 (m, 2H), 2.17 (q, 2H), 3.01 (s, 3H), 5.39 (m, 2H), 6.44 (dd, 1H); ^{13}C NMR ($CDCl_3$) δ 9.6, 22.5, 25.8, 45.2, 73.2, 119.4, 130.6; mass spectrum (EI) m/e 221, 220, 194, 193, 192 (100%), 137, 135, 107, 106, 93, 79; exact mass calcd 221.1164, found 221.1168.

Partial hydrogenation of 48-Vin. To a stirred solution of **48-Vin** (80 mg, 0.37 mmol) in 1.5 mL ethyl acetate was added 5 mg of activated palladium on carbon. The solution was degassed (using a Firestone valve) and left under vacuum. Hydrogen gas (8.2 mL, 0.37 mmol) was added via syringe, and the flask was brought to atmospheric pressure by adding nitrogen. After 10 min, the solution was degassed and filtered through Celite. ^1H NMR indicated a 1:2:1 mixture of **48-Vin**, **-EV**, and **-Et**. The mixture was partially purified

by preparative TLC, eluting 3 times with pentane/ether (2:1) and collecting the middle 2/3 of the band. The resulting mixture was further purified by HPLC using a Whatman Partisil 10 ODS-3 column and cyclohexane/isopropanol (99:1) at 10 mL/min. Yield 10 mg of **48-EV** (45%, assuming 1:2:1 product mixture).

1-Ethenyl-4-ethyl-2,3-diazabicyclo[2.1.1]hex-2-ene (47-EV). Both methods described for **47-Vin** were used for the preparation of **47-EV** though Method B was found preferable. ^{1}H NMR ($CDCl_3$) δ 1.09 (t, 3H), 1.89 (m, 2H), 2.2 (m, 4H), 5.35 (m, 2H), 6.57 (dd, 1H); ^{13}C NMR ($CDCl_3$) δ 10.4, 22.5, 62.1, 88.2, 89.0, 119.2, 133.0; UV ($CDCl_3$) λ_{max} 345 nm.

1,4-Diethenyl-2,3-diazabicyclo[2.1.1]hex-2-ene N-oxide (65). A stirred solution of urazole **48-Vin** (16 mg, 0.073 mmol) in 0.2 mL ethylene glycol and 0.5 mL 30% hydrogen peroxide was heated to 50 °C. A solution of potassium hydroxide (295 mg, 87%, 4.6 mmol) in 0.35 ml water was added over 5 min. An additional 0.1 mL hydrogen peroxide was added every 30 min. After 3 h, the solution was extracted with dichloromethane. The extracts were dried over magnesium sulfate and purified by flash chromatography using pentane/ethyl acetate (3:1). A colorless oil (6.6 mg, 60%) was obtained. ^{1}H NMR ($CDCl_3$) δ 2.75 (m, 2H), 2.96 (m, 2H), 5.45 (m, 4H), 6.26 (m, 2H); ^{13}C NMR ($CDCl_3$) δ 61.5, 80.1 (low S/N), 90.2 (low S/N), 119.4, 122.2, 128.1, 132.1; mass

spectrum (DCI/NH3), m/e 151, 134, 121 (100%), 120, 105, 93, 91, 78, 67, 65.

Photolysis Experiments. Photolyses were performed using an Oriel 1000-W mercury-xenon arc lamp. Direct photolysis utilized the Schott filter combination WG-305/KG-5/UG-11 while for sensitized photolyses the combination WG-360/GG-375 was used.

Photolysis of 46-Vin. Direct photolysis of **46-Vin** was done in deuteriochloroform at -50 °C, 77K, and 4K, and also in methanol-$\underline{d}_4$ at -80 °C. In all cases, ^{1}H NMR indicated that 1,3-divinylbicyclo[1.1.0]butane (**63-Vin**) was the sole product. Similarly, thioxanthone-sensitized photolysis at -50 °C in deuteriochoroform and benzophenone-sensitized photolysis in deuteriochloroform at 4 K showed only formation of **63-Vin**. ^{1}H NMR ($CDC1_3$) δ 1.32 (s, 2H); 2.16 (s, 2H), 5.03 (m, 4H) 5.82 (dd, 2H); ^{13}C NMR ($CDC1_3$) δ 35.8, 113.4, 133.2.

Photolysis of 46-EV. Direct photolysis of **46-EV** was done in deuteriochloroform at -50 °C and 77 K; thioxanthone-sensitized photolysis was done in deuteriochloroform at -50 °C. All experiments gave only 1-ethyl-3-vinylbicyclo[1.1.0]butane (**63-EV**), as monitored by ^{1}H NMR. ^{1}H NMR ($CDC1_3$) δ 0.85 (m, 5H), 1.65 (m, 4H), 4.96 (m, 2H), 6.00 (dd, 1H).

EPR Experiments. A Varian E-Line Century Series X-band Spectrometer equipped with an Oxford Instruments

ESR-900 continuous liquid-helium flow cryostat was used to obtain EPR spectra at low temperature. The temperature was calibrated using a calibrated carbon-glass thermistor (Lakeshore Cryotronics) placed inside a sample tube. During each experiment, the temperature was monitored continuously using a gold-chromel thermocouple fixed 1 cm below the sample in the quartz dewar. The temperature was varied using either the helium flow rate or the automatic DTC2 temperatrure controller.

An Oriel 1000-W mercury-xenon arc lamp was focussed into the microwave cavity for photolysis. Various optical filters (Schott, Corning, Oriel) or a grating monochromator (Oriel Model 77250) were used to obtain narrow bands of light in the desired wavelength range.

Samples were prepared from solutions of 1-3 mg of diazene in 300 μL of solvent. MTHF was freshly vacuum-transferred from benzophenone-ketyl and other solvents (except solvent mixtures) were also vacuum transferred. The solutions were placed in 4 or 4.5 mm o.d. quartz EPR tubes equipped with high-vacuum stopcocks. The samples were then degassed (five freeze-pump-thaw cycles), frozen in liquid nitrogen, and further cooled inside the EPR cavity.

References for Chapter 3

1. Dowd, P. J. Am. Chem. Soc. 1966, 88, 2587-2589.
2. Borden, W. T., Ed. "Diradicals"; Wiley: New York, 1982.
3. (a) Berson, J. A., Ibid.; Chapter 4. (b) Platz, M. S., Ibid.; Chapter 5.
4. Dowd, P. Acc. Chem. Res. 1972, 5, 242-248.
5. Dowd, P.; Chang, W.; Paik, Y. H. J. Am. Chem. Soc. 1986, 108, 7416-7417.
6. Borden, W. T. In "Diradicals", Borden, W. T., Ed.; Wiley: New York, 1982; Chapter 1.
7. (a) Buchwalter, S. L.; Closs, G. L. J. Am. Chem Soc. 1979, 101, 4688-4694. (b) Jain, R.; Snyder, G. J.; Dougherty, D. A. J. Am. Chem. Soc. 1984, 106, 7294-7295.
8. Goldberg, A. H.; Dougherty, D. A. J. Am. Chem. Soc. 1983, 105, 284-290.
9. Most of the work described in this chapter will appear in a forthcoming publication: Jain, R.; Sponsler, M. B.; Coms, F. D.; Dougherty, D. A., manuscript in preparation.
10. Chang, M. H.; Jain, R.; Dougherty, D. A. J. Am. Chem. Soc. 1984, 106, 4211-4217.
11. Jain, R. Ph.D. Dissertation, California Institute of Technology, 1987.

12. Similar photochemical additions have previously been reported: Amey, R. L.; Smart, B. E. J. Org. Chem. 1981, 46, 4090-4092.

13. Boland, W.; Ney, P.; Jaenicke, L. Synthesis 1980, 1015-1017.

14. Kanazawa, R.; Tokoroyama, T. Synthesis 1976, 526-527.

15. Nystrom, R. F.; Chaikin, S. W.; Brown, W. G. J. Am. Chem. Soc. 1949, 71, 3245-3246.

16. Brown, M. S.; Rapoport, H. J. Org. Chem. 1963, 28, 3261-3263.

17. (a) Herscovici, J.; Egron, M.-J.; Antonakis, K. J. Chem. Soc., Perkin Trans. 1 1982, 1967-1973. (b) Corey, E. J.; Suggs, J. W. Tetrahedron Lett. 1975, 2647-2650. (c) Sharpless, K. B.; Akashi, K. J. Am. Chem Soc. 1975, 97, 5927-5928.

18. Mancuso, A. J.; Huang, S.-L.; Swern, D. J. Org. Chem. 1978, 43, 2480-2482.

19. Partch, R. E. J. Org. Chem. 1965, 30, 2498-2502.

20. Cookson, R. C.; Stevens, I. D. R.; Watts, C. T. J. Chem. Soc., Chem. Commun. 1966, 744.

21. Binkley, R. W. J. Org. Chem. 1976, 41, 3030-3031.

22. Hassner, A.; Alexanian, V. Tetrahedron Lett. 1978, 4475-4478.

23. Sonnet, P. E. Tetrahedron 1980, 36, 557-604.

24. Moussebois, C.; Dale, J. J. Chem. Soc. C 1966, 260-264.

25. Still, W. C.; Kahn, M.; Mitra, A. J. Org. Chem. 1978, 43, 2923-2925.

26. Behan, J. M.; Johnstone, R. A. W.; Wright, M. J. J. Chem. Soc., Perkin 1 1975, 1216-1217.

27. Snyder, G. J.; Dougherty, D. A. J. Am. Chem. Soc. 1985, 107, 1774-1775.

28. Engel, P. S. Chem. Rev. 1980, 80, 99-150.

29. Chang, M. H.; Dougherty, D. A. J. Am. Chem. Soc. 1982, 104, 2333-2334.

30. Dolbier, W. R., Jr.; Matsui, K.; Michl, J.; Horak, D. V. J. Am. Chem. Soc. 1977, 99, 3876-3877.

31. Olsen, H.; Snyder, J. P. J. Am. Chem. Soc. 1977, 99, 1524-1536.

32. For a comprehensive review, see Gordy, W. "Theory and Applications of Electron Spin Resonance"; Wiley: New York, 1980; Chapter 10.

33. Conrad, M. P.; Pitzer, R. M.; Schaefer, H. F., III. J. Am. Chem. Soc. 1979, 101, 2245-2246.

34. See Chapter 2.

35. Rule, M.; Matlin, A. R.; Seeger, D. E.; Hilinski, E. F.; Dougherty, D. A.; Berson, J. A. Tetrahedron 1982, 38, 787-798.

36. Snyder, L. C.; Amos, T. J. Chem. Phys. 1965, 42, 3670-3683.

37. Amos, T.; Snyder, L. C. J. Chem. Phys. 1964, 41, 1773-1783.

38. (a) Muller, J.-F.; Muller, D.; Dewey, H. J.; Michl, J. J. Am. Chem. Soc. 1978, 100, 1629-1630. (b) Grivet, J.-P. Mol. Phys. 1970, 19, 389-398.

39. Morton, J. R. Chem. Rev. 1964, 64, 453-471.

40. Kottis, P.; Lefebvre, R. J. Chem. Phys. 1964, 41, 379-393.

41. Fischer, H. In "Free Radicals"; Kochi, J. K., Ed.; Wiley: New York, 1973; Vol. II, pp. 446-448.

42. Snyder, G. S.; Dougherty, D. A. J. Am. Chem. Soc. 1986, 108, 299-300.

43. Maier, G.; Reisenauer, H. P.; Rohde, B.; Dehnicke, K. Chem. Ber. 1983, 116, 732-740.

44. Coffey, C. E. U. S. Patent 3,657,317, April 18, 1972.

CHAPTER 4

MATRIX-ISOLATION DECAY KINETICS OF 1,3-DIVINYL- AND 3-ETHYL-1-VINYLCYCLOBUTANEDIYL

Relatively few thermal reactions have been thoroughly studied at cryogenic temperatures,[1] and very few below the boiling point of liquid nitrogen (77 K).[2] Reactions at these temperatures must be generally studied in the solid phase, thereby eliminating the majority of bimolecular chemistry, and must involve highly reactive species in order to proceed at reasonable rates. A convenient method of generation of the reactive species from a less reactive precursor is required, almost necessarily involving photo- or radiochemistry. In addition to these obstacles, one must deal with the analysis problems commonly encountered for solid-state kinetics (see below).

All of the cyclobutanediyls described in the previous chapter undergo thermal decay at cryogenic temperatures. However, analysis of the decay kinetics proved difficult due to the nonexponential nature of the decay. In this chapter, we describe the development of two methods for the analysis of such rate-dispersive kinetics. These methods have been applied both separately, and in combination, to the decay reactions of 1,3-divinylcyclobutanediyl (**46-Vin**) and 3-ethyl-1-vinylcyclobutanediyl (**46-EV**). The combined procedure has been found to be an effective means of discerning small differences in stability.[3]

Biradical Decay Process

Prior to investigating the cyclobutanediyl decay kinetics, we attempted to establish the identity of the decay

process. The possible involvement of quantum-mechanical tunneling, as suggested by Closs' results on cyclopentanediyl (**4**),[4] made knowledge of the decay process even more crucial, since the rate of a tunneling process depends on the mass of the tunneling particle.

We considered three possibilities for the decay process, shown in Figure 4.1. Radical hydrogen-abstraction from the solvent matrix, by far the most common reaction observed at cryogenic temperatures,[1b,c,2b] was ruled out by several lines of evidence. First, the observed decay of the cyclobutanediyls is much faster than any known abstraction process. Indeed, hydrogen abstraction by radicals and carbenes is most often studied at 77 K or higher,[1b,c] whereas we have been unable to observe any of the cyclobutanediyls above 60 K. Second, decay of the triplet signals corresponding to **46** is <u>not</u> accompanied by growth of any doublet signals, which would be expected from the resulting cyclobutyl (**66**) and solvent radicals. Finally, comparison of decay rates in protio vs. deuterio solvents (**46-Vin** in pentane vs. pentane-d_{12} and **46-Me** in acetone vs. acetone-d_6) shows no difference in rates. Abstraction of deuterium should be much slower than that of protium, especially if the process occurs via tunneling.

The other two possible decay processes, closure to give bicyclobutanes (**63**) and 1,2-hydrogen shift to give cyclobutenes (**67**), will be considered together. Fisher and Michl[5] have observed analogous closure <u>and</u> hydrogen-shift

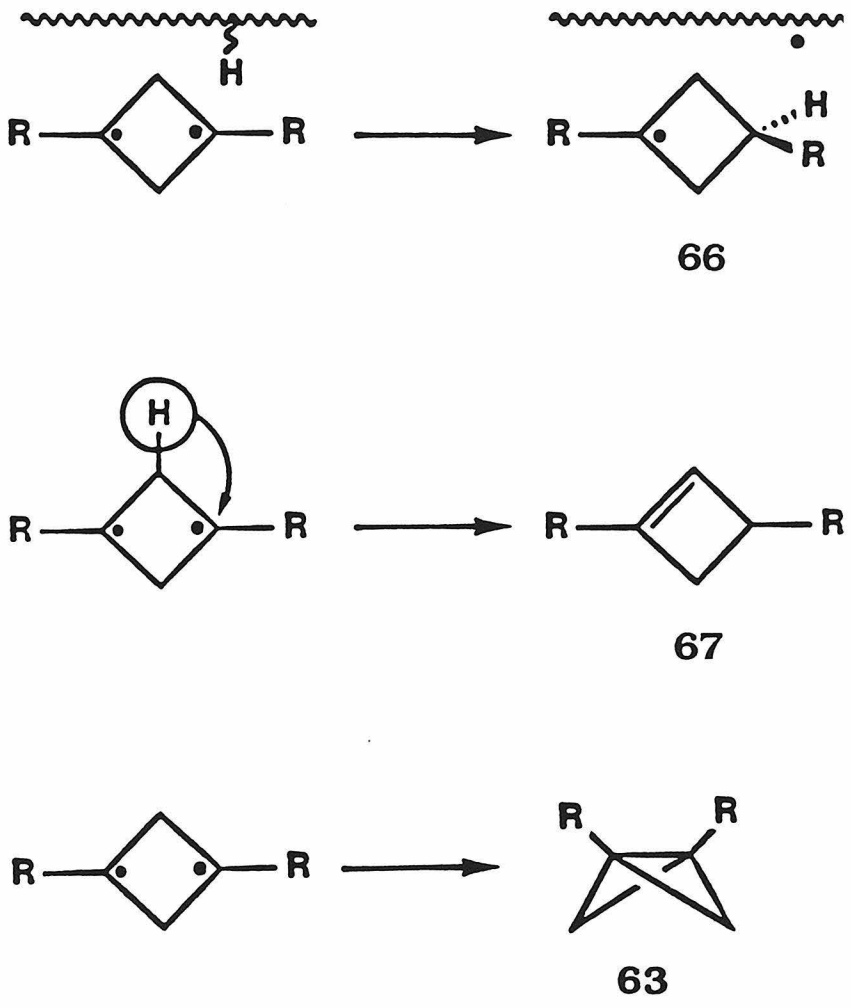

Figure 4.1. Three possible decay processes for cyclobutanediyls.

processes in the same biradical, a naphthoquinodimethane (**68**), under separate conditions. The hydrogen-shift reaction, producing **69**, occurred in a purely exponential fashion, and activation parameters were obtained for it. In contrast, the closure process, giving **70**, was characterized by nonexponential kinetics attributed to a matrix effect resulting from a larger geometrical change.[5] Cyclobutanediyls **46** display <u>strongly</u> nonexponential decay. Although this is in part due to lower activation energies (see below), this behavior is more consistent with the closure pathway, as shown by Michl's work.

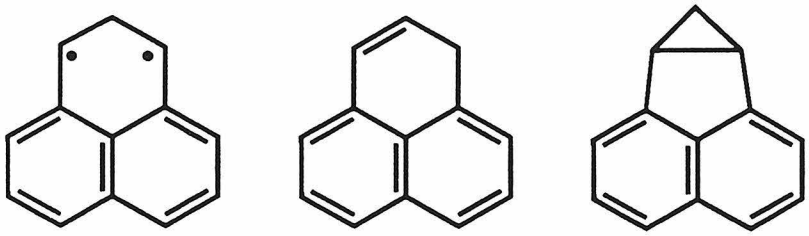

68 **69** **70**

Further evidence comes from product analysis of EPR samples. NMR analysis of a sample of **47-Vin** (in deuteriochloroform), which had been photolyzed many times in EPR experiments, showed no signs of a cyclobutene product. A similar result was obtained for a sample of **47-Me** in acetone-d_6 under both NMR and GC analyses.[6] In addition, solution-phase thermal chemistry and photochemistry of the various diazenes have shown no evidence of cyclobutene products.[6,7] While the high sensitivity of EPR makes it possible that the biradical is formed with a very low quantum

yield, and hence its decay product is too dilute to detect, we feel that the available evidence indicates closure as the cyclobutanediyl decay process.

Decay Kinetics

A major goal of this work was to evaluate the effects of various substituents on the stability of the triplet biradicals. These effects might at first seem readily predictable from the well-known chemistry of free radicals.[8] However, the presence of two low-energy states in a biradical, singlet (S) and triplet (T), results in complications.

The relative energies of the low-lying singlet and triplet states is a crucial issue,[9] especially since only the triplet can be detected by EPR. The observation of a triplet signal at 4 K is a strong indication that the triplet is indeed the ground state.[10] Thermal population of the triplet from a singlet ground state would require not only an S-T energy gap of less than 0.1 kcal/mol but also a singlet that is stable with respect to closure and other spin-allowed processes. Theoretical calculations indicate that both the parent and dimethyl cyclobutanediyls have triplet ground states (see Chapter 2).

If the ground state of the substituted cyclobutanediyls is the triplet, then three possibilities exist for the decomposition pathway. The rate-determining step may involve a reaction on the triplet or singlet surfaces or intersystem

crossing[11] from the triplet to the singlet surface. Consideration of the latter possibility reveals that the S-T gap may have a strong effect on triplet stability in the form of an enthalpic barrier to intersystem crossing (see Figure 4.2a).

What effect, then, should radical-delocalizing substituents have upon triplet cyclobutanediyl stability? Drawing upon the analogy to radical chemistry,[8] one should expect a thermodynamic stabilization of both spin states. However, as the radical electrons are delocalized away from each other, exchange interactions, which stabilize T relative to S, would be reduced. Thus, conjugating substituents might produce a smaller S-T gap, or even a singlet ground state.

The consequences of these two electronic effects can be predicted by using potential energy diagrams. Figure 4.2, part a, shows a set of hypothetical potential surfaces for the closure coordinate of diethylcyclobutanediyl (**46-Et**). The presence of a barrier to closure on the singlet surface is in question (see Chapter 2), but the barrier, if there, would be small. In part b, the surfaces have been modified for substitution of delocalizing groups, such as vinyl or phenyl, according to the previous discussion. Both surfaces are stabilized, but the energy-lowering is most significant for the planar biradical, which enjoys the full effect of delocalization. As the bicyclobutane geometry is approached, delocalization becomes relatively unimportant, so the

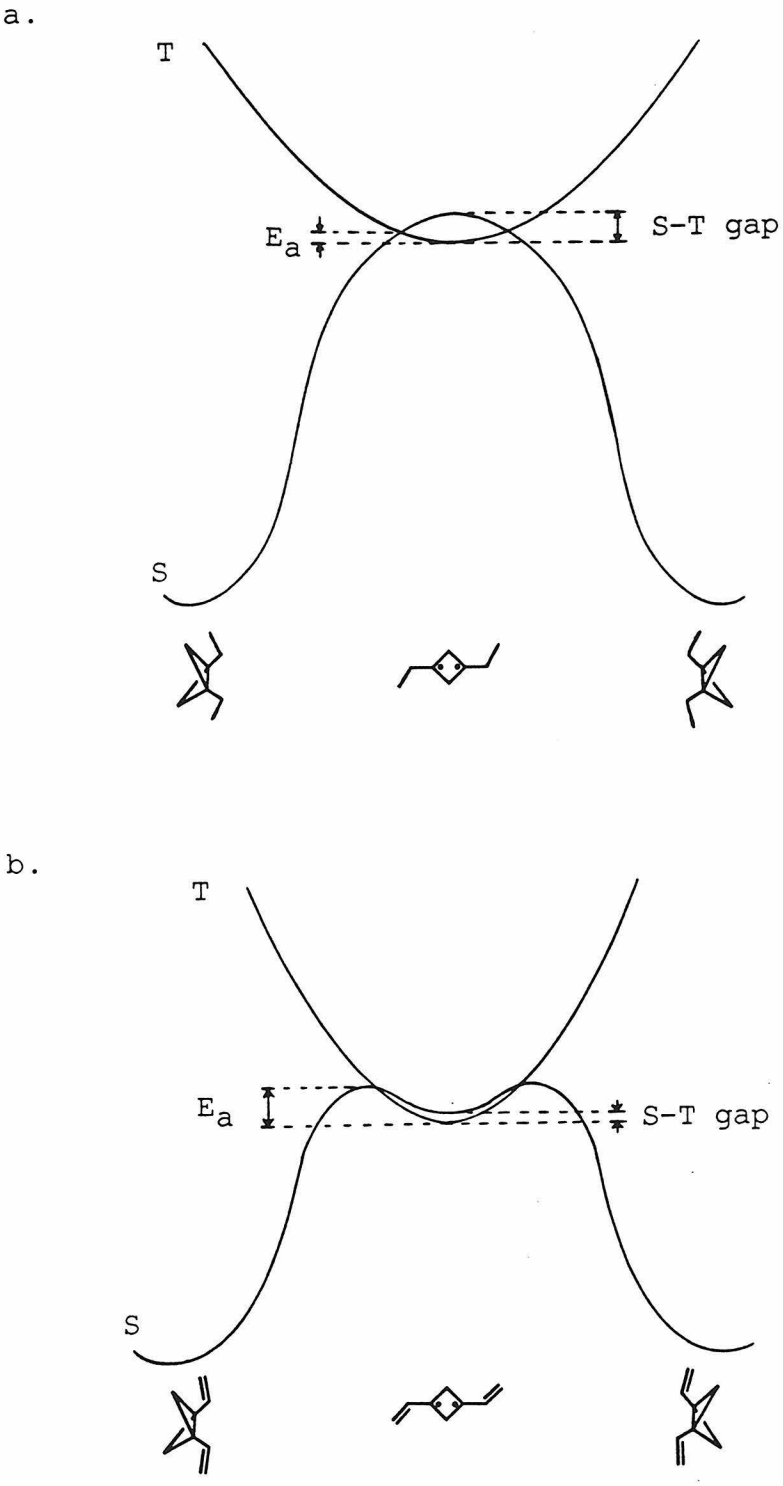

Figure 4.2. Hypothetical potential energy surfaces for the closure coordinates of a) **46-Et** and b) **46-Vin**.

stabilization is small. A smaller S-T gap is also depicted in part b.

Figure 4.2 demonstrates that delocalizing substituents can introduce (or increase) a barrier to closure on the singlet surface.[12] While this exercise is qualitative and does not require the presence of such a barrier, it does suggest that a change of mechanism can occur. In Figure 4.2a, the closure process requires only intersystem crossing, with the geometric distortion at the crossing point providing a barrier. However, in part b, an additional barrier on the singlet surface must be overcome. Our kinetic data for **46-Et, -EV,** and **-Vin** suggest that a change in mechanism does occur for this series, and it is conveniently explained by Figure 4.2 (see below).

Two other substituent effects concerning stability are mass and steric effects. Addition of mass can tremendously retard a tunneling reaction, and this effect has been invoked to rationalize the stability differences in **8, 46-Me,** and **-Et.**[6] Variations in substituent size may also affect the decay rate by altering the steric interactions between the biradical and the solvent matrix. Neither of these effects should be important for the series **46-Et, -EV** and **Vin,** due to the mass and size similarity of the ethyl and vinyl groups.

All of the triplet cyclobutanediyls studied decay in some temperature range between 4 and 55 K. Quantifying the decay kinetics is quite difficult, however, due to the

matrix-site effect.[13] We have developed and employed two methods, described below, to analyze the kinetics.

The Matrix-Site Effect and Quantitative Kinetics

Matrix isolation has been an invaluable tool for the observation of reactive intermediates.[14] Reactive species are stabilized in two ways: isolation in an inert material inhibits bimolecular reactions, and cryogenic temperatures retard unimolecular reactions. Also eliminated are processes such as conformational motions and solvent reorganization, which normally average instantaneous differences between molecules. Therefore, compounds in matrix isolation may display a static distribution of properties. This "matrix-site effect" manifests itself in the broadening or splitting of spectroscopic lines and also in the nonexponential kinetics of first-order unimolecular processes.

Extraction of useful rate information from matrix-perturbed kinetic traces has proven to be highly challenging to chemists and physicists, though several methods have been used with success.[3a,13,15] A common approach for first-order processes involves the assumption, implied above, that the observed nonexponential decay arises from a superposition of exponential decays, each arising from a different type of matrix site. The matrix reaction is thus characterized by a probability distribution of first-order rate constants instead of a single rate constant (i.e., a delta-function distribution, see Figure 4.3). This type of

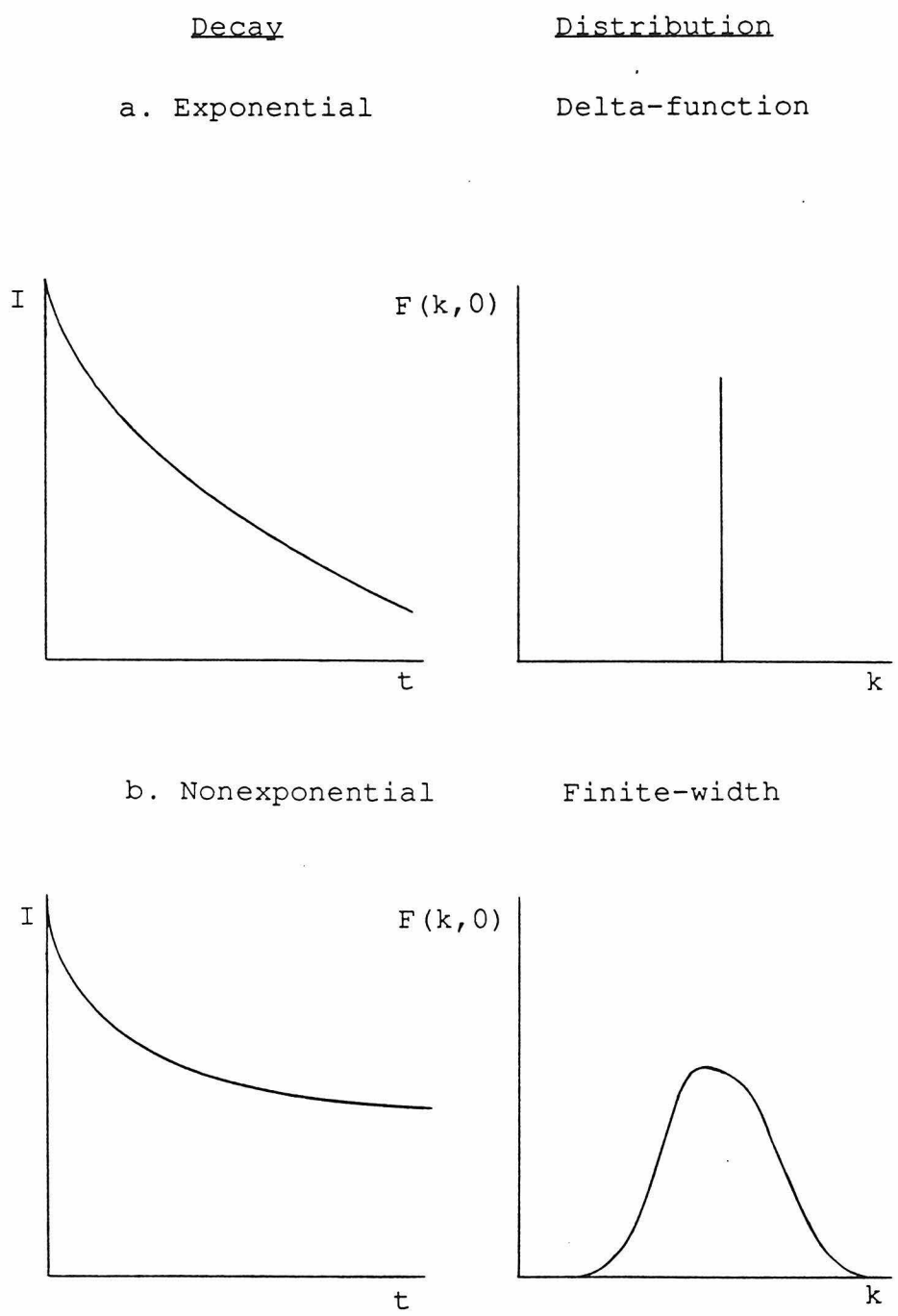

Figure 4.3. Rate-constant distributions and their observed kinetics: a) delta function, corresponding to exponential decay, and b) a broad distribution, corresponding to strongly nonexponential decay.

kinetic behavior, sometimes called composite first-order, is usually identified by the observation that the shapes of the kinetic traces do not depend on the initial concentration of reactant.[16] This distribution model, though intuitive and simple, has found little experimental verification other than good agreement with kinetic data.[17] An alternative model, which assumes equivalent, nonfirst-order sites, sometimes also gives good agreement.[13] However, we have obtained strong experimental support for the distribution model in the decay of cyclobutanediyls (see below).

The goal of all methods under the distribution model is to obtain the initial rate-constant distribution, or at least its maximum, the most probable rate constant. If we denote the distribution at a given time as F(k,t), then the kinetic observable f(t) is related to the initial distribution, F(k,0), by the Laplace transform (eq. 4.1).[17] This

$$f(t) = \int_0^\infty F(k,0)e^{-kt}dk \qquad (4.1)$$

relationship, illustrated graphically in Figure 4.4, implies that the desired distribution can be obtained by Laplace inversion of the kinetics trace, as indicated in equation 4.2. Unfortunately, numerical Laplace inversion is an

$$F(k,0) = \mathcal{L}^{-1}\,[f(t)] \qquad (4.2)$$

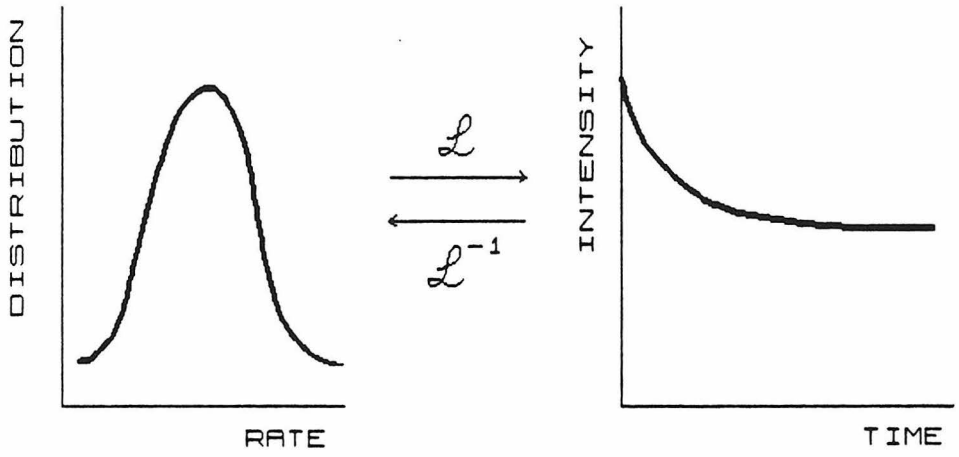

Figure 4.4. A generalized rate constant distribution and its Laplace-transform relationship to observed decay.

ill-conditioned transformation,[18] and though it is possible, given certain assumptions about the distribution, this method is generally more difficult than the alternatives discussed below.

Another approach involves fitting the kinetic data to an appropriate function whose analytical inverse Laplace transform is known.[3a,17] An example is the "stretched exponential," which is commonly used to described physical processes such as dielectric relaxation.[19]

A third alternative involves assumption of a distribution shape, then adjustment of the distribution width and position on the rate axis in order to achieve a good fit to the kinetic data via the numerical Laplace transform (which is well-behaved in the forward sense).[13,15] This method offers maximum flexibility both in the sense of allowing comparison of distribution shapes (and thus distinguishing between physical interpretations) and in the sense of adapting to experimental circumstances (see below).

A convenient and common assumption in the distribution model, and one that we will use, is that the rate dispersion arises from a distribution of activation energies (E_a), i.e., that the Arrhenius pre-exponential term (log A) is a constant. This assumption can be justified in two ways. First, for the low-temperature processes studied in matrix isolation, the rate is much more sensitive to small variations in E_a than in log A. For example, for a process undergoing reaction at 20 K, a change of 0.1 kcal/mol

in E_a is equivalent to a change of more than one log A unit. Therefore, a distribution that covers a small range over both log A and E_a can usually be approximated by a distribution over E_a alone. Second, a distribution over E_a sometimes has a clearer physical interpretation.[13] For example, a Gaussian E_a distribution might arise from the static, random variation of a structural parameter upon which E_a depends. Very recently, Siebrand attributed a Gaussian E_a distribution for the methyl radical hydrogen-abstraction from methanol glass to a random distribution of transfer distances.[13] Though the physical interpretation is less clear for the closure reaction of a cyclobutanediyl, it seems reasonable that random variations in one or more structural parameters, such as site size and shape or biradical conformation, could result in a Gaussian E_a distribution.

Before we discuss our results, consideration of typical kinetic behavior at cryogenic temperatures, with and without a matrix effect, would be helpful. Presuming, for a moment, that the reaction under study shows exponential and Arrhenius (nontunneling) behavior, the temperature range in which the reaction would occur on a reasonable timescale would be quite small. For example, Figure 4.5a shows predicted decay traces for a process with log A = 8 and E_a = 1.5 kcal/mol at 25, 30 and 35 K. Over a range of 10 degrees, the reaction rate varies by nearly four orders of magnitude. Such a reaction would present severe obstacles to

a.

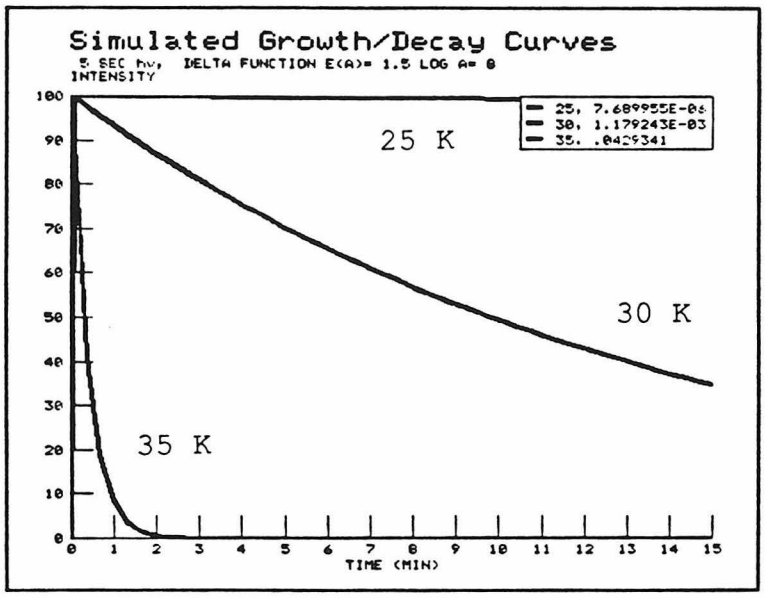

b.

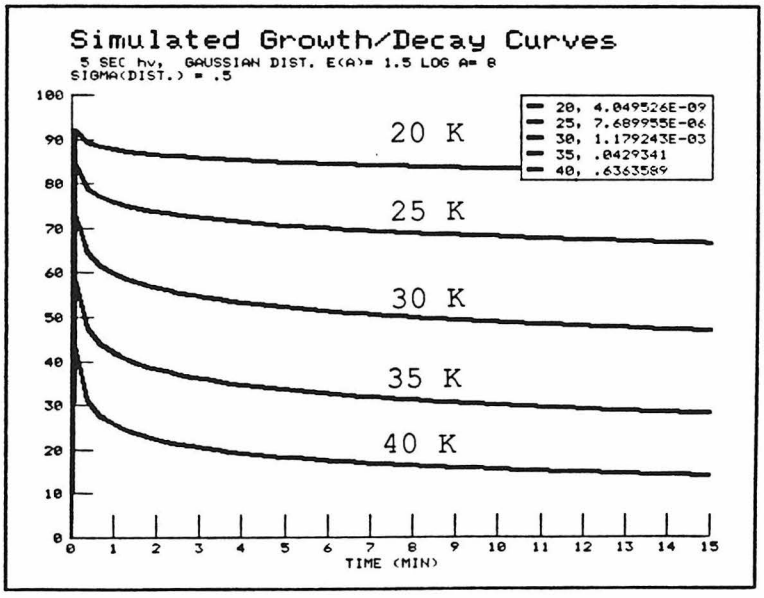

Figure 4.5. Simulated decay of an Arrhenius process, a) with a single rate constant, and b) with a distribution of rate constants.

anyone attempting to measure its activation parameters, since temperatures would have to be maintained with high precision and measured with high accuracy, both difficult tasks below 77 K.

Suppose next that the reaction has a distribution of activation energies but still displays Arrhenius behavior. Simulated decay is shown in Figure 4.5b, assuming the same activation parameters as in part a and a Gaussian E_a distribution with a standard deviation of 0.5 kcal/mol. The temperature range over which decay is observable is clearly much larger than in part a, even though the most probable rates are the same at a given temperature. This situation represents a trade-off for the experimentalist in search of activation parameters; in return for the expanded temperature range, the complexity of the problem has increased tremendously.

An important point illustrated by Figure 4.5 is the fact that the high- and low-temperature decay traces in a composite first-order system are very similar in shape, differing mainly in intensity. This observation can be explained by dividing the distribution into three components for any given decay trace, as done for the 20 and 40 K traces in Figure 4.6. The three components are 1) the "fast sites," which have rate constants too high to allow observation at the given temperature, 2) the "slow sites," which are completely stable on the time scale of the experiment, and 3) the "intermediate sites" (shaded in

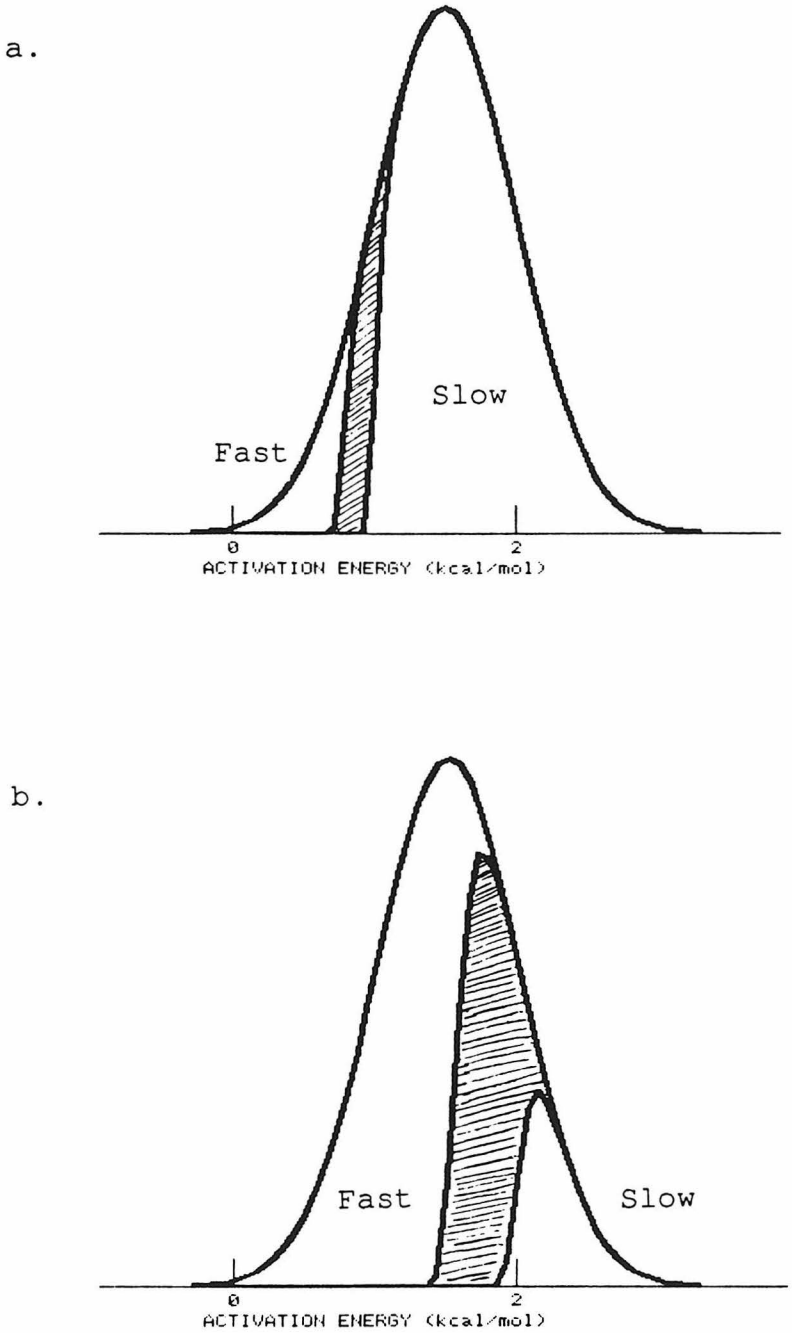

Figure 4.6. Division of a distribution into fast, intermediate (shaded), and slow sites at a) 20 K and b) 40 K.

Figure 4.6), which account for all of the observed decay. The intermediate sites for the two temperatures have the same range of rate constants, which explains the similarity in the shape of the decay traces. The important feature in determining shape, then, is simply the ratio of intermediate sites to slow sites.

Figure 4.6 prompts discussion of an apparent paradox.[20] Though a distribution is usually considered a form of <u>disorder</u>, it actually imparts a large degree of <u>order</u> to the kinetics. That is, molecules react in hierarchical fashion: fast sites, then intermediate sites, then slow sites. In the absence of a distribution, there is no such order; molecules react in a purely random fashion. Thus, along with the increased complexity of distribution kinetics comes an increase in information content. Solution of the distribution problem then affords valuable information about the nature of the reactant-matrix interaction.

This information inherent in any distribution was successfully probed by Siebrand and Wildman in the previously-mentioned methyl radical hydrogen-abstraction from methanol.[13] Having related the Gaussian E_a distribution to a distribution of transfer distances, they began a more detailed investigation of the methyl radical environment. By using known mixtures of methanol and deuterium-labeled methanol and observing changes in the E_a distribution, they obtained not only the number of neighboring methanol molecules around a given

radical, but also their relative distances. This work clearly showed that the complexity of nonexponential decay can be used to great advantage, once the analysis problem is solved.

Very recent work has shown that distribution kinetics may also be observed in solution if the observation time scale is faster than solvent reorganization. Cruz et al.,[21] investigated the absorption-spectrum recovery of organic dyes in solution on the 10-100 femtosecond time scale following photochemical hole-burning by a 10 femtosecond pulse. They found the recovery to be strongly nonexponential, suggesting the existence of different "sites" on this time scale. Thus, information regarding solute-solvent interactions in solutions might also be obtainable through distribution-analysis methods.

Collection of Kinetic Data

Decay traces for **46-Vin** in MTHF at eight temperatures are shown in Figure 4.7. The signals were generated by photolysis of **47-Vin** for the durations shown, ranging from 5 to 30 seconds. The signal decays, digitized and stored for later analysis, were followed for 12 to 25 minutes, even though at the lower temperatures only a small fraction of the signal decayed during this interval. Monitoring large fractions (e.g., 75%) of the signal decay, though desirable as always in quantitative kinetics, was impractical in our experiments. In most cases, this would have required

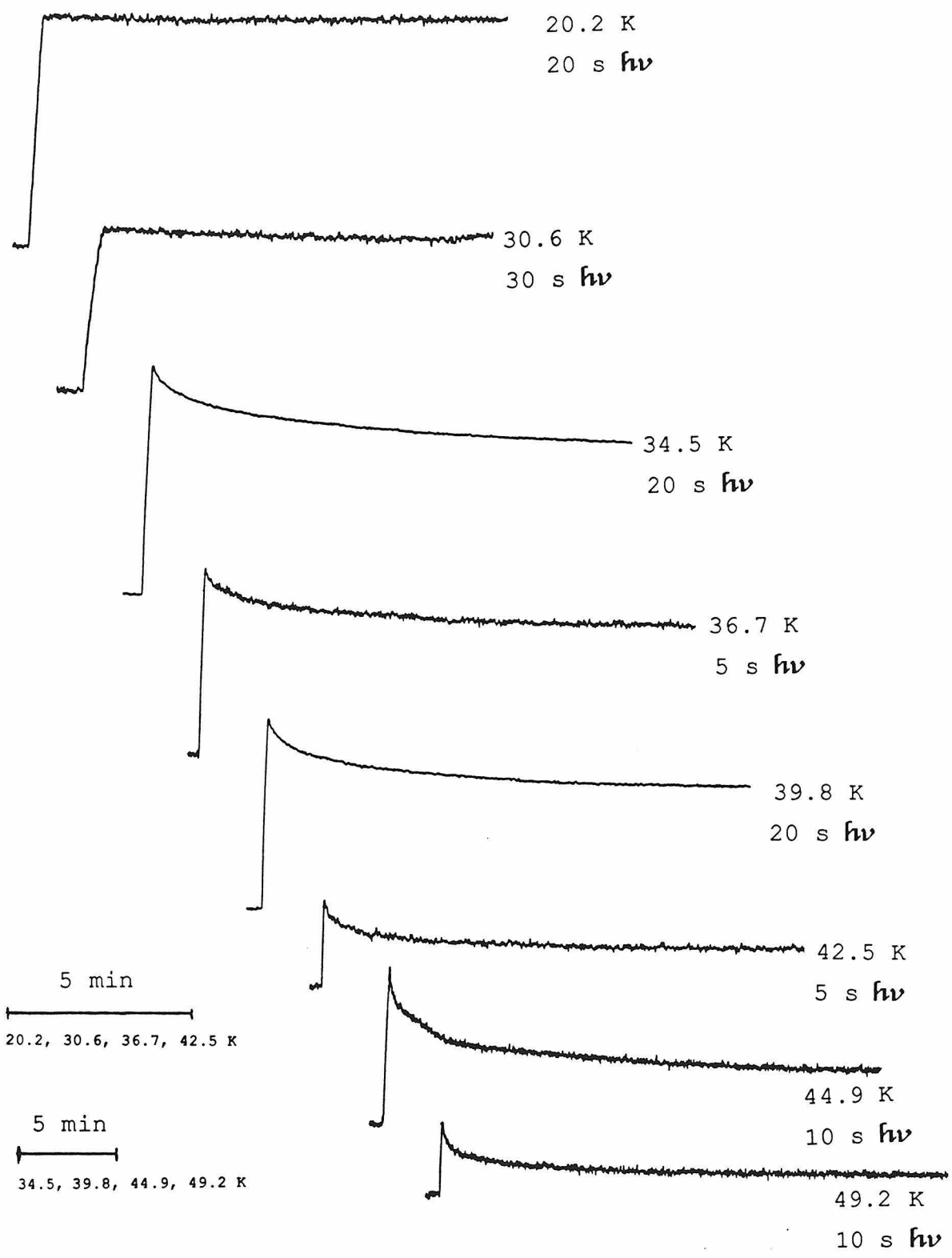

Figure 4.7. Experimental decay traces for **46-Vin** in MTHF.

experiments lasting days or weeks. Though experiments on the order of several hours may have been possible, these would not have resulted in any significant improvement.

The decay of **46-Vin** was studied quantitatively in MTHF and heptane. The decay traces appeared very similar in these solvents, and the analysis results verify this observation. Although not analyzed, decay traces were also recorded for several other matrices: pentane, pentane-$\underline{d}_{12}$, chloroform-$\underline{d}_1$, dichloromethane, iodomethane-$\underline{d}_3$, adamantane, methanol/ethanol (1:1), and methylcyclohexane/isopentane (4:1). These matrices all gave very similar behavior. Adamantane was tried with the idea that a roughly spherical matrix molecule might provide more uniform sites and hence more nearly exponential decay, but this was not observed.

Decay kinetics for **46-EV** were studied in MTHF. Qualitatively, the decay traces for this biradical were comparable to those of **46-Vin**, but the photolytic generation efficiency was much lower. As a result, somewhat longer photolysis intervals were necessary for this case, ranging from 10 to 60 seconds. In heptane, **46-EV** is somewhat less stable, making decay kinetics in this solvent impractical, because of the very long photolysis intervals required.

The kinetic experiments were occasionally troubled by strange behavior, already documented for the dialkyl cyclobutanediyls,[6] though inadequately explained. This behavior, examples of which are shown in Figure 4.8, is characterized by increases in signal intensity lasting up to

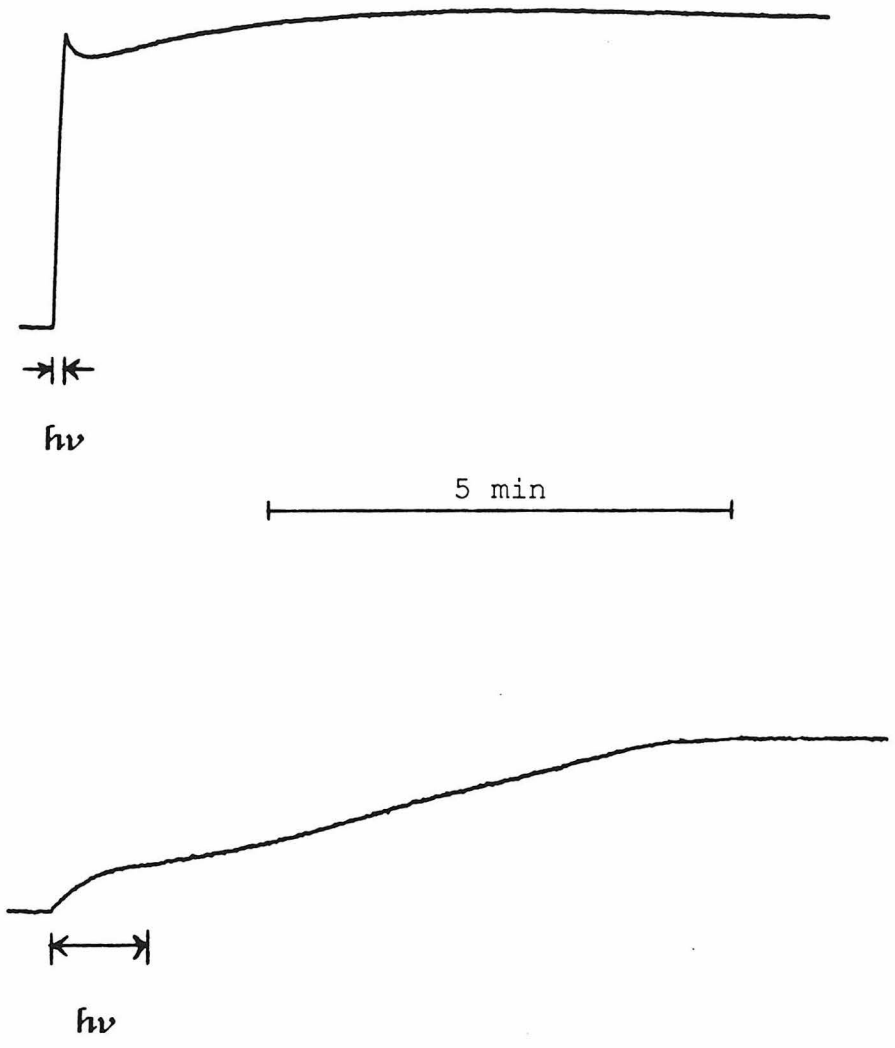

Figure 4.8. Two examples of anomalous behavior attributed to a phonon bottleneck.

15 minutes after the irradiation has ceased. We now believe that this effect can be explained by invoking a saturation phenomenon known as the phonon bottleneck.[22] Normally, the recovery of a signal from saturation is characterized by the spin-lattice relaxation time, which relates to the efficiency of energy transfer from the spin system to the lattice vibrational modes (phonons). However, if the energy transfer from the phonons to the cooling bath is substantially slower, then the phonon bottleneck can occur. The result of the bottleneck is a relaxation time that is much longer than either the spin-lattice relaxation time or the phonon-bath relaxation time. Upon saturation by microwave power or momentary heating, the signal can take minutes to recover to its original intensity. If the light energy warms the matrix during the photolysis interval, then a slow increase in signal intensity after the photolysis interval might correspond to such a recovery from saturation.

Although we still cannot account adequately for the intermittance of the problem with the phonon-bottleneck explanation, we have eliminated several other possible explanations. First, we showed that the temperature itself, though it did increase during photolysis, did not take minutes to recover. By photolyzing our temperature-sensor tube, we found that the temperature returned to the lower value within a few seconds (at most) after photolysis was stopped. Second, we demonstrated that the signal growth was indeed a saturation effect, not a chemical phenomenon.

The same slow recovery was observed when the microwave power was momentarily increased. However, the power increase did not cause the problem through normal spectroscopic saturation, since the even power increases at nonresonant field settings resulted in saturated signals. Absorption of microwave energy also may have occurred via electric field interactions. This possibility is supported by our observation that the problem was much more frequent with larger tubes, being almost unavoidable with 5 mm o.d. tubes (at 4 K). The problem was rarely encountered with 4 mm o.d. tubes. Electric field absorption with large samples is well-documented, especially for fluid samples.[23]

In summary, the unusual behavior depicted in Figure 4.8 is thought to be caused by a phonon-bottleneck saturation aggravated by electric field absorption of microwave energy. We have not discovered a means of avoiding the problem completely, but fortunately, it is intermittent. Only data recorded in its absence were used.

We have indicated that photolysis of the matrix can lead to a momentary increase in temperature. This effect, a further complication to the kinetic analysis, will be discussed in detail in later sections.

Analysis of Decay Kinetics

Numerical Laplace Inversion

Our initial attempts at obtaining a rate distribution included numerical Laplace inversion of the decay trace to

give the distribution directly (eq. 4.2, rewritten here as eq. 4.3). This method was appealing since it is the most

$$F(k,0) = \mathcal{L}^{-1} [f(t)] \qquad (4.3)$$

direct method. The major difficulty with the method, and in fact with any of the procedures for obtaining the distribution, is that the Laplace inverse is not stable to small changes.[18] In other words, very small changes in f(t) can result in very large changes in F(k,0).

As a consequence of this instability, no general procedure is available for numerically inverting the Laplace transform.[18] However, a number of methods have been developed for specific circumstances, and several publications are available for help in applying an appropriate method to a new problem.[18,24] We chose to modify a published procedure based on numerical quadrature and dynamic programming.[18] Without entering into the mathematics, the procedure first requires the reasonable assumption that the distribution is a smooth, continuous curve. A recursive algorithm, based on a matrix-algebra approximation to equation 4.3, is used to first obtain three points that approximate the distribution. This three-point solution is then interpolated to obtain an approximate four-point solution. Next, the four-point solution is refined, and a five-point approximation is obtained. This process is continued through fifteen points, giving a final

distribution that is defined by a total of 3+4+5+...+15 = 117 points.

When we applied this method to our decay traces, we obtained single-maximum rate distributions, which were well-defined by the available points. However, converting the calculated distributions back to the form of decay traces via the forward Laplace transform, a straightforward computation, resulted in poor agreement with the actual decay traces. Although better agreement may have been obtained through refinement of our procedure or adaptation of other procedures, we concluded that the less direct methods were more promising.

Analytical Laplace Solutions

A popular method for obtaining rate distributions involves fitting decay traces to a function whose analytical Laplace inverse is known.[3] The procedure is quite simple, once the function has been chosen, involving adjustment of one or two parameters to produce the best fit, followed by a simple calculation of the most probable rate. A disadvantage is that the shape of the distribution, determined by the function chosen, rarely has any physical significance and is therefore arbitrary.

In studying the rebinding of carbon monoxide to myoglobin following photodissociation, Austin, et al.,[2a] found that the kinetic data could be fit to the function,

$$f(t) = (1 + t/t_0)^{-n}, \qquad (4.4)$$

where n and t_0 are adjustable parameters. This function implies a rate-constant distribution with the form,

$$F(k,0) = n(t_0\lambda)^n \, e^{(-t_0\lambda)} / \, RT \, \Gamma(n+1), \qquad (4.5)$$

which has its maximum at $k_0 = n/t_0$. The most probable rate, k_o, is thus easily obtained from the best fit to equation 4.4. However, when we attempted to fit decay data for **46-Vin** to this function, we did not achieve acceptable agreement.

The failure of equation 4.4 (and other functions)[17] to fit our data was probably caused, at least in part, by an inherent assumption of this method that is invalid in our case. All of the functions describe the decay as starting from t=0 and ignore the perturbation of a finite generation time. This approximation presents no difficulty for a situation in which there are no fast sites, since the decay can be presumed to start at the end of the photolysis. However, if an appreciable fraction of the sites decay during photolysis, which is certainly the case in our higher temperature traces, then the time t=0 is not well-defined. In addition, the initial intensity may not be known, presenting another problem for many of the functions.

In order to use analytical functions to successfully fit our data, we would need to collect the decay traces in a

manner that eliminates fast sites, i.e., one that allows observation of all the sites. The only way to accomplish this would be to decrease the photolysis time. However, the photolyses had already been kept only as long as necessary to generate reasonably intense signals, and intervals several orders of magnitude shorter would be needed to satisfy this requirement. Therefore, we abandoned this method of analysis.

Numerical Fitting Using an Assumed Distribution

The only kinetic analysis method that we have used successfully is a simple numerical approach based on the forward Laplace transform.[13,15] The procedure calls for an initial assumption of distribution shape, then adjustment of parameters to produce the simulated decay trace that best fits the actual trace. Typically, distributions have two adjustable parameters, one relating to width and one relating to position on the rate axis.

This method has a common disadvantage with the previous method in that the distribution shape must be chosen a priori. However, in this case, the shape is not limited to known Laplace functions, so any appropriate shape (e.g., the one with the most physical significance) can be selected. Furthermore, many different shapes can be tried and compared, if desired.

Studies using this method have been described in the literature,[13,15] though some of the computational procedures

suggested diminish the flexibility of the method. These procedures fit the data in essentially the same manner as the analytical Laplace functions, thus introducing the same problem discussed earlier involving fast sites.

We recognized that this method had the potential for dealing with fast sites, so we developed a straightforward algorithm to accomplish this. The procedure involves computing the simulated decay trace point-by-point in a chronological sense. The distribution at each point is calculated from the distribution at the previous point, accounting for the decay occurring over the intervening time interval. The intensity at each point is simply the area under the current distribution. With this procedure, the generation period can be included explicitly, accounting for both growth and decay during the period.

We have incorporated this algorithm into two programs: a simulation program, DECAY.BAS (listed in Appendix A), and a fitting program, FIT.BAS (listed in Appendix B). DECAY.BAS serves two purposes: (1) simulated growth/decay traces are produced given log A, the most probable E_a, the choice of distribution shape and its width, the temperature, and the time scale desired for the decay trace; and (2) the E_a distribution at any point during the growth or decay can be displayed. (This program was used to produce the simulations in Figures 4.5 and 4.6.) An option is included which simulates a specified temperature increase during the photolysis period, taking into account signal attenuation due

to both the Curie law (eq. 4.6) and additional decay caused by the higher temperature.

$$\text{Intensity} \propto 1/\text{Temperature} \tag{4.6}$$

FIT.BAS produces growth/decay trace simulations in the same manner as DECAY, but the results are compared to an experimental trace. The distribution is handled on a logarithmic rate scale, which is proportional to E_a, so that log A input is not necessary. The distribution width and/or position on the axis can be optimized to produce the best fit. The rate (position) optimization can be chosen to achieve either the best overall fit or the best fit at the end of the decay trace. (Agreement at the end of the trace is especially important when a large fraction of sites is still present at the end.)

At this point, the relationship between the E_a and rate axes should be clarified. First, using the Arrhenius equation (eq. 4.7),

$$k = Ae^{-E_a/RT}, \tag{4.7}$$

we can relate the most probable rate constant, k_0, to the most probable E_a, E_0:

$$k_0 = Ae^{-E_0/RT}. \tag{4.8}$$

Combining equations 4.7 and 4.8 gives:

$$\ln(k/k_0) = (\Delta E)/RT, \qquad (4.9)$$

where $\Delta E = E_0 - E_a$. Equation 4.9 shows that the $\ln(k/k_0)$ and ΔE scales are directly proportional. Further, whereas ΔE is temperature-independent, $\ln(k/k_0)$ varies inversely with temperature. The effect of this relationship is that an E_a distribution remains constant at all temperatures, while the corresponding $\ln(k/k_0)$ distribution becomes narrower as the temperature increases.

In preliminary fitting experiments, we allowed three degrees of freedom in the fitting procedure: distribution width and position, and "initial" concentration of biradical. We did not know the fraction of fast (unobservable) sites, so rather then fixing the intensity scale arbitrarily, we decided to scale the data to match the simulated maximum for each iteration in the optimizations. In this manner, the best agreement over all three degrees of freedom was obtained.

Using this technique, we fitted eight decay traces for **46-Vin** in heptane recorded at temperatures ranging from 29 K to 54 K. We used four distribution shapes: Gaussian, box (rectangular), and right-triangular (left and right facing). The decay trace fits for the Gaussian distribution are shown in Figure 4.9; the fits for the other distributions were of comparable quality. For each distribution, the width

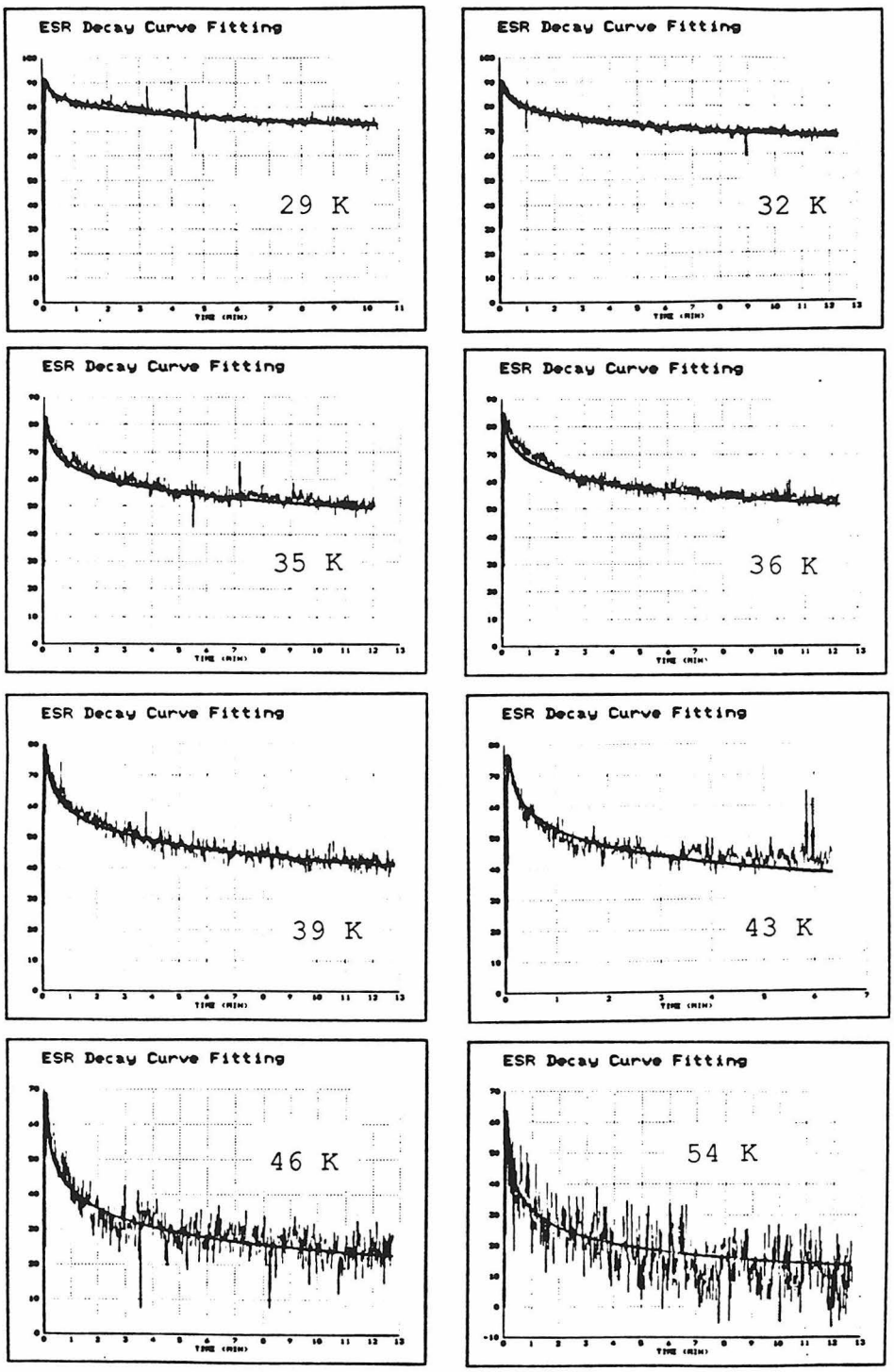

Figure 4.9. Preliminary fits to decay traces for **46-Vin** in heptane with the assumption of a Gaussian E_a distribution. Heating during photolysis was not accounted for.

over $\ln(k/k_0)$ was optimized for each decay trace. The average of these values was then used to obtain the most probable rates. When the most probable rate constants obtained from the fitting procedure were plotted in an Arrhenius fashion ($\ln k_0$ vs. $1/T$, eq. 4.10), linear graphs were obtained. The Arrhenius plot corresponding to the

$$\ln k = \ln A - E_a/RT \qquad (4.10)$$

Gaussian distribution is shown in Figure 4.10 along with a linear least-squares fit (the other distributions showed similar correlations), and the activation parameters so obtained are shown for all four distributions in Table 4.1.

A number of comments are necessary concerning these results. First, the observation of Arrhenius behavior is remarkable, since we are aware of no reactions that obey the Arrhenius equation in this temperature range,[25] but especially because the dialkylcyclobutanediyls show strongly non-Arrhenius behavior.[6] The fact that such differently shaped distributions seemed to explain the data equally well was disconcerting, but a simple exercise helped to explain this. Using the Arrhenius equation (eq. 4.10), the four distributions were all plotted on the same $\ln(k/k_0)$ scale at a given temperature (35 K, see Figure 4.11). The distributions display a maximum possible overlap, given their

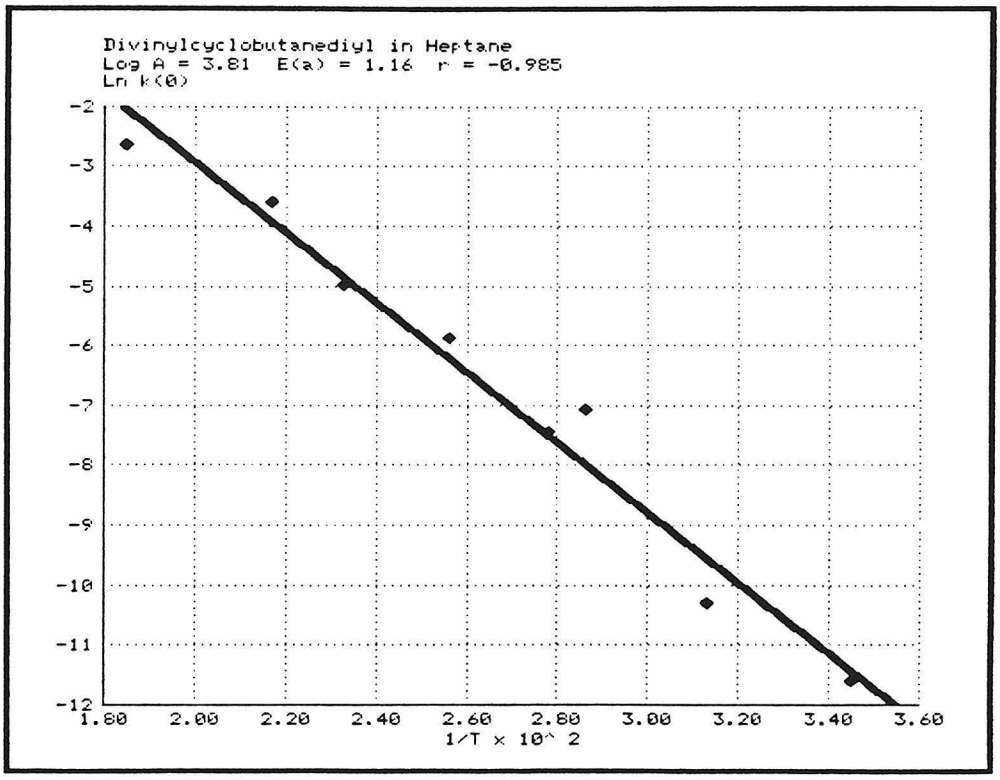

Figure 4.10. Arrhenius plot obtained using the most probable rate constants obtained from the preliminary Gaussian fits.

Table 4.1 Preliminary Activation Parameters from Decay Trace Fitting for **46**-Vin in Heptane

Log A	E_a Distribution kcal/mol
3.8	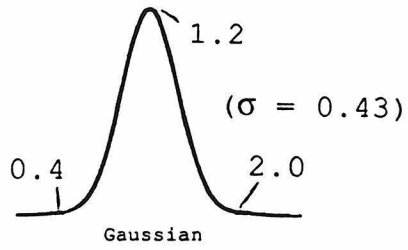
4.3	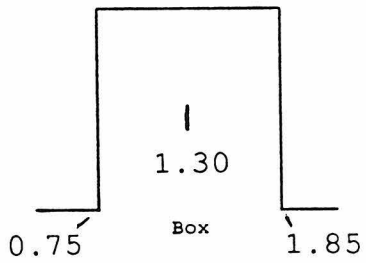
5.4	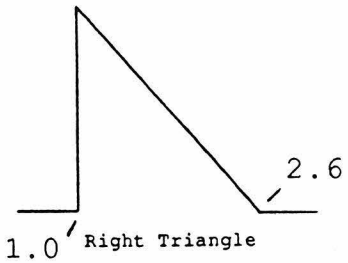
3.4	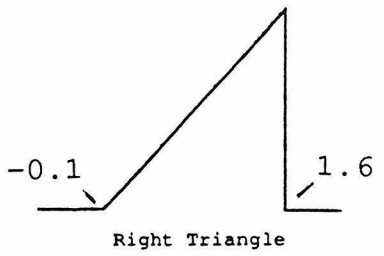

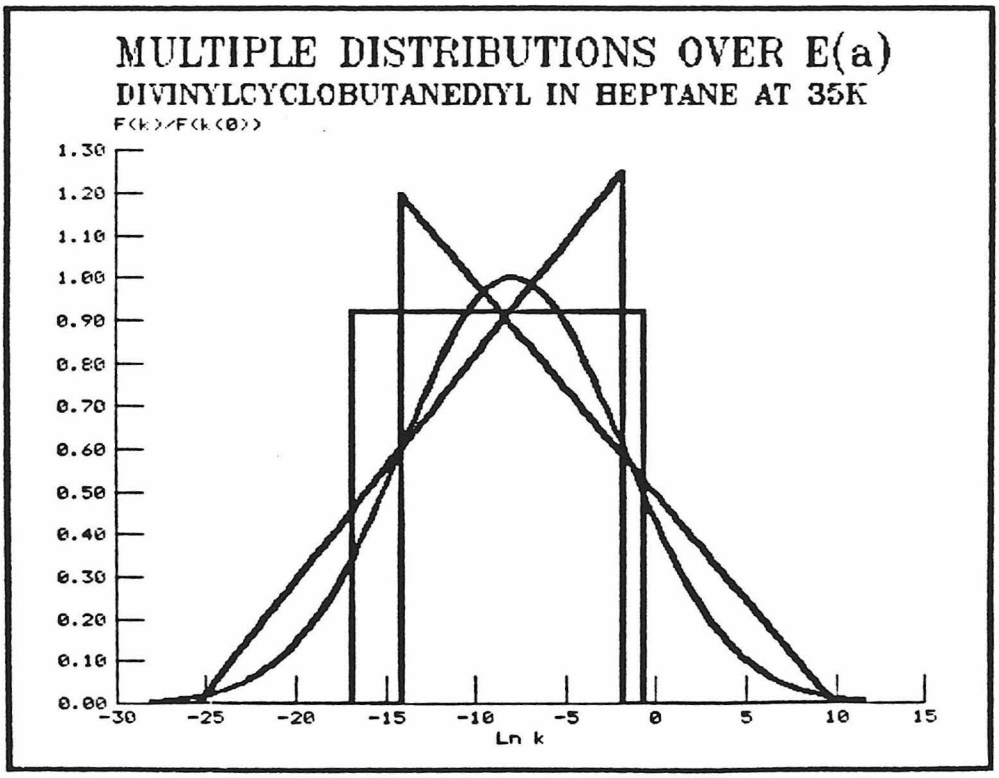

Figure 4.11. Overlapping plot of four distribution shapes which successfully modeled the decay traces of **46-Vin** in heptane.

different shapes, and seem to depict, as nearly as possible, the same distribution. The fact that the results are insensitive to the shape variations is a consequence of the Laplace inverse instability: very slight changes in F(t) correspond to large changes in F(k,0).[18]

Based upon later experiments, we now believe that the activation parameters obtained from these preliminary results (Table 4.1) are erroneous. Our method of freely scaling the experimental intensities, combined with the problem alluded to earlier concerning temperature increases during photolysis, caused a systematic error in the scaling process. Even though the photolysis intervals are relatively short, temperature increases of 1-3 degrees (which is the observed order of magnitude) in the photolysis interval can significantly increase the number of fast sites at the expense of intermediate sites. This can dramatically change the shape of the decay trace, especially near the beginning. To illustrate this effect, the 35 K simulation from Figure 4.5 is plotted in Figure 4.12 along with a simulation in which the temperature is taken as 37 K during the photolysis interval. The latter simulation shows much less apparent decay than the former, and the fitting program, not accounting for such heating, would clearly scale such a trace incorrectly.

We have attempted through several means to quantify the temperature increases caused by photolysis. Evidence that the temperature <u>does</u> increase exists in the decay

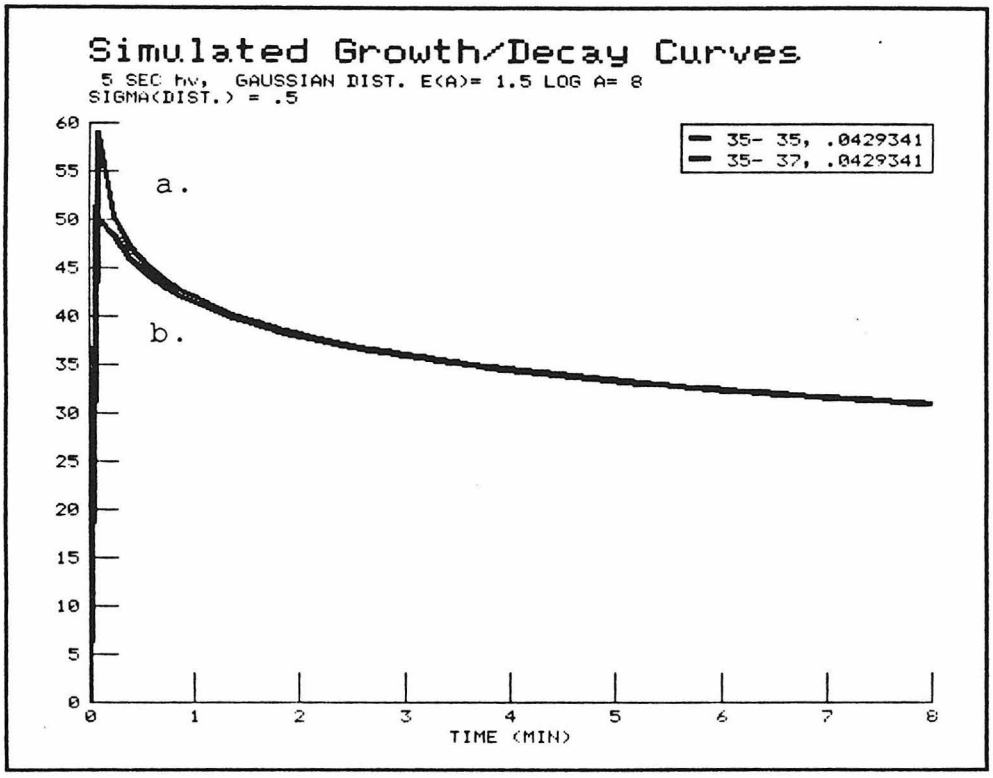

Figure 4.12. Comparison of 35 K decay simulations assuming a) no warming during photolysis, and b) warming of 2 K.

traces, or at least in the lower temperature traces. The signal growth in these traces extends past the cessation of photolysis, usually by a second or two, and is presumably caused by the Curie effect (eq. 4.6) as the matrix recools. The effect sometimes disappears at higher temperatures, due to a much smaller Curie effect and a relatively larger number of fast sites. The Curie law can theoretically be used to calculate the higher temperature as follows:

$$T(\text{higher, during photolysis}) = T(\text{lower}) \frac{\text{Intensity (lower T)}}{\text{Intensity (higher T)}} \qquad (4.11)$$

However, other factors, such as fast-site decay and the spectrometer time-constant, interfere with this calculation.

Equation 4.11 still seemed to be a viable means for quantifying the heating effect, so we sought more favorable experimental conditions for its use. For example, photolysis of a large signal composed of only slow sites should produce an initial signal drop according to equation 4.11, interfered with by a relatively small amount of signal growth due to the photolysis.[26] However, this method worked only at very low temperatures where the Curie effect is large enough to overwhelm the new growth.

We also tried this experiment with signals from other paramagnetic species in the same solvents, in order to avoid the interfering signal growth. For example, iodomethane in MTHF was irradiated with short wavelength light (<300 nm) to produce a doublet signal. However, the signal was highly

saturated and therefore much less temperature-sensitive than a signal which obeys the Curie law. Thus, when this sample was irradiated with the usual filter combination, no change in signal intensity was observable.

Direct photolysis of the temperature sensor in ethylene glycol, an experiment that must be considered suspect because of the large perturbation, nevertheless indicated that the photolysis-induced warming was approximately two degrees, independent of temperature. The higher temperature was reached within one second and remained constant until photolysis had ceased, when the temperature recovered immediately (within 2-3 seconds at higher temperatures). Similar photolysis of a chromel vs. gold (0.7% iron) thermocouple in heptane indicated temperature increases of approximately 0.7 degrees.

Being unable to adequately quantify the photolysis-heating effect, we needed a method for determining the experimental intensity scale (i.e., the number of fast sites). If the signal intensity at any point in the decay trace could be related to the intensity of an intact distribution generated with the same amount of photolysis, the problem would be solved. This might be possible by using the Curie law to normalize all the decay traces to a similar photolysis at 3.8 K, where there is no decay.

First, a control experiment was necessary to demonstrate that the photochemical efficiency of biradical formation is insensitive to temperature. This was shown by

comparing the signal intensities measured at 3.8 K following two different experiments. In the first experiment, the sample was photolyzed at 3.8 K, warmed to 28 K for one minute, then recooled to 3.8 K to determine signal intensity. In the second experiment, the photolysis was conducted at 28 K. The signal was allowed to decay for one minute, after which the sample was cooled to 3.8 K for intensity measurement. These experiments showed that the photochemical efficiency is not strongly temperature-sensitive.

In order to use the Curie law, all signals must be nonsaturated. This is a difficult requirement to meet at 3.8 K, but fortunately, the half-field transitions of both **46-Vin** and **46-EV** are nonsaturated at microwave powers less than or equal to 0.02 mW in the solvents used.[27] At the temperatures of the decay traces, all transitions could be made nonsaturated.

Several corrections were necessary to normalize the signal intensities. Aside from temperature, differences in microwave power and receiver gain had to be accounted for. A further correction was necessary since decay traces were monitored using the largest peak, one of the $\Delta m_s = 1$ transitions, and at 3.8 K, only the half-field transition could be measured without saturation. An appropriate intensity-ratio correction factor was obtained as an average from several completely nonsaturated spectra.

By using the Curie law and the method just described, eight decay traces for **46-Vin** in MTHF were obtained and normalized to analogous traces at 3.8 K. FIT.BAS was then modified to accept intensity input and scale the data accordingly. A routine that optimizes the amount of warming during photolysis (if desired) after the width and rate optimization was also added. Gaussian-distribution fits to the decay data are shown in Figure 4.13. An Arrhenius plot of the resulting most probable rates is linear and is shown in Figure 4.14, along with the activation parameters.

The results in Figure 4.14 are obviously much different than the preliminary results listed in Table 4.1. The earlier results depicted a more stable biradical, erring in the expected direction based on the improper scaling discussed earlier. This can be illustrated by considering the 29 K decay trace in Figure 4.9. Since there is little apparent decay, the best fit was obtained by scaling the maximum intensity to essentially 100%, ignoring the photolysis warming effect. However, the corrected results show that there are a substantial number of fast sites at 29 K, implying a less stable species.

Although this method of intensity scaling is far superior to the original method, it is not without problems. Photochemical efficiency appears to be constant for most of the decay traces, but occasionally a trace was recorded that was much stronger or weaker than expected. This

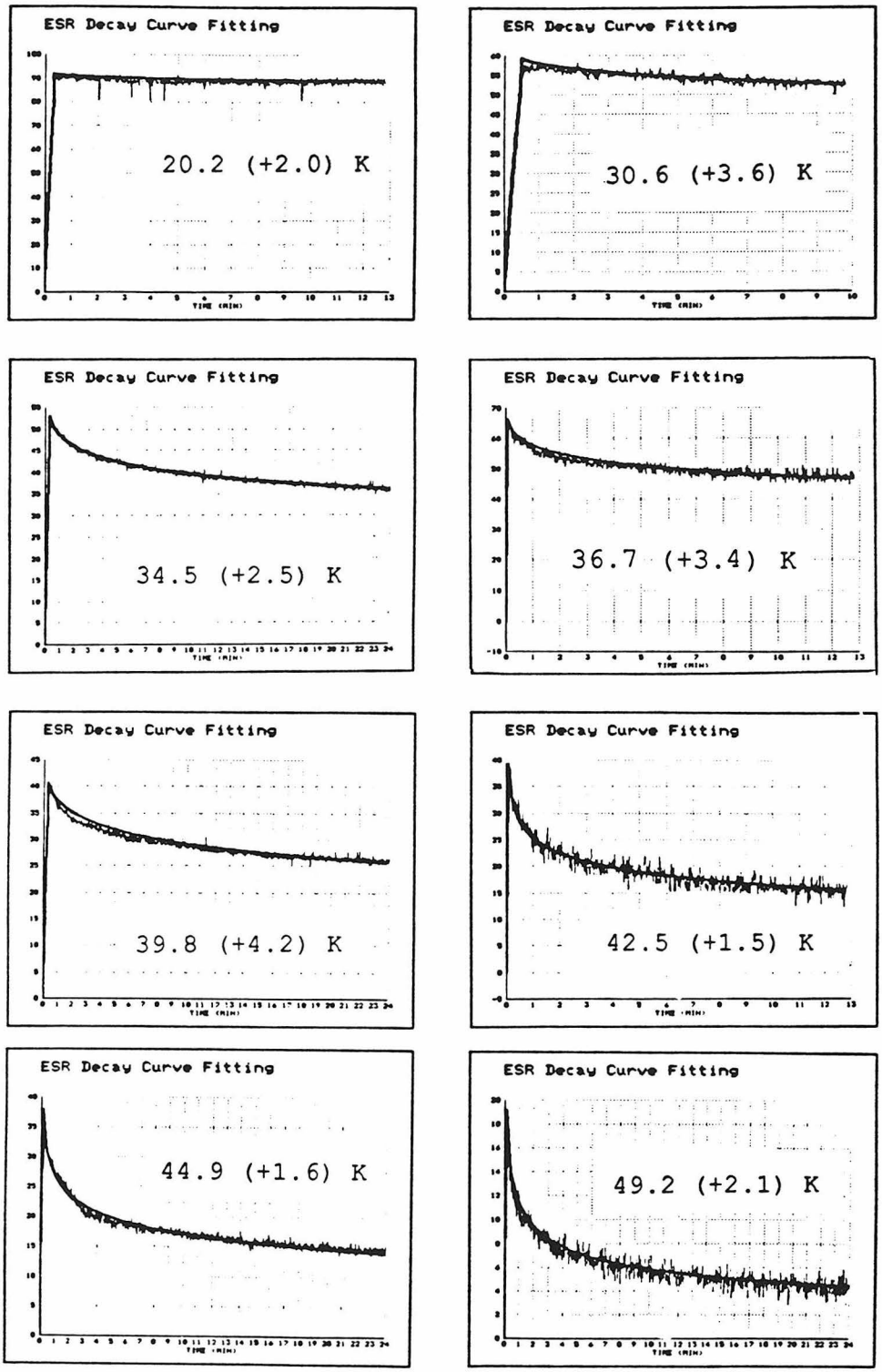

Figure 4.13. Gaussian-distribution fits to normalized data for decay of **46-Vin** in MTHF. Temperatures are indicated with increases due to photolysis in parentheses.

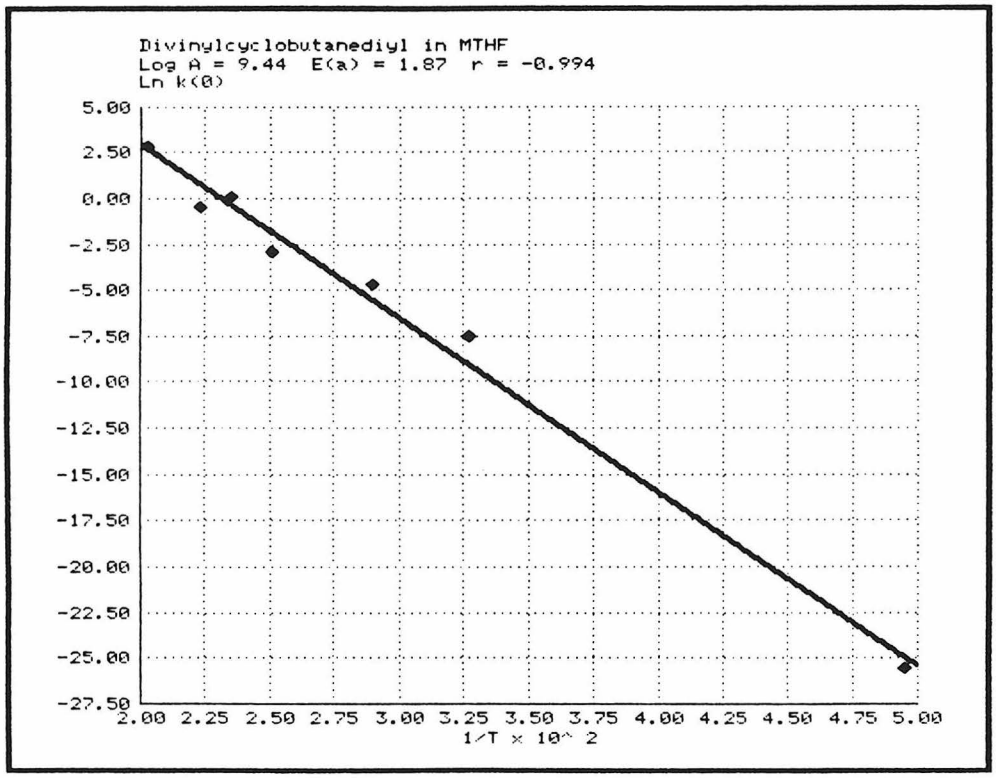

Figure 4.14. Arrhenius plot obtained from decay-trace fitting of normalized data for **46-Vin** in MTHF.

behavior probably represents differences in optical properties of the matrix, rather than photochemical efficiency. For example, it was observed in the glassy MTHF but not in heptane, which is polycrystalline. Traces of this sort (i.e., the 36.7 K trace in Figure 4.13) were not used in the analysis.

Another problem is that the large number of corrections necessary for the intensity normalization can lead to substantial errors. One particular consideration is that changes with temperature in the relative transition probabilities between the $\Delta m_s = 1$ and 2 peaks might lead to errors in the relative peak intensity correction. That this might be the case was suggested by some observed discrepancies. Therefore, after each decay trace was completed, the sample was cooled to 3.8 K, and a spectrum was recorded. This spectrum serves as a double check on the intensity normalization, since the normalization to this spectrum should give the same result as the procedure described above. In most cases, the two normalizations were similar, but there were some differences.

In order to determine the seriousness of these discrepancies with respect to the activation parameters, the fitting procedure was also carried out using the alternative normalization procedure just described. The resulting decay trace fits are shown in Figure 4.15 and the Arrhenius plot with activation parameters, in Figure 4.16. The alternative procedure leads to some differences in the most probable

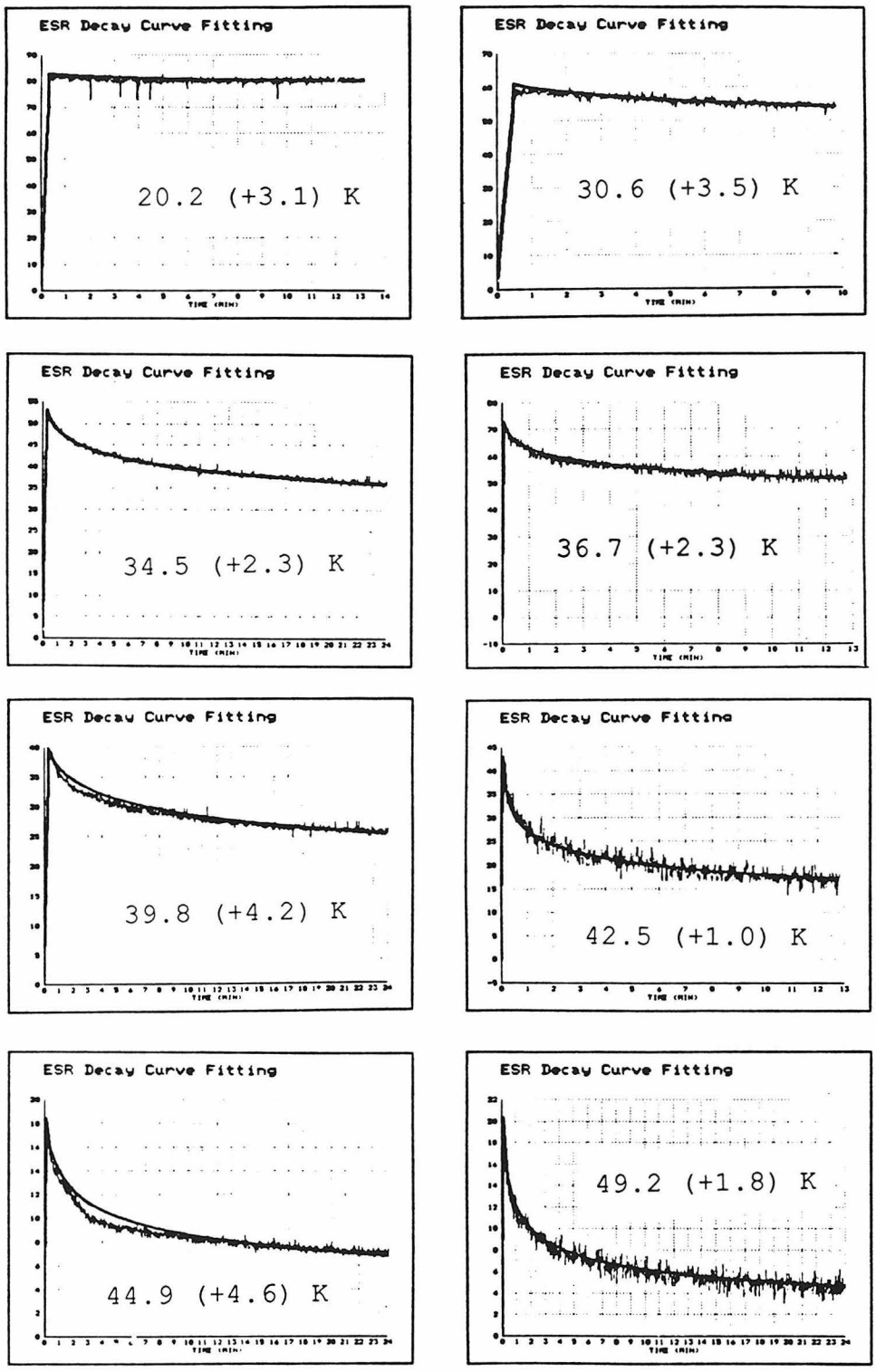

Figure 4.15. Gaussian-distribution fits to **46-Vin**/MTHF decay traces which have been normalized using spectra recorded at 3.8 K after each decay trace.

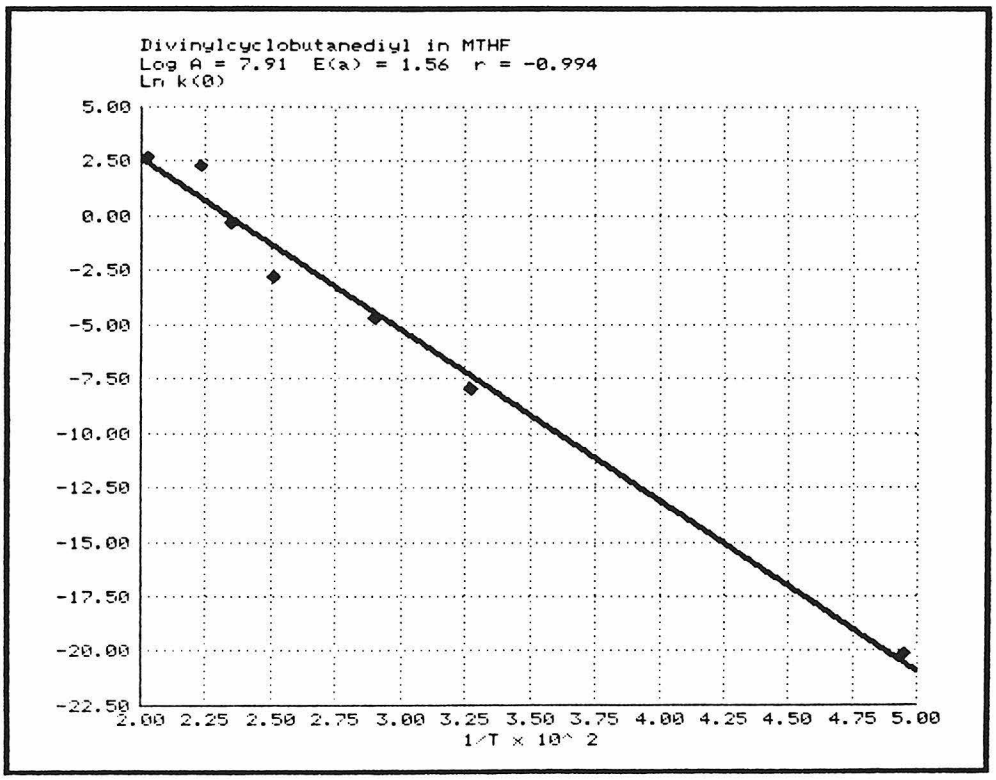

Figure 4.16. Arrhenius plot obtained for **46-Vin** in MTHF using the alternative normalization procedure, in which decay traces are scaled based upon spectra recorded after each trace at 3.8 K.

rate constants, most notably for the 20.2 K decay trace. The activation parameters are similar to those in Figure 4.14, offering encouragement.

One further problem that exists with all of the normalization procedures is that changes in the distribution width affect the activation parameters more than the agreement in the decay-fitting procedure. In other words, a range of distribution widths gives satisfactory agreement to the decay data, enlarging the error limits on the activation parameters.

Before pursuing this type of analysis any further, we will introduce a different type of kinetic experiment, which we have developed. After describing some results using the new method, we will show how the two methods may be combined to address some of the difficulties discussed above.

Distribution Slicing

In addition to decay-trace fitting, the cyclobutane-diyls were studied by a new kinetics technique, which we call "distribution slicing." This procedure is complementary to decay-trace fitting in the information provided, and it represents a third method for determining the intensity scale of the decay traces. Very importantly, the method provides distribution-shape information and verifies the use of the distribution model in the first place.

Conceptually and experimentally, the distribution-slicing method is very simple. The idea is to generate a

signal that represents an intact E_a distribution by photolysis at a low enough temperature, i.e., 3.8 K for **46-Vin** or **-EV**. Then, by warming the matrix to successively higher temperatures, fast sites are in effect sliced off the distribution in layers (see Figure 4.17). By recooling to 3.8 K in-between warming cycles and measuring the signal intensity, the size of each "slice" (relative to the complete distribution) can be obtained. Reconstruction of the distribution from the constituent slices then produces a crude image of the distribution (Figure 4.17).

An obvious limitation of this method is that the distribution must be broad relative to the resolution attainable in the slicing (see Figure 4.18). This resolution corresponds to an approximate rate ratio of 100, which is equivalent to an E_a difference of about 0.25 kcal/mol at 30 K, well below the distribution widths obtained in the previous section. Though this limitation is easily met in our case, it is undoubtedly part of the reason this method has not been reported previously.

Consider the single slice shown in Figure 4.18. Our objective in the experiment is to assign an E_a value to the slice so that the E_a distribution may be reconstructed directly. This may be accomplished using the Arrhenius equation, which has been solved for E_a in equation 4.12:

$$E_a = -RT \ln(k/A). \qquad (4.12)$$

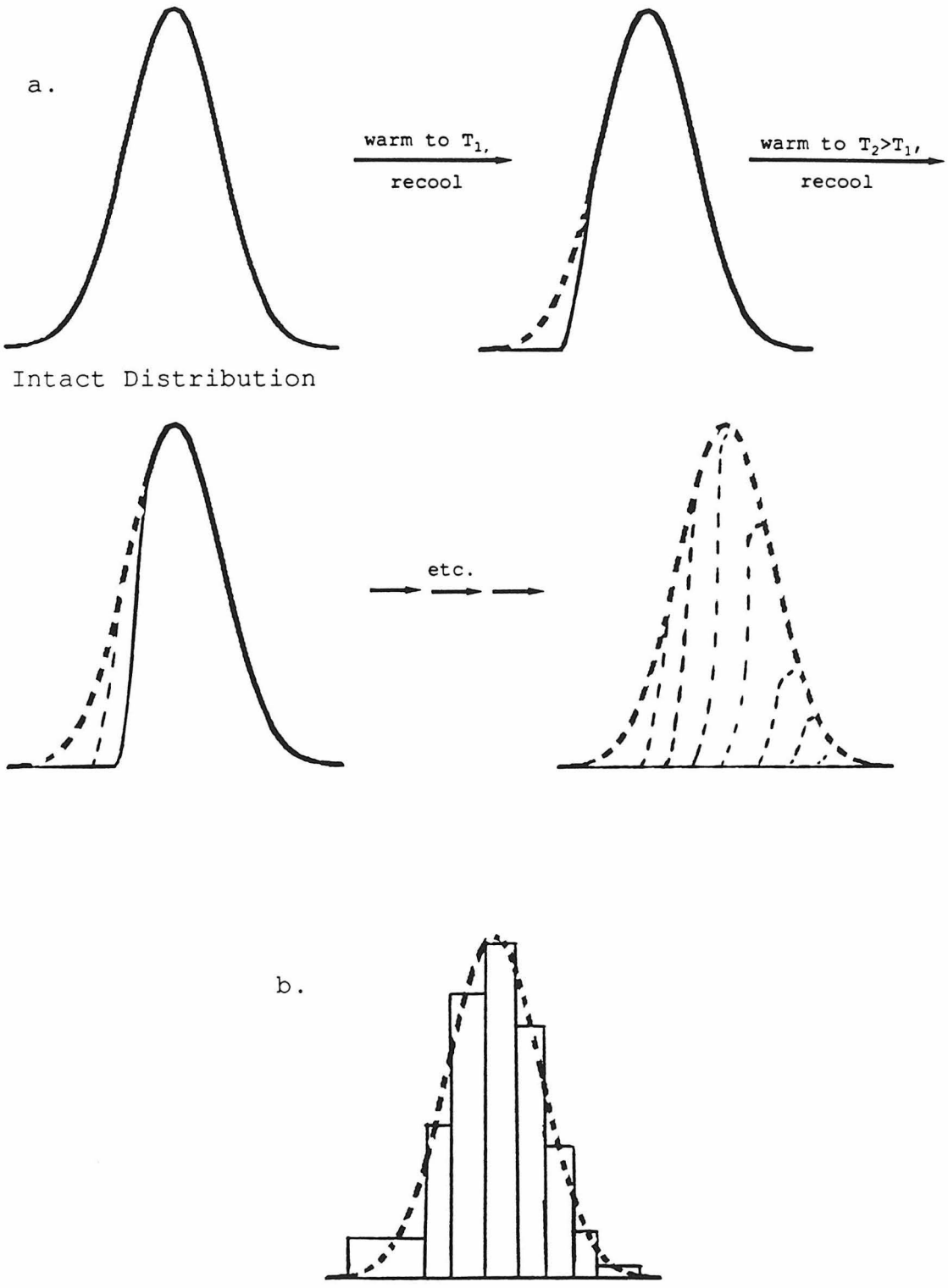

Figure 4.17. Distribution-slicing experiment. a) Evolution of the distribution during the data collection. b) Reconstructed distribution.

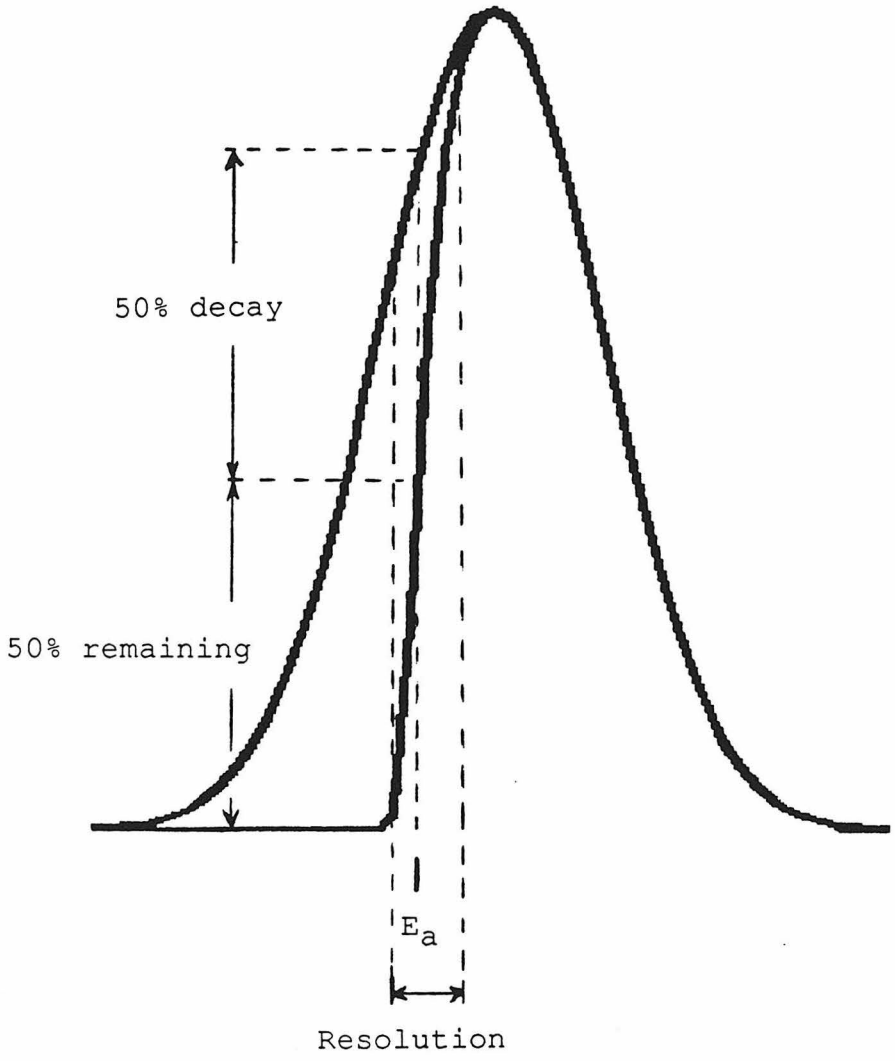

Figure 4.18. The parameters of E_a and kinetic resolution, which describe a given warming cycle.

In this equation, T is known from the experiment, k can be calculated as described below, and we must assume a value for A. The rate that we desire, k, is the one that defines the center of slice, corresponding to 50% decay during the warming interval (see Figure 4.18). In other words, the warming interval corresponds to exactly one half-life. Therefore,

$$\text{warming interval} = t = (\ln 2)/k. \qquad (4.13)$$

Substituting into equation 4.12 gives

$$E_a = -RT \ln((\ln 2)/At). \qquad (4.14)$$

Thus, E_a is easily calculated from the experimental temperature and warming interval.

Reconstruction of the distribution from the slicing experiment as shown in Figure 4.17 involves conversion of the intensity data into areas under the distribution and as such constitutes a form of numerical differentiation. This type of process always results in magnification of errors, and for this reason we will usually present results in the integrated (intensity vs. E_a) form. Distribution-shape information is still available in this format, and Figure 4.19 compares the expected shapes for Gaussian, box, and right-triangle distributions.

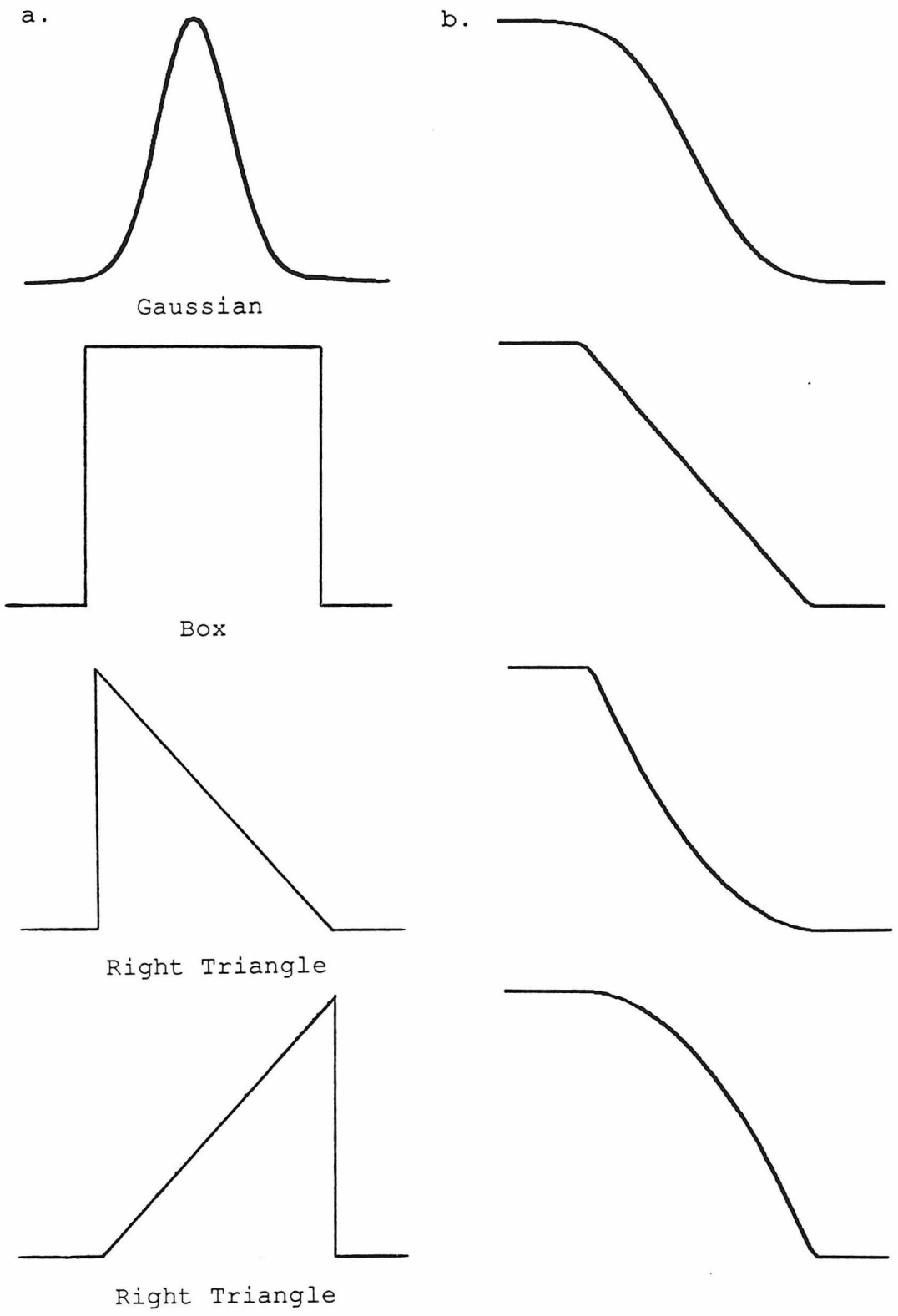

Figure 4.19. a) Distribution shapes (probability vs. E_a) and b) "integrated" distributions (intensity vs. E_a).

As an example, data from a distribution-slicing experiment for **46-Vin** in MTHF are listed in Table 4.2. The raw data include for each cycle the temperature to which the matrix was warmed, the warming interval, and the intensity recorded upon recooling. In order to plot the data, the temperature and time values were first converted to E_a values by using equation 4.14 and assuming log A = 8. (The choice of log A affects only the E_a values, not the distribution shape.) The plot of intensity vs. E_a is shown in Figure 4.20. This graph, when compared to the curves in Figure 4.19, clearly agrees best with the Gaussian distribution curve. Thus, the distribution shape, which completely eludes all the decay-fitting procedures as noted in the earlier discussion, is effectively "photographed" by this comparatively simple procedure!

In addition to providing shape information, this experiment serves to verify the distribution model itself through simple, qualitative observations. For example, whenever consecutive warming cycles involve the same temperature, the majority of the decay always occurs during the first cycle. Subsequent cycles show very little decay, since the fast sites and many of the sites in the intermediate region have already been depleted. An example of this behavior is shown in Table 4.2 for the low-E_a region of the distribution, though similar behavior has been observed throughout the distribution. Furthermore, any subsequent warming cycles to lower temperatures show no

Table 4.2. Distribution-Slicing Data for **46-Vin** in MTHF

T(K)	t(s)	Intensity (%)	E_a (kcal/mol)[a]
3.8	600	100.0	0.19
10.1	98	99.0	0.47
17.8	135	96.8	0.84
17.8	350[b]	95.3	0.87
22.7	270	90.1	1.10
27.2	270	80.1	1.32
34.3	295	53.5	1.67
39.4	190	37.3	1.88
44.5	190	22.4	2.13
50.2	270	9.5	2.43
55.5	270	3.7	2.69

[a]Calculated using equation 4.14 with log A=8. [b]The experimental time interval for this slice was 215 s. The value shown represents the total time spent at 17.8 K. See Experimental Section.

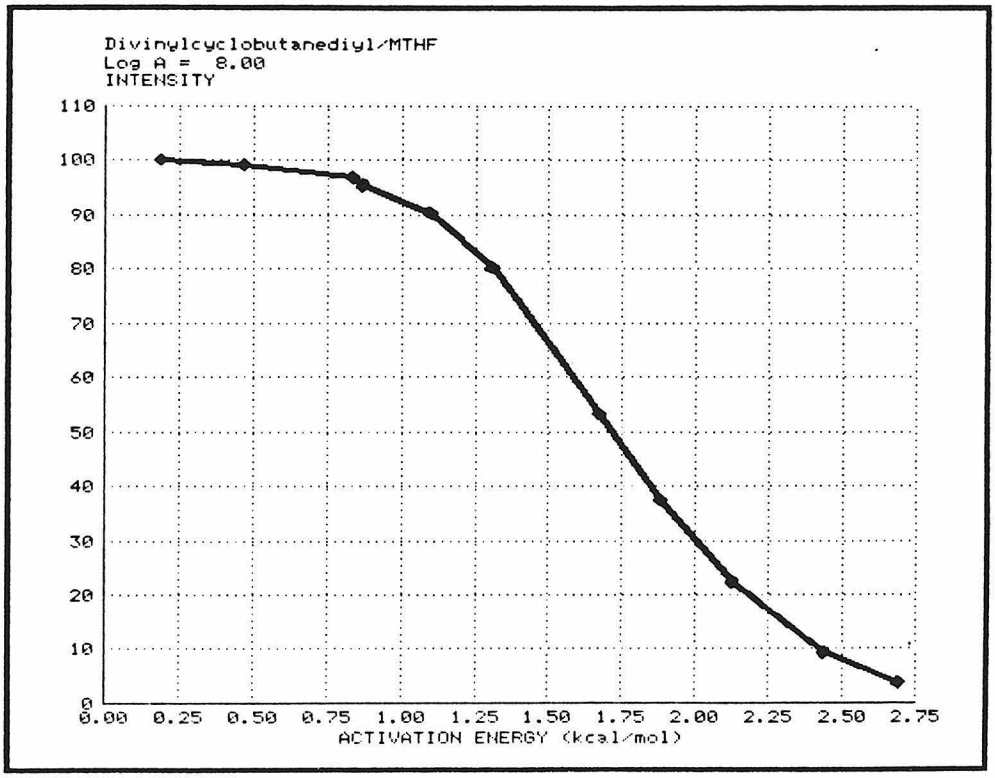

Figure 4.20. Intensity vs. Ea plot of **46-Vin** data in MTHF.

decay at all on a reasonable timescale. As far as we are aware, these observations constitute the most direct evidence to date in support of a distribution model.[28]

If the warming intervals are kept constant throughout a slicing experiment, then T becomes directly proportional to E_a (eq. 4.14). Therefore, the intensity data (or distribution) can be plotted on a temperature scale. This type of plot illustrates the complementary relationship between the decay-trace and distribution-slicing experiments: the former measures intensity vs. time at constant temperature, while the latter measures intensity vs. temperature with a constant time. Thus, if one plots signal intensity as a two-dimensional surface over time and temperature, as in Figure 4.21, then the two experiments represent orthogonal cross sections.

This comparison also serves to illustrate the greater flexibility of the distribution-slicing experiment. While the decay-trace experiment must follow a constant-temperature cross section of the surface in Figure 4.21, the distribution-slicing experiment can follow virtually any "all-downhill" path.[29] Though a tortuous path would appear complicated in three dimensions, it can easily be projected onto a simple two-dimensional plot over E_a. If desired, distribution slicing can even be used to reproduce a decay trace.

The experimental procedure used in distribution slicing has several intrinsic advantages and disadvantages

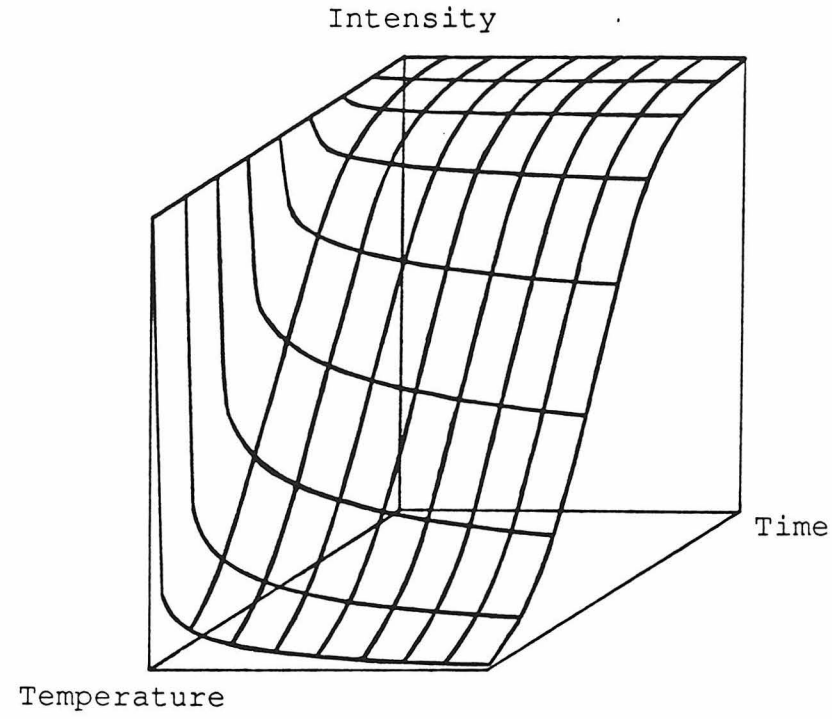

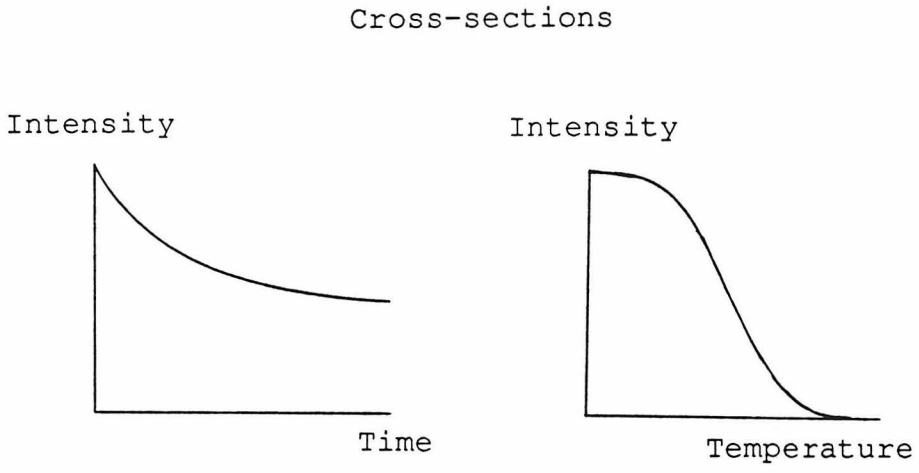

Figure 4.21. Three-dimensional representation of reactivity. Temperature cross sections represent normal decay traces, while time cross sections may be obtained through distribution slicing.

when compared to normal decay kinetics. A significant advantage is that even though the decay may be probed over a large temperature range, all intensity measurements are made at the same temperature. Therefore, there is no need for intensity normalization of any sort. Furthermore, the measurement temperature, usually 3.8 K, is the easiest temperature to attain accurately when using a liquid helium cryostat. Considering the decay-trace normalization problems discussed earlier, this automatic normalization is a very important feature.

A disadvantage of the distribution-slicing method is that the higher temperatures must be equilibrated quickly and without overshooting. Low-temperature distribution kinetics are characterized by a much greater dependence on temperature than on time, so temperature equilibration is a crucial issue. Our cryostat typically allowed complete equilibration after 3-5 minutes, which was also a typical warming time interval. Therefore, a 1-2 degree range of temperatures was usually probed instead of a single temperature. The temperature range during equilibration was generally greater at higher temperatures. Model calculations (see Experimental Section) showed that such a temperature band causes decay that is in general equivalent to that caused by a single temperature very close to the maximum of the band. We thus believe that errors incurred through this slow equilibration are small.

Another experimental difficulty with the distribution-slicing procedure is that temperatures must be calibrated either before or after the entire experiment, so the time interval between a given warming cycle and its calibration point(s) may be quite large. A typical experiment with 8-10 cycles may take about two hours to complete. If the cooling system is subject to any slow drift in calibration, then this delay might cause significant calibration errors. We occasionally had to discard results from entire experiments when such a problem was detected; however, the problems usually did not occur.

Since our results (such as the example in Figure 4.20) resembled the Gaussian model so closely, we developed a program to fit the results to the model. The program, called DSFIT.BAS and listed in Appendix C, accepts as input from a data file the raw temperature, time, and intensity data (e.g., Table 4.2). The only additional input necessary is log A; the most probable E_a and distribution width are optimized unless fixed values are desired. The fit obtained for the **46-Vin** example is shown in Figure 4.22a using log A = 8. As is apparent, the agreement is quite good, and the E_a distribution obtained compares well to the decay-fitting results (Figures 4.14 and 4.16). The Gaussian-E_a distribution implied by this fit is shown in Figure 4.22b.

Another program, SLICE.BAS (listed in Appendix D), was developed to be used in conjunction with DSFIT in order to test the validity of the distribution-slicing method. Using

a.

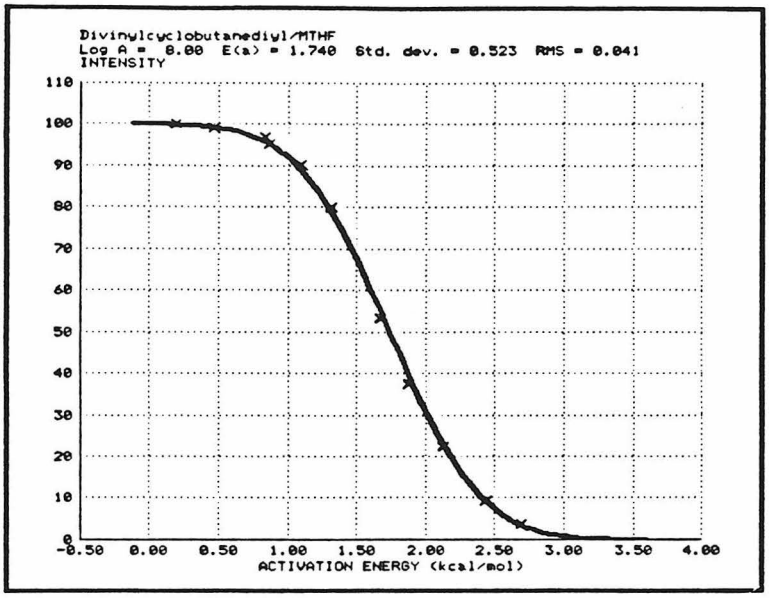

b.

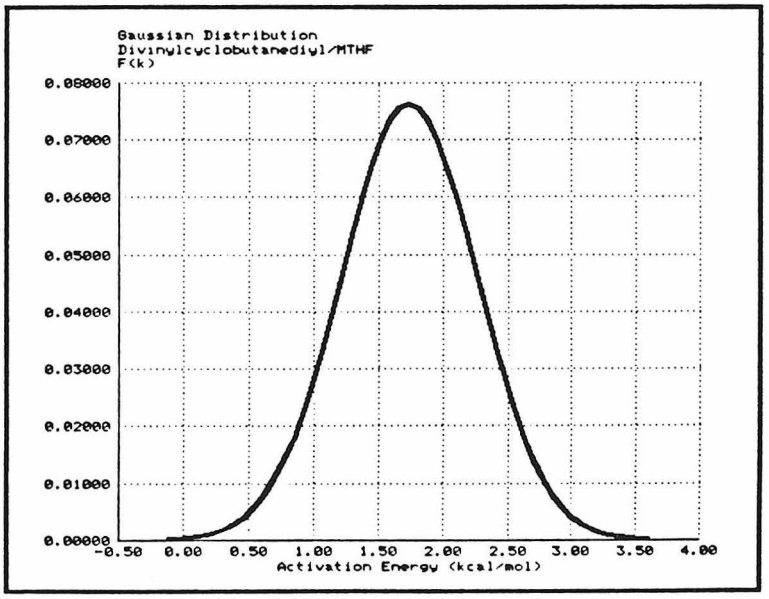

Figure 4.22. Distribution-slicing results for **46-Vin** in MTHF, assuming log A = 8: a) intensity vs. E_a fit to a Gaussian, and b) the optimized Gaussian-E_a distribution.

the same basic algorithm employed in DECAY and FIT, SLICE simulates distribution slicing data based upon an assumed Gaussian shape. The simulated data can be fit using DSFIT in the same manner as experimental data. The fit to a nine-cycle simulation, with similar log A, E_a, and width values to those in the above example, is shown in Figure 4.23a.

The near-perfect agreement obtained for the simulation, though indeed welcome, was at first surprising. A basic approximation in the distribution-slicing method, illustrated in Figure 4.24, is that the kinetic resolution may be assumed to be perfect. In other words, the slices are assumed to be vertical. In reality, this is never the case: some slower sites decay and some faster sites remain. However, these perturbations largely cancel each other, allowing for a much higher apparent resolution.

The reason the simulation in Figure 4.23a fits the model as well as it does was alluded to earlier: the width of the distribution is large compared to the kinetic resolution. To demonstrate this, an identical simulation to the previous one, except that the width has been reduced to 0.1 kcal/mol, is displayed in Figure 4.23b. The much worse agreement in this simulation can be identically obtained by instead increasing the E_a by a factor of 5, to 7.5 kcal/mol. Recalling the relationship between the E_a and $\ln(k/k_0)$ scales (eq. 4.9) makes apparent the fact that <u>both</u> of the above operations decrease the distribution width on the

a.

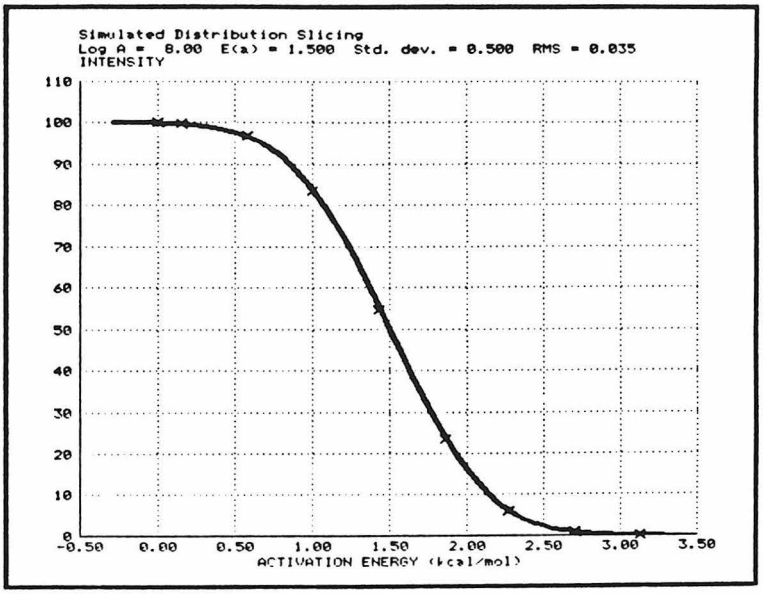

b.

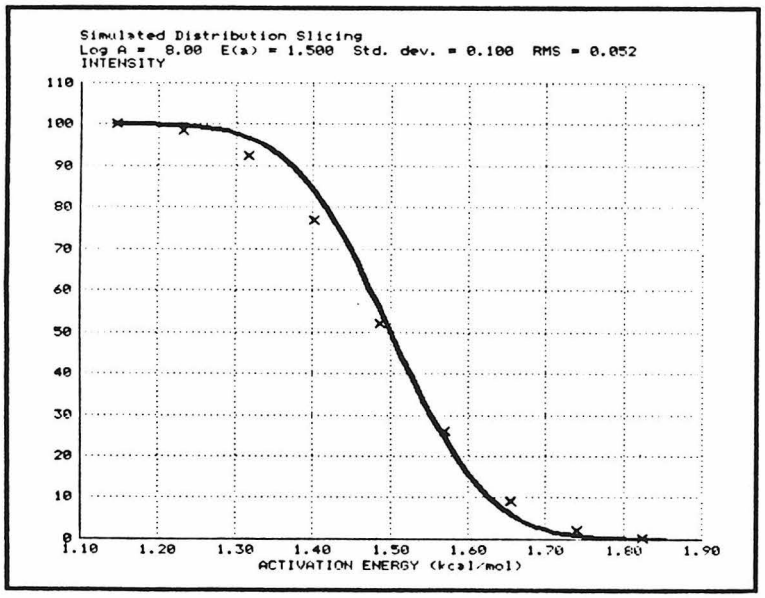

Figure 4.23. DSFIT.BAS fit to simulated distribution-slicing data, obtained from SLICE.BAS: a) wide distribution and b) narrow distribution.

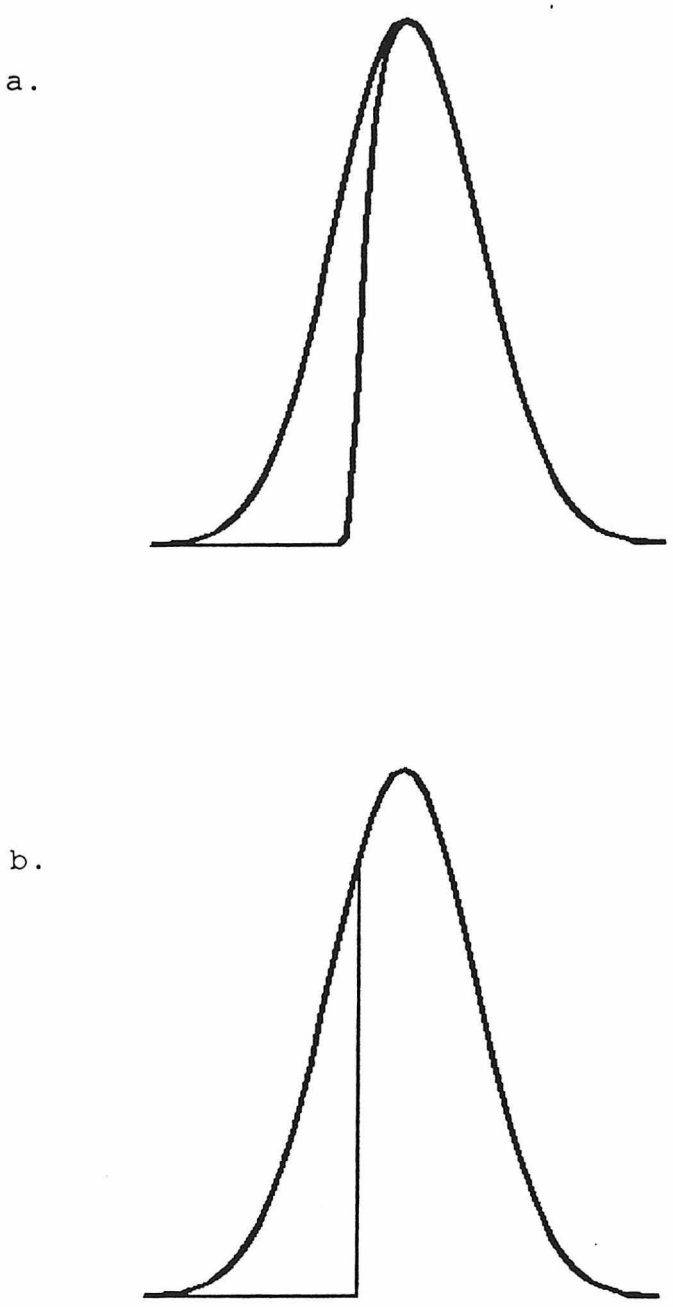

Figure 4.24. Basic approximation in the distribution-slicing method. a) Realistic distribution slice. b) Approximated, vertical slice.

$\ln(k/k_0)$ scale, the latter one by increasing the temperature of the reaction.

The above exercise illustrates the stringent limitations on the effective application of this method. As shown by the simulations in Figures 4.23a and b, the total width of the E_a distribution must be large relative to the most-probable E_a to insure good resolution. In other words, the distribution must extend nearly to zero on the E_a axis. However, if it reaches too close to zero (or past zero), then generation of an intact distribution becomes impossible, also complicating the analysis.

A further consideration is the range of distribution widths that might be attainable. Considering the nonbonding, steric nature of the interactions that presumably cause the distribution, the observation of E_a distributions with standard deviations much larger than 0.5 kcal/mol seems unlikely. Therefore, the reactions for which distribution slicing may be used effectively may be limited to those with E_a in the range 1-5 kcal/mol.[30] We are apparently fortunate enough to have chosen a reaction whose E_a falls in the optimum range.

Combination of Methods

The complementary nature of the decay-trace fitting and distribution-slicing procedures makes combination of the methods quite advantageous. As indicated previously, the strength of automatic intensity normalization in

distribution slicing can be used to solve the normalization problem of the decay traces. Conversely, the distribution-slicing weakness of low information density (being a point-by-point method) can be compensated by the high information-density (continuous curve) decay traces.

The combined method that we have developed is purely a merged analysis; no modifications are necessary in the recording of data. Since the shape of the distribution is defined through the slicing experiments alone, the goals of the combined analysis are the determination of log A, the most-probable E_a (E_0), and the distribution width (σ).

In general, the combined procedure consists of the following steps: (1) intensity normalization of the decay traces using the distribution-slicing data, (2) fitting of the distribution-slicing data using DSFIT to provide E_0 and σ for a given log A, (3) fitting of the normalized decay traces using FIT and σ as the width, and (4) plotting the resulting most-probable rates on an Arrhenius plot, giving log A and E_0, which can be compared with the distribution-slicing results. The choice of log A in step 2 can be guided by any available information, or several values can be used for comparison.

The first step in the analysis is the normalization of the decay traces. Two methods are actually available for this task using the distribution-slicing data. The first procedure, which we call the direct method, involves scaling

each decay trace to a corresponding warming cycle, both involving the same temperature. If exact matches are not available, the scaling can be done by interpolation (see Experimental Section).

The second normalization procedure involves prior fitting of the distribution-slicing data to a Gaussian using DSFIT. Since each point on a decay trace corresponds to a particular E_a-value, according to equation 4.14, the decay trace can be scaled to the distribution-slicing fit using any point on the trace. This type of normalization was accomplished using a program called MERGE.BAS, which scales using the end of each trace and is listed in Appendix E. This program performs the scaling as described above and also allows plotting of the decay traces, using the distribution-slicing format, intensity vs. E_a. If desired, MERGE will create a single graphics file containing all of the normalized traces. As an example, the eight traces for **46-Vin** in MTHF are plotted in Figure 4.25, assuming log A = 8.

The two normalization procedures have an important difference in that the latter requires assumption of a log A value, while the former does not. This difference represents a potential means of determining the actual log A value. Thus, if the scaling, as performed by MERGE, depends strongly upon the choice of log A, then the best choice could be found by comparing the scaling results with those from the direct method.

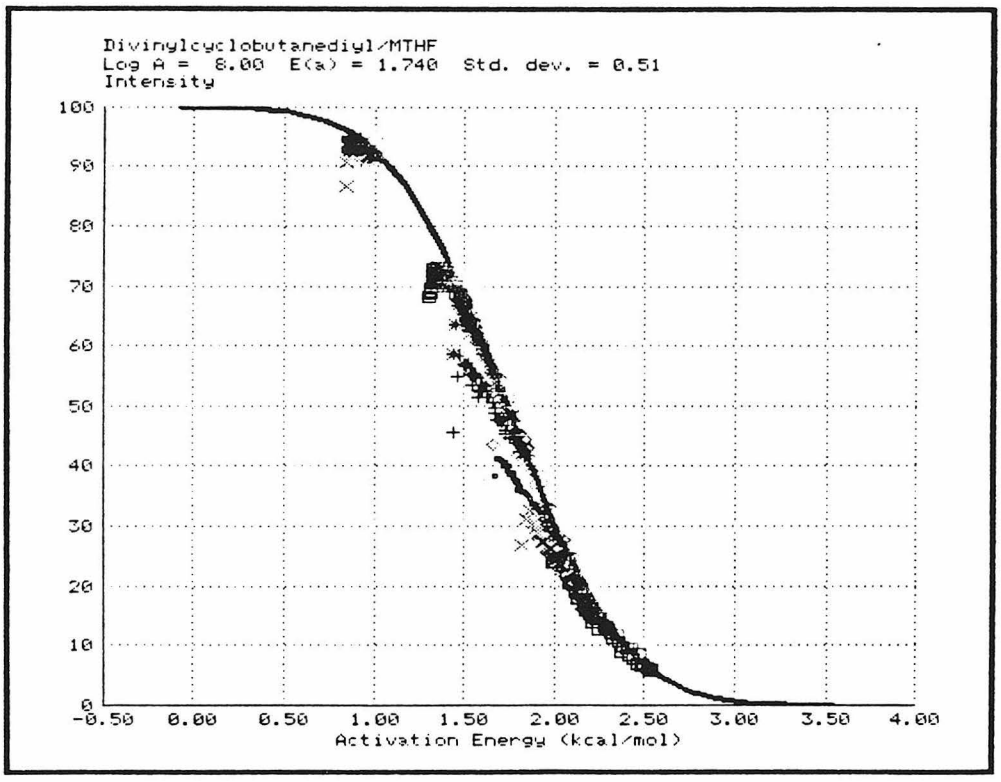

Figure 4.25. Decay traces for **46-Vin** in MTHF plotted in the intensity vs. E_a format of a distribution-slicing experiment. The discrepancies near the beginning of each trace are due to matrix warming during photolysis.

When applied to the **46**-Vin/MTHF data, this dual normalization procedure did allow a log A determination. Table 4.3 lists the scaling results from the direct method and the log A-dependent method for five values of log A. The scaling results from the latter method do, in general, show a strong dependence on log A. The log A preference of each decay trace was thus determined by interpolation, and these results are also listed in the table. Five of the eight traces show a clear preference in the log A range from 6-10, the average being 7.5 ± 0.7 (one standard deviation). One of the remaining traces (20.2 K) gave a normalization which was in satisfactory agreement for all log A values in the range. The two highest temperature traces seemed to prefer higher log A values. We reasoned that this result might reflect larger experimental errors (especially in the distribution-slicing data, see above) at higher temperatures. We therefore discarded these points, taking 7.5 as the approximate log A.

Qualitative support for a log A in this range can be obtained through merged decay-trace plots such as the one for log A = 8 in Figure 4.25. For comparison, merged plots of the same traces are shown in Figure 4.26 for log A = 5 and 14. The agreement for log A = 5 is much poorer than in Figure 4.25, suggesting that the actual log A value lies closer to 8. The minor discrepancies for log A = 8 can be attributed to matrix heating during photolysis, but the

Table 4.3. Log A Determination for **46-Vin** via Comparison of Normalization Results

Decay Trace	YMAX(%)[a]	YMAX(%) from MERGE using log A =					
Temp.(K)	Direct	6	7	8	9	10	log A
20.2	86.8	85.2	85.7	86.1	86.6	86.3	-
30.6	66.6	65.1	66.8	67.7	68.6	68.3	7.0
34.5	57.7	53.7	57.1	58.9	60.3	60.8	7.6
36.7	44.4	42.2	44.8	46.0	46.8	47.1	6.8
39.8	39.8	33.8	37.4	39.1	40.3	41.2	8.6
42.5	43.9	39.2	43.2	44.7	45.5	46.5	7.5
44.9	33.9	22.8	26.5	28.1	29.0	30.4	-
49.2	27.7	19.8	24.1	26.1	26.9	28.9	-

[a]YMAX is the intensity of the decay trace at the end of the photolysis interval.

a.

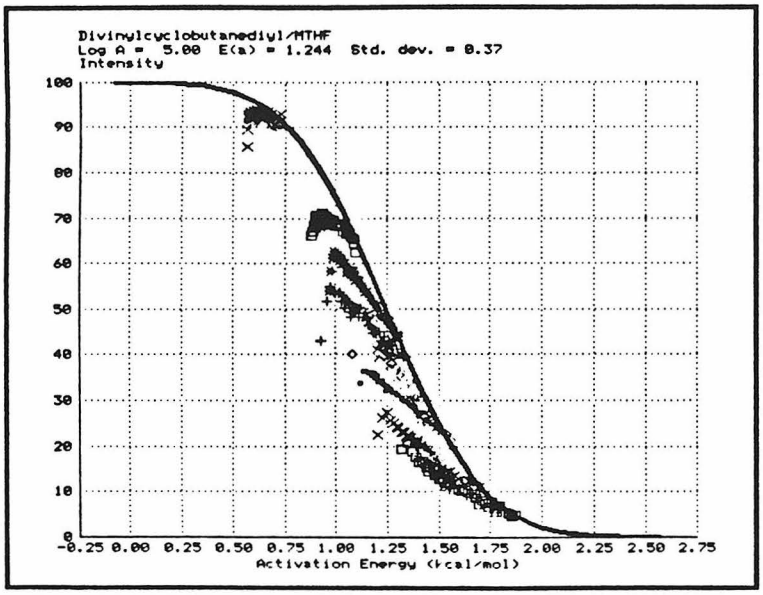

b.

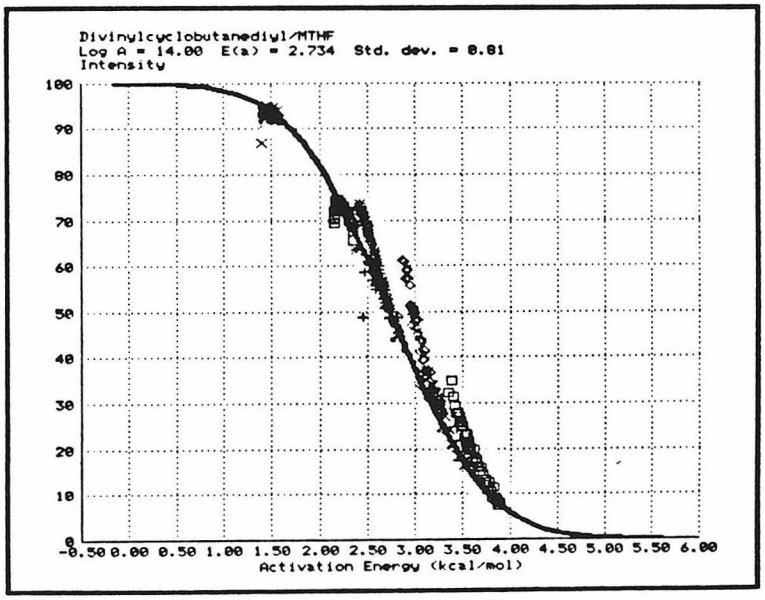

Figure 4.26. Merged decay traces for **46-Vin** in MTHF assuming a) log A = 5 and b) log A = 14.

discrepancies for log A = 14 are in the wrong direction to be explained in this manner.

Having normalized the decay traces (using the direct method), we next fitted them to simulated decay using FIT. Previously, we determined the distribution widths by optimizing the width and computing the mean. This procedure was fairly arbitrary due to the width-insensitivity of the fits and the photolysis-heating effect, which introduces substantial errors in the optimum width. Therefore, we used the distribution-slicing data to obtain the width. Using log A = 7.5, DSFIT gives E_a = 1.665 kcal/mol and σ = 0.488 kcal/mol (see Figure 4.27). This procedure for determining the width has the disadvantage of indirectly introducing a log A assumption into the fitting, but having obtained an approximate log A, we did not consider this to be a large problem.

With both the intensity and the width predetermined, the decay-trace fitting becomes a one-dimensional optimization over rate. The decay-trace fits using the direct normalization scheme are displayed in Figure 4.28, and the Arrhenius plot using the most probable rates is shown in Figure 4.29. The activation parameters from the Arrhenius plot, log A = 7.39 and E_0 = 1.67, agree closely with the distribution-slicing parameters (Figure 4.27); however, this agreement is somewhat artificial, since the same width was used for the two analyses. When we repeated the fitting procedure using widths obtained from different log A

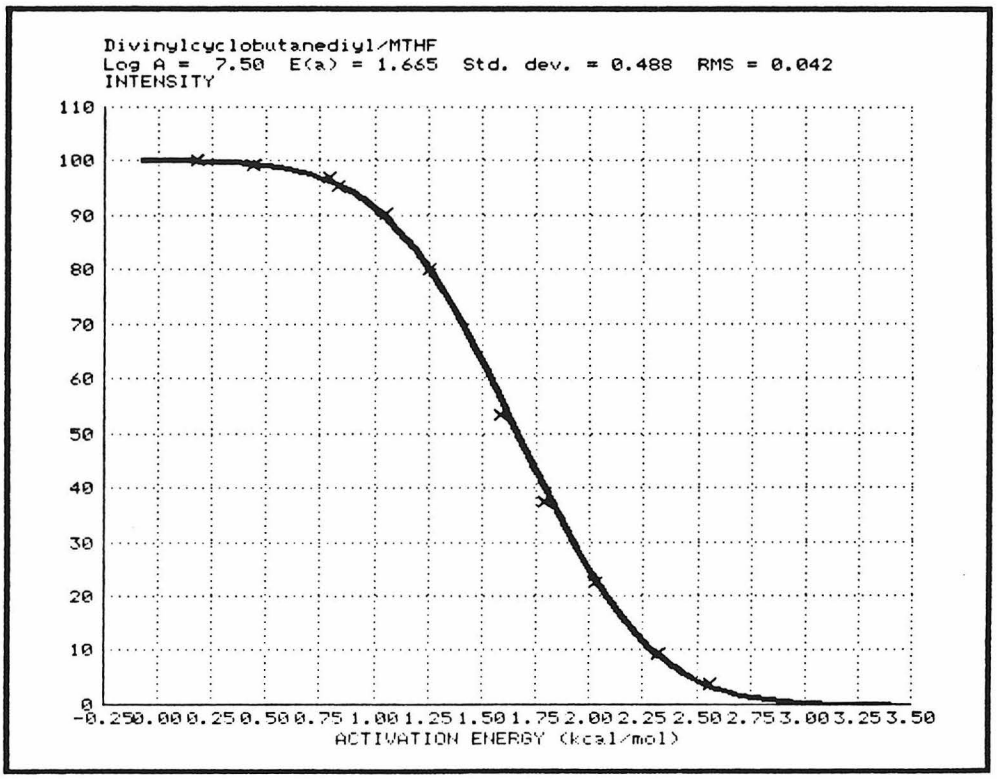

Figure 4.27. Distribution-slicing intensity vs. Ea plot for **46-Vin** in MTHF, using the approximate log A value of 7.5.

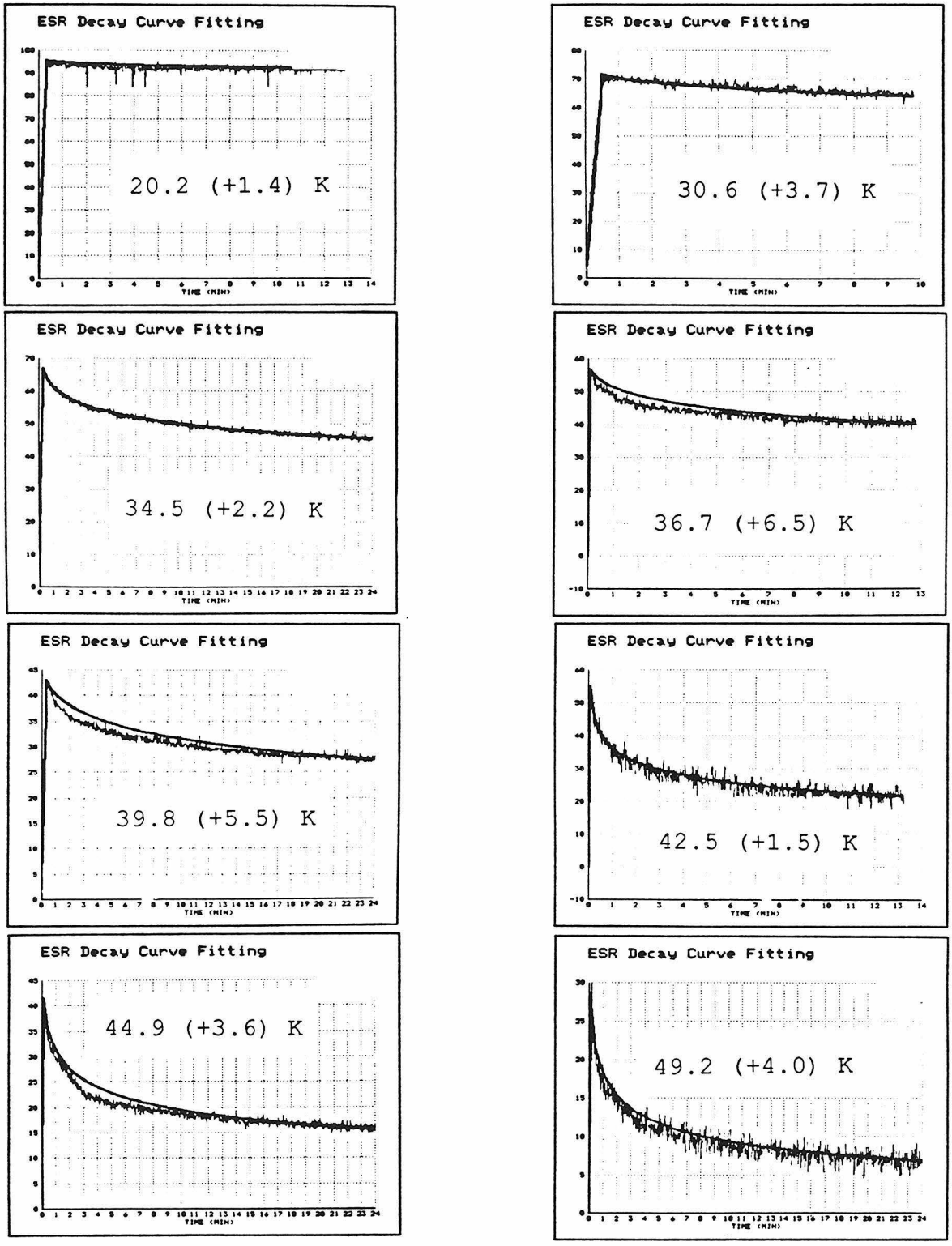

Figure 4.28. Gaussian-distribution fits to decay traces for **46-Vin** in MTHF from FIT.BAS. Intensities were normalized by the direct method.

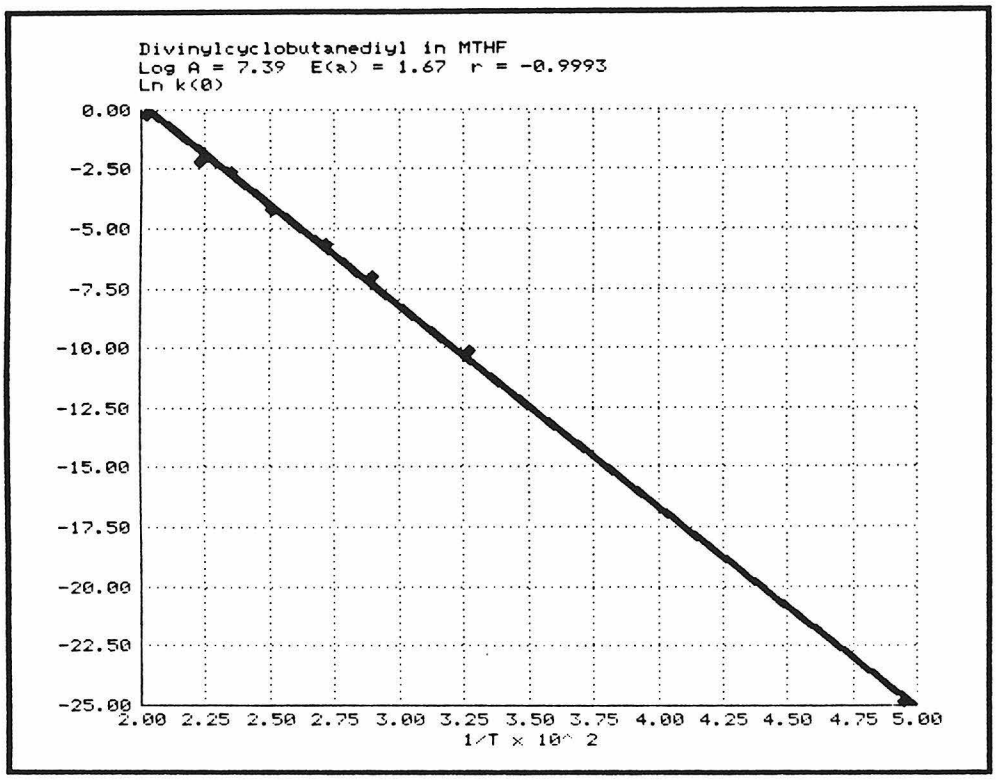

Figure 4.29. Arrhenius plot for **46-Vin** in MTHF using the most probable rate contants from Figure 4.28.

distribution-slicing fits, the parameters more closely matched the new distribution-slicing parameters. Although the match cannot be taken as support for the absolute activation parameters, it does show that the results from the two experiments are consistent with each other. This tracking of Arrhenius parameters was more severe for the log A-dependent normalization scheme, since both the width and intensities were matched before the decay-trace fitting. For this reason, we report here only fittings using the direct normalization.

Heating due to photolysis was optimized in the fitting after the rate optimization. The value during the rate optimization was usually taken to be zero, unless the heating effect was strong enough to influence the optimized rate, in which case a near-optimum heating amount was used. The temperature increases during photolysis, shown with the fits in Figure 4.28, vary randomly from 1.4 to 6.5 K. Given our earlier estimate of 1-2 K for the heating effect, these results seem too large. A likely possibility is that errors from other sources, such as temperature, width, and intensity normalization, may be funneled into the heating optimization, since it is the last operation.

Kinetic data were also analyzed for **46-Vin** in heptane in order to help determine the role of the matrix material in biradical stability. A distribution-slicing fit to a Gaussian using log A = 7.5 is shown in Figure 4.30. The agreement is quite good, and the E_0 of 1.43 kcal/mol

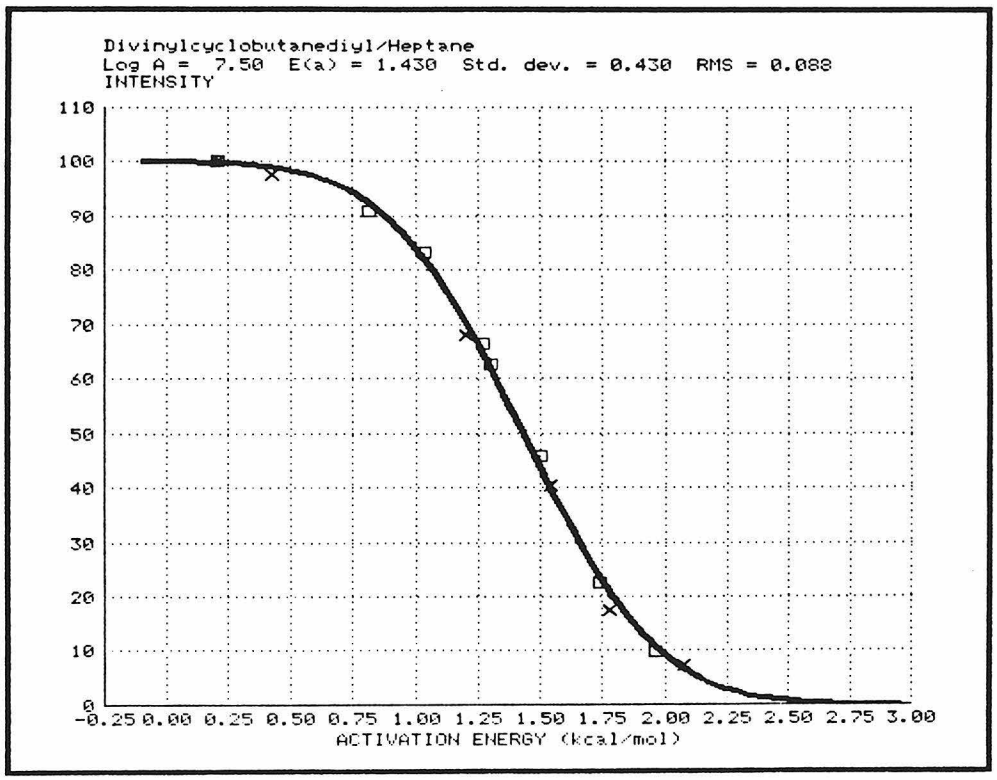

Figure 4.30. Distribution-slicing experiment for **46-Vin** in heptane. The different markers represent different experiments. Log A was assumed to be 7.5.

suggests that **46-Vin** is slightly less stable in heptane compared to MTHF (1.67 kcal/mol).

Determination of log A via dual normalization was unsuccessful for the heptane data. The scalings obtained from MERGE were not strongly dependent upon log A, and they did not even vary smoothly with log A. The reason behind this behavior has not been determined, though it may be related to a stronger photolytic heating in heptane (see below). The same value as for MTHF, log A = 7.5, was thus used in the fitting analysis.

The decay-trace fits for **46-Vin** in heptane are shown in Figure 4.31 and the resulting Arrhenius plot in Figure 4.32. Once again, the activation parameters, log A = 7.30 and E_0 = 1.44 kcal/mol, match closely with the distribution-slicing experiment, log A = 7.50 and E_0 = 1.43 kcal/mol. The photolytic heating effect appears even larger than in the MTHF data, but whether this represents a true increase in heating or in errors from other sources remains unclear. The heating effect at 3.8 K in heptane was sometimes as large as 5 K (increasing to 9 K, as determined using eq. 4.11), suggesting that the heating effect in this solvent might also be stronger at higher temperatures.[31]

The combined method was applied also to **46-EV** in MTHF. However, the distribution-slicing fit (Figure 4.33) was not as good as for the **46-Vin** plots, making the errors in the dual-normalization log A determination too large to allow its use. Therefore, log A was taken to be 7.5 for

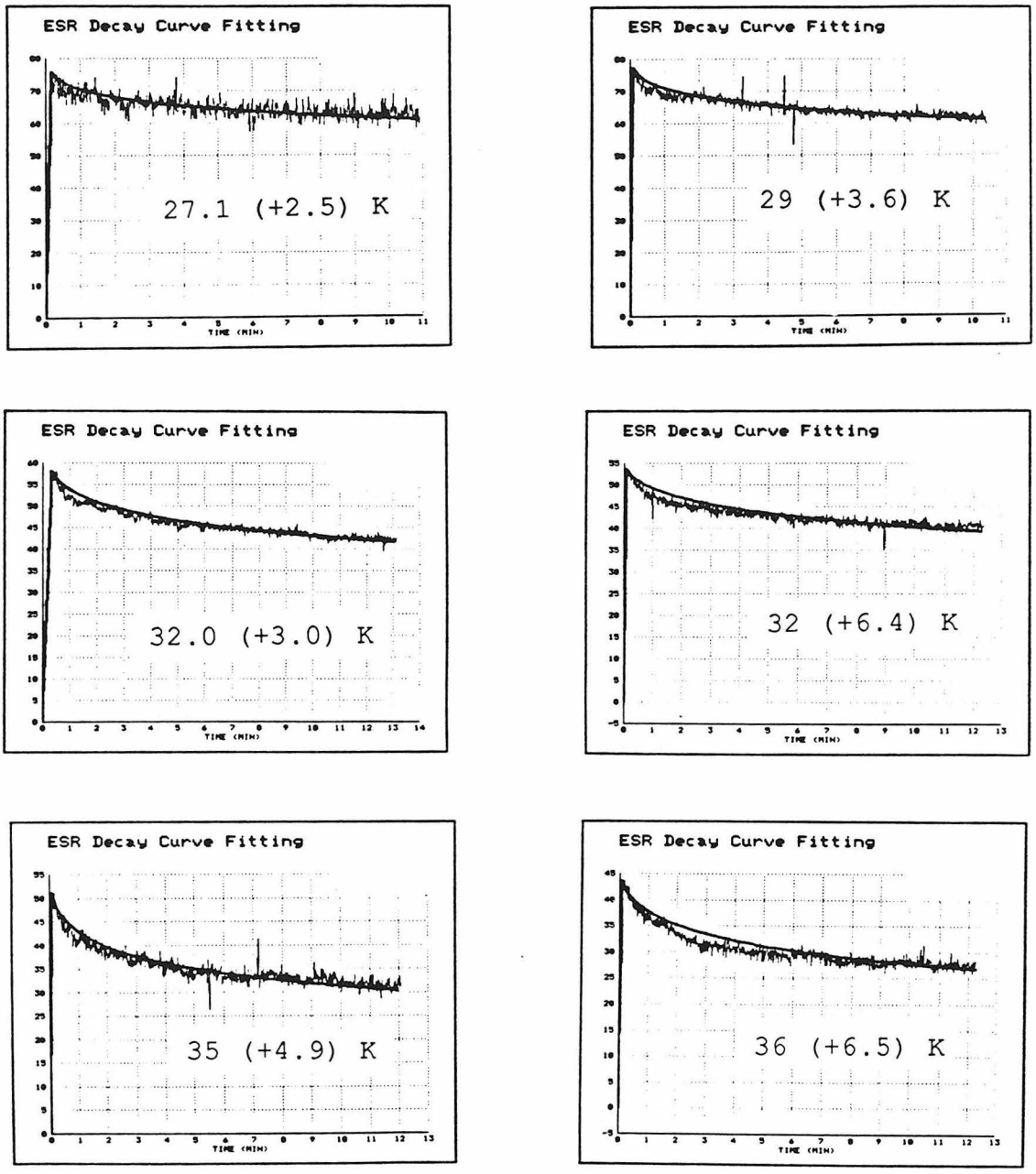

Figure 4.31. Gaussian-distribution fits (from FIT.BAS) to decay traces for **46-Vin** in heptane using direct normalization.

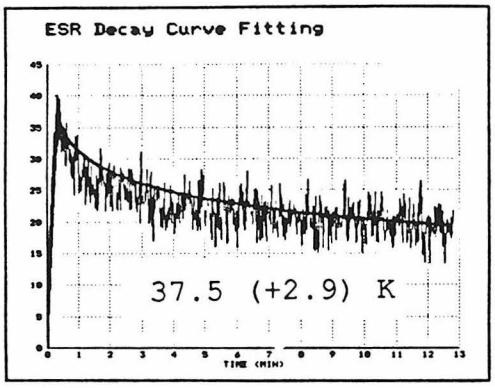

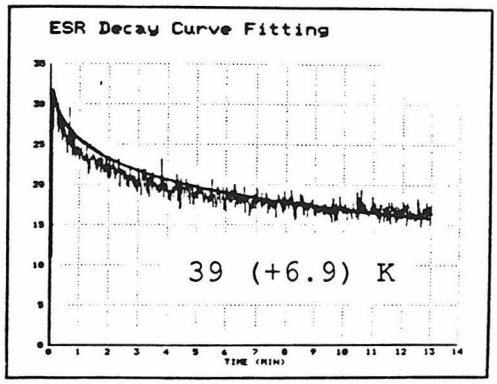

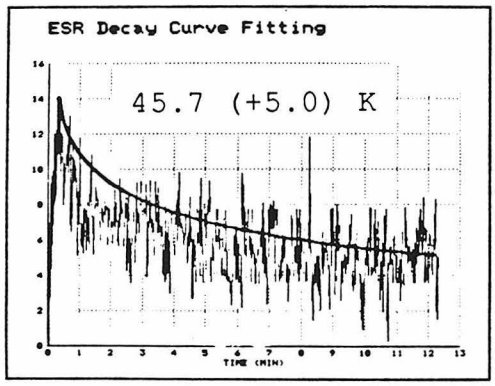

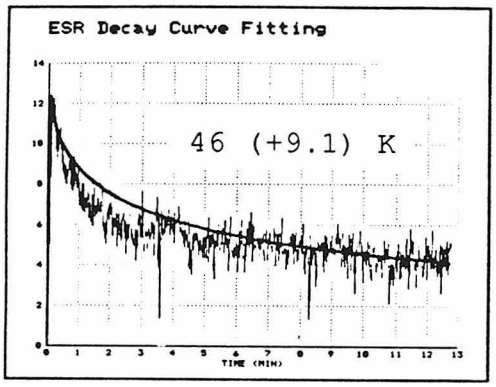

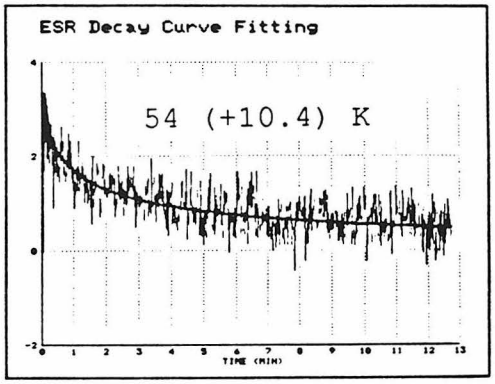

Figure 4.31 (cont.). Gaussian-distribution fits (from FIT.BAS) to decay traces for **46-Vin** in heptane using direct normalization.

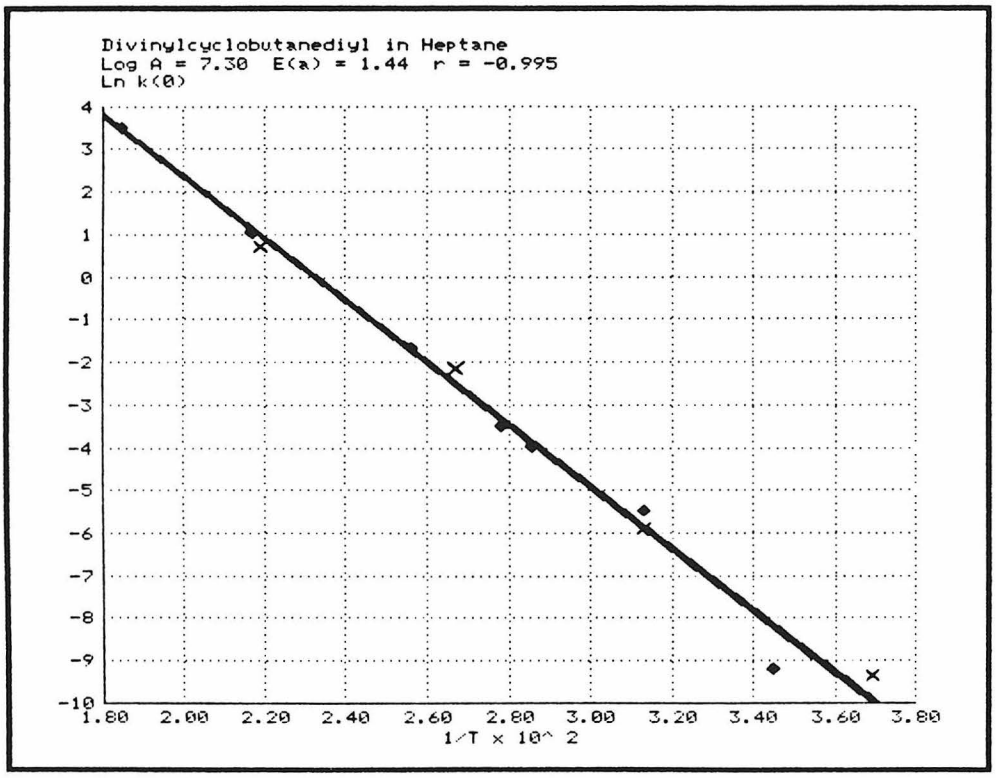

Figure 4.32. Arrhenius plot for decay of **46-Vin** in heptane, based on a Gaussian distribution and using direct normalization.

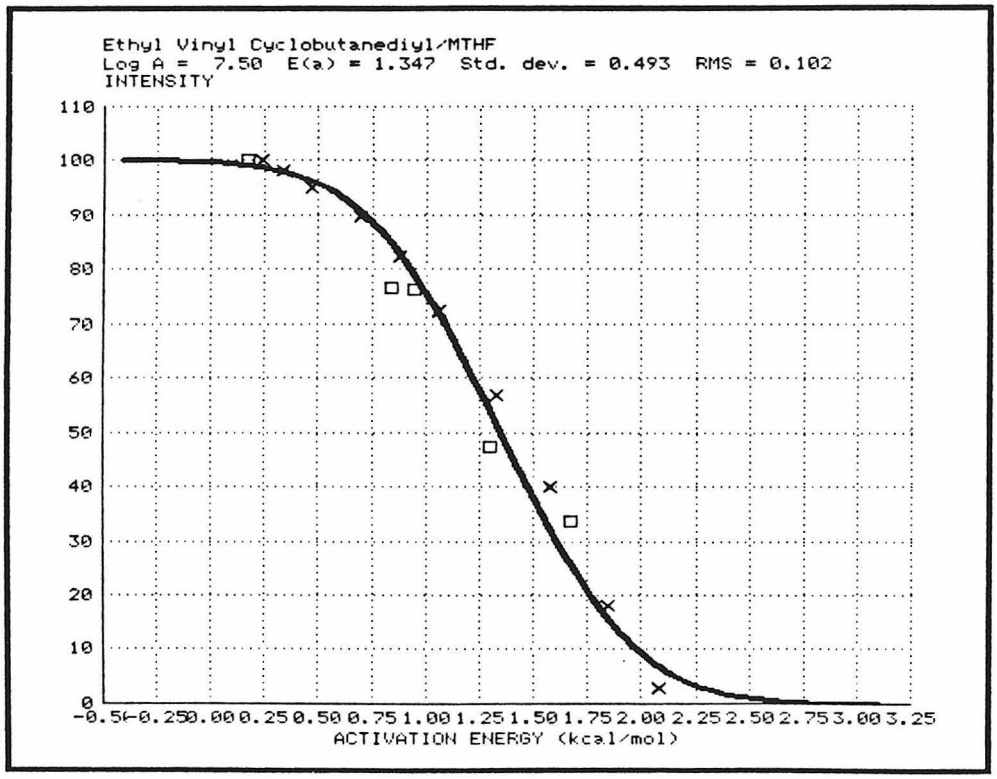

Figure 4.33. Distribution-slicing results for **46-EV** in MTHF, assuming log A = 7.5.

these data also. The distribution-slicing experiment suggests that **46-EV** (E_0 = 1.35 kcal/mol) is somewhat less stable than **46-Vin** (E_0 1.67 kcal/mol).

The decay-trace fits are shown in Figure 4.34 and the Arrhenius plot in Figure 4.35. In spite of good fits to all the traces and low photolytic heating, the Arrhenius plot shows a relatively poor correlation. This is apparently due to errors in the normalization, since the fitting of the traces scaled using MERGE gave a correlation coefficient of -0.9998 for the Arrhenius plot.

Unfortunately, inefficient photochemical generation prevented the recording of decay traces for **46-EV** in heptane; however, several distribution-slicing experiments were done. The results, shown in Figure 4.36, imply a much larger solvent effect than was observed for **46-Vin** in MTHF and heptane. The curve for **46-EV** could not be fit with the assumption of an intact Gaussian distribution at 3.8 K, as was done for all the previous data. However, very good agreement was obtained by allowing about 10% decay at the lowest temperature. The result is E_0 = 0.90 kcal/mol (with log A = 7.5), substantially lower than E_0 = 1.35 kcal.mol, obtained for MTHF.

We also investigated the stability of **46-Vin** in deuteriochloroform, using the distribution-slicing technique. The results, shown in Figure 4.37, indicate that the biradical is significantly less stable in this matrix than in MTHF or heptane, showing E_0 = 1.20 for

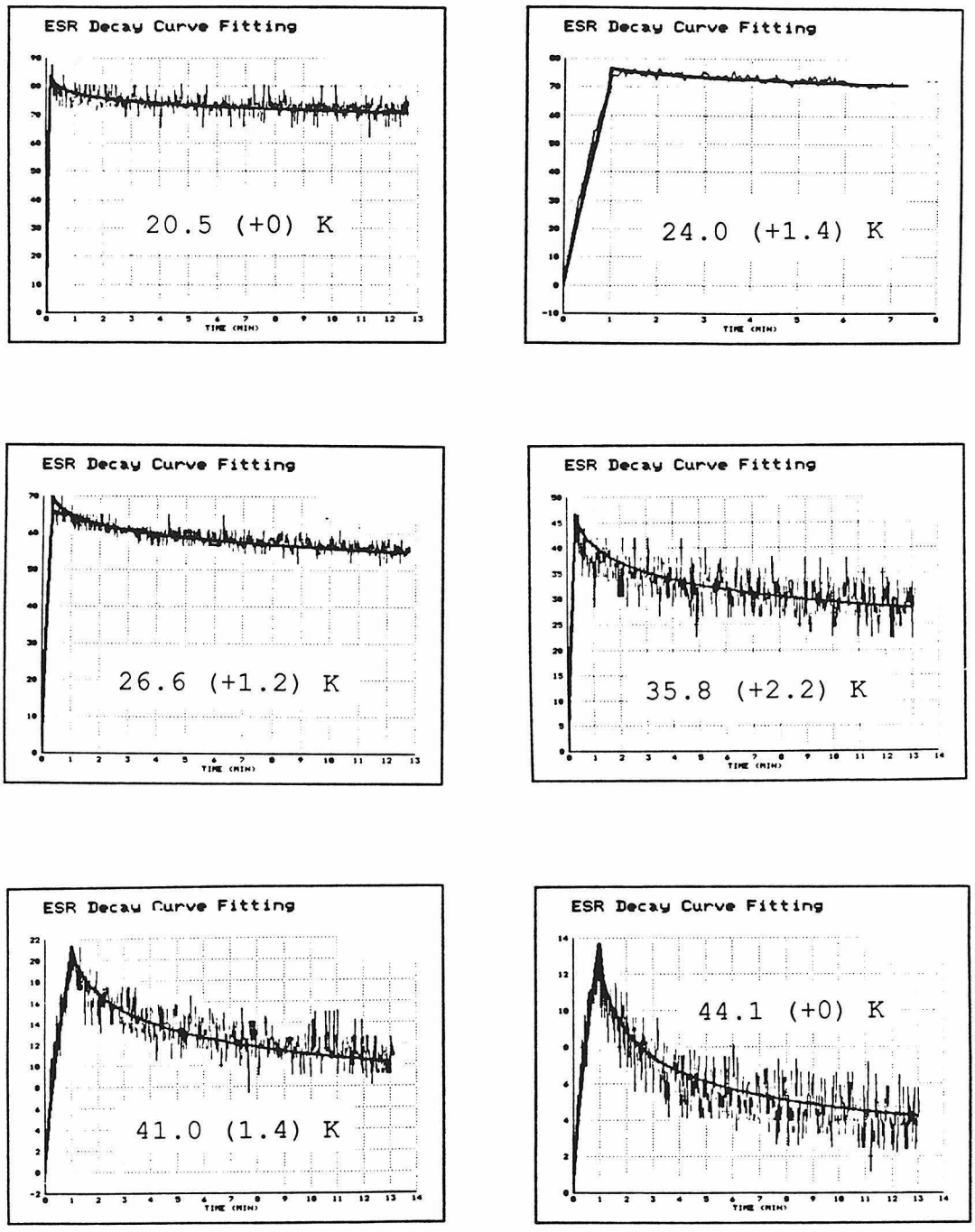

Figure 4.34. Gaussian-distribution fits (from FIT.BAS) to decay traces for **46-EV** in MTHF using direct normalization.

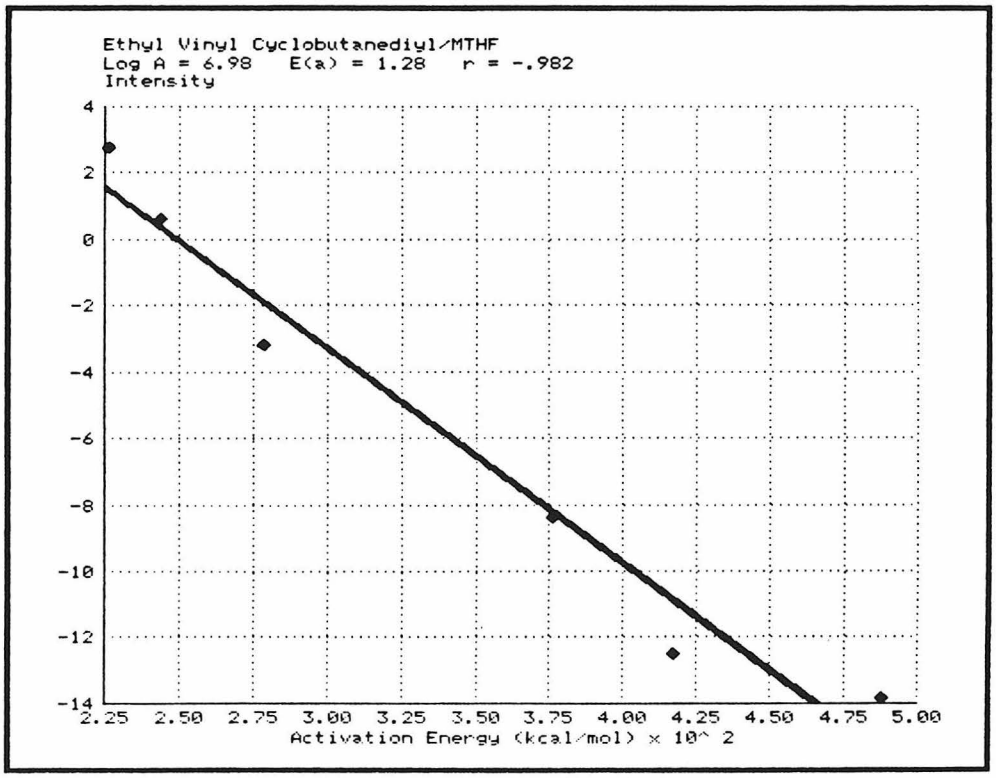

Figure 4.35. Arrhenius plot for decay of **46-EV** in MTHF, using the most probable rate constants from Figure 4.34.

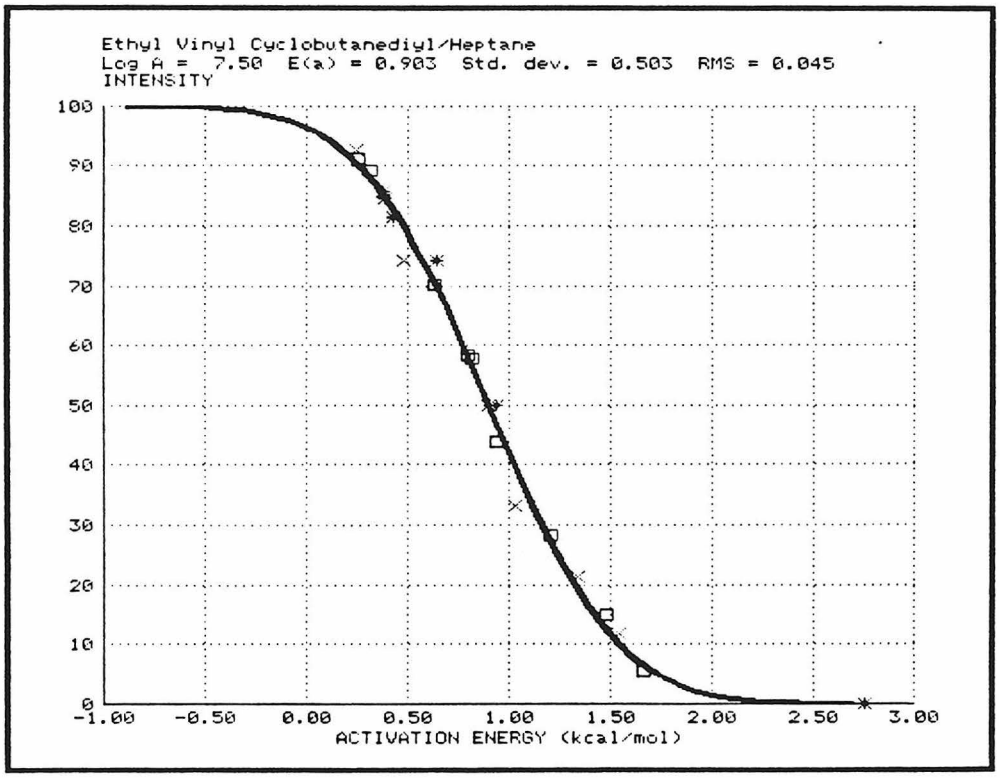

Figure 4.36. Distribution-slicing results for **46-EV** in heptane, assuming log A = 7.5.

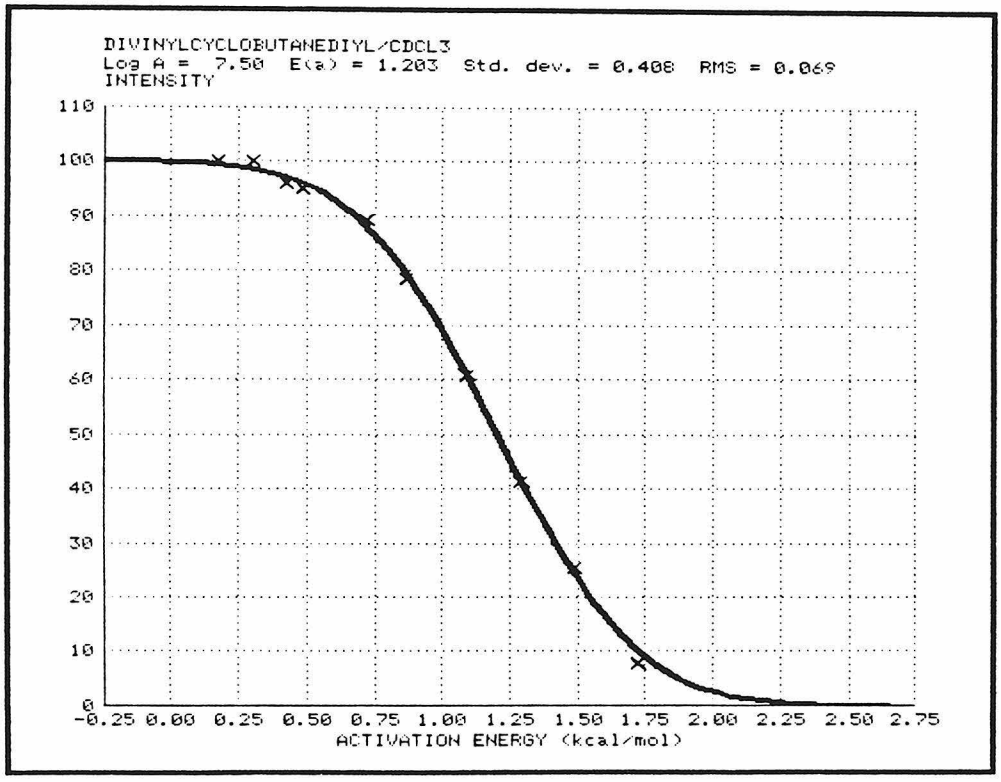

Figure 4.37. Distribution-slicing results for **46-Vin** in deuteriochloroform, assuming log A = 7.5.

= 7.5. The structural reasons behind these differences is log A = 7.5. The structural reasons behind these differences is not clear, but variations in matrix-site shape and size

In order to show that the probability distribution itself can be obtained from these experiments, the intensity vs. E_a data plotted in Figure 4.37 have been converted into distribution form, and the result is displayed in Figure 4.38. This plot accentuates even more clearly that the distribution is Gaussian in character.

Summary of Results

We have presented a variety of procedures for studying low-temperature matrix kinetics, and have found a combination of distribution-slicing and decay-trace fitting to give the best results. Even though the determination of activation parameters has not been achieved with high precision, the combination of methods allowed discrimination of small reactivity differences between the different biradicals and solvent matrices.

The results for **46-Vin** and **-EV** are summarized in Table 4.4. The approximate log A value for **46-Vin** in MTHF is reported as 7.5 ± 2. These error limits represent more than two standard deviations in the dual-normalization determination of the value, and we believe them to be conservative. Placing error limits upon the most probable E_a is difficult, since the value depends upon log A. However, for a given log A, E_0 can be determined easily

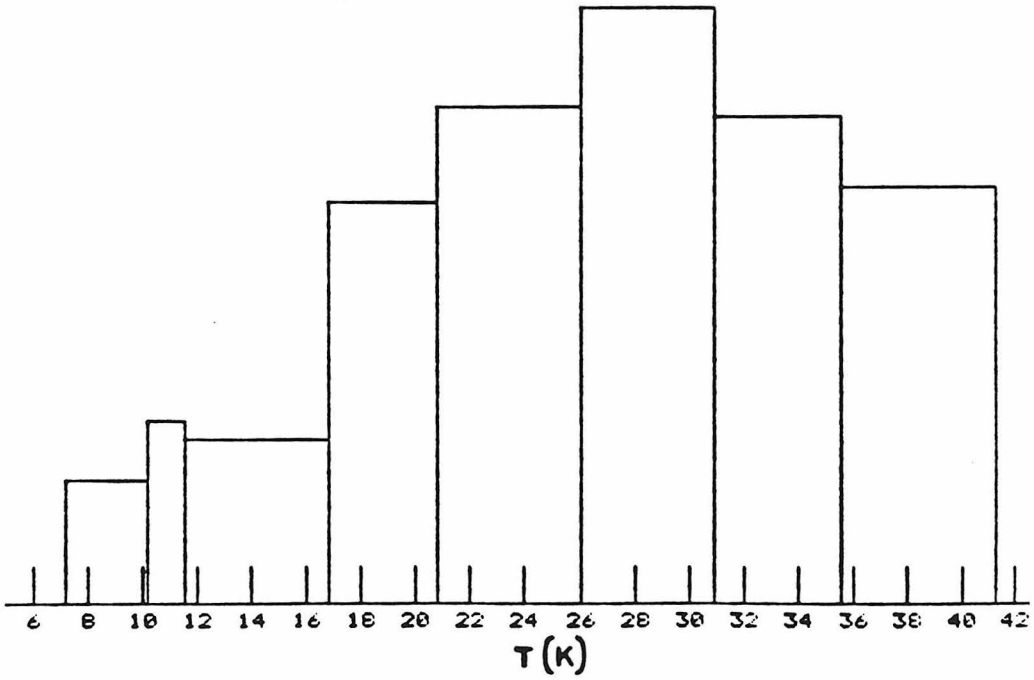

Figure 4.38. Reconstructed distribution for **46-Vin** in deuteriochloroform (plotted over temperature).

Table 4.4. Summary of Kinetic Results

				
	Dist. slicing	Decay fit.	Dist. slicing	Decay fit.
		MTHF		
log A	7.5 ± 2[a]	7.39	7.5[b]	6.98
E_0	1.665	1.67	1.347	1.28
σ	0.488		0.493	
RMS	0.042		0.102	
r		-0.9993		-0.982
		Heptane		
log A	7.5[b]	7.30	7.5[b]	
E_0	1.430	1.44	0.903	
σ	0.430		0.503	
RMS	0.088		0.045	
r		-0.995		
		$CDCl_3$		
log A	7.5[b]			
E_0	1.203			
σ	0.408			
RMS	0.069			

[a]Approximate value obtained via dual-normalization. [b]Assumed value.

within error limits of ±0.1 kcal/mol. Assigning error limits to the assumed log A value for the other results would be rather meaningless; however, we have no reason to suspect significantly different log A values for these reactions.

The approximate log A value is similar to others reported for triplet biradical reactions.[32] Closs reported an approximate log A value of 8 for the closure of **4**[4] and Fisher and Michl reported a value of 5.1 for the 1,2-hydrogen-shift reaction in **68**.[5] A survey of other triplet reactions shows that log A usually falls in the range from 6 to 10.

In order to aid comparisons amongst the results in Table 3.6, the Gaussian-E_a distributions implied by the slicing results have all been plotted on a common graph (Figure 4.39). The first observation is that **46-Vin** is more stable than **46-EV**. The difference in E_0 values is small, though significant, compared to the magnitude of E_0. In fact, in the absence of a distribution, the reactivity of the compounds would be strikingly different, with a relative rate ratio of 3000 at 20 K, assuming the E_0 values from MTHF (or 6×10^5 using the values from heptane). The distribution effect largely equalizes the decay behavior, making determination of even the order of reactivity difficult without analysis of the type described.

An important observation is that the distribution width is very similar for all the data sets (Figure 4.39),

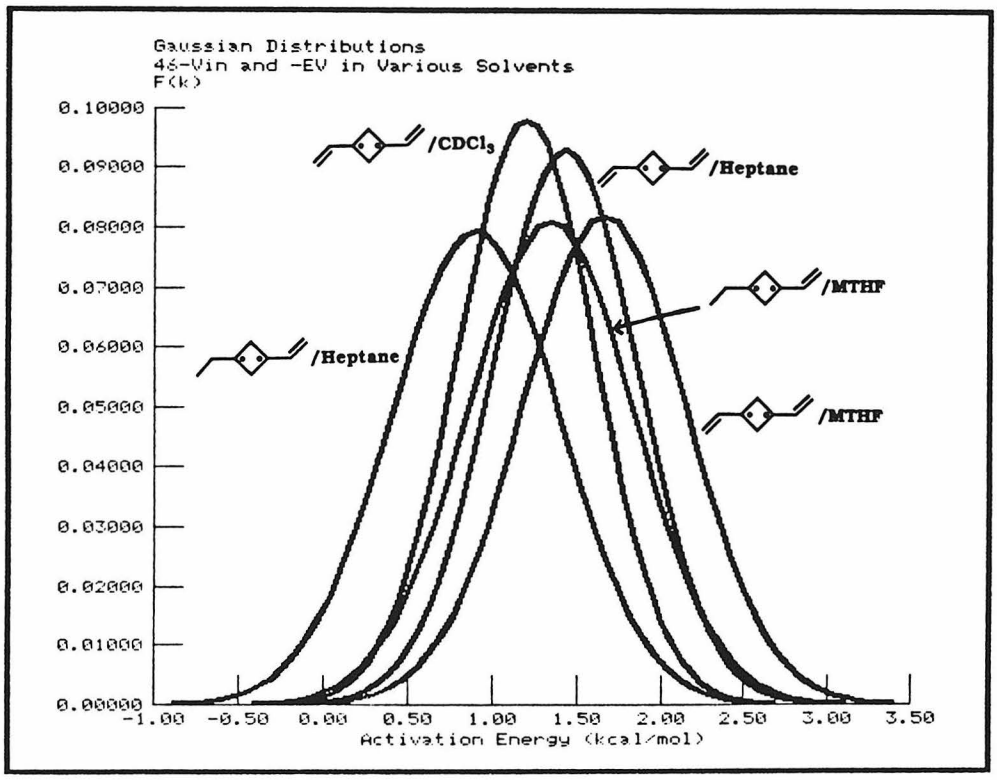

Figure 4.39. Area-normalized Gaussian-E_a distributions for **46-Vin** and **-EV** in various solvents obtained from distribution-slicing experiments. Log A = 7.5 for all the distributions.

varying only from 0.4 to 0.5 kcal/mol. This is consistent with an interpretation in which the most probable E_a depends mainly on the intrinsic reactivity of the biradical, with the distribution width reflecting interactions between the biradical and matrix. However, the biradical-matrix interactions do have some effect on E_0, as shown by the solvent comparisons.

Comparison with results for the dialkyl cyclobutanediyls is also instructive. The main difference between these results is that tunneling (non-Arrhenius) behavior has not been observed in the present study. One rationalization of this difference is that a lower E_0 in the dialkyl species allows tunneling to occur in these biradicals. However, even the fastest sites in **46-Vin** and **-EV**, which have E_a very near zero, are indefinitely stable at 3.8 K. Therefore, this explanation can be eliminated.

Since **46-Et**, **-EV**, and **-Vin** have comparable masses, the differences in their propensities to undergo tunneling are most likely due to changes in barrier width. Interestingly, the hypothetical potential surfaces considered previously (Figure 4.2, redrawn in Figure 4.40) do portray such a change. Thus, biradical stabilization due to delocalization may be expected to increase significantly the barrier width, causing virtual elimination of the tunneling reaction. While such an explanation must be considered speculative at this stage, it is consistent with the kinetic results for all the cyclobutanediyls.

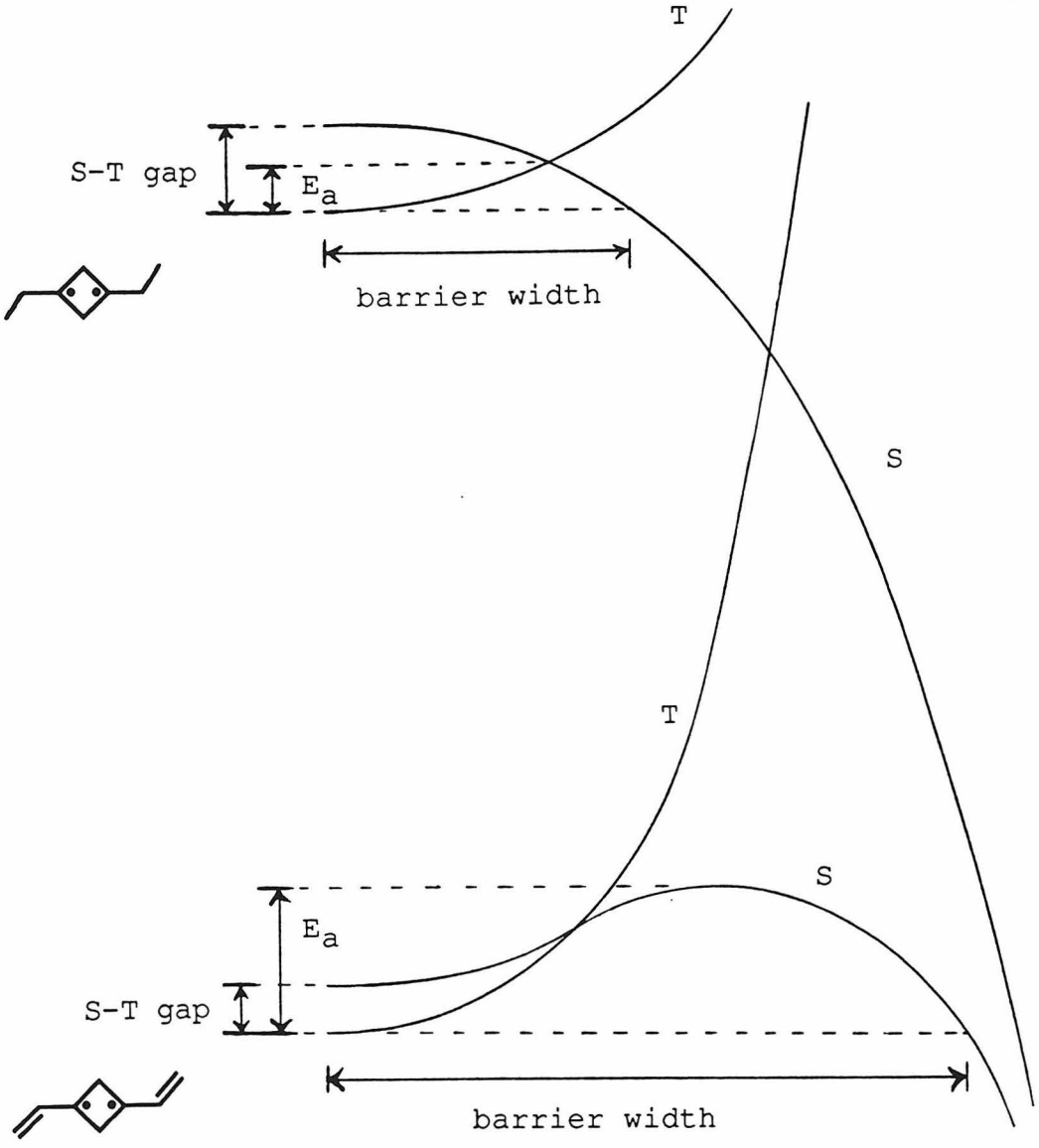

Figure 4.40. Hypothetical potential energy surfaces from Figure 4.2, expanded to show the region near the biradical.

Figure 4.40 also implies the possible generation (or deepening) of a well on the singlet surfaces for **46-Vin** and **-EV**. If the potential surfaces in Figure 4.40 were accurate, the singlet biradicals might be expected to exist in equilibrium with the triplets. This possibility suggests that the singlet biradicals might be observable under appropriate conditions.

EXPERIMENTAL SECTION

General. See Chapter 3 for instruments used.

A. Decay-Trace Fitting.

The sample preparation and EPR instrumentation used for the decay traces have been described in Chapter 3. Decay traces were recorded by first equilibrating to the desired temperature, which was determined by calibration immediately before and/or after the trace. With the spectrometer on time-drive and set to the field of the largest transition (3000 G for **46-Vin**; 2840 G for **46-EV**), a signal was generated by photolysis through a combination of three Schott Filters: WG-305, KG-5, and UG-11. Photolysis intervals were controlled by using a Vincent Associates Model SD-10 timed shutter and kept only as long as necessary to generate a reasonably sized signal. Baseline measurements at an off-resonance field were recorded before the generation and after the decay as part of the trace to allow later correction for any observed drift. The traces were digitized and stored on disk as collected using a Compaq Plus computer and a data collection program called EPR.FOR.[32] Each data file contained 1000 intensity measurements and a sample file is listed in Appendix F. Decay traces were normally recorded at nonsaturating microwave power, but higher power was sometimes used to allow shorter photolyses. No difference was distinguishable between saturated and nonsaturated traces, and the two types were fitted equally well in the

analysis.

Before data files could be used with the fitting program, several modifications were necessary. The point numbers (1 to 1000) corresponding to six events were inserted into line 69 of the file. The six values were: IX1, the last point of the initial baseline measurement; IX2, the last point before the start of photolysis; IX3, the last point of photolysis; IX4, the last point of the decay; IX5, the first point of the initial baseline (usually 0 or 1, indicating the beginning of the file); and IX6, the last point of the final baseline (usually 0 or 1000, indicating the end of the file). The temperature of the trace, the photolysis interval (s), and the scan time (min) were also inserted. In addition, any obvious noise spikes were removed.

The use of FIT.BAS is described in its documentation (Appendix B) and in the Chapter Text. In general, rate optimizations were done using the option based upon the end of the decay trace.

Normalization of Decay Traces. The decay traces were intensity-normalized by using four different methods, as described in text. The first two schemes involved correction for experimental variables and were based upon the following definition:

$$I'' = \frac{T \cdot \text{Intensity}(\Delta m_S=2,\ \text{peak-peak},\ \text{mm}) \cdot 10^4}{\text{hv interval(s)} \cdot \text{Gain} \cdot (\text{Power},\ \text{mW})^{0.5}}, \qquad (4.15)$$

where I" is the normalized intensity. In the first method, I" for each decay-trace maximum was calculated directly from equation 4.15. In the second method, I" was calculated for a spectrum taken at 3.8 K immediately following the trace. I" at the end of the decay was assumed to be equivalent to this value, and the entire trace was scaled accordingly. In both methods, the intensity relative to the intensity of an intact distribution was calculated by dividing I" by the I" from a signal generated at 3.8 K. This intensity ratio for IX3, reported as a percentage, was termed YMAX. YMAX is the intensity input requested by FIT.BAS.

The third normalization scheme has been termed the direct method and required a set of distribution-slicing data. If the temperature of a given decay trace matched that of one of the slices, normalization was performed by scaling the intensity of the point on the decay trace corresponding to the warming time interval to match the intensity after the warming cycle. Whenever a decay trace was directly compared to a slicing experiment such as this, the time axis of the trace was redefined so that t=0 corresponded to the midpoint of the photolysis interval, since the biradical, on average, was generated at this point.

If no match was available in the distribution-slicing data, then the two surrounding slices were interpolated to obtain the desired intensity. In order to interpolate properly on the temperature axis, however, the warming times

had to be the same. To achieve this, one of the slices was scaled so as to match the other's warming interval, using a decay trace recorded at approximately the same temperature. Interpolation over temperature then gave an intensity to which the decay trace was scaled. If the temperature of a decay trace was outside the range of the distribution-slicing data, then normalization of that trace was done by using the next method.

The final scaling procedure was performed by using MERGE.BAS (Appendix E). The use of this program is described in the text and in its documentation.

B. Distribution Slicing

Collection of data. A strong triplet signal was generated at 3.8 K by prolonged photolysis (20 s to 12 min). The intensity was measured continuously (to best keep track of the warming intervals) with occasional reference to an off-resonance baseline. Warming of the matrix was accomplished either by restricting helium flow or by using the heater and automatic temperature control. In either case, equilibration was completed as quickly as possible without overshooting the desired temperature. Calibration of temperature was generally done before and after the experiment, the experimental temperatures being determined by interpolation of the available calibration points. The intensity after each slice was obtained by re-equilibrating to 3.8 K.

Theory. The theory behind the distribution-slicing method has largely been discussed in text. Here we will consider the basic approximations of the method and their implications for experimental design.

The center of a given slice (see Figure 4.18) can be defined as the point in the distribution that experiences 50% decay during the warming interval, t, at temperature T. Assumption of exponential decay for each point in the distribution implies:

$$e^{-kt} = 0.5, \tag{4.16}$$

where k is the rate constant corresponding to the center of the slice. Taking the logarithm of both sides in eq. 4.16 gives:

$$kt = \ln 2. \tag{4.17}$$

Substitution for k using the Arrhenius equation (eq. 4.7) gives:

$$Ate^{-E_a/RT} = \ln 2, \tag{4.18}$$

which can be solved for E_a:

$$E_a = -RT \ln [(\ln 2)/At]. \tag{4.19}$$

This equation, identical to equation 4.14, allows direct calculation of E_a from the experimental parameters, assuming a constant A-value.

Consider the second slice in a distribution slicing experiment. Since the distribution is not intact at the beginning of the cycle, rigorous treatment of this slice must account also for the first slice. By analogy to equation 4.16,

$$e^{-k_1 t_1} \cdot e^{-k_2 t_2} = 0.5, \tag{4.20}$$

where k_1 and k_2 are defined by equations 4.21 and 4.22.

$$k_1 = Ae^{-E_a/RT_1} \tag{4.21}$$

$$k_2 = Ae^{-E_a/RT_2} \tag{4.22}$$

The subscripts of 1 and 2 for k,t, and T refer to the first or second slice. Thus, the center of the second slice is characterized by a single E_a as before; however, two separate rate contants now describe this point due to the different temperatures. Proceeding as before, we obtain

$$k_1 t_1 + k_2 t_2 = \ln 2, \tag{4.23}$$

and substitution gives,

$$At_1e^{-E_a/RT_1} + At_2e^{-E_a/RT_2} = \ln 2. \qquad (4.24)$$

Equation 4.24 is much more complicated than equation 4.18 and cannot be solved for E_a directly. An iterative procedure is required to obtain E_a from the experimental parameters.

We can avoid such complicated calculations if we place a simple restriction upon the experiment. If T_2 is sufficiently large compared to T_1, then the first term in equation 4.24 may be neglected. For example, if the second slice is centered at E_a = 1.5 kcal/mol, with T_1 = 30 K, T_2 = 34 K, and $t_1 = t_2$, then the first term contributes less than 5% of the sum. If this term is neglected, then the equation reduces to equation 4.18, allowing the use of 4.19 to obtain E_a. For this reason, our slicing data were generally obtained with intervals of at least four degrees between slices.

An alternative way to simplify equation 4.24 is to let $T_1 = T_2$. In this case, we get:

$$(t_1+t_2)Ae^{-E_a/RT_2} = \ln 2, \qquad (4.25)$$

and solving for E_a:

$$E_a = -RT_2\ln[(\ln 2)/A(t_1+t_2)]. \qquad (4.26)$$

Thus, consecutive slices to the same temperature allow

calculation of E_a in the normal manner by simply substituting t_1+t_2 for t.

Another approximation is required by our inability to instantly equilibrate the matrix at the higher temperature. A range of temperatures was always encountered, typically 1-2 degrees. This problem is very similar to the one just described concerning consecutive slices to different temperatures and can be modeled by equation 4.24. Here we approximate a continuous warming by two intervals at the end-point temperatures. Taking T_1 = 30 K and T_2 = 32 K, with log A = 8 and $t_1 = t_2$ = 150 seconds, an iterative calculation gives E_a = 1.525. Using equation 4.19, one can easily show that this E_a would also be obtained if the temperature were constant at 31.34 K. Thus, the effective temperature is nearer to the maximum temperature of the range.

Our situation is somewhat better than is indicated by this model, since in the equilibration more time is spent near the higher temperature, further weighting the effective temperature in this direction. In fact, complete equilibration was attained in many of the slices, which should bring the effective temperature very near to the maximum temperature. For this reason, we used the maximum temperatures in the analysis.

References for Chapter 4

1. (a) Muller, J.-F.; Muller, D.; Dewey, H. J.; Michl, J. J. Am. Chem. Soc. 1978, 100, 1629-1630. (b) French, W. G.; Willard, J. E. J. Phys. Chem. 1968, 72, 4604-4608. (c) Williams, F.; Sprague, E. D. Acc. Chem. Res. 1982, 15, 408-415.
2. (a) Austin, R. H.; Beeson, K.; Eisenstein, L.; Freuenfelder, H.; Gunsalus, I. C.; Marshall, V. P. Phys. Rev. Lett. 1974, 32, 403-405. (b) Doba, T.; Ingold, K. U. Siebrand, W.; Wildman, T. A. J. Phys. Chem. 1984, 88, 3165-3167.
3. The work described in this chapter will be published: Sponsler, M. B.; Jain, R.; Coms, F. D.; Dougherty, D. A., manuscript in preparation.
4. Buchwalter, S. L.; Closs, G. L. J. Am. Chem. Soc. 1979, 101, 4688-4694.
5. Fisher, J. J.; Michl, J. J. Am. Chem. Soc. 1987, 109, 583-584.
6. Jain, R. Ph.D. Dissertation, California Institute of Technology, 1987.
7. Chang, M. H.; Jain, R.; Dougherty, D. A. J. Am. Chem. Soc. 1984, 106, 4211-4217.
8. Kochi, J. K., Ed. "Free Radicals"; Wiley: New York, 1973; Vol. II, pp. 275-524.
9. Turro, N. J.; Kraeutler, B. In "Diradicals"; Borden, W. T., Ed.; Wiley: New York, 1982; Chapter 6.

10. Dervan, P. B.; Dougherty, D. A. Ibid., p 138.

11. Goldberg, A. H.; Dougherty, D. A. J. Am. Chem. Soc. 1983, 105, 284-290.

12. Salem and Rowland have implied that this is the only way to produce a significant singlet barrier: Salem, L.; Rowland, C. Angew. Chem., Int. Ed. Engl. 1972, 11, 92-111.

13. Siebrand, W.; Wildman, T. A. Acc. Chem. Res. 1986, 19, 238-243.

14. For example, see Ber. Bunsenges Phys. Chem. 1978, 82, 2-139.

15. (a) Jankowiak, R.; Richert, R.; Bassler, H. J. Phys. Chem. 1985, 89, 4569-4574. (b) Albery, W. J.; Bartlett, P. N.; Wilde, C. P.; Darwent, J. R. J. Am. Chem. Soc. 1985, 107, 1854-1858.

16. Hudson, R. L.; Shiotani, M.; Williams, F. Chem. Phys. Lett. 1977, 48, 193-196.

17. Doba, T.; Ingold, K. U. Siebrand, W. Chem. Phys. Lett. 1984, 103, 339-342.

18. Bellman, R.; Kalaba, R. E.; Lockett, J. A. "Numerical Inversion of the Laplace Transform"; American Elsevier: New York, 1966.

19. Williams, G.; Watts, D. C.; Dev, S. B.; North, A. M. Trans. Faraday Soc. 1971, 67, 1323-1335.

20. Siebrand, W.; Wildman, T. A. Int. Rev. Phys. Chem. 1986, 5, 251-257.

21. Cruz, C. H. B.; Fork, R. L.; Knox, W. H.; Shank, C. V. Chem. Phys. Lett. 1986, 132, 341-344.

22. Abragam, A.; Bleaney, B. "Electron Paramagnetic Resonance of Transition Ions"; Clarendon: Oxford, 1970; pp. 574-583.

23. Wertz, J. E.; Bolton, J. R. "Electron Spin Resonance"; McGraw-Hill: New York, 1972; pp. 27, 459-460.

24. Phillips, D. L. J. Assoc. Comp. Machinery 1962, 9, 84-97.

25. Reactions which follow Arrhenius behavior with very low E_a have been reported from flash photolysis studies at higher temperatures. For example, see Zimmt, M. B.; Doubleday, C., Jr.; Gould, I. R.; Turro, N. J. J. Am. Chem. Soc. 1985, 107, 6724-6726.

26. Of course, the interference by signal growth could be avoided by using a different filter combination; however, the results would then have no direct bearing on the kinetic experiments.

27. Signals were considered non-saturated if the signal intensity was found to be proportional to the square root of the microwave power.

28. Less-direct evidence has been based upon variation of the photolysis intervals and hence the number of fast sites. See reference 13.

29. The only restriction is that enough decay must occur in each slice so that the previous slices can be

ignored in the E_a calculation. This restriction does not apply to consecutive slices involving the same temperature. See Experimental Section.

30. The range may be extended below 1 kcal/mol for smaller widths.

31. The traces labelled MS-41 through 47 (Figure 4.31) were photolyzed using only the KG-5 and UG-11 filters (no WG-305). Therefore, higher intensity light may account for some extra heating for these traces.

32. Witt, S. N.; Gelles, J.; Chan, S. I., unpublished work.

APPENDIX A

DECAY.BAS

```
      REM                          DECAY.BAS
      REM
      REM Program to calculate and display growth and decay curves for
      REM intermediates whose decay process have a distribution over
      REM activation energy.  This is one way to simulate the "matrix
      REM effect."  Thermal heating of the matrix has been modeled by
      REM allowing a higher temperature (described by the heating
      REM amount, HVD) during the photolysis.  The distribution at any
      REM time during the growth or decay may also be plotted.
      REM The program is written in compiled BASIC (IBM, version 2.00)
      REM using the IBM Plotting System.  It should be more or less device-
      REM independent; an IBM PC-AT with Enhanced Graphics Adaptor was used.
      REM
      REM    VARIABLES:
      REM      ADJ       Temperature independent width factor.
      REM      D1(I)     Amount of decay (at TEMP+HVD) during time DT1.
      REM      D2(I)     Amount of decay (at TEMP) during time DT2.
      REM      DT1       Time interval between points in the photolysis time.
      REM      DT2       Time interval in the decay portion.
      REM      F(I)      Amount of intermediate with rate R(I).
      REM      G(I)      Distribution over ln(k/k(0).
      REM      G1(I)     Amount of increase at rate R(I) during time DT1.
      REM      HV(K)     Temporary array of desired heating amounts.
      REM      HVD(K)    Array of desired heating amounts.
      REM      HVT       Photolysis time.
      REM      I         Counter over rate.
      REM      J         Counter over time.
      REM      K         Counter over temperature/heating amount.
      REM      KK!       Rate constant at TEMP.
      REM      KK#       Rate constant at TEMP+HVD.
      REM      N         Number of temperature/heating amount combinations.
      REM      NDIS      Number of distributions to be plotted.
      REM      NDT       Number of intervals in the photolysis time.
      REM      NIMB      Choice from second menu.
      REM      NUMB      Choice from first menu.
      REM      R(I)      Width independent ln(k/k(0)) axis.
      REM      R1(I)     Ln(k/k(0)) axis for the distribution.
      REM      R2(I)     Ln(k/k(0)) for the higher temperature.
      REM      RATE(K)   Most probable rates calculated from E(a) and log A.
      REM      RATEH(K)  Most probable rates at the higher temperature.
      REM      RATEHL    Natural logarithm of the most probable rate.
      REM      RATEL     Logarithm of most probable rate at higher temperature.
      REM      RRR       Logarithm of rate at a given point in the distribution.
      REM      RRRH      Same as RRR, for the higher temperature.
      REM      SADJ      Temperature independent width factor (in kcal/mol).
      REM      TEM(K)    Temporary array of desired temperatures.
      REM      TEMP(K)   Array of the desired temperatures.
      REM      TH        Factor of thermal heating due to photolysis.
      REM      WID       Temperature dependent width factor.
      REM      X(I)      The time axis for the growth/decay curves.
      REM      Y(K,I)    Simulated intensity axis.

            DEFINT I-N
200         DIM X(50),Y(10,50),Y1(50),D1(50),G(50),G1(50),R(50),F(50,50)
            DIM D2(50),TH(10),LABEL$(10),R1(50),E(52),RATE(10),F1(52),HVD(10)
            DIM TEMP(10),TEM(10),HV(10),RATEH(10),R2(50)
210         CLEAR ,,5000
230         CLS
            IREP = 0
            T$="Simulated Growth/Decay Curves"
            XA$="TIME (MIN)"
            STFLAG=1
            STRNG$="DISPLAY"
            STRNG2$="PRINTER"
            HVT=5
            RG=0.001987
            NUMB=10
```

```
    REM Input block.
        PRINT "CHOOSE A DISTRIBUTION:"
        PRINT "1. GAUSSIAN (DEFAULT)"
        PRINT "2. SIEBRAND"
        PRINT "3. SLATER"
        PRINT "4. DELTA (BOX) FUNCTION"
        PRINT "5. TWO DELTA FUNCTIONS"
        PRINT "6. TRIANGLE (SLOW)"
        PRINT "7. TRIANGLE (FAST)"
        INPUT LL
        IF LL=0 THEN LL=1
    REM This ON GOSUB tailors the width input to the chosen distribution
    REM and calculates the distribution.  Continuous distributions are
    REM approximated with 51 delta functions of appropriate intensities.
259     SUMG=0
        ON LL GOSUB 260,270,280,290,292,294,296
239     INPUT "ACTIVATION ENERGY, E(A) (kcal/mol)";E0
        INPUT "LOG A";ALA
    REM Up to ten combinations of temperature and heating amount are allowed.
238     INPUT "DESIRED NUMBER OF TEMPERATURES (1 TO 10)";NTEMP
        IF NTEMP>10 OR NTEMP<1 GOTO 238
        FOR K=1 TO NTEMP
        INPUT "TEMPERATURE (KELVIN)";TEM(K)
        NEXT K
        IF NTEMP>5 THEN NH=1:GOTO 245
        NHM=FIX(10/NTEMP)
240     PRINT "DESIRED NUMBER OF HEATING AMOUNTS (1 TO";NHM;")"
        INPUT NH
        IF NH>NHM OR NH<1 GOTO 240
245     FOR K=1 TO NH
        INPUT "HEATING DUE TO PHOTOLYSIS (DEGREES K)";HV(K)
        NEXT K
250     INPUT "DECAY TIME (MIN)";TIME

    REM Each selected heating amount will be used with each temperature.
        N=NTEMP*NH
        K=0
        FOR K1=1 TO NTEMP
        FOR K2=1 TO NH
        K=K+1
        TEMP(K)=TEM(K1)
        HVD(K)=HV(K2)
        TH(K)=(TEMP(K)+HVD(K))/TEMP(K)
        NEXT K2
        NEXT K1

255     PRINT:PRINT "Calculating..."
    REM Most probable rates are calculated from the E(a), log A, and temp. data.
        EAR=E0/RG
        AVAL=10^ALA
        FOR K=1 TO N
        RATE(K)=AVAL*EXP(-EAR/TEMP(K))
        RATEH(K)=AVAL*EXP(-EAR/(TH(K)*TEMP(K)))
        NEXT K

    REM The entire growth curve must be displayed.
        IF TIME<HVT/60 THEN TIME=HVT/60
    REM This normalizes the growth curve so that if no decay occurs
    REM during the photolysis, the curve will reach 100%.
        PFK=100/HVT
    REM The decay time is divided into 50 intervals.
        NDT=(HVT/(60*TIME))*50
        IF NDT=0 THEN NDT=1
        DT1=HVT/NDT
        IF NDT=50 GOTO 300
        DT2=((60*TIME)-HVT)/(50-NDT)
```

```
    REM The time scale is calculated (in min.).
300     FOR J=1 TO NDT
        X(J)=J*DT1/60
        NEXT J
        FOR J=NDT+1 TO 50
        X(J)=(HVT+(J-NDT)*DT2)/60
        NEXT J

    REM This is the main loop, in which the growth/decay curves are computed.
        FOR K=1 TO N
        LABEL$(K)=STR$(TEMP(K))+"-"+STR$(TEMP(K)+HVD(K))+","+STR$(RATE(K))
    REM These subroutines make the necessary width adjustments.
        ON LL GOSUB 510,500,520,530,531,531,531
        IF RATE(K)=0 THEN RATE(K)=1E-30
        RATEL=LOG(RATE(K))
        IF RATEH(K)=0 THEN RATEH(K)=1E-30
        RATEHL=LOG(RATEH(K))
350     FOR I=0 TO 50
        RRR=RATEL+R1(I)
        RRRH=RATEHL+R2(I)
    REM This statement prevents a possible overflow (as does line 351).
        IF RRRH>50 THEN G1(I)=0:D1(I)=0:GOTO 351
        KK#=EXP(RRRH)
    REM In this statement the decay during photolysis is calculated explicitly.
    REM for the signal that is generated during the same interval.
    REM The decay of any previous signal is accounted for in D1.
    REM The condition is necessary to avoid errors arising from division
    REM of two very small numbers.  The use of double-precision for KK#
    REM also helps eliminate this error.  The equation for DD was derived
    REM by solving an integral from 0 to DT1 with the following integrand:
    REM EXP(-KK#*(DT1-t))*dt.
        IF RRRH<-12 THEN DD=DT1 ELSE DD=(1-EXP(-KK#*DT1))/KK#
        G1(I)=(G(I)/SUMG)*PFK*DD
    REM Note that D1 and D2 have the form of exponential decay: EXP(-kt).
        D1(I)=EXP(-KK#*DT1)
351     IF RRR>50 THEN D2(I)=0:GOTO 352
        KK!=EXP(RRR)
        D2(I)=EXP(-KK!*DT2)
352     NEXT I
    REM Arrays are cleared.
        FOR J=0 TO 50
        Y(K,J)=0
        FOR I=0 TO 50
        F(I,J)=0
        NEXT I
        NEXT J
    REM The developing distribution, F(I), and intensity, Y(K,J) are
    REM iteratively calculated.  The intensity at a given time is equal
    REM to the sum over the entire distribution at that time.
        FOR J=1 TO NDT
        FOR I=0 TO 50
        F(I,J)=F(I,J-1)*D1(I)+G1(I)
        Y(K,J)=Y(K,J)+F(I,J)
        NEXT I
        NEXT J
        FOR J=NDT+1 TO 50
        FOR I=0 TO 50
        F(I,J)=F(I,J-1)*D2(I)
        Y(K,J)=Y(K,J)+F(I,J)
        NEXT I
        NEXT J
    REM The intensity during photolysis is adjusted using the Curie law.
        FOR J=1 TO NDT
        Y(K,J)=Y(K,J)/TH(K)
        NEXT J
        IF DFLAG=1 GOTO 620
        NEXT K
```

```
400     PRINT:PRINT "HIT F1 TO QUIT"
        PRINT "     F2 TO PRINT GRAPH"
        PRINT "     F3 TO CHANGE TEMPERATURES"
        PRINT "     F4 TO CHANGE DECAY TIME"
        PRINT "     F5 TO CHANGE DISTRIBUTION"
        PRINT "     F6 TO CHANGE E(A)"
        PRINT "     F7 TO CHANGE LOG A"
        PRINT "     F8 TO CHANGE HEATING AMOUNTS"
        PRINT "     F9 TO SEE SECOND MENU"
        PRINT "     F10 TO REPLOT (DEFAULT)"
        IF NIMB=10 OR NUMB<>10 THEN NIMB=0:NUMB=10:GOTO 100
        IF STFLAG=0 GOTO 410
        ST$=STR$(HVT)+" SEC hv,"+DIST$+" E(A)="+STR$(E0)+" LOG A="+STR$(ALA)
410     IF IREP = 1 THEN CALL PRSDAT(ST%):GOTO 21
        GOTO 960

260     REM  GAUSSIAN DISTRIBUTION
        DIST$="  GAUSSIAN DIST."
        INPUT "STANDARD DEV. OF GAUSSIAN (kcal/mol)";SADJ
        ADJ = 1.976E-6/(SADJ*SADJ)
        YA$="SIGMA(DIST.) ="+STR$(SADJ)
        FOR I=0 TO 50
        R(I)=-2.5+I*0.1
        G(I)=EXP(-R(I)*R(I))
        SUMG=SUMG+G(I)
        NEXT I
        RETURN
270     REM  SIEBRAND DISTRIBUTION
        DIST$="  SIEBRAND DIST."
        YA$="INTENSITY"
        FOR I=0 TO 50
        R1(I)=-2.0+I*.24
        G(I)=EXP(R1(I))*(EXP(R1(I)+EXP(-R1(I))-1))^(-3/2)
        SUMG=SUMG+G(I)
        NEXT I
        RETURN
280     REM  SLATER DISTRIBUTION
        DIST$="  SLATER DIST."
        INPUT "FULL WIDTH AT HALF HEIGHT (kcal/mol)";SADJ
        ADJ=2.755E-3/SADJ
        YA$="FWHM ="+STR$(SADJ)
        FOR I=0 TO 50
        R(I)=-4+I*0.16
        G(I)=EXP(-ABS(R(I)))
        SUMG=SUMG+G(I)
        NEXT I
        RETURN
290     REM  DELTA (BOX) FUNCTION
        INPUT "WIDTH OF BOX (kcal/mol) [0 for DELTA FUNCTION]";ADJ
        IF ADJ>0 GOTO 291
        DIST$="  DELTA FUNCTION"
        YA$="INTENSITY"
        FOR I=0 TO 50
        R1(I)=-2.5+I*.1
        G(I)=0
        NEXT I
        G(25)=1
        SUMG=1
        RETURN
291     DIST$="  BOX FUNCTION"
        YA$="WIDTH ="+STR$(ADJ)
        FOR I=0 TO 50
        R(I)=-0.5+I*0.02
        G(I)=1
        NEXT I
        SUMG=51
        RETURN
```

```
292       REM  TWO DELTA FUNCTIONS
          DIST$="  TWO DELTA FUNCTIONS"
          INPUT "DISTANCE BETWEEN DELTA FUNCTIONS (kcal/mol)";ADJ
          INPUT "RELATIVE HEIGHT (RIGHT/LEFT)";RELH
          YA$="DISTANCE B/W DELTA FUNCTIONS ="+STR$(ADJ)+", REL. HT. ="+STR$(RELH)
          FOR I=0 TO 50
          R(I)=-0.5+I*0.02
          G(I)=0
          NEXT I
          G(0)=RELH
          G(50)=1
          SUMG=RELH+1
          RETURN
294       DIST$="  TRIANGLE (SLOW)"
          INPUT "BASE WIDTH (kcal/mol)";ADJ
          YA$="BASE WIDTH ="+STR$(ADJ)
          FOR I=0 TO 50
          R(I)=I*0.02
          G(I)=50-I
          NEXT I
          SUMG=1275
          RETURN
296       DIST$="  TRIANGLE (FAST)"
          INPUT "BASE WIDTH (kcal/mol)";ADJ
          YA$="BASE WIDTH ="+STR$(ADJ)
          FOR I=0 TO 50
          R(I)=-1.0+I*0.02
          G(I)=I
          NEXT I
          SUMG=1275
          RETURN

500 REM No width adjustment for this distribution.
          RETURN
510 REM Gaussian distribution.
          WID=ADJ*TEMP(K)*TEMP(K)
          WIDH=ADJ*TEMP(K)*TEMP(K)*TH(K)*TH(K)
          FOR I=0 TO 50
          R1(I)=R(I)/SQR(WID)
          R2(I)=R(I)/SQR(WIDH)
          NEXT I
          RETURN
520 REM Slater distribution.
          WID=ADJ*TEMP(K)
          WIDH=ADJ*TEMP(K)*TH(K)
          FOR I=0 TO 50
          R1(I)=R(I)/WID
          R2(I)=R(I)/WIDH
          NEXT I
          RETURN
530 REM Delta (Box) function.
          IF ADJ<=0 THEN RETURN
531 REM Box, two deltas, triangles.
          WID=ADJ/(TEMP(K)*RG)
          WIDH=ADJ/(TEMP(K)*TH(K)*RG)
          FOR I=0 TO 50
          R1(I)=R(I)*WID
          R2(I)=R(I)*WIDH
          NEXT I
          RETURN

960 REM Open the Plotting System.
          R0=0.0:R1=100.0:I1=1:I2=2:I8=8:I9=9
          I3=3:I4=4:I5=5:I6=6:I7=7:I102=102:I103=103:I20=20:I105=105:I15=15
          wdth=11.0:height=8.5:I10=10
          YTYP%=1
5         CALL POPNPS(ST%)
          CALL PSSURF(WDTH,HEIGHT,ST%)
          CALL PRSDAT(ST%) '
```

```
    REM Assign Plotting System output device, display.
10      CALL PPSOT(STRNG$,ST%)

        NTOT=51
21      for K=1 to N
        FOR J=0 TO 50
        Y1(J)=Y(K,J)
        NEXT J
    REM For logarithmic plots, the zero point is avoided.
        IF YTYP%=2 THEN Y1(0)=Y1(1)
        CALL PDSXY(K,NTOT,X(0),Y1(0),ST%)
        CALL PDSWID(K,I5,ST%)
28      CALL PLINE(K,ST%):GOTO 29
29      IC=K+1
        IF IC>7 THEN IC=IC-7
        CALL PDSCLR(K,IC,ST%)
        CALL PDSNM(K,LABEL$(K),ST%)
        NEXT K

    REM Assign titles, axis labels, legend, etc.
40      CALL PTHD(T$,ST%)
        CALL PTHFNT(I105,ST%)
        CALL PTHHGT(I15,ST%)
        CALL PTSUB(ST$,ST%)
        CALL PTSFNT(I105,ST%)
        CALL PTSHGT(I10,ST%)
        CALL PTAX(I1,XA$,ST%) :
        CALL PTAX(I2,YA$,ST%)
        CALL PLLOC(I1,I1,R1,R1,ST%)
        CALL PLALIN(I3,I3,ST%)
        CALL PXVFRM(I1,I5,ST%)
        CALL PAXTYP(I1,YTYP%,ST%)

    REM Output the currently defined chart.
        CALL PSFORE(I6,ST%)
        CALL PPLTIT(ST%)

    REM Enable the keyboard.
50      CALL PPSIN(STRNG$,ST%)
        IREP = 1
    REM Read the selected option.
100     CALL PRQCH(I10,NUMB,ST%)
        ON NUMB GOTO 55,51,105,110,115,120,125,130,135,255

    REM Print the graph.
51      CALL PCLIO(STRNG$,ST%)
52      CALL PPSOT(STRNG2$,ST%)
53      CALL PPLTIT(ST%)
54      CALL PCLEAR(ST%)
        CALL PCLIO(STRNG2$,ST%)
        GOTO 10

    REM Quit.
55      CALL PCLIO(STRNG$,ST%)
60      CALL PCLSPS(ST%)
70      GOTO 80

    REM Other options.
105     NTM=FIX(10/NH)
106     PRINT "NUMBER OF TEMPERATURES (1 TO";NTM;")"
        INPUT NTEMP
        IF NTEMP>NTM GOTO 106
        FOR K=1 TO NTEMP
        INPUT "TEMPERATURE (KELVIN)";TEM(K)
        NEXT K
        GOTO 132
110     INPUT "ENTER NEW DECAY TIME (MIN.) ";TIME : GOTO 100
```

```
115     PRINT "1. GAUSSIAN (DEFAULT)"
        PRINT "2. SIEBRAND"
        PRINT "3. SLATER"
        PRINT "4. DELTA (BOX) FUNCTION"
        PRINT "5. TWO DELTA FUNCTIONS"
        PRINT "6. TRIANGLE (SLOW)"
        PRINT "7. TRIANGLE (FAST)"
        INPUT "ENTER NEW DISTRIBUTION TYPE ";LL
        IF LL=0 THEN LL=1
        SUMG=0
        ON LL GOSUB 260,270,280,290,292,294,296
        GOTO 400
120     INPUT "ENTER NEW E(A) (kcal/mol) ";EO:GOTO 100
125     INPUT "ENTER NEW LOG A ";ALA:GOTO 100
130     NHM=FIX(10/NTEMP)
131     PRINT "DESIRED NUMBER OF HEATING AMOUNTS (1 TO";NHM;")"
        INPUT NH
        IF NH>NHM OR NH<1 GOTO 131
        FOR K=1 TO NH
        INPUT "HEATING AMOUNT (DUE TO PHOTOLYSIS)";HV(K)
        NEXT K
132     N=NTEMP*NH
        K=0
        FOR K1=1 TO NTEMP
        FOR K2=1 TO NH
        K=K+1
        TEMP(K)=TEM(K1)
        HVD(K)=HV(K2)
        TH(K)=(TEMP(K)+HVD(K))/TEMP(K)
        NEXT K2
        NEXT K1
        GOTO 400

    REM Second menu of options.:
135     PRINT:PRINT "HIT F1 TO CHANGE PHOTOLYSIS TIME"
        PRINT "     F2 TO CHANGE TITLE"
        PRINT "     F3 TO GET STANDARD TITLE"
        PRINT "     F4 TO CHANGE SUBTITLE"
        PRINT "     F5 TO GET STANDARD SUBTITLE"
        PRINT "     F6 TO PLOT INTENSITY ON A LOG SCALE"
        PRINT "     F7 TO PLOT INTENSITY ON A STANDARD SCALE"
        PRINT "     F8 TO PLOT DISTRIBUTION"
        PRINT "     F10 TO RETURN TO FIRST MENU (DEFAULT)"
140     CALL PROCH(I10,NIMB,ST%)
        ON NIMB GOTO 145,150,155,160,165,170,175,600,400,400
145     INPUT "ENTER NEW PHOTOLYSIS TIME (sec.)";HVT:GOTO 140
150     INPUT "ENTER NEW TITLE";T$:GOTO 140
155     PRINT "DEFAULT TITLE":t$="Simulated Growth/Decay Curves":GOTO 140
160     INPUT "ENTER NEW SUBTITLE";ST$:STFLAG=0:GOTO 140
165     PRINT "DEFAULT SUBTITLE"
        ST$=STR$(HVT)+" SEC hv,"+DIST$+" E(A)="+STR$(EO)+" LOG A="+STR$(ALA)
        STFLAG=1:GOTO 140
170     PRINT "LOG SCALE":YTYP%=2:GOTO 140
175     PRINT "STANDARD SCALE":YTYP%=1:GOTO 140

600 REM The following routine generates a distribution plot.
    REM DFLAG is a flag that allows the main program to be used as a subroutine.
        DFLAG=1
        CALL PRSDAT(ST%)
        NDIS=0
        K=1:KD=1:IC=2
        NDPT=51:LLI=1
        ON LL GOSUB 510,500,520,530,531,531,531
    REM The activation energy scale is calculated.
        FOR I=1 TO 51
        E(I)=EO-RG*TEMP(K)*R1(I-1)
        NEXT I
        INPUT "PLOT INTACT DISTRIBUTION ALSO";YN$
        IF YN$="N" OR YN$="n" GOTO 605
```

```
    REM The intact distribution is set up.
        NDIS=NDIS+1
        LAB$="INTACT"
        CALL PDSNM(NDIS,LAB$,ST%)
        FOR I=1 TO 51
        F1(I)=100*G(I-1)/SUMG
        NEXT I
        ON LL GOSUB 680,680,680,685,690,695,695
        CALL PDSXY(NDIS,NDPT,E(LLI),F1(LLI),ST%)
        CALL PDSWID(NDIS,I5,ST%)
        CALL PLINE(NDIS,ST%)
        CALL PDSCLR(NDIS,IC,ST%)
605     PRINT "SELECT TEMP. AND HEATING AMOUNT: 1  (";TEMP(1);"+";HVD(1);"K)"
        FOR K=2 TO N
        PRINT "                                    ";K;" (";TEMP(K);"+";HVD(K);"K)"
        NEXT K
        K=KD
        PRINT "(DEFAULT =";K;")"
        INPUT KD
        IF KD=0 THEN KD=K
        K=KD
        NDIS=NDIS+1
        INPUT "TIME AT WHICH DISTRIBUTION IS TO BE PLOTTED (sec.)";TD
    REM The time nearest the desired time is selected.
        IF TD<=HVT THEN JD=TD/DT1 ELSE JD=NDT+(TD-HVT)/DT2
    REM The main program is used to calculate the distribution.  This is
    REM necessary because there is not enough memory to store the distributions
    REM for all the temperatures/heating factors simultaneously."
610     GOTO 350
620     LAB$=STR$(TEMP(K))+"K,"+STR$(CINT(10*X(JD)*60)/10)+" s"
        CALL PDSNM(NDIS,LAB$,ST%)
        FOR I=1 TO 51
        F1(I)=F(I-1,JD)
        NEXT I
        CALL PDSXY(NDIS,NDPT,E(LLI),F1(LLI),ST%)
        CALL PDSWID(NDIS,I5,ST%)
        CALL PLINE(NDIS,ST%)
        IC=IC+1:IF IC=8 THEN IC=1
        CALL PDSCLR(NDIS,IC,ST%)
        INPUT "PLOT ANY OTHER DISTRIBUTIONS ON THE SAME GRAPH";YN$
        IF YN$="Y" OR YN$="y" GOTO 605
    REM Labels are assigned.
640     DD$=DIST$
        IF RIGHT$(DD$,5)="DIST." THEN DD$=MID$(DD$,I1,LEN(DD$)-1)+"RIBUTION"
        STD$="E(a)="+STR$(EO)+" LOG A="+STR$(ALA)+" ("+STR$(HVT)+" SEC. HV)"
        XD$="ACTIVATION ENERGY (kcal/mol)"
        YD$=YA$
        IF YD$="INTENSITY" THEN YD$="REL. AMOUNT"
        CALL PTHD(DD$,ST%)
        CALL PTSUB(STD$,ST%)
        CALL PTAX(I1,XD$,ST%)
        CALL PTAX(I2,YD$,ST%)
        CALL PAXTYP(I1,I1,ST%)
    REM Plot distribution(s).
        CALL PPLTIT(ST%)
        DFLAG=0
    REM Pause.
650     A$=INKEY$:IF A$="" GOTO 650
    REM Return to second menu.
        GOTO 135
    REM The following routines provide perfectly vertical lines.
680 REM No vertical lines needed for this distribution.
        RETURN
685     IF ADJ>0 GOTO 695
    REM Delta function.
        E(24)=E(25)
        E(26)=E(25)
        RETURN
```

```
690 REM Box function.
        E(2)=E(1)
        E(50)=E(51)
695 REM Triange functions.
        NDPT=53:LLI=0
        E(0)=E(1):F1(0)=0
        E(52)=E(51):F1(52)=0
        RETURN
80      END
```

APPENDIX B

FIT.BAS

```
REM                                FIT.BAS
REM
REM This program fits experimental growth/decay curves to simulated
REM curves, optimizing any or all of the following: distribution
REM width, most probable rate, and matrix heating during photolysis.
REM Several different distribution shapes are available as options.
REM In addition, the intensity scale of the trace may be either
REM specified, or allowed to vary freely, in effect optimizing this
REM parameter.  (It is recommended that the intensity scale be
REM normalized by some method, prior to fitting.)  The width and
REM rate parameters are optimized together, followed by the heating
REM optimization.  The rate optimization may be performed either to
REM produce the best fit at the end of the trace or the best overall
REM fit.  The width optimization is based on the best overall fit,
REM and the heating optimization is based on the end of the growth.
REM Output files from EPR.FOR can be used directly as input data files,
REM with the addition of IX1-6, TEMP, HVT, and SCT.  Noise spikes,
REM often observed in the digitized data, are best removed to
REM to keep them from influencing the optimizations.  In particular,
REM any spikes that rise above the growth curve maximum will cause
REM errors in the photolytic heating optimization.
REM
REM    VARIABLES:
REM      ADJ       Temperature independent width factor.
REM      D2(I)     Amount of decay (at TEMP+HVD) during time DT.
REM      D3(I)     Amount of decay (at TEMP) during time DTS.
REM      DT        Time interval between points in the experimental data.
REM      DTP       Time interval between start of hv and the 1st data point.
REM      DTS       Time interval for the simulated decay.
REM      F(I)      Amount of intermediate with rate R(I).
REM      G(I)      Distribution over ln(k/k(0).
REM      G1(I)     Amount of increase at rate R(I) during time DTP.
REM      G2(I)     Amount of increase at rate R(I) during time DT.
REM      HVD(IH)   Heating amount.
REM      HVT       Photolysis time (s).
REM      I         Counter over rate.
REM      IH        Counter for the heating optimization.
REM      ITER      Counter for the rate optimization.
REM      IW        Counter for the width optimization.
REM      IX1       Last point of the initial baseline (reference field).
REM      IX2       Last point of the initial baseline (monitoring field).
REM      IX3       Point corresponding to the end of photolysis.
REM      IX4       Last point of the decay.
REM      IX5       First point of the initial baseline (ref.; default=1)
REM      IX6       Last point of the final baseline (ref.; default=1000)
REM      J         Counter over time.
REM      KK!       Rate constant at TEMP.
REM      KK#       Rate constant at TEMP+HVD.
REM      NDT       Number of intervals in the photolysis time.
REM      NUMB      Choice from menu.
REM      R(I)      Width independent ln(k/k(0)) axis.
REM      R1(I)     Ln(k/k(0)) axis for the distribution.
REM      R2(I)     Ln(k/k(0)) for the higher temperature.
REM      RATE(K)   Most probable rates calculated from E(a) and log A.
REM      RATEH(K)  Most probable rates at the higher temperature.
REM      RATEHL    Natural logarithm of the most probable rate.
REM      RATEL     Logarithm of most probable rate at higher temperature.
REM      RMS       Root-mean-squared deviation of the fit.
REM      RRR       Logarithm of rate at a given point in the distribution.
REM      RRRH      Same as RRR, for the higher temperature.
REM      SADJ      Temperature independent width factor (in kcal/mol).
REM      SCT       Experimental scan time (min).
REM      TEMP      Sample temperature (K).
REM      TH        Factor of thermal heating due to photolysis.
REM      WID       Temperature dependent width factor.
REM      X(I)      The time axis for the growth/decay curves.
REM      YE(J)     Experimental intensity.
REM      Y1(J)     Simulated intensity.
REM      Y2(J)     Experimental intensity (fewer points-to match simulation).
```

```
        DEFINT I-N
200     DIM X(1001),Y1(201),G(51),G1(51),R(51),F(51),RATE(200),DIFA(200)
        DIM D2(51),DAT$(68),X1(201),YE(1010),D3(51),G2(51),Y2(201),Q(200)
        DIM WID(200),W(200),A2(200),Z(200),AL(200),R1(51),R2(51),TH(200)
        DIM HVD(200)
210     CLEAR ,,5000
230     CLS
        T$="ESR Decay Curve Fitting"
        XA$="TIME (MIN)"
        YA$="INTENSITY"
        STRNG$="DISPLAY"
        STRNG2$="PRINTER"
        EXL$="EXPTL"
        RG=0.001987
        NUMB=10
        FLAG=0

        PRINT "PROGRAM TO FIT EPR KINETIC DATA TO SIMULATED DECAY TRACES BASED"
        PRINT "ON A DISTRIBUTION OF FIRST-ORDER RATE CONSTANTS.":PRINT
        INPUT "NAME OF DATA FILE";FIL$
    REM If no file extension is given, .DAT is assumed.
        LE=LEN(FIL$)
        FOR I=1 TO LE
        IF MID$(FIL$,I,1)="." GOTO 233
        NEXT I
        FIL$=FIL$+".DAT"
233     OPEN "I",#1,FIL$
    REM The file is read in a somewhat awkward manner, but this is unavoidable,
    REM since BASIC does not have a formatted input statement.
        INPUT#1,DUM$
        FOR I=1 TO 67
        INPUT#1,DAT$(I)
        WHILE (LEN(DAT$(I))<60)
        DAT$(I)="0"+DAT$(I)
        WEND
        NEXT I
        K=0
        FOR I=1 TO 67
        FOR J=1 TO 57 STEP 4
        K=K+1
        YE(K)=VAL(MID$(DAT$(I),J,4))
        NEXT J
        NEXT I
    REM This input defines the growth, decay, baselines, temp., etc.
    REM These parameters must be inserted into the file manually.
        INPUT#1,IX1,IX2,IX3,IX4,IX5,IX6,TEMP,HVT,SCT
        IF IX5=0 THEN IX5=1
        IF IX6=0 THEN IX6=1000
        IF HVT=0 THEN HVT=5:SCT=16
        DT=SCT*60/1000
        NDT=FIX(HVT/DT)
        NDT1=NDT+1
        DTP=(HVT/DT-NDT)*DT
    REM This normalizes the growth curve so that if no decay occurs
    REM during the photolysis, the curve will reach 100%.
        PFK=100/HVT
    REM The time scale is calculated (in min.).
        FOR I=1 TO 1000
        X(I)=(DTP+DT*(I-1))/60
        NEXT I

    REM Initial baseline (reference field).
        SUMYE=0
        FOR I=IX5 TO IX1
        SUMYE=SUMYE+YE(I)
        NEXT I
        AAV=SUMYE/(IX1+1-IX5)
```

```
    REM Initial baseline (monitoring field).
        SUMYE=0:INB=IX1+10
        FOR I=INB TO IX2
        SUMYE=SUMYE+YE(I)
        NEXT I
        BAV=SUMYE/(IX2+1-INB)
    REM Final baseline (reference field).
        SUMYE=0:INC=IX4+10
        FOR I=INC TO IX6
        SUMYE=SUMYE+YE(I)
        NEXT I
        CAV=SUMYE/(IX6+1-INC)
    REM Baseline drift correction.
        BDC=(AAV-CAV)/((IX6+INC-IX1-IX5)/2)
        FOR I=IX2 TO IX4
        YE(I)=YE(I)+BDC*I-BAV
        NEXT I
        NT=IX4-IX3+NDT1
    REM The baselines are chopped off.
        FOR I=1 TO NT
        YE(I)=YE(IX3-NDT1+I)
        NEXT I
        DTS=DT*10
        NTS=NDT1+FIX((NT-NDT1)/10)
        NTS1=NTS+1
    REM The time axis is calculated again with the larger spacing in the decay.
        FOR I=1 TO NDT1
        X1(I)=(DTP+DT*(I-1))/60
        NEXT I
232     FOR I=NDT1+1 TO NTS
        X1(I)=X1(NDT1)+(I-NDT1)*DTS/60
        NEXT I
    REM YMAX is the normalized intensity at the end of the photolysis.
    REM Note that this often does not coincide with the maximum of the
    REM growth curve, presumably because of the photolytic heating effect.
    REM If YMAX is not specified, then the data will be scaled to match
    REM the simulation at the beginning of the decay for each iteration.
234     INPUT "YMAX (ENTER -1 IF NOT DETERMINED)";YMAX
        IF YMAX=-1 GOTO 235
        SCALE=YMAX/YE(NDT1)
        FOR I=1 TO NT
        YE(I)=YE(I)*SCALE
        NEXT I

    REM Option input block.
235     NTSP=NTS
        NTP=NT
        PRINT "CHOOSE A DISTRIBUTION:"
        PRINT "1. GAUSSIAN (DEFAULT)"
        PRINT "2. SIEBRAND"
        PRINT "3. SLATER"
        PRINT "4. DELTA (BOX) FUNCTION"
        PRINT "5. TWO DELTA FUNCTIONS"
        PRINT "6. TRIANGLE (SLOW)
        PRINT "7. TRIANGLE (FAST)
        INPUT LL
        IF LL=0 THEN LL=1
        SUMG=0
    REM This ON GOSUB tailors the width input to the chosen distribution
    REM and calculates the distribution.  Continuous distributions are
    REM approximated with 51 delta functions of appropriate intensities.
        ON LL GOSUB 260,270,280,290,292,294,296
241     INPUT "WIDTH OPTIMIZATION (Y/N)";ANS$
        IF (ANS$="Y" OR ANS$="y") AND LL=1 THEN PRINT "SORRY, NO WIDTH ADJUSTMEN
T AVAILABLE FOR THIS DISTRIBUTION."
242     INPUT "STARTING GUESS FOR K(0) IN 1/SEC";RATE(1)
        PRINT "RATE OPTIMIZATION USING END (1) OR ENTIRE CURVE (2)"
        INPUT "(ENTER 0 FOR NO RATE OPTIMIZATION)";IO
        IF (IO<1 OR IO>2) THEN IO=3
```

```
        INPUT "HEATING DUE TO PHOTOLYSIS (DEGREES K)";HVD(1)
        TH(1)=(TEMP+HVD(1))/TEMP
        INPUT "OPTIMIZE HEATING (AFTER WIDTH, RATE OPT.)";H$
        IF H$="N" OR H$="n" THEN HOPT=1 ELSE HOPT=0
    REM Log A is needed for the heating optimization.
        IF HVD(1)<>0 OR HOPT=0 THEN INPUT "APPROX. LOG A (FOR HEATING OPT.)";ALA
         ELSE ALA=8
        AVAL=10^ALA

258     WOPT=0:IW=0:WFAC=0:WF0=2:IH=1
    REM Width optimization loop.
259     WHILE WOPT=0
        IW=IW+1
        IF IW>1 THEN RATE(1)=RATE(ITER)
        IF ANS$<>"Y" AND ANS$<>"y" THEN WOPT=1
        ON LL GOSUB 610,600,620,630,631,631,631
        IF IQ=3 GOTO 309
        PRINT:IF IQ=1 THEN PRINT "ITER.","K(0)","DIF" ELSE PRINT "ITER.","K(0)",
          "% CHANGE","RMS"
309     KOPT=0:ITER=0:FAC=0:F0=2
    REM Rate optimization loop.
        WHILE KOPT=0
        ITER=ITER+1
310     SUMX=0:SUMY=0:SUMXY=0:SUMX2=0
311     RATEL=LOG(RATE(ITER))
        RATEHL=2.303*ALA+LOG(RATE(ITER)/AVAL)/TH(IH)
        FOR I=0 TO 50
        RRRH=RATEHL+R2(I)
    REM This statement prevents a possible overflow.
        IF RRRH>50 THEN G1(I)=0:G2(I)=0:D2(I)=0:GOTO 351
        KK#=EXP(RRRH)
        IF RRRH<-12 THEN DD1=DTP:DD2=DT:GOTO 349
    REM In these statements, decay during photolysis is calculated explicitly
    REM for the signal that is generated during the same interval.
    REM The decay of any previous signal is accounted for in D2.
    REM The condition above is necessary to avoid errors arising from division
    REM of two very small numbers.  The use of double-precision for KK#
    REM also helps eliminate this error.  These equations were derived
    REM by solving an integral from 0 to DT with the following integrand:
    REM EXP(-KK#*(DT-t))*dt.
        DD1=(1-EXP(-KK#*DTP))/KK#
        DD2=(1-EXP(-KK#*DT))/KK#
    REM The growth/decay aliquots for DTP and DT are computed.  Note
    REM that the growth terms (G1 and G2) include a factor for decay
    REM during the photolysis interval.
349     G1(I)=(G(I)/SUMG)*PFK*DD1
        G2(I)=(G(I)/SUMG)*PFK*DD2
    REM Note that D2 and D3 have the form of exponential decay: EXP(-kt).
        D2(I)=EXP(-KK#*DT)
351     RRR=RATEL+R1(I)
    REM This statement prevents a possible overflow.
        IF RRR>50 THEN D3(I)=0:GOTO 352
        KK!=EXP(RRR)
        D3(I)=EXP(-KK!*DTS)
    REM Arrays are cleared.
352     F(I)=0
        NEXT I
        FOR J=1 TO NTS
        Y1(J)=0
        NEXT J
    REM The developing distribution, F(I), and intensity, Y1(J) are
    REM iteratively calculated.  The intensity at a given time is equal
    REM to the sum over the entire distribution at that time.
        FOR I=1 TO 50
        F(I)=F(I)+G1(I)
        Y1(1)=Y1(1)+F(I)
        NEXT I
```

```
        FOR J=2 TO NDT1
        FOR I=0 TO 50
        F(I)=F(I)*D2(I)+G2(I)
        Y1(J)=Y1(J)+F(I)
        NEXT I
        NEXT J
        FOR J=NDT1+1 TO NTS
        FOR I=0 TO 50
        F(I)=F(I)*D3(I)
        Y1(J)=Y1(J)+F(I)
        NEXT I
        NEXT J
    REM The intensity during photolysis is adjusted using the Curie law.
        FOR J=1 TO NDT
        Y1(J)=Y1(J)/TH(IH)
        NEXT J

        IF YMAX<>-1 THEN IF Y2(NDT1)=0 GOTO 320 ELSE GOTO 322
    REM This segment (until 320) is used only if YMAX was not specified.
    REM The experimental curve is scaled to match the simulation at the
    REM end of the growth curve.
        YMX=YE(1)
        FOR I=2 TO NTP
        IF YE(I)>YMX THEN YMX=YE(I)
        NEXT I
        SCALE=Y1(NDT1)/YMX
        FOR I=1 TO NTP
        YE(I)=YE(I)*SCALE
        NEXT I
320     FOR I=1 TO NTS
        IF (I<=NDT1) THEN J=I ELSE J=NDT1+(I-NDT1)*10
        Y2(I)=YE(J)
        NEXT I
    REM FLAG=1 if the heating is currently being optimized.  In this
    REM case, the above sequence is used as a subroutine.
322     IF FLAG=1 THEN RETURN
        ON IQ GOSUB 340,370,391
        WEND

390 REM The rate optimization is complete.
        GOSUB 500
        PRINT:PRINT "OPTIMIZED RATE= ",RATE(ITER)
        PRINT "RMS DEVIATION= ",RMS

        IF WOPT<>0 GOTO 331
        W(IW)=RMS
        IF IW<3 GOTO 329
    REM The next width is calculated from the previous three using a
    REM quadratic fit of the rms deviation over width.  Cramer's rule is used.
        L1=IW-2:L2=IW-1:L3=IW
        FOR I=L1 TO L3
        AL(I)=LOG(WID(I))
        A2(I)=AL(I)*AL(I)
        NEXT I
        DN=AL(L1)*(A2(L3)-A2(L2))+AL(L2)*(A2(L1)-A2(L3))+AL(L3)*(A2(L2)-A2(L1))
        IF DN=0 GOTO 329
        AN=(AL(L1)*(W(L3)-W(L2))+AL(L2)*(W(L1)-W(L3))+AL(L3)*(W(L2)-W(L1)))/DN
        IF AN<=0 GOTO 329
        BN=W(L1)*(A2(L3)-A2(L2))+W(L2)*(A2(L1)-A2(L3))+W(L3)*(A2(L2)-A2(L1))
        BN=BN/DN
        WID(IW+1)=EXP(-BN/(2*AN))
        WFAC=0
        GOTO 330
    REM If less than 3 points are available, or if the quadratic method
    REM failed, the next width is calculated in a cruder manner. The
    REM direction of error is determined and an arbitrary step is taken
    REM in that direction.  To avoid stepping back and forth between two
    REM values, the step size is reduced if the direction changes.
```

```
329     OWFAC=WFAC
        IF Y2(FIX(NTS/4))>Y1(FIX(NTS/4)) THEN WFAC=WF0 ELSE WFAC=1/WF0
        IF (LL>5 AND LL<10) THEN WFAC=1/WFAC
        IF ABS(OWFAC*WFAC-1)<0.01 THEN WFAC=SQR(WFAC):WF0=SQR(WF0)
        WID(IW+1)=WID(IW)*WFAC
330     CR=(WID(IW+1)-WID(IW))/WID(IW)
        PRINT:PRINT "WIDTH ITERATION: ";IW:PRINT SADJ,CR,W(IW)
    REM If the step size is small enough, convergence is declared.
        IF ABS(CR)<0.01 THEN WOPT=1
331     WEND
        FLAG=1

332     IF HOPT=1 GOTO 337
    REM The end of the growth curve is found.
        YMX=YE(1)
        FOR I=2 TO NTP
        IF YE(I)>YMX THEN YMX=YE(I)
        NEXT I
        PRINT:PRINT "ITER.","DEG","DIF","RMS"
        T0=2:IH=0:TRM=100
    REM Heating optimization loop.  Heating is optimized by using a least-
    REM squares method, which minimizes the difference between the
    REM experimental and simulated intensities at the end of the growth curve.
        WHILE HOPT=0
        IH=IH+1
        SUMX=0:SUMY=0:SUMXY=0:SUMX2=0
        IF IH=1 GOTO 333
        ON LL GOSUB 610,600,620,630,631,631,631
        GOSUB 311
333     GOSUB 500
        YM1=Y1(NDT1)
        IF Y1(NDT1+1)>YM1 THEN YM1=Y1(NDT1+1)
        DIFA(IH)=(YMX-YM1)*100/YM1
        PRINT IH,HVD(IH),DIFA(IH),RMS
    REM Convergence test.
        IF ABS(DIFA(IH))<0.1 THEN HOPT=1:GOTO 337
        IF IH=1 GOTO 335
    REM If no progress has been made, more drastic measures are called for.
        IF DIFA(IH)=DIFA(IH-1) GOTO 335
        IT=IH-3:IF IT<1 THEN IT=1
        ITN=IH-IT+1
        FOR I=IT TO IH
        SUMX=SUMX+HVD(I)
        SUMY=SUMY+DIFA(I)
        SUMXY=SUMXY+HVD(I)*DIFA(I)
        SUMX2=SUMX2+HVD(I)*HVD(I)
        NEXT I
        P=ITN*SUMXY-SUMX*SUMY
        XM=ITN*SUMX2-SUMX*SUMX
        HVD(IH+1)=(P*SUMX-XM*SUMY)/(ITN*P)
        TRM=100
        GOTO 336
    REM If this is the first iteration, or if the least-squares method
    REM failed, a cruder method is used.
335     OTRM=TRM
        IF DIFA(IH)>0 THEN TRM=-T0 ELSE TRM=T0
        IF OTRM+TRM=0 THEN TRM=TRM/2:T0=T0/2
        HVD(IH+1)=HVD(IH)+TRM
336     TH(IH+1)=(TEMP+HVD(IH+1))/TEMP
337     WEND
    REM Heating optimization is complete.
        IF HVD(IH)>=0 GOTO 338
    REM Cooling during photolysis is not allowed.
        HVD(IH)=0:TH(IH)=1
        ON LL GOSUB 610,600,620,630,631,631,631
        GOSUB 311
        GOSUB 500
        PRINT:PRINT " ",HVD(IH)," ",RMS
```

```
338     HVD$=STR$(FIX(HVD(IH)*100)/100)
        ST$=" "+STR$(HVT)+" SEC hv,"+DIST$+" "+FIL$+" "+STR$(TEMP)+"K (+"+HVD$+
          " during hv)"
        NOTE$="WIDTH ="+STR$(WID(IW))+"  RMS DEV.="+STR$(RMS)
        YA$=Y$+STR$(SADJ)

    REM Option menu.  Many of the options do not work properly for us
    REM because of memory limitations.  They have been left in place for
    REM those who have more available memory.
400     PRINT:PRINT "HIT F1 TO QUIT"
        PRINT "     F2 TO PRINT GRAPH"
        PRINT "     F3 TO FIT DIFFERENT DATA"
        PRINT "     F4 TO CHANGE RATE OPTIMIZATION (DEFAULT)"
        PRINT "     F5 TO CHANGE DISTRIBUTION (WIDTH)"
        PRINT "     F6 TO CHANGE DECAY TIME"
        PRINT "     F7 TO PLOT INTENSITY ON LOG SCALE"
        PRINT "     F8 TO PLOT INTENSITY ON STANDARD SCALE"
        PRINT "     F9 TO REMOVE GRID"
        PRINT "     F10 TO REFIT"
        IF NUMB<>10 THEN NUMB=10:GOTO 50
        GOTO 960

    REM The chosen distribution shape is calculated.  Initial width
    REM calculations are also done by these routines.
260     DIST$="  GAUSSIAN DIST."
        INPUT "STANDARD DEV. OF GAUSSIAN (kcal/mol)";SADJ
        ADJ=1.976E-6/(SADJ*SADJ)
        WID(1)=ADJ*TEMP*TEMP
        Y$="SIGMA(DIST.) ="
        FOR I=0 TO 50
        R(I)=-2.5+I*0.1
        G(I)=EXP(-R(I)*R(I))
        SUMG=SUMG+G(I)
        NEXT I
        RETURN
270     DIST$="  SIEBRAND DIST."
        WOPT=1
        FOR I=0 TO 50
        R1(I)=-2.0+I*.1
        R2(I)=R1(I)
        G(I)=(EXP(R1(I)+EXP(-R1(I))-1))^(-3/2)
        SUMG=SUMG+G(I)
        NEXT I
        RETURN
280     DIST$="  SLATER DIST."
        INPUT "FULL WIDTH AT HALF HEIGHT (kcal/mol)";SADJ
        ADJ=2.755E-3/SADJ
        WID(1)=ADJ*TEMP
        Y$="FWHM ="
        FOR I=0 TO 50
        R(I)=-4+I*0.16
        G(I)=EXP(-ABS(R(I)))
        SUMG=SUMG+G(I)
        NEXT I
        RETURN
290     INPUT "WIDTH OF BOX (kcal/mol) [0 for DELTA FUNCTION]";ADJ
        IF ADJ>0 GOTO 291
        DIST$="  DELTA FUNCTION"
        WOPT=1
        FOR I=0 TO 50
        R1(I)=-2.5+I*.1
        R2(I)=R1(I)
        G(I)=0
        NEXT I
        G(25)=1
        SUMG=1
        RETURN
```

```
291     DIST$="  BOX FUNCTION"
        WID(1)=ADJ/(TEMP*RG)
        Y$="WIDTH ="+STR$(ADJ)
        FOR I=0 TO 50
        R(I)=-0.5+I*0.02
        G(I)=1
        NEXT I
        SUMG=51
        RETURN
292     DIST$="  TWO DELTAS"
        INPUT "DISTANCE B/W DELTA FUNCTIONS (kcal/mol)";ADJ
        INPUT "RELATIVE HEIGHT (RIGHT/LEFT)";RELH
        WID(1)=ADJ/(TEMP*RG)
        Y$="Distance ="+STR$(ADJ)+", Rel. Ht. ="+STR$(RELH)
        FOR I=0 TO 50
        R(I)=-0.5+I*0.02
        G(I)=0
        NEXT I
        G(0)=RELH
        G(50)=1
        SUMG=RELH+1
        RETURN
294     DIST$="  TRIANGLE (SLOW)"
        INPUT "BASE WIDTH (kcal/mol)";ADJ
        WID(1)=ADJ/(TEMP*RG)
        Y$="BASE WIDTH ="+STR$(ADJ)
        FOR I=0 TO 50
        R(I)=I*0.02
        G(I)=50-I
        NEXT I
        SUMG=1275
        RETURN
296     DIST$="  TRIANGLE (FAST)"
        INPUT "BASE WIDTH (kcal/mol)";ADJ
        WID(1)=ADJ/(TEMP*RG)
        Y$="BASE WIDTH ="+STR$(ADJ)
        FOR I=0 TO 50
        R(I)=-1+I*0.02
        G(I)=I
        NEXT I
        SUMG=1275
        RETURN

    REM Rate optimization (fitting the end of the curve).  A least-squares
    REM method is used.
340     IEND=NTS-4
        SUM1=0:SUM2=0
        FOR I=IEND TO NTS
        SUM1=SUM1+Y1(I)
        SUM2=SUM2+Y2(I)
        NEXT I
        AVE1=SUM1/5
        AVE2=SUM2/5
        DIFA(ITER)=(AVE2-AVE1)*100/Y1(NDT1)
        PRINT ITER,RATE(ITER),DIFA(ITER)
    REM Convergence test.
        IF ABS(DIFA(ITER))<0.1 THEN KOPT=1:GOTO 360
        IF ITER=1 GOTO 350
        IF DIFA(ITER)=DIFA(ITER-1) GOTO 350
        IT=ITER-3:IF IT<1 THEN IT=1
        ITN=ITER-IT+1
        FOR I=IT TO ITER
        SUMX=SUMX+RATE(I)
        SUMY=SUMY+DIFA(I)
        SUMXY=SUMXY+RATE(I)*DIFA(I)
        SUMX2=SUMX2+RATE(I)*RATE(I)
        NEXT I
        P=ITN*SUMXY-SUMX*SUMY
        XM=ITN*SUMX2-SUMX*SUMX
        RATE(ITER+1)=(P*SUMX-XM*SUMY)/(ITN*P)
        IF RATE(ITER+1)>0 GOTO 360
```

```
350       IF DIFA(ITER)>0 THEN FAC=0.5 ELSE FAC=2
          RATE(ITER+1)=RATE(ITER)*FAC
360       RETURN

      REM Rate optimization (fitting the entire curve).  A quadratic fit,
      REM similar to the width optimization (above), is used.
370       GOSUB 500
          Q(ITER)=RMS
          IF ITER<3 GOTO 380
          L1=ITER-2:L2=ITER-1:L3=ITER
          FOR I=L1 TO L3
          Z(I)=RATE(I)*RATE(I)
          NEXT I
          DN=RATE(L1)*(Z(L3)-Z(L2))+RATE(L2)*(Z(L1)-Z(L3))+RATE(L3)*(Z(L2)-Z(L1))
          IF DN=0 GOTO 380
          AN=(RATE(L1)*(Q(L3)-Q(L2))+RATE(L2)*(Q(L1)-Q(L3))+RATE(L3)*(Q(L2)-Q(L1))
)/DN
          IF AN<=0 GOTO 380
          BN=(Q(L1)*(Z(L3)-Z(L2))+Q(L2)*(Z(L1)-Z(L3))+Q(L3)*(Z(L2)-Z(L1)))/DN
          IF BN>=0 GOTO 380
          RATE(ITER+1)=-BN/(2*AN)
          FAC=0
          GOTO 385
380       OFAC=FAC
          IF Y2(NTS)>Y1(NTS) THEN FAC=1/F0 ELSE FAC=F0
          IF ABS(OFAC*FAC-1)<0.01 THEN FAC=SQR(FAC):F0=SQR(F0)
          RATE(ITER+1)=RATE(ITER)*FAC
385       CR=(RATE(ITER+1)-RATE(ITER))/RATE(ITER)
          PRINT ITER,RATE(ITER),CR,Q(ITER)
          IF ABS(CR)<0.01 THEN KOPT=1
          RETURN

391   REM No rate optimization.
          KOPT=1
          RETURN

      REM RMS calculation.
500       SUMSQ=0
          FOR I=1 TO NTS
          DIF=Y2(I)-Y1(I)
          SUMSQ=SUMSQ+DIF*DIF
          NEXT I
          RMS=SQR(SUMSQ/NTS1)*100/Y1(NDT1)
          RETURN

      REM The ln(k/k(0)) width during photolysis is calculated for the
      REM appropriate distribution.  The actual values of log(k/k(0)) are
      REM also calculated.
600   REM No width adjustment for this distribution.
          RETURN
610   REM Gaussian distribution.
          WIDH=WID(IW)*TH(IH)*TH(IH)
          FOR I=0 TO 50
          R1(I)=R(I)/SQR(WID(IW))
          R2(I)=R(I)/SQR(WIDH)
          NEXT I
      REM The standard deviation for the current width is calculated.
          SADJ=SQR(1.976E-6/(WID(IW)/(TEMP*TEMP)))
          RETURN
620   REM Slater distribution.
          WIDH=WID(IW)*TH(IH)
          FOR I=0 TO 50
          R1(I)=R(I)/WID(IW)
          R2(I)=R(I)/WIDH
          NEXT I
          RETURN
630   REM Delta (box) function.
          IF ADJ<=0 THEN RETURN
```

```
631 REM Box, two deltas, triangles.
        WIDH=WID(IW)/TH(IH)
        FOR I=0 TO 50
        R1(I)=R(I)*WID(IW)
        R2(I)=R(I)*WIDH
        NEXT I
        RETURN

960 REM Open the Plotting System.
        I1=1:I2=2:I0=0:R0=0.0:R100=100.0:WDTH=11.0:HEIGHT=8.5
        I3=3:I4=4:I5=5:I6=6:I7=7:I102=102:I103=103:R2=50.0:R3=3.0
        YTYP%=1:IGRID=1
5       CALL POPNPS(ST%)
        CALL PSSURF(WDTH,HEIGHT,ST%)
10      CALL PPSOT(STRNG$,ST%)
20      YE1=YE(1):Y10=Y1(0):Y11=Y1(1)
        IF YTYP%=2 THEN YE(1)=YE(2):Y1(0)=Y1(2):Y1(1)=Y1(2)
    REM Define the experimental curve.
        CALL PDSXY(I1,NT,X(1),YE(1),STATUS%)
        CALL PLINE(I1,STATUS%)
        CALL PDSCLR(I1,I2,STATUS%)
        CALL PDSNM(I1,EXL$,STATUS%)
    REM Define the simulated curve.
        CALL PDSXY(I2,NTS1,x1(0),y1(0),STATUS%)
        YE(1)=YE1:Y1(0)=Y10:Y1(1)=Y11
28      CALL pline(I2,STATUS%)
29      CALL PDSCLR(I2,I5,STATUS%)
        CALL PDSWID(I2,I5,STATUS%)
        CALL PDSNM(I2,STR$(RATE(ITER)),STATUS%)
40      CALL PTHD(T$,STATUS%)
        CALL PTHFNT(I102,STATUS%)
        CALL PTHHGT(I4,STATUS%)
        CALL PTSUB(ST$,STATUS%)
        CALL PTSFNT(I103,STATUS%)
        CALL PTSHGT(I2,STATUS%)
        CALL PTAX(I1,XA$,STATUS%)
        CALL PTAX(I2,YA$,STATUS%)
        CALL PTAHGT(I1,I2,STATUS%)
        CALL PTAHGT(I2,I2,STATUS%)
        CALL PLLOC(I1,I1,R100,R100,STATUS%)
        CALL PLALIN(I3,I3,STATUS%)
        CALL PXGRID(IGRID,I2,IGRID,I2,STATUS%)
        CALL PXVFRM(I1,I5,STATUS%)
        CALL PSFORE(I6,STATUS%)
        CALL PAXTYP(I1,YTYP%,ST%)

    REM Output the currently defined chart.
        CALL PPLTIT(STATUS%)
49      CALL PSNHGT(I2,STATUS%)
        CALL PSNCLR(I3,STATUS%)
        CALL PNOTE(I2,R3,R3,NOTE$,STATUS%)

        CALL PPSIN(STRNG$,STATUS%)
    REM Options.
50      CALL PRQCH(I4,NUMB,STATUS%)
        ON NUMB GOTO 78,51,78,54,56,58,60,62,64,78
51      CALL PCLIO(STRNG$,STATUS%)
        CALL PCLIO(STRNG$,STATUS%)
        CALL PPSOT(STRNG2$,STATUS%)
        CALL PPLTIT(STATUS%)
        CALL PSNHGT(I1,STATUS%)
        CALL PNOTE(I2,R3,R3,NOTE$,STATUS%)
        CALL PCLEAR(STATUS%)
        CALL PCLIO(STRNG2$,STATUS%)
        GOTO 10
54      INPUT "STARTING GUESS FOR K(0) IN 1/SEC";RATE(1)
        PRINT "RATE OPTIMIZATION USING END (1) OR ENTIRE CURVE (2)"
        INPUT "(ENTER 0 FOR NO RATE OPTIMIZATION)";IQ
        IF (IQ<1 OR IQ>2) THEN IQ=3
        GOTO 400
```

```
56      PRINT "CHOOSE A DISTRIBUTION:"
        PRINT "1. GAUSSIAN (DEFAULT)"
        PRINT "2. SIEBRAND"
        PRINT "3. SLATER"
        PRINT "4. DELTA (BOX) FUNCTION"
        PRINT "5. TWO DELTA FUNCTIONS"
        PRINT "6. TRIANGLE (SLOW)
        PRINT "7. TRIANGLE (FAST)
        INPUT LL
        IF LL=0 THEN LL=1
        SUMG=0
        ON LL GOSUB 260,270,280,290,292,294,296
        INPUT "WIDTH OPTIMIZATION (Y/N)";ANS$
        GOTO 400
58      INPUT "NEW DECAY TIME TO BE FITTED (min)";TDEC
        IF TDEC<HVT/60 THEN TDEC=HVT/60
        IF TDEC>X1(NTSP) THEN TDEC=X1(NTSP)
        NTS=(TDEC*60-HVT)/DTS+NDT1
        NTS1=NTS+1
        NT=10*(NTS-NDT1)+NDT1
        GOTO 50
60      PRINT "LOG SCALE"
        YTYP%=2
        GOTO 78
62      PRINT "STANDARD SCALE"
        YTYP%=1
        GOTO 78
64      IGRID=0
78      CALL PCLIO(STRNG$,STATUS%)
        CALL PCLSPS(STATUS%)
        ON NUMB GOTO 80,80,210,80,80,80,5,5,5,258
80      END
```

APPENDIX C

DSFIT.BAS

```
    REM                              DSFIT.BAS
    REM
    REM       This program reads distribution-slicing data (temperatures,
    REM times, and intensities), calculates activation energies using an
    REM input log A value, then fits the resulting intensity vs. E(a)
    REM data to an integrated Gaussian distribution.  Both the width
    REM (standard deviation) and most probable E(a) may be optimized.
    REM The intensity vs. E(a) data and simulation may be output to a
    REM file in a format readable by GR.BAS.
    REM
    REM Variables:
    REM   ALA       Log A value.
    REM   AVAL      A value.
    REM   DEV(I)    Deviation of each point from the Gaussian curve.
    REM   EA(I)     Activation energies for the data points.
    REM   EAG(I)    Activation energies for the Gaussian curve.
    REM   EAO       Activation energy optimization switch.
    REM   EOPT      Activation energy optimization flag.
    REM   EO(IE)    Most probable activation energy.
    REM   G(I)      Gaussian distribution over ln(k/k(0)).
    REM   G1(I)     Normalized Gaussian distribution over ln(k/k(0)).
    REM   IE        Counter for activation energy optimization.
    REM   IS        Counter for standard deviation optimization.
    REM   N(I)      Number of data points in a given set.
    REM   NL        Number of data sets.
    REM   NT        Total number of data points.
    REM   R(I)      Width independent ln(k/k(0)) axis.
    REM   RATE      Rate corresponding to a given data point (=ln(2)/TIME).
    REM   RE        Spacing between EAG(I) points.
    REM   RMS(IS)   Root-mean-square deviation for a given SD iteration.
    REM   RMSE(IE)  Optimum RMS for a given EO.
    REM   SD(IS)    Standard deviation.
    REM   SDO       Standard deviation optimization switch.
    REM   SOPT      Standard deviation optimization flag.
    REM   T(I)      Temperature for each data point.
    REM   TIME(I)   Warming time interval for each data point.
    REM   Y(I)      Signal intensity for each data point.
    REM   YG(I)     Intensities for the Gaussian curve.
    REM   YMX       Intact distribution intensity for a given data set.
    REM
        DEFINT I-N
200     DIM T(100),Y(100),TIME(100),EA(100),N(100),SD(200),EO(100)
        DIM RMS(200),RMSE(100),R(50),G(50),G1(50),YG(50),DEV(100)
        DIM EAG(50),Z(200)
210     CLEAR ,,5000
230     CLS
        RG=0.001987

        PRINT "PROGRAM TO FIT DISTRIBUTION SLICING DATA TO A GAUSSIAN"
        PRINT
        INPUT "NAME OF DISTRIBUTION SLICING FILE";FIL$
    REM If no extension is supplied, .DAT is assumed.
        LE=LEN(FIL$)
        FOR I=1 TO LE
        IF MID$(FIL$,I,1)="." GOTO 233
        NEXT I
        FIL$=FIL$+".DAT"
    REM Input block.
233     OPEN "I",1,FIL$
        INPUT#1,T$
        INPUT#1,NL
        NT=0
        FOR I=1 TO NL
        INPUT#1,N(I)
        NT=NT+N(I)
        NEXT I
```

```
        K=0
        FOR I=1 TO NL
        INPUT#1,YMX
        FOR J=1 TO N(I)
        K=K+1
        INPUT#1,T(K),TIME(K),Y(K)
        Y(K)=100*Y(K)/YMX
        NEXT J
        NEXT I
        INPUT "LOG A";ALA
        EA0=0:SD0=0
        INPUT "OPTIMIZE E(a)";EA$
        IF EA$="N" OR EA$="n" THEN EA0=1:INPUT "E(a)";E0(1)
        INPUT "OPTIMIZE WIDTH";SD$
        IF SD$="N" OR SD$="n" THEN SD0=1:INPUT "Std. dev.";SD(1)

    REM Activation energies are calculated for each data point.
        AVAL=10^ALA
        FOR I=1 TO NT
        RATE=LOG(2.0)/TIME(I)
        EA(I)=-RG*T(I)*LOG(RATE/AVAL)
        NEXT I

    REM The Gaussian distribution is calculated.
        SUMG=0
        FOR I=0 TO 50
        R(I)=2.5-I*0.1
        G(I)=EXP(-R(I)*R(I))
        SUMG=SUMG+G(I)
        NEXT I
    REM The distribution is normalized and integrated.
        G1(0)=(G(0)/SUMG)*100
        YG(0)=100-G1(0)/2
        FOR I=1 TO 50
        G1(I)=(G(I)/SUMG)*100
        YG(I)=YG(I-1)-(G1(I-1)+G1(I))/2
        NEXT I

        IS=1
    REM The initial guess for the standard deviation is calculated.
        IF SD0=0 THEN SD(IS)=(EA(NT)-EA(1))/4
    REM The approximate center of the experimental distribution is found.
        I=1
        WHILE Y(I)>50
        I=I+1
        WEND
        I50=I
        IF EA0=1 GOTO 300
    REM The initial guess for most probable E(a) is calculated.
        E0(1)=EA(I-1)+(EA(I)-EA(I-1))*(Y(I-1)-50)/(Y(I-1)-Y(I))
        T0=E0(1)/10
300     PRINT "E(a)","% change","Std. dev.","% change","RMS"

    REM The E(0) optimization constitutes the outer loop.
        EOPT=0:TERM=100:IE=0
        WHILE EOPT=0
        IE=IE+1
    REM The optimized width from the last iteration becomes the initial guess.
        SD(1)=SD(IS)
        IF EA0=1 THEN EOPT=1

    REM The width optimization is the inner loop.
        SOPT=0:IS=0:PCS=0:F0=2:FAC=0:CC=0
        WHILE SOPT=0
        IS=IS+1
    REM The goodness of fit is evaluated.
        GOSUB 1000
        IF IS=200 GOTO 1200
        IF SD0=1 THEN SOPT=1:GOTO 455
```

```
    REM Every fifth width iteration is reported.
        CC=CC+1
        IF CC=1 THEN PRINT " "," ",SD(IS),PCS,RMS(IS)
        IF CC=5 THEN CC=0
        IF IS<3 GOTO 400

    REM The next width is calculated from the previous three using a
    REM quadratic fit of the root-mean-squared deviation over standard
    REM deviation.  Cramer's Rule is used.  This method gives best
    REM results on data which has little scatter.  Problems sometimes
    REM arise with poorer data sets, because the rms deviation does not
    REM vary smoothly with width or E(0).  For cases such as these, a
    REM grid-type optimization, in which many values of SD and E0 are
    REM used and the best fit then selected, may work better.
        L1=IS-2:L2=IS-1:L3=IS
        FOR I=L1 TO L3
        Z(I)=SD(I)*SD(I)
        NEXT I
        DN=SD(L1)*(Z(L3)-Z(L2))+SD(L2)*(Z(L1)-Z(L3))+SD(L3)*(Z(L2)-Z(L1))
        IF DN=0 GOTO 400
        AN=(SD(L1)*(RMS(L3)-RMS(L2))+SD(L2)*(RMS(L1)-RMS(L3))+SD(L3)*(RMS(L2)-
           RMS(L1)))/DN
        IF AN<=0 GOTO 400
        BN=RMS(L1)*(Z(L3)-Z(L2))+RMS(L2)*(Z(L1)-Z(L3))+RMS(L3)*(Z(L2)-Z(L1))
        BN=BN/DN
        IF BN>=0 GOTO 400
        SD(IS+1)=-BN/(2*AN)
        FAC=0
        GOTO 450

    REM If less than 3 points are available, or if the quadratic method
    REM failed, the next width is calculated in a cruder manner.  The
    REM direction of error is determined and an arbitrary step is taken
    REM in that direction.  To avoid stepping back and forth between two
    REM values, the step size is reduced if the direction changes.
400     SUMDEV=0:OFAC=FAC
        FOR I=1 TO NT
        IF I<I50 THEN DEV(I)=-DEV(I)
        SUMDEV=SUMDEV+DEV(I)
        NEXT I
        IF SUMDEV>0 THEN FAC=F0 ELSE FAC=1/F0
        IF ABS(OFAC*FAC-1)<0.01 THEN FAC=SQR(FAC):F0=SQR(F0)
        SD(IS+1)=SD(IS)*FAC

    REM If the step size is small enough, convergence is declared.
450     PCS=(SD(IS+1)-SD(IS))/SD(IS)
        IF ABS(PCS)<0.001 THEN SOPT=1
455     WEND

        RMSE(IE)=RMS(IS)
        IF IE=100 THEN GOSUB 1100
        IF EOPT=1 GOTO 555
        IF IE<3 GOTO 500

    REM The next E0 is calculated using the same method as for SD.
        L1=IE-2:L2=IE-1:L3=IE
        FOR I=L1 TO L3
        Z(I)=E0(I)*E0(I)
        NEXT I
        DN=E0(L1)*(Z(L3)-Z(L2))+E0(L2)*(Z(L1)-Z(L3))+E0(L3)*(Z(L2)-Z(L1))
        IF DN=0 GOTO 500
        AN=(E0(L1)*(RMSE(L3)-RMSE(L2))+E0(L2)*(RMSE(L1)-RMSE(L3))+E0(L3)*
          (RMSE(L2)-RMSE(L1)))/DN
        IF AN<=0 GOTO 500
        BN=(RMSE(L1)*(Z(L3)-Z(L2))+RMSE(L2)*(Z(L1)-Z(L3))+RMSE(L3)*
          (Z(L2)-Z(L1)))/DN
        IF BN>=0 GOTO 500
        E0(IE+1)=-BN/(2*AN)
        TERM=100
        GOTO 550
```

```
    REM The backup method for obtaining the next E0 is the same as for
    REM SD, except that here the technique is additive instead of
    REM multiplicative.
500     OTERM=TERM:SUMDEV=0
        GOSUB 1000
        FOR I=1 TO NT
        SUMDEV=SUMDEV+DEV(I)
        NEXT I
        IF SUMDEV>0 THEN TERM=T0 ELSE TERM=-T0
        IF OTERM+TERM=0 THEN TERM=TERM/2:T0=T0/2
        E0(IE+1)=E0(IE)+TERM

550     PCE=(E0(IE+1)-E0(IE))/E0(IE)
        PRINT E0(IE),PCE,SD(IS),PCS,RMSE(IE)
        IF ABS(PCE)<0.001 THEN EOPT=1
555     WEND

    REM This is a convenient way to calculate the spacing on the E(a)
    REM scale.  The standard Gaussian calculated above has SD=SQR(0.5),
    REM so the next statement gives a scaling factor.
        RE=SD(IS)/SQR(.5)
    REM The E(a) scale is calculated for the simulation.
        FOR I=0 TO 50
        EAG(I)=E0(IE)-R(I)*RE
        NEXT I
    REM The results are reported.
        PRINT:PRINT "GIVEN LOG A =";ALA
        PRINT " THEN E(a)  =";E0(IE)
        PRINT "  Std. dev. =";SD(IS)
        PRINT "       RMS  =";RMSE(IE)

        INPUT "OUTPUT FILE (RETURN FOR NO FILE)";FILOUT$
        IF FILOUT$="" GOTO 2000
    REM The data and simulation are output in GR.BAS format.
        OPEN "O",2,FILOUT$
        PRINT#2,T$
        PRINT#2,USING"Log A =###.##  E(a) =##.###  Std. dev. =##.###  RMS =##.##
#";ALA;E0(IE);SD(IS);RMSE(IE)
        PRINT#2,"ACTIVATION ENERGY (kcal/mol)"
        PRINT#2,"INTENSITY"
        PRINT#2,NL+1
        PRINT#2,"51"
        FOR I=1 TO NL
        PRINT#2,N(I)
        NEXT I
        FOR I=0 TO 50
        PRINT#2,EAG(I),YG(I)
        NEXT I
        FOR I=1 TO NT
        PRINT#2,EA(I),Y(I)
        NEXT I
        GOTO 2000
```

```
    REM Goodness of fit calculation
    REM The E(a) scaling factor for the current width is calculated.
1000    DE=0.1*SD(IS)/SQR(.5)
        SUMSQ=0
        FOR I=1 TO NT
    REM P is the position of a given point in the Gaussian distribution.
        P=(EA(I)-EQ(IE))/DE+25
        IF P<0 THEN YF=100:GOTO 1010
        IF P>=50 THEN YF=0:GOTO 1010
    REM II is the nearest E(a) index for a given point.
        II=CINT(P)
    REM YF is the interpolated value of the Gaussian at the current
    REM point's E(a).
        YF=YG(II)-(P-II)*G1(II)
    REM The deviation of the point from the Gaussian is calculated, first
    REM vertically, then at a perpendicular to the Gaussian.  If the
    REM vertical deviation is used in the optimization, points near 50%
    REM decay are weighted too heavily.
1010    DEV(I)=Y(I)-YF
        IF P-II<0 THEN II=II-1
        DY=YG(II)-YG(II+1)
        HYP=SQR(DE*DE+DY*DY)
        DEV(I)=DEV(I)*DE/HYP
        SUMSQ=SUMSQ+DEV(I)*DEV(I)
        NEXT I
        RMS(IS)=SQR(SUMSQ/NT)
        RETURN

    REM Bail out of EQ optimization.
1100    PRINT:PRINT "100 E(a)'S HAVE BEEN CONSIDERED WITHOUT CONVERGENCE."
        INPUT "DO YOU WISH TO CONTINUE (1) OR TAKE THE BEST OF 100 (2)";ANS
        IF ANS=1 GOTO 1110
        RMIN=RMSE(1):IE=1
        FOR I=2 TO 100
        IF RMSE(I)<RMIN THEN IE=I
        NEXT I
        EOPT=1
        RETURN
    REM The arrays are reset to continue the optimization.
1110    EQ(1)=EQ(98):EQ(2)=EQ(99):EQ(3)=EQ(100)
        RMSE(1)=RMSE(98):RMSE(2)=RMSE(99):RMSE(3)=RMSE(100)
        IE=3
        RETURN

    REM Bail out of width optimization
1200    PRINT:PRINT "TAKING THE BEST OF 200 WIDTHS"
        RMIN=RMS(1):IS=1
        FOR I=2 TO 200
        IF RMS(I)<RMIN THEN IS=I
        NEXT I
        SOPT=1
        GOTO 455
2000    END
```

APPENDIX D

SLICE.BAS

```
    REM                          SLICE.BAS
    REM
    REM      This program generates simulated distribution-slicing data
    REM using the basic algorithm of DECAY.BAS.  The experiment is
    REM simulated in a chronological sense.  The distribution after each
    REM warming interval is calculated from that after the previous cycle
    REM by calculating the decay over the interval.  The simulated data
    REM is output in a format readable by DSFIT.BAS.
    REM
    REM Variables:
    REM   ADJ       Temperature independent width.
    REM   ALA       Log A value.
    REM   AVAL      A value.
    REM   D         Fraction of decay for a given rate constant, TIME, and TEMP.
    REM   EA(I)     Activation energies for the data points.
    REM   EO        Most probable activation energy.
    REM   F         Distribution component.
    REM   G(I)      Gaussian distribution over ln(k/k(0)).
    REM   NT        Total number of data points.
    REM   R(I)      Width independent ln(k/k(0)) axis.
    REM   RATLOG    Natural logarithm of the most probable rate contant.
    REM   RHALF     Rate corresponding to a given data point (=ln(2)/TIME).
    REM   RE        Ln(k/k(0)) scaling factor.
    REM   RR        Temperature/Ea conversion factor.
    REM   RRR       Natural logarithm of a given rate constant.
    REM   SD        Standard deviation.
    REM   TEMP(I)   Temperature for each data point.
    REM   THALF     Warming time interval.
    REM   WID       Temperature dependent width.
    REM   Y(I)      Signal intensity for each data point.
    REM   YMX       Intact distribution intensity for a given data set.
    REM
10      DEFINT I-N
        DIM R(50),G(50),Y(50),EA(50),TEMP(50)
        RG=0.001987
        CLS

50      PRINT "PROGRAM FOR SIMULATION OF DISTRIBUTION SLICING (GAUSSIAN)"
        PRINT
    REM Input block.
        INPUT "LOG A";ALA
        INPUT "ACTIVATION ENERGY (kcal/mol)";EO
        INPUT "STANDARD DEVIATION (kcal/mol)";SD
        INPUT "WARMING TIME (sec)";THALF
        INPUT "NUMBER OF SLICES (2 TO 51)";NT
    REM The number of slices may not be exactly the same as requested
    REM because of round-off error.
        ISTEP=FIX(50/(NT-1))
        NT=50/ISTEP+1
        PRINT "WILL USE";NT;"SLICES"

    REM Preliminary calculations.
100     AVAL=10^ALA
        EAR=EO/RG
        RHALF=LOG(2.0)/THALF
        RR=LOG(RHALF/AVAL)*RG
        SUMG=0
        ADJ=1.976E-6/(SD*SD)
        RE=RG/SQR(ADJ)
    REM The Gaussian distribution is calculated, along with Ea and TEMP scales.
        FOR I=0 TO 50
        R(I)=2.5-I*0.1
        G(I)=EXP(-R(I)*R(I))
        SUMG=SUMG+G(I)
        EA(I)=EO-R(I)*RE
        TEMP(I)=-EA(I)/RR
    REM Negative temperatures are not allowed.
        IF TEMP(I)<=0 THEN TEMP(I)=1E-6
        NEXT I
```

```
    REM The main loop.
150     FOR K=0 TO 50 STEP ISTEP
        RATLOG=2.303*ALA-EAR/TEMP(K)
        WID=ADJ*TEMP(K)*TEMP(K)
        Y(K)=0
        FOR I=0 TO 50
        R1=R(I)/SQR(WID)
        RRR=RATLOG+R1
    REM This statement avoids a possible overflow.
        IF RRR>50 THEN D=0:GOTO 200
        D=EXP(-EXP(RRR)*THALF)
200     F=D*G(I)/SUMG
        Y(K)=Y(K)+F*100
        NEXT I
        NEXT K

    REM Output block.
250     OPEN "O",#1,"SLICE.DAT"
        PRINT#1,"Simulated Distribution Slicing"
        PRINT#1,"1"
        PRINT#1,NT
        PRINT#1,Y(0)
        FOR K=0 TO 50 STEP ISTEP
        PRINT#1,TEMP(K),THALF,Y(K)
        NEXT K
300     PRINT:PRINT "OUTPUT IN SLICE.DAT"
        END
```

APPENDIX E

MERGE.BAS

```
      REM                              MERGE.BAS
      REM
      REM       This program reads in activation parameters (log A, most
      REM probable E(a), and standard deviation of the Gaussian E(a)
      REM distribution) and integrates to give an intensity vs. E(a) curve.
      REM Decay-trace data files are then read in and normalized to the
      REM Gaussian curve by using the end of each trace.  YMAX, a parameter
      REM needed to use FIT.BAS, is output.  If desired, the entire set
      REM of decay traces are output in the form of a merged intensity vs.
      REM E(a) plot, along with the idealized Gaussian curve.  This output
      REM file can be read and plotted by using GR.BAS.
      REM
      REM Variables:
      REM   ALA       Log A value.
      REM   AVAL      A value.
      REM   DTL       Logarithmic spacing between output decay trace points.
      REM   EA(I)     Activation energies for the data points.
      REM   EAEND     Activation energy at the end of a decay trace.
      REM   EAG(I)    Activation energies for the Gaussian curve.
      REM   EO        Most probable activation energy.
      REM   G(I)      Gaussian distribution over ln(k/k(0)).
      REM   G1(I)     Normalized Gaussian distribution over ln(k/k(0)).
      REM   NF        Number of data files.
      REM   NT        Total number of data points.
      REM   NTL       Number of points in an output decay trace.
      REM   R(I)      Width-independent ln(k/k(0)) axis.
      REM   RATE      Rate corresponding to a given data point (=ln(2)/TIME).
      REM   RE        Spacing between EAG(I) points.
      REM   SD        Standard deviation.
      REM   TEMP      Temperature for a given decay trace.
      REM   X(I)      Time axis for a given decay trace.
      REM   YE(I)     Intensity scale for a given decay trace.
      REM   YG(I)     Intensities for the Gaussian curve.
      REM   YMAX      Intensity at the end of photolysis.
      REM
50        DEFINT I-N
          DIM YE(1005),YG(50),R(50),G(50),G1(50),EAG(50),EA(50),X(1000)
          DIM DAT$(67)
          CLEAR ,,5000
          CLS
          RG=0.001987

          PRINT "PROGRAM TO MERGE DECAY TRACES INTO A SINGLE PLOT OF"
          PRINT "INTENSITY VS. E(a).  ALSO PROVIDES YMAX FOR DECAY FITTING."
          PRINT
      REM Input block.
          INPUT "LOG A";ALA
          INPUT "ACTIVATION ENERGY (kcal/mol)";EO
          INPUT "STANDARD DEVIATION OF DIST. (kcal/mol)";SD
          INPUT "NUMBER OF DECAY TRACES TO BE READ";NF
          INPUT "DO YOU WANT A MERGED OUTPUT FILE";MOF$
          IF MOF$="Y" OR MOF$="y" THEN MOF=1 ELSE MOF=0

          AVAL=10^ALA
          ADJ=1.976E-6/(SD*SD)
          RE=RG/SQR(ADJ)
          SUMG=0
      REM The Gaussian distribution is calculated.
          FOR I=0 TO 50
          R(I)=2.5-I*0.1
          G(I)=EXP(-R(I)*R(I))
          SUMG=SUMG+G(I)
          EAG(I)=EO-R(I)*RE
          NEXT I
      REM The distribution is normalized.
          YG(0)=100*(1-(G(0)/SUMG)/2)
          FOR I=1 TO 50
          G1(I)=(G(I)/SUMG)*100
          YG(I)=YG(I-1)-(G1(I-1)+G1(I))/2
          NEXT I
```

```
    REM Preliminary output to the merged file.
        IF MOF=0 GOTO 100
        INPUT "NAME OF OUTPUT FILE";OFIL$
        OPEN "O",#2,OFIL$
        INPUT "TITLE";T$
        PRINT#2,T$
        PRINT#2,USING"Log A =###.##  E(a) =##.###  Std. dev. =##.##";ALA;EO;SD
        PRINT#2,"Activation Energy (kcal/mol)"
        PRINT#2,"Intensity"
        PRINT#2,NF+1
        PRINT#2,"51"
        FOR I=1 TO NF
        PRINT#2,"50"
        NEXT I
        FOR I=0 TO 50
        PRINT#2,EAG(I),YG(I)
        NEXT I

100     FOR L=1 TO NF
        PRINT:PRINT "NAME OF DATA FILE NUMBER";L
        INPUT FIL$
    REM If no extension is supplied, .DAT is assumed.
        LE=LEN(FIL$)
        FOR I=1 TO LE
        IF MID$(FIL$,I,1)="." GOTO 150
        NEXT I
        FIL$=FIL$+".DAT"
    REM The following is the input/baseline correction routine from FIT.BAS.
150     OPEN "I",#1,FIL$
        INPUT#1,DUM$
        FOR I=1 TO 67
        INPUT#1,DAT$(I)
        WHILE (LEN(DAT$(I))<60)
        DAT$(I)="0"+DAT$(I)
        WEND
        NEXT I
        K=0
        FOR I=1 TO 67
        FOR J=1 TO 57 STEP 4
        K=K+1
        YE(K)=VAL(MID$(DAT$(I),J,4))
        NEXT J
        NEXT I
        INPUT#1,IX1,IX2,IX3,IX4,IX5,IX6,TEMP,HVT,SCT
        CLOSE #1
        IF IX5=0 THEN IX5=1
        IF IX6=0 THEN IX6=1000
        DT=SCT*60/1000
        FOR I=1 TO 1000
        X(I)=DT*(I-1)
        NEXT I
        SUMYE=0
        FOR I=IX5 TO IX1
        SUMYE=SUMYE+YE(I)
        NEXT I
        AAV=SUMYE/(IX1+1-IX5)
        SUMYE=0:INB=IX1+10
        FOR I=INB TO IX2
        SUMYE=SUMYE+YE(I)
        NEXT I
        BAV=SUMYE/(IX2+1-INB)
        SUMYE=0:INC=IX4+10
        FOR I=INC TO IX6
        SUMYE=SUMYE+YE(I)
        NEXT I
        CAV=SUMYE/(IX6+1-INC)
        BDC=(AAV-CAV)/((IX6+INC-IX1-IX5)/2)
        FOR I=IX2 TO IX4
        YE(I)=YE(I)+BDC*I-BAV
        NEXT I
```

```
        NT=IX4-IX3+1
        FOR I=1 TO NT
        YE(I)=YE(IX3+I-1)
        NEXT I

    REM The intensity at the end of the trace is determined.  An average
    REM of 15 values is used to avoid errors due to noise.
200     SUMEND=0
        FOR I=NT-14 TO NT
        SUMEND=SUMEND+YE(I)
        NEXT I
        YEND=SUMEND/15
        EAEND=-RG*TEMP*LOG(LOG(2.0)/(AVAL*(X(NT-7)+HVT/2)))
    REM YMAX is calculated by locating EAEND in the Gaussian and interpolating.
        P=(EAEND-E0)/(0.1*RE)+25
        IF P<0 THEN YMAX=100:GOTO 250
        IF P>=50 THEN YMAX=0:GOTO 250
        II=CINT(P)
        YMAX=(YG(II)-(P-II)*G1(II))*YE(1)/YEND
    REM YMAX is output to the screen.
250     PRINT USING"YMAX FOR & =###.##";FIL$;YMAX

        IF NT<=50 THEN NTL=NT:GOTO 300
        NTL=50
    REM The decay-trace points to be output are assigned.  A logarithmic
    REM time scale is used to give an even Ea spacing.
        DTL=LOG(X(NT))/NTL
        JL=0
        FOR I=1 TO NTL
    REM The next four lines assure that points are not repeated near the
    REM beginning of the trace.
        TL=DTL*(I-1)
        J=(EXP(TL)-1)/DT+1
        IF J<=JL THEN J=JL+1
        JL=J
        YE(I)=YE(J)
        X(I)=X(J)
        NEXT I
    REM The time axis is adjusted to reflect the fact that on average,
    REM species are generated halfway through the photolysis.
        FOR I=1 TO NTL
        X(I)=X(I)+HVT/2
        NEXT I

    REM The decay-trace intensities are scaled according to YMAX.
300     SCALE=YMAX/YE(1)
        FOR I=1 TO NTL
        YE(I)=YE(I)*SCALE
    REM Activation energies are calculated for each data point.
        EA(I)=-RG*TEMP*LOG(LOG(2.0)/(AVAL*X(I)))
        NEXT I
        IF MOF=0 GOTO 350
    REM The decay trace is output to the merged file.
        FOR I=1 TO NTL
        PRINT#2,EA(I),YE(I)
        NEXT I
        IF NTL=50 GOTO 350
    REM Short traces are padded to give 50 points.
        FOR I=NTL+1 TO 50
        PRINT#2,EA(NTL),YE(NTL)
        NEXT I
350     NEXT L
400     END
```

APPENDIX F

FIT.BAS DATA FILE FORMAT

```
FILE # 24MBS4                  10/25/86            FROM EPR DATA
 604 574 611 583 579 624 543 591 608 542 572 604 600 583 608
 572 624 608 600 591 624 609 640 591 583 611 624 608 574 600
 583 608 611 606 640 627 595 606 591 583 593 583 585 608 591
 604 609 592 579 573 600 609 583 572 543 583 572 608 569 572
 579 511 560 579 583 556 543 547 551 579 569 600 568 577 543
 577 572 579 582 561 542 642 572 579 542 577 574 561 582 572
 572 577 593 576 577 572 579 559 542 608 568 576 582 542 577
 542 542 551 577 577 576 543 503 561 579 611 728 99012401484
171919522128229725032673284629593009297429512936295629102915
287829122883288528472831284828812846280728302840281128302818
280028192779276727912784275028162759275527442745275227552718
273627182736272727032736271626812699271227022716269126842694
268426952693267326632663269227022672263926222656267226592656
263926222652262226542623265726312620263726382627263126302616
262226572625262725752625262425992599260425922616259325882616
258326242624259325752567255925532527257825432549258825882576
254325512608256125432531254725472574253525682576254525522535
253525442511254225472545251125442531252725262560254425262531
253125292519253625362524252225442535256025312520252025032495
250325642529251125102504249424992502249525602494249249924922492
249824972488246224292496249924632497246224472463250224882447
248824622463249924712455244724712481249724672465249724962463
244724882462246224622478250124632465249724292496248024622444
244624462431249724602446246524482447246024352439242824292464
242824392465242824322435243924482446249724352428242424332433
239824382419243924462424243824382417241724172421241724172424
239924352419241924322416242424382428243324382396240724242416
242424282424239324092395239824382425240324012416236723962398
239624162416238024332400238323823243224162383241624342383242424
240023642367240424162432240623832375237524162367237523832366
238323642375238224012388238024342375236123642400237524002400
240023712360237024012401240023642350235823712367233322992371
236924322369236823192343237523752371236023712371233223532369
236023362370236423602364233423322352233523602334236823682319
233523642369233523712353235223602360236024322368234323552337
233323602339234323602360233423602319235223192353235223603052
232723342334236023692368235023352360235223112368233923432319
233223192319233223192367229923182336233223182318232823392319
232722992319230323112318231222912369230723182291230023182319
231923322322300231123192316231123372310231122992311229723332
230723522300231923182368231123112307231822952291232022952297
232822972310231622912297233223162289231622712318231123282328
231622912316232022972311227923102289232023102310227522892275
232822752279229122962279231230823162279228723122296229423002
227522962296227923042308231223062305231623162275228923082271
229622882273227523162275227923082312229622632316226322702279
229622472247227523042291227522642275227522552279230022552316
230822922289228822682308225522652236227522842312226822752275
227522552296228922552255227522752273228822882247228822732255
227022882254225422732273227322892272223622882268227322732256
226422642259227022732254226222472265227322882243224722472273
230422882238227322682247223922572238225722392288226822722236
228822412272225422552308220722412241228822382238225422412241
227322552273225722472247224722542243224322362236223822072207
225222722273224122472232225622432247224722322247224322332236
224122412207223622412232220622472272223622322273224722412273
227222072243224322322241227322592238223322472236224322432234
223222292232224722322382207223822232273223822062308227222232
223222352227230822362215224122362233220721752240224322062240
222322322432232224122472236222522062207222522722233224022244
220722402282422272215219122252232220722232206224122072243223 9
224322062207224022322322242241222152207224322432240220422242
224122252215222422432224220722412209220422062240222422422208
220522412206224022472228223622041164 606 606 608 574 608 583
 600 574 590 609 624 575 624 595 598 591 583 579 644 574 590
 568 608 624 591 583 511 574 575 624 575 583 572 609 608 574
 600 579 608 575 575 572 591 608 642 604   0   0   0   0   0
  58 115 126 953   0   0 34.5 20  30   0   0   0   0   0   0
 3.0000000E+03 1.0000000E+00 1.0000000E+00 3.0000000E+01 1.0000000E+01
 1.0000000E-01 3.0000000E+01 9.2510000E+00  .0000000E+00  .0000000E+00
  .0000000E+00  .0000000E+00 1.5000000E+01 2.4000000E+01 1.0000000E+00
  .0000000E+00 2.0000000E+04 1.0000000E+02 1.0000000E+00 1.0000000E+03
 1.0000000E+00 2.8700000E+02 3.0090000E+03
MBS          10/25/86                MBS4         657
DIVINYL AZO IN MTHF (MS-II-201A)
KINETICS UPON 20 SEC HV (WG-305, KG-5, UG-11)
```